FUNCTIONAL BRAIN NETWORKS UNDERLYING WORKING MEMORY PERFORMANCE IN SCHIZOPHRENIA: A MULTI-EXPERIMENT APPROACH

by

NICOLE A. SANFORD
B.A., McGill University, 2010
M.Sc., University of British Columbia, 2014

A DISSERTATION SUBMITTED IN PARTIAL FULFILLMENT OF
THE REQUIREMENTS FOR THE DEGREE OF

DOCTOR OF PHILOSOPHY

in

THE FACULTY OF GRADUATE AND POSTDOCTORAL STUDIES
(Neuroscience)

THE UNIVERSITY OF BRITISH COLUMBIA
(Vancouver)

December 2019

The following individuals certify that they have read, and recommend to the Faculty of Graduate and Postdoctoral Studies for acceptance, the dissertation entitled:

Functional Brain Networks Underlying Working Memory Performance in Schizophrenia: A Multi-Experiment Approach

submitted by Nicole Sanford in partial fulfillment of the requirements for

the degree of Doctor of Philosophy

in Neuroscience

Examining Committee:

Todd Woodward, Psychiatry
Supervisor

Christine Tipper, Psychiatry
Supervisory Committee Member

Alan Kingstone, Psychology
University Examiner

Anthony Herdman, Audiology and Speech Sciences
University Examiner

Martin Lepage, Psychiatry (McGill University)
External Examiner

Additional Supervisory Committee Members:

Rebecca Todd, Psychology
Supervisory Committee Member

Lawrence Ward, Psychology
Supervisory Committee Member

Abstract

Working memory (WM), defined as actively holding and/or manipulating information in mind, is central in guiding behaviour. WM is also a core domain of impairment in schizophrenia which substantially impacts functional outcome. Although the dorsolateral prefrontal cortex (DLPFC) has been implicated as a source of WM deficits in schizophrenia, these deficits may be better characterized within the framework of functional connectivity of distributed brain regions. However, in task-state functional magnetic resonance imaging (fMRI) research, the sluggish hemodynamic response hinders the separation of cognitive sub-processes in WM tasks. Moreover, findings from an individual fMRI task may not be broadly clinically meaningful even if reliable effects are detected. The present research used whole-brain, multi-experiment, functional connectivity analyses to obtain more refined characterizations of WM networks and their activity in schizophrenia across a variety of cognitive tasks. Study 1 demonstrated a novel method of combining a verbal WM task with a thought generation task, which produced a finer delineation of networks than when the WM task was analysed alone. Study 2 reported individual analyses of four tasks (i.e., verbal WM, thought generation, visuospatial WM, and set-switching Stroop tasks), providing basic characterizations of their dominant networks in healthy individuals. Finally, study 3 consolidated all four datasets into a unified analysis to examine differences between healthy controls and schizophrenia patients in the resulting networks, as well as correlations between these networks and task performance. A visual attention network – engaged during encoding of memory sets, and diminished in patients – was associated with accuracy in the verbal and visuospatial WM tasks, and with WM capacity measured in separate out-of-scanner testing sessions. A frontoparietal network including the DLPFC – possibly underlying internally-oriented attention – exhibited hypoactivity in patients as expected, but was not correlated with behaviour-

al WM measures. These findings suggest that dysfunction in a given network cannot be assumed to underlie poor task performance, as this may depend on the cognitive sub-process it supports. This work also demonstrates that a network may be concealed in an individual task when it does not account for a distinct portion of variance, yet may exhibit reliable activity when examined across multiple tasks.

Lay Summary

Working memory is a core aspect of cognitive impairment in schizophrenia which substantially impacts daily living. This research examined brain networks engaged during working memory and other cognitive tasks in individuals with a diagnosis of schizophrenia and in healthy controls. A multi-experiment analysis was used which allowed for the examination of activity in a given network across different types of cognitive demands. This resulted in a finer separation of brain networks which had been obscured when analyzed using more conventional methods. While schizophrenia patients exhibited diminished activity in a number of networks, one network was particularly notable because its activity was correlated with accuracy in verbal and visuospatial working memory tasks, and with working memory span. As this network was engaged during the initial encoding of items to be remembered, the results suggest that working memory deficits in schizophrenia may be due to problems during early memory encoding.

Preface

This dissertation is the original intellectual product of the author, Nicole Sanford. The analyses reported in this dissertation comprise secondary use of data from previously completed studies as well as new data collected for this work. All data collection carried out at the University of British Columbia (UBC) was approved by the UBC Clinical Research Ethics Board (Certificate numbers: H07-02786 and H14-02687).

The Spatial Capacity (SCAP) Task data, analysed in Chapters 4 and 5, were obtained from the OpenfMRI database (https://openfmri.org/dataset/ds000030/; accession number is ds000030), and originally collected as part of the UCLA Consortium for Neuropsychiatric Phenomics LA5c Study (Poldrack et al., 2016). Data for the Thought Generation Task (TGT), analyzed in Chapters 3-5, were obtained from a previously completed study (certificate H07-02786) carried out in the Cognitive Neuroscience of Schizophrenia Lab at UBC, under the supervision of Dr. Todd Woodward. Primary data collection of the verbal Working Memory (WM) task and the Task-Switch Inertia (TSI) task was also carried out under the supervision of Dr. Woodward (certificate H14-02687); I was involved in development of the research design, testing protocols, hypotheses, and assisted with data collection. Dr. Jennifer Whitman programmed the first version of the verbal WM task implemented in this work, and I added minor revisions to facilitate task instruction. I programmed the TSI task and carried out initial pilot testing.

The work reported in Chapter 3, "Finer Separation of Working Memory Networks Using Multi-Experiment fMRI-CPCA", has been accepted for publication in the journal *Cortex* as "Sanford, N., Whitman, J. C., & Woodward, T. S. W. (In Press). Task-merging for finer separation of functional brain networks in working memory. *Cortex*." Some revisions have been made for coherence with the rest of this dissertation. As first author, I designed and carried out the

analysis, and wrote the original manuscript. Dr. Whitman programmed the original version of the WM task as stated above, and was involved in discussions of the results and in suggesting revisions to an earlier draft. Dr. Woodward was the principal investigator on this research and contributed throughout the project with respect to design, analysis, and manuscript revisions.

Table of Contents

List of Tables

List of Figures

List of Abbreviations

AHPQ	Annett Hand Preference Questionnaire
ANOVA	Analysis of variance
BA	Brodmann area
BOLD	Blood oxygen level-dependent
ci	Task-switch from incongruent colour-naming block
cn	Task-switch from neutral colour-naming block
(C)PCA	(Constrained) principal component analysis
CRT	Cognitive remediation therapy
DLPFC	Dorsolateral prefrontal cortex
DMN	Default mode network
DSM	Diagnostic and Statistical Manual of Mental Disorders
FIR	Finite impulse response
(f)MRI	(Functional) magnetic resonance imaging
HDR	Hemodynamic response
HRF	Hemodynamic response function
ICA	Independent component analysis
IQ	Intelligence quotient
ITI	Inter-trial interval
ITP	Increase-to-peak
MINI	Mini International Neuropsychiatric Interview
MNI	Montreal Neurological Institute
PLS	Partial least squares

ROI	Region of interest
RT	Reaction time
RTB	Return-to-baseline
SANS	Scale for the Assessment of Negative Symptoms
SAPS	Scale for the Assessment of Positive Symptoms
SCAP	Spatial Capacity
SD	Standard deviation
SEM	Standard error of the mean
SES	Socioeconomic status
SIRP	Sternberg Item Recognition Paradigm
SMA	Supplementary motor area
SSPI	Signs and Symptoms of Psychotic Illness
TGT	Thought Generation Task
TR	Time to repetition
TSI	Task-Switch Inertia
UBC	University of British Columbia
WAIS	Wechsler Adult Intelligence Scale
WI	Incongruent word-reading sitmulus
WM	Working memory
WMS	Wechsler Memory Scale
WN	Neutral word-reading stimulus

Acknowledgements

I would like to express my sincere gratitude to my supervisor, Dr. Todd Woodward, for his mentorship, support, and opportunities provided over the years. I would also like to thank current and past members of the Cognitive Neuroscience of Schizophrenia (CNOS) Lab who have made this research possible, including but not limited to Sarah Flann, Jennifer Riley, Kelsey Block, Meighen Roes, Julia O'Loughlin, Jessica Khangura, Marina Ren, and Judy So. I owe an enormous thank you to John Paiement for his development of the fMRI-CPCA software, as well as a thank you to Ryan Lim and Hafsa Zahid for updating its features in recent years. I am also grateful to Dr. Jennifer Whitman, Dr. Paul Metzak, and Dr. Katie Lavigne for their early guidance when I first joined the CNOS lab.

I would also like to thank the members of my supervisory committee, Dr. Christine Tipper, Dr. Rebecca Todd, and Dr. Lawrence Ward, for their helpful feedback throughout my doctoral studies. I am incredibly grateful to the University of British Columbia, Cordula and Gunter Paetzold, and the BC Children's Hospital Research Institute for their financial support. Many thanks to the team of technologists at the University of British Columbia 3T MRI Research Centre for their vital role in data collection.

Finally, I would like to thank my family for their encouragement, and most especially my husband, Eric Nanka, whose abundant support and enthusiasm has carried me through many challenges.

Chapter 1: Introduction

1.1. Neurocognitive Impairment in Schizophrenia

1.1.1. Background

Schizophrenia is a severe and chronic neuropsychiatric disorder that typically manifests in late adolescence or early adulthood (Karlsgodt et al., 2008). Schizophrenia is clinically defined by three clusters of symptoms: (1) positive symptoms, such as reality distortion symptoms (i.e., delusions and hallucinations) and disorganization (e.g., disorganized speech, inappropriate affect), (2) negative symptoms, which are the absence of normally present behaviours and mood (e.g., anhedonia, flattened affect, and avolition), and (3) neurocognitive impairment, including deficits in working memory, processing speed, verbal memory, and a variety of other domains (Diagnositic and Statistical Manual of Mental Disorders, DSM-V; American Psychiatric Association, 2013). While positive symptoms are the most visible symptom cluster, neurocognitive impairment is more predictive of functional outcome, such as maintaining employment and self-sufficiency (Lepage, Bodnar, & Bowie, 2014; McGurk, Mueser, Harvey, LaPuglia, & Marder, 2003). Neurocognitive impairment is persistent and is independent of positive symptom severity (Keefe et al., 2006), which typically cycles through periods of acute psychosis and remission over the course of weeks or months. Further, neurocognitive impairment is present before the onset of a first episode of psychosis, and may comprise vulnerability markers for transition to psychosis in high-risk individuals (Carrión et al., 2018; Lutgens, Lepage, Iyer, & Malla, 2014). These deficits are present in drug-naïve schizophrenia patients (Fatouros-Bergman, Cervenka, Flyckt, Edman, & Farde, 2014), and are not explained by comorbid substance abuse (Pencer & Addington, 2003; Wobrock et al., 2013). Therefore, neurocognitive impairment is

considered to be a core aspect of schizophrenia rather than a secondary outcome of the illness progression, medication effects, or comorbidities.

Working memory (WM), defined as actively holding and/or manipulating information in temporary store (Baddeley, 2012), is fundamental to executive processes such as cognitive control and is a prevailing domain of interest in cognitive neuroscience (D'Esposito & Postle, 2015). WM is also considered to be a core domain of neurocognitive impairment in schizophrenia, as identified by the Measurement and Treatment Research to Improve Cognition in Schizophrenia initiative (MATRICS; Green et al., 2004) and the Cognitive Neuroscience Treatment Research to Improve Cognition in Schizophrenia initiative (CNTRICS; Carter et al., 2008). While there have been several conceptualizations of WM, the most influential is the multicomponent model first proposed by Baddeley and Hitch (1974). The original model describes distinct processes that produce a unified manifestation of WM capacity. These include two possible "buffer" systems underlying temporary memory storage, which are referred to as the phonological loop (e.g., verbal rehearsal of a set of digits) and the visuospatial sketchpad (e.g., internally visualizing the locations of stimuli). In addition, a central executive system is described as a more complex component that controls attention. By contrast, state-based models conceptualize WM as either attention to activated long-term memory (for maintaining symbolic stimuli in mind, such as letters, digits, etc.) or sensorimotor recruitment (for maintaining basic perceptual features such as location, colour, etc.). Activated long-term memory models posit that when symbolic stimuli are presented, their long-term memory representations are accessed and subsequently maintained in an elevated state of attention until this information is no longer needed. Sensorimotor recruitment models posit that the same systems that are engaged in the perception of information also support the short-term retention of that information. The commonality among all WM models is that it is

conceptualized as a process involving engagement of attention to internal representations, but does not refer to executive control per se (which may be a domain-general skill). The ability to actively hold a number of items in mind may be a crucial and fundamental building block for guiding behaviour, and as such is tied to daily living. This is exemplified in its relationship to functional outcome in schizophrenia, as WM capacity has been found to predict interpersonal behaviour, community activities, and work skills in schizophrenia patients either directly or indirectly through mediating effects of social and/or functional competence and living skills (Bowie et al., 2008). WM function also predicts short-term clinical outcome following a first episode of psychosis (Bodnar, Malla, Joober, & Lepage, 2008), and as such, its underlying neurological mechanisms may have direct clinical implications.

1.1.2. Neurological underpinnings of working memory deficits in schizophrenia

WM deficits in schizophrenia have generally been thought to arise from dysfunction in the dorsolateral prefrontal cortex (DLPFC, encompassing the middle and superior frontal gyri, including Brodmann areas 9 and 46; Glausier & Lewis, 2018; Rajkowska & Goldman-Rakic, 1995). The most widely accepted neurobiological mechanism of this is insufficient dopamine D_1 transmission in the prefrontal cortex (Arnsten, Girgis, Gray, & Mailman, 2017; O'Tuathaigh, Moran, Zhen, & Waddington, 2017; Slifstein et al., 2015). The relation of WM demand to DLPFC activity reflects an inverted-U shaped function, with activation increasing with increasing demand to the point that capacity is reached, at which point activation declines (Van Snellenberg et al., 2016). In schizophrenia, this hypothetical curve is thought to be shifted to the left, such that WM capacity is reached at a lower level of demand (Callicott et al., 2003; Karlsgodt et al., 2007; Manoach, 2003).

Schizophrenia has been theorized to be a disorder of brain connectivity (Canuet, Aoki, Ishii, & Maestú, 2016; Karlsgodt et al., 2008), a concept referred to as the "disconnection hypothesis" (Friston, 1999). Moreover, although the key role of the prefrontal cortex in WM and other executive functions is well-known (Duncan & Owen, 2000; Stuss, 2011; Yuan & Raz, 2014), it has become apparent with the growth of functional connectivity-based approaches that WM is supported by coordinated activation of regions distributed across remote brain regions rather than within the prefrontal cortex alone (e.g., Cohen & D'Esposito, 2016). Resting-state research also suggests that the brain is intrinsically organized as a collection of networks characterized by coordinated fluctuations of activity across distributed brain regions (Buckner, Krienen, Castellanos, Diaz, & Yeo, 2011; Choi, Yeo, & Buckner, 2012; Yeo et al., 2011). Therefore, the relationship between DLPFC function and cognitive deficits in schizophrenia may be better understood within the framework of its functional integration with the rest of the brain.

1.2. Functional Brain Networks and Working Memory Capacity

1.2.1. Functional brain networks underlying working memory

It has been proposed that there is a "core" WM network comprising DLPFC, premotor cortex, anterior insula, supplementary motor area (SMA), and intraparietal sulcus (Rottschy et al., 2012). However, it is also known that such patterns of frontoparietal activity are ubiquitous across tasks involving goal-directed cognitive demand (Duncan, 2010; Duncan & Owen, 2000; Fedorenko, Duncan, & Kanwisher, 2013). The question of whether WM is subserved by a "multiple demands" network, or whether there is a core WM network that appears to be ubiquitous because WM itself is fundamental to many cognitive tasks, is as yet unresolved. What is evident, however, is that WM is not a unitary cognitive construct; distinct processes are expected to be involved in a WM task, including – at minimum – encoding external stimuli, maintaining inter-

nal representations, and selecting/executing a response. This notion is supported by findings from data-driven approaches such as component-based analyses, which allow for multiple networks to emerge that exhibit coordinated activation and/or deactivation in a cognitive task. The emergence of multiple frontoparietal networks subserving WM is exemplified in studies using methods including but not limited to independent component analysis (ICA; e.g., Meda, Stevens, Folley, Calhoun, & Pearlson, 2009; Steffener, Habeck, & Stern, 2012; Wong & Stevens, 2012), constrained principal component analysis (CPCA; e.g., Braunlich, Gomez-Lavin, & Seger, 2015; Metzak et al., 2011; Metzak et al., 2012; Woodward et al., 2006; Woodward, Feredoes, Metzak, Takane, & Manoach, 2013), and partial least squares (PLS; e.g., Kim et al., 2010).

1.2.2. Functional connectivity during working memory in schizophrenia

In discussing findings related to DLPFC dysfunction in schizophrenia in the context of brain connectivity, it is important to distinguish between results from studies that used a region of interest (ROI) selection approach (e.g., seed-based connectivity) to examine connectivity with DLPFC versus studies that used a whole-brain approach. While ROI-driven approaches are important for answering specific questions about a previously identified effect, an overly-specific focus on one region may result in overlooking other anatomical configurations that contribute to WM deficits in schizophrenia. To that end, a number of connectivity studies using whole-brain, data-driven approaches have indeed found that networks comprising DLPFC exhibit patterns suggesting an attenuation and/or inefficiency of activity in schizophrenia patients during WM tasks. For example, using ICA, Kim et al. (2009) found evidence of inefficient processing in a frontoparietal network comprising left-lateralized DLPFC, inferior parietal lobule, and cingulate gyrus, that was engaged during a Sternberg Item Recognition Paradigm (SIRP) WM task. This network was more engaged in individuals with schizophrenia compared with healthy controls at

a medium level of cognitive load, but was less engaged in schizophrenia patients at lower and higher levels of cognitive load. However, it is not clear whether this network subserved a specific cognitive sub-process such as encoding or maintenance. In a similar ICA study, Meda et al. (2009) also found a frontoparietal network including left-lateralized DLPFC that differed between schizophrenia patients and healthy controls, which was specifically correlated with the encoding phase of the task (although it is important to note that only the encoding and response phases were modelled in this analysis). In this study, patients exhibited less engagement in this network compared with controls at all levels of cognitive load that were implemented. Using CPCA, Metzak et al. (2012) found that individuals with schizophrenia exhibited greater engagement than healthy controls of a network including DLPFC at a medium level of cognitive load, but the groups exhibited similar degrees of engagement at lower and higher levels of cognitive load. This network appeared to underlie the encoding and maintenance phases of the task. Using a PLS approach, Kim et al. (2010) found that individuals with schizophrenia exhibited an exaggerated inverted-U relationship between activity and cognitive load in a frontoparietal network including DLPFC, despite comparable levels of task performance between schizophrenia patients and healthy controls.

Together, some important observations should be noted from these studies. First, the nature of group differences clearly varies with task design and cognitive load, which is an issue that has been previously noted in research focused specifically on the DLPFC (Karlsgodt et al., 2009). Second, in all of these studies, group differences were not limited to a DLPFC-related network; rather, other independently-activated task-related networks exhibited differences between patients and controls as well, including aberrant patterns of default mode network (DMN) deactivation (Kim et al., 2009; Meda et al., 2009; Metzak et al., 2012). This highlights the im-

portance of comprehensive investigations with respect to identifying brain activity underlying WM deficits in schizophrenia; ideally, studies should minimize a priori assumptions about the location or the timing of meaningful brain activity, and should allow for the evaluation of several networks engaged over the course of the post-stimulus time series. Most importantly, the variety of findings also raises the question of whether clinically meaningful conclusions can be drawn from the results of any individual WM study in isolation.

1.3. Measuring Task-State Functional Connectivity

1.3.1. Measuring connectivity with functional magnetic resonance imaging

Functional magnetic resonance imaging (fMRI) measures brain activity by detecting changes associated with blood flow using the blood oxygen level-dependent (BOLD) contrast. The BOLD contrast reflects neural activity-dependent changes in the relative concentration of oxygenated and deoxygenated blood. This is possible due to the different magnetic properties of deoxyhemoglobin (dHb) and oxygenated hemoglobin (Hb). The BOLD contrast increases upon neural activation due to the increased cerebral blood flow, which overcompensates for the decrease in oxygen and delivers an oversupply of oxygenated blood. Although the BOLD signal is an indirect measure of neural activity, there is a strong correlation between BOLD responses and local field potentials, the electrophysiological signals generated by the electric currents flowing from neurons within a small region of neural tissue (Logothetis & Wandell, 2004). fMRI provides a time series of BOLD signal from hundreds of thousands of brain points (voxels), with each point being just a few millimeters across. As the BOLD response primarily reflects the input and local processing of neuronal information (Logothetis & Wandell, 2004), this allows for inferences of localized neural activity with high spatial resolution. However, the biological

mechanism underlying the BOLD signal – namely, the oversupply of oxygenated blood – takes several seconds to peak, and as such, neural events cannot be measured in real time.

Some approaches being increasingly used in fMRI include multivariate modeling of variance sources (e.g., PLS, CPCA, and ICA; McIntosh & Lobaugh, 2004; Metzak et al., 2011; Stone, 2004), multivoxel pattern analysis and machine learning (Mahmoudi, Takerkart, Regragui, Boussaoud, & Brovelli, 2012), and topological network analysis using graph theory (Rubinov & Sporns, 2010). Each of these approaches has certain advantages and disadvantages for modeling the functional brain networks underlying cognitive processes, but fundamentally, all connectivity methods involve computing the intercorrelations in BOLD signal among all voxels (or select network nodes) in the brain over time, as opposed to treating each voxel as an independent entity. Methods employing multivariate modeling of variance sources utilize dimension reduction to identify components that reflect highly intercorrelated voxels. Notably, these approaches allow for the whole brain to be analyzed, and can produce several network configurations which capture distinct sources of variance in BOLD signal. These approaches do not require the selection of ROIs, and in many cases, they allow the post-stimulus time courses associated with each network to be evaluated.

1.3.2. Limitations of task-state connectivity research

In task-state research, the timing of evoked hemodynamic responses (HDRs), and how they differ between task conditions, provides a basis for interpreting the function of a brain network in relation to the task design. However, the nature of the BOLD signal presents significant challenges in delineating task-related networks and their evoked HDRs. One limitation in task-state fMRI research is that task-related brain activity accounts for only a fraction of BOLD signal changes over and above ongoing fluctuations in brain activity and other physiological processes.

A conventional solution to this problem entails modelling the recorded BOLD signal by convolving the post-stimulus time series with either canonical hemodynamic response functions (HRFs) or empirically-derived HRFs from simple motor responses (e.g., Aguirre, Zarahn, & D'Esposito, 1998). For example, a typical use in ICA is to obtain the spatial map of each component by applying ICA to the preprocessed BOLD data, and then determine which components underlie task-related processes by computing the fit between HRF-convolved event timing and the constructed time courses of each component (e.g., Meda et al., 2009). However, relying exclusively on models that assume specific HDR shapes introduces the risk of missing valuable information provided by HDR shapes that do not match the models, but are nevertheless elicited by cognitive processes engaged during the task. Another limitation of BOLD data is that neural activity cannot be measured in real time because the biological process on which functional images rely (i.e., the oversupply of oxygenated blood to the area(s) of increased activity) is maximized several seconds after the actual change in neural activity, and the resultant HDR can take 20 seconds or longer to exhibit a full response and return to baseline (Logothetis & Wandell, 2004). Although jittered and partial trial designs help ameliorate confounds arising from HDRs overlapping across task trials (Burock, Buckner, Woldorff, Rosen, & Dale, 1998; Dale, 1999; Serences, 2004), this does not improve the temporal resolution of within-trial activations. A major implication of these limitations is that coinciding cognitive processes and their underlying brain activity may blur together, such that a given network and its HDR may actually reflect a combination of multiple cognitive processes, despite being theoretically separable onto different cognitive operations and different networks.

1.3.3. Multi-experiment comparisons

Toward this goal of characterizing task-related brain activity, it is beneficial to compare different experiments reported in existing literature with theoretically meaningful differences and similarities in elicited cognitive operations. In theory, this should help form a basis for determining what function(s) a network serves by identifying conditions under which the network is engaged versus conditions when it is not. This is the basic idea behind coordinate-based meta-analyses such as activation likelihood estimation (ALE), which allows investigators to create brain activation maps from published experimental contrasts (Turkeltaub, Eden, Jones, & Zeffiro, 2002). Although coordinate-based meta-analyses are valuable for creating brain activation maps that reflect consensus across vast collections of studies, they do not provide the corresponding timing information that would allow for a more refined evaluation of network function based on the HDRs elicited by a range of tasks. Moreover, comparisons between studies are inherently confounded by differences in study design, analysis methods, and other decisions made by investigators (Carp, 2012). A framework that allows an evaluation of HDR shapes for a given brain network across different datasets, without imposing restrictive assumptions about the shape of the HDR or the spatial configuration of the brain networks, could be more informative. A multivariate approach that allows such a comparison between tasks/datasets has been previously put forward (Lavigne, Metzak, & Woodward, 2015; Lavigne & Woodward, 2018; Ribary et al., 2017), which is referred to as multi-experiment constrained principal component analysis for fMRI (fMRI-CPCA, described in detail in the next chapter). This approach was first used to compare HDR shapes from different versions of the same cognitive task (examining the construct of evidence integration; Lavigne, Metzak, et al., 2015), and was more recently used with task merging to clarify findings regarding speech versus non-speech auditory perception in

schizophrenia patients (Lavigne & Woodward, 2018). In the present study, task merging with fMRI-CPCA was used to characterize functional brain networks underlying temporally correlated WM processes, by allowing a finer separation of networks than could be observed from the analysis of a single task in isolation. This also allowed for a more refined evaluation of the resulting networks by examining activity across different tasks and cognitive demands, and in turn, a more refined understanding of the networks that exhibited some irregularity in schizophrenia patients.

1.4. Dissertation Overview

1.4.1. Aims

The general aims of this research were to characterize the brain networks underlying WM and related cognitive functions, and to identify networks that may underlie WM deficits in individuals with schizophrenia. More specifically, this worked aimed to:

1. Obtain a more refined characterization of functional brain networks subserving distinct WM processes using multi-experiment functional connectivity analyses of task-state fMRI data.
2. Identify networks underlying task performance and WM capacity.
3. Identify networks which exhibit aberrant patterns of activity in schizophrenia patients across different cognitive tasks, with an emphasis on networks underlying WM processes.

The present research used whole-brain, data-driven functional connectivity approaches to achieve these goals. It was expected that networks reflecting multiple temporally correlated processes within a given task would separate into constituent networks when multiple tasks with relevant overlapping and non-overlapping cognitive demands were simultaneously analysed using a

unified computational framework. Although a multi-experiment approach was used to characterize networks engaged across a variety of cognitive constructs, the overarching purpose of this work was centered around identifying aberrant patterns of connectivity in schizophrenia with respect to WM capacity in particular.

1.4.2. Outline

Chapter 2 provides an overview of the methods that were used in this work, and the findings are reported in Chapters 3-5. Chapter 3 describes a multi-experiment fMRI connectivity study combining a verbal WM task with a thought generation task. This study illustrates the advantages of a multi-experiment design while keeping the collection of results relatively limited, and reflects a preliminary step that was carried out in addressing the first aim. Chapter 4 reports four single-experiment fMRI connectivity analyses – including the verbal WM task and thought generation task examined in Chapter 3, as well as a set-switching Stroop task and a visuospatial WM task – and provides a general characterization of the networks that dominate the task-related BOLD signal in healthy individuals. Chapter 5 reports a multi-experiment analysis combining all four of the tasks analyzed in Chapter 4. In line with the overarching goal of this work, this four-task analysis includes examining differences between healthy controls and schizophrenia patients, as well as correlations between network (de)activation and task performance/WM capacity. Finally, the findings of this research are summarized and discussed in Chapter 6.

Chapter 2: Methods

The present research employed task-state fMRI and multivariate functional connectivity analyses to better understand the neural underpinnings of WM deficits in schizophrenia. Of particular interest was delineating activity in networks that replicate across different cognitive tasks, as widely observed networks may be more clinically meaningful with respect to neurocognitive deficits in schizophrenia than task-specific patterns. As the data and tasks employed overlap across analysis chapters, information regarding participants, tasks, data processing, and statistical computations are detailed in the following sections.

2.1. Participants

Study-specific sample characteristics and testing procedures are described in the appropriate chapters. Across all studies, participants were eligible if they were between 19-60 years of age, fluent in English, had an estimated IQ > 70, had intact or corrected visual acuity of at least 20/50, and intact colour perception. Exclusion criteria included a history of neurological illness or infection (e.g., stroke, epilepsy, encephalitis, etc.), history of head trauma resulting in loss of consciousness for > 10 minutes, and current or recent alcohol/substance dependence. Further exclusion criteria for healthy controls included a recurrent history of psychiatric illness or a family history of psychosis. Patients were required to have a primary diagnosis of schizophrenia or related disorder (e.g., schizoaffective disorder). Exclusion criteria related to MRI contraindications included being pregnant, wearing a pacemaker, having had aneurysm surgery, having metal implants, having metallic fragments in or near eyes, and the participant feeling that they would be uncomfortable in the confined space of the MRI scanner.

2.2. fMRI Tasks

2.2.1. Working Memory Task (WM)

The WM task design is presented in Figure 2.1. A modified Sternberg Item Recognition Paradigm (SIRP; Sternberg, 1966) was administered in which a string of 4 or 6 upper case consonants was displayed for 4 seconds, and then a single probe letter was displayed for 2 seconds. Participants were asked to respond "yes" or "no" with a button-press as to whether this probe letter was part of the first string of letters, using an MRI-compatible response device. Both the cognitive load (4 or 6 letters in the item set) and delay period (0 or 4 seconds between the letter string and probe) were manipulated so as to facilitate identification of the functional brain networks distinctly involved in encoding, maintenance, and responding. The task was programed using Neurobehavioral Systems Presentation software (https://www.neurobs.com/). The 4-letter strings were flanked by a pound character ("#") on each end to match stimulus size between the two cognitive load conditions, and the text was presented in white, 40-point Arial font against a black background. A fixation marker was displayed throughout inter-trial intervals (ITIs) lasting 2, 4, 6, or 12 seconds. Stimuli were projected onto a screen attached to the bore of the MRI scanner, and participants viewed the reflection of this image in a mirror positioned in their visual field. The task took approximately 25 minutes to complete over two 12.5-minute runs, with a total of 112 trials (14 trials per condition per run, which were randomly generated within each task run). A 30-second rest break was included halfway through each task run, during which the text "Short break. Please remain still" was displayed. Prior to the scanning session, participants completed a practice run with a computerized version of the task to familiarize themselves with the experimental procedure. Once in the scanner, participants were reminded of the instructions and were asked to provide "yes" and "no" button-press responses to demonstrate that they under-

stood which buttons to press before starting the task. The task was automatically initiated by a pulse from the MRI scanner, following an initial four dummy scans that were carried out to allow the magnetization to stabilize to a steady state. A 5-second countdown was displayed prior to the first trial of the task run and at the end of the 30-second rest break.

2.2.2. Spatial Capacity Task (SCAP)

The data for the SCAP fMRI task were obtained from the OpenfMRI database (https://openfmri.org/dataset/ds000030/; accession number is ds000030). The SCAP task, shown in Figure 2.2, is also an item-recall task, but it is a visuospatial memory task with no verbal content. First, a target array of either 1, 3, 5, or 7 yellow dots (positioned pseudo-randomly around a central fixation) is presented during a 2-second encoding period. After a 1.5-second (1.5s), 3-second (3.0s), or 4.5-second (4.5s) delay, a single green dot (i.e., the probe) is displayed for 3 seconds. Participants are asked to respond with a button-press as to whether the probe dot was in the same position as one of the target dots. 4 load levels × 3 delay lengths resulted in 12 task conditions, and 4 trials per condition are presented in the task (total = 48 trials). A central fixation is visible throughout the trials. Jittered ITIs ranged from 1-4 seconds (mean = 2 seconds), during which the central fixation is visible. The task was programmed in MATLAB (Mathworks) using the Psychtoolbox program (http://psychtoolbox.org/). Participants viewed the task stimuli through MRI-compatible goggles and responded with their right hand on an MR-compatible button box. Before starting the in-scanner task, subjects underwent a training session outside of the scanner, and once in the scanner were reminded of the instructions.

2.2.3. Task-Switch Inertia Task (TSI)

The TSI task design is presented in Figure 2.3. This task is a set-switching Stroop task which involves responding to Stroop stimuli in alternating blocks of colour-naming (i.e., naming

the font colour of text displayed) and word-reading (i.e., reading the word displayed) of neutral and incongruent stimuli. A neutral word-reading stimulus is one in which a colour word ("GREEN", "RED", "YELLOW", or "BLUE") is displayed in white font against a black background, and a neutral colour-naming stimulus is one in which a string of Xs is displayed in green, red, yellow, or blue font. Incongruent stimuli are colour words ("GREEN", "RED", "YELLOW", or "BLUE") displayed in incongruent green, red, yellow, or blue font. Congruent Stroop stimuli, in which the font colour matches the colour word displayed, were not used in this study because the cognitive and neurological processes affected by response inhibition demands – not facilitation – were of primary interest. Moreover, the facilitation effect may be absent under task-switching conditions anyway (Rogers & Monsell, 1995).

The TSI task was programmed using Neurobehavioral Systems Presentation software (https://www.neurobs.com/). This task consisted of 12 blocks of 10 trials and lasted approximately 11 minutes. Each time the task was switched, an instruction screen was displayed for 9 seconds with reminders for which buttons to use for responding. Stimuli were presented in 40-point Helvetica font against a black background. Two commercially-available MRI-compatible fiber optic response devices with two buttons each were used for the participants' responses. For each trial, the stimulus was displayed for 1900ms, followed by a blank screen for 100ms. The response was recorded within the total 2000ms trial, which was followed by a jittered ITI of 900ms–6000ms during which a fixation cross was displayed. In total, 30 incongruent and 30 neutral colour-naming trials and 30 incongruent and 30 neutral word-reading trials are presented. The task was automatically initiated by a pulse from the MRI scanner, following an initial four dummy scans that were carried out to allow the magnetization to stabilize to a steady state. A 20-second rest break was included halfway through the task run, during which the text "Short break.

Please remain still" was displayed. In a previous study published by our lab, incongruent and neutral stimuli were interspersed within each block of colour-naming and word-reading (Woodward, Leong, Sanford, Tipper, & Lavigne, 2016). However, a consideration in this new version was to examine whether the slowing of responses due to task-switching is dependent on the level of prepotent response inhibition required in the previous task set, which would suggest that shifting ability is impacted by response inhibition demands and not merely the change of task rules per se. Therefore, in this revised version of the task, the colour-naming blocks alternated between exclusively neutral stimuli and exclusively incongruent stimuli, whereas the word-reading blocks always consisted of a mix of neutral and incongruent stimuli.

Immediately prior to the scanning session, participants completed a practice run outside of the scanner to familiarize themselves with the testing procedure and key-response mapping (left middle finger = "green", left index finger = "red", right index finger = "yellow", and right middle finger = "blue"). Beginning with neutral word stimuli, participants practiced responding, and received on-screen feedback after errors ("Incorrect") or responses exceeding 1900ms ("Too slow"). After the participant responded with at least 90% accuracy over 10 trials, the presentation of neutral word stimuli stopped and switched to a series of neutral colour-naming stimuli, which was followed by a series of both neutral and incongruent word-reading stimuli, and finally a series of incongruent colour-naming stimuli. Once in the scanner, participants were reminded of the instructions, and asked to provide "green", "red", "yellow" and "blue" responses to demonstrate that they understood which buttons to press, and then finally completed one more practice run in the scanner to ensure that they had memorized which buttons to press.

2.2.4. Thought Generation Task (TGT)

The TGT task design is presented in Figure 2.4. This task was originally designed to investigate the neurological basis of internal generation versus external processing of speech in schizophrenia, and specifically for examining differences between hallucinating and non-hallucinating patients (Lavigne, Rapin, et al., 2015; Rapin et al., 2012). Participants were presented with an object noun and its corresponding image (e.g., pillow) for five seconds and instructed to either mentally generate or listen to a simple definition of the word (e.g., "Something you rest your head on when sleeping"). The two experimental conditions (i.e., generating and hearing) were presented in alternating blocks of 15 trials (30 trials total for each condition across two runs), with a 60-second rest break in between the two conditions. Trials were cued with the words "something you…" or "listen…" presented under the images in the generating and hearing conditions, respectively. Stimuli were randomly assigned to each condition for each participant. Participants were administered a post-scan questionnaire where they were asked, for each trial, whether they generated a definition and, if so, what that definition was. Hearing tests were carried out using an audiometer (AMBCO 650AB, http://www.ambco.com/) to ensure absence of hearing impairment prior to testing. The task was automatically initiated by a pulse from the MRI scanner, following an initial four dummy scans that were carried out to allow the magnetization to stabilize to a steady state.

Three 30-word lists of nouns were created using the MRC psycholinguistic database (Coltheart, 1981). Only nouns with scores >500 on familiarity, concreteness, and imageability criteria ratings were chosen (maximum value = 700). The three word lists (i.e., list A, B and C) were matched by mean values on these parameters. All nouns were objects of neutral affective content within the categories of food, houseware, furniture, clothing, and transportation devices.

Each audio stimulus was recorded by a female native English speaker in a quiet room, and lasted on average 2.22 seconds (SD = 0.62). Two out of the three word lists were randomly assigned to the two conditions for each participant, resulting in six potential word set combinations (i.e., AB, BA, AC, CA, CB, and CB), which were counterbalanced across participants.

Prior to fMRI scanning, participants were familiarized with the experimental procedure in a computerized practice run, using 10 words that were different from those presented in the scanner. In addition, to facilitate the generation of definitions while in the scanner, participants practiced audibly generating definitions for the 30 words in the thought generation condition. No training was carried out for the hearing condition material to minimize the likelihood of participants self-generating definitions during hearing trials. The task was programmed using Neurobehavioral Systems Presentation software (https://www.neurobs.com/). Stimuli were projected onto a screen placed at the bore of the MRI scanner, and participants viewed a reflection of the image in a mirror positioned in their visual field. In the hearing condition, the audio file containing the definition was presented 700ms after the onset of the word and illustration. The recorded definitions always began with the words “Something you”, and participants were instructed that mentally generated definitions should also start with “Something you”, to ensure that at least some words were mentally generated on every trial, and to minimize confounds between conditions. To prevent participants from internally reviewing the most recently generated or heard definition, a display of generic circles moving in an orbiting motion was presented during the ITIs of either 2, 4, 6, 8, 16, or 20 seconds (mean = 4.46 seconds). The order of presentation of the ITIs, conditions, and words within each block were randomized.

2.3. fMRI Data Acquisition and Preprocessing

2.3.1. Data acquisition

Task-specific scanning parameters and protocols are presented in Table 2.1. In all studies, functional image volumes were collected using a T2*-weighted sequence covering the whole brain. A T1-weighted structural image was also acquired from each participant for co-registration of functional images with structural templates used in the fMRI normalization procedure. Data collection for the WM task, TSI task, and TGT was carried out at the UBC MRI Research Centre on a Philips Achieva 3.0 Tesla scanner with quasar dual gradients (maximum gradient amplitude, 80 mT/m; maximum slew rate, 200 mT/m/s). The WM data and TSI data were collected in the same study in largely overlapping samples (participants completed the TSI task and then the WM task in the same scanning session), with the exception of a subset of the WM data which had been previously collected in an earlier study overlapping with the TGT dataset. The data for the SCAP task were obtained from the OpenfMRI database (https://openfmri.org/dataset/ds000030/; accession number is ds000030). The MRI data were originally acquired on one of two 3.0 Tesla Siemens Trio scanners at either the Ahmanson-Lovelace Brain Mapping Center (Siemens version syngo MRI B15) or the Staglin Center for Cognitive Neuroscience (version syngo MR B17). Complete details for this project are provided in Poldrack et al. (2016).

2.3.2. Preprocessing

Functional images were reconstructed offline and preprocessed using Statistical Parametric Mapping 12 (SPM12; Wellcome Trust Centre for Neuroimaging, UK). First, each participant's functional and T1 scans were manually inspected and reoriented to the anterior commissure. Next, each functional run was slice timing-corrected, realigned to the first image of the run,

co-registered to the structural (T1) image, normalized to the Montreal Neurological Institute (MNI) T1 brain template (voxel size = 3 × 3 × 3 mm) using the segmentation and normalization algorithms applied in SPM12, and spatially smoothed with an 8 × 8 × 8 mm full width at half maximum Gaussian filter. Runs for which realignment exceeded 4 mm or 4° on any scan were excluded from all analyses. The six realignment parameters (i.e., translation in x, y, and z dimensions, and rotation in pitch, roll, and yaw directions) were regressed out of the BOLD time series prior to statistical analyses to minimize effects of head movement. Linear and quadratic trends, which may arise as an artifact of scanner drift, were also regressed out of the BOLD time series.

2.4. Constrained Principal Component Analysis for fMRI

2.4.1. General framework

Functional connectivity analyses were carried out using constrained principal component analysis for fMRI (fMRI-CPCA; Metzak et al., 2011). CPCA is a general method for structural analysis of multivariate data, which combines multivariate multiple regression with principal component analysis (PCA) into a unified framework (Hunter & Takane, 2002; Takane & Hunter, 2001). fMRI-CPCA applies this framework to reveal temporally orthogonal sources of task-related BOLD signal by employing PCA on the portion of variance in activity that is predictable from the task timing. In the present research, data-driven estimates of the post-stimulus time courses of hemodynamic responses (HDRs) were obtained by using a finite impulse response (FIR) model in the regression stage of the CPCA. A FIR model makes no assumptions about the shape of the HDR; instead, it produces separate estimates for each post-stimulus scan for each condition and each participant. Performing PCA after regression with a FIR model allows investigators to (1) identify the spatial configurations of multiple functional brain networks simultaneously involved in performing a cognitive task, (2) estimate the post-stimulus HDR of each

functional network, and (3) statistically test the effect of experimental manipulations and group differences in HDR shapes in each functional brain network. The estimated HDR shapes aid interpretation of the cognitive processes engaged from examining the relative timing and duration of the different peaks, which in turn helps inform our understanding of the role of the functional brain systems involved. A general overview of the steps involved in a typical fMRI-CPCA is presented in Figure 2.5. The mathematical equations as applied to fMRI data are detailed below.

2.4.2. Matrix equations

2.4.2.1. Multivariate multiple regression

Two matrices are constructed for the fMRI-CPCA analysis. The first matrix, *Z*, contains the intensity values for the preprocessed BOLD time series of each voxel, with one column per voxel and one row per scan. The second matrix, *G*, consists of a FIR basis set, with one column per estimated post-stimulus scan per condition, and one row per acquired scan. The value 1 is placed in rows of *G* for which BOLD signal amplitude is to be estimated, and the value 0 in all other rows (i.e., "mini boxcar" functions). The *G* matrix estimates subject- and condition-specific effects by including a separate FIR basis set for each condition and for each subject. Each column of *Z* and *G* is standardized for each subject separately.

The first step in CPCA involves partitioning the total variability in *Z* (BOLD signal) into variance that is predictable by *G* (design matrix) and variance that is not predictable by *G*, producing a matrix of predicted scores (the *GC* matrix) and a matrix of residuals (the *E* matrix). To achieve this, multivariate least-squares linear multiple regression is carried out, whereby the BOLD time series (*Z*) is regressed onto the design matrix (*G*):

$$ {}_sZ_b = {}_sG_eC_b + {}_sE_b \quad (1) $$

where Z = the dependent variable, G = the independent variable, C = the weights applied to G to produce a matrix of predicted scores (GC), E is a matrix of residuals, s = acquired scans, b = voxels, and e = FIR estimates. The C matrix represents condition-specific regression weights, which are akin to the beta images produced by conventional univariate fMRI analyses, and are obtained by:

$$ {}_eC_b = ({}_eG_s'G_e)^{-1}\,{}_eG_s'Z_b \quad (2) $$

Therefore, GC represents the variability in Z that is predictable from the design matrix G (i.e., the task-related variability in Z).

2.4.2.2. Principal component analysis (PCA)

The next step in CPCA is to apply PCA, a special case of singular value decomposition, to the GC matrix so that the resulting components can be examined. PCA uses orthogonal transformation to convert a set of observed variables into a set of linearly uncorrelated variables called principal components, such that the first principal component accounts for the largest possible amount of variance in the data, and each succeeding component has the highest possible variance under the constraint that it is orthogonal to the preceding components. PCA is typically used for dimension reduction, as it allows a large set of variables to be reduced to a few principal components that reflect common variance among the variables that are most highly related to each component. In the case of fMRI-CPCA, it is performed on the vertically concatenated GC matrices of the entire sample of participants. As such, each component is constructed from the temporal intercorrelations of estimated BOLD activity among all voxels in the brain – that is, their *functional connectivity.* This is an important distinction from the patterns of *co-activation* that arise from traditional mass-univariate approaches to task-state fMRI research.

The singular value decomposition of *GC* (comprising all subjects and scans) results in:

$$[{}_sU_mD_mV_b'] \approx {}_sG_e\,C_b \tag{3}$$

where U = matrix of left singular vectors, D = diagonal matrix of singular values, and V = matrix of right singular vectors after reduction of dimensionality to m components. Each column of $\left(VD/\sqrt{b-1}\right)$, where b is the number of columns (i.e., voxels) in Z, is overlaid on a structural brain image to allow spatial visualization of the brain regions dominating each functional network. The rescaled VD is referred to as a loading matrix, and the values are correlations between the component scores (U) and the columns (i.e., voxels) in GC.

The number of components to retain is typically chosen based on the amount of variance each one accounts for, indicated by their respective eigenvalues (i.e., the squared singular values obtained from singular value decomposition of the mean centered and normalized data matrix). In the present research, the plotted eigenvalues (i.e., the scree plot) were evaluated to identify the components contributing a meaningful and unique portion of variance (Cattell, 1966; Cattell & Vogelmann, 1977). If more than one component is extracted, the interpretability of the components can be increased by redistributing the variance via rotating the components. The rotation method used in the present research, varimax rotation (Kaiser, 1958), redistributes the variance captured by the original eigenvectors, stopping optimization when the matrix of component loadings optimally matches a "simple structure", which is characterized by the following conditions: (1) any given variable (i.e., voxel) has a high loading on a single component (i.e., brain network), and near-zero loadings on the others, and (2) any given component consists of only a small subset of variables with high loadings, with the remaining variables all having near-zero loadings.

2.4.2.3. Predictor weights

Post-stimulus HDRs are estimated by regressing the component scores of each component extracted from *GC* onto the independent variables in *G* (i.e., FIR estimates), producing a matrix of predictor weights, *P*, that estimate the degree to which each variable in *G* is related to the corresponding components extracted from *GC*. That is, predictor weights in matrix *P* are the weights that, when applied to each column of the matrix of predictor variables (*G*), create *U* (i.e., component scores) such that:

$$ {}_sU_m = {}_sG_eP_m \quad (4) $$

Each subject- and condition-specific set of predictor weights is expected to take the shape of an HDR when plotted over post-stimulus time, with the highest values corresponding to the HDR peaks. Note that positive predictor weights do not necessarily reflect activation, as this depends on whether the component loadings are positive or negative. To avoid confusion as to whether a given HDR shape reflects activation or deactivation, all plots in the present research are oriented such that values above the X axis reflect activation, and values below the X axis reflect deactivation (which means that the Y axis may be reversed in some instances).

As fMRI-CPCA predictor weights are produced for each component for each combination of post-stimulus time bin, task condition, and participant, activity in each of the extracted networks is statistically examined by applying repeated measures analysis of variance (ANOVA) to the predictor weights to examine effects of post-stimulus time and experimental conditions in each task. As a further step in fMRI, to verify that the resulting components primarily capture biologically plausible BOLD signal rather than noise, a visual examination of their HDR shapes and anatomical organization is performed, and repeated measures ANOVA is carried out on the predictor weights to confirm the presence of significant effects of post-stimulus time. In the pre-

sent research, Mauchley's test of sphericity was carried out for each analysis, and the Greenhouse-Geisser correction was applied in cases where the assumption of sphericity was violated; corrected degrees of freedom are reported where the correction changed statistical results. Inspection of the HDR shapes while considering the experimental designs facilitated assignment of each network to one or more cognitive processes.

2.4.3. Multi-experiment fMRI-CPCA

As the regression step in CPCA (equation 1) is performed separately for each subject, the *G* matrices need not be comprised of the same number of conditions or columns across all subjects; this allows for a simple extension of the CPCA framework to multi-experiment analyses. In simultaneous analyses of multiple datasets, identifying networks which are spatially identical across tasks, an advantage of fMRI-CPCA is that it can describe how the time-courses of post-stimulus activity in those networks vary (or do not vary) across tasks. Some examples of other multi-experiment approaches include joint sparse representation analysis (jSRA; Ramezani, Marble, Trang, Johnsrude, & Abolmaesumi, 2015), joint independent component analysis (jICA; Calhoun et al., 2006), multimodal canonical correlation analysis (mCCA; Sui et al., 2010), combined CCA + ICA (Sui et al., 2010), and multi-task PLS (Grady, Springer, Hongwanishkul, McIntosh, & Gordon Winocur, 2006). jSRA, jICA, mCCA, and CCA + ICA are all second-level analyses that involve identifying common sources from experimental contrast images extracted from different tasks using statistical matches (e.g., beta weights) to modelled HDR shapes, and as such, these methods do not provide the corresponding temporal information that would allow for a more refined evaluation of network function based on the HDRs elicited by a range of tasks. PLS is somewhat similar to CPCA in that it identifies patterns of brain activity that covary with features of the experimental design, but due to differences in the nature of the matrices that

are covaried, does not provide an estimated condition-specific HDR shape as an integral part of the output (see Metzak et al., 2011, p. 869, for a detailed explanation of how the general framework of CPCA differs mathematically and conceptually from PLS and other multivariate methods). Moreover, multi-task PLS is used to identify what is common between tasks without allowing for activations that may be exclusive to a particular task.

While all of the above approaches involve identifying sets of brain regions that overlap across different tasks, multi-experiment fMRI-CPCA expands on this to allow statistical evaluation of network-specific HDR time courses, which may or may not be engaged in all tasks/conditions. Importantly, multi-experiment fMRI-CPCA produces estimated HDRs and connectivity-based spatial maps in a data-driven manner (i.e., no reliance on statistical matches to assumed HRFs, or a set of a-priori assumed ROIs) while keeping the spatial pattern of each network constant across the tasks to be compared, regardless of whether it is a within- or between-subjects design. The degree to which each functional brain network replicates its involvement across tasks is determined by comparing the magnitude and temporal pattern of the HDR shapes associated with each network (Lavigne, Metzak, et al., 2015; Lavigne & Woodward, 2018). This provides an opportunity to use differences between tasks, and the cognitive operations they putatively elicit, to help determine the cognitive function served by a given network (Ribary et al., 2017). For example, if a particular cognitive process is engaged in two tasks, but its timing differs due to different task designs, HDRs for the underlying network should be elicited in both tasks but display different shapes. However, if a cognitive process is elicited by one task but not the other, the task not eliciting this process should show a flat HDR shape for that network. This raises the possibility of a finer delineation of networks to emerge: when two (or more) distinct processes consolidate into one network in a single task due to the

low temporal resolution of fMRI, it is possible that these processes will separate onto different networks when one process is engaged in both tasks (resulting in an HDR for both tasks), but the other is engaged in only one task (resulting in an HDR for only one task). The next chapter presents an example of these concepts being applied in a preliminary multi-experiment analysis that was designed to obtain finer separation of task-related networks – and the cognitive processes they support – engaged in a verbal WM task.

2.5. Chapter 2 Tables

Table 2.1. fMRI acquisition parameters for all datasets included in present research.

	WM	SCAP	TSI	TGT
Functional images				
Sequence	T2*-weighted gradient-echo spin pulse	T2*-weighted echo-planar imaging (EPI)	T2*-weighted gradient-echo spin pulse	T2*-weighted gradient-echo spin pulse
Slices	35	34	35	36
Slice thickness/gap	3/1 mm	4/0 mm	3/1 mm	3/1 mm
Acquisition matrix	96 × 96	64 × 64	96 × 96	80 × 80
Repetition time (TR)	2000 ms	2000 ms	2000 ms	2500 ms
Echo time (TE)	30 ms	30 ms	30 ms	30 ms
Flip angle (FA)	90°	90°	90°	90°
Field of view (FOV)	288 × 288 × 139 mm	192 × 192 × 136 mm	288 × 288 × 139 mm	240 × 240 × 143 mm
Volumes per run	374	291	330	176
Runs	2	1	1	2
	WM	SCAP	TSI	TGT
Structural image				
Sequence	T1-weighted Fast Field Echo (FFE)	T1-weighted magnetization-prepared rapid gradient-echo (MPRAGE)	T1-weighted Fast Field Echo (FFE)	T1-weighted Fast Field Echo (FFE)
Slices	190 sagittal	176 sagittal	190 sagittal	182 coronal
Slice thickness/gap	1/0 mm	1/0 mm	1/0 mm	1/0 mm
Acquisition matrix	256 × 256	256 × 256	256 × 256	256 × 256
Repetition time (TR)	8.1 ms	1.9 s	8.1 ms	8.1 ms
Echo time (TE)	3.7 ms	2.26 ms	3.7 ms	3.7 ms
Flip angle (FA)	8°	7°	8°	8°
Field of view (FOV)	190 × 256 × 256 mm	176 × 256 × 256 mm	190 × 256 × 256 mm	256 × 182 × 256 mm
Voxel dimensions	1 × 1 × 1 mm	1 × 1 × 1 mm	1 × 1 × 1 mm	1 × 1 × 1 mm
Total scanning time	7 min 23 sec	6 min 3 sec	7 min 23 sec	6 min 22 sec

2.6. Chapter 2 Figures

Figure 2.1. Working Memory (WM) task design; example of a trial presented in the 4-letter load condition with a 4-second delay. Participants were instructed to try to remember the string of letters displayed at the start of each trial. As the four task conditions were randomly intermixed within each fMRI run, it was explained that there would be either four or six letters to remember on any given trial, and that on some trials there would be a four-second delay before the probe letter was displayed, while on other trials the probe letter would be displayed immediately after the initial string of letters disappeared from the screen. Participants were instructed to use their right index finger to respond "yes" if the probe letter had been included in the letter string displayed at the start of the trial, and use their right middle finger to respond "no" if the probe letter had not been included in the letter string.

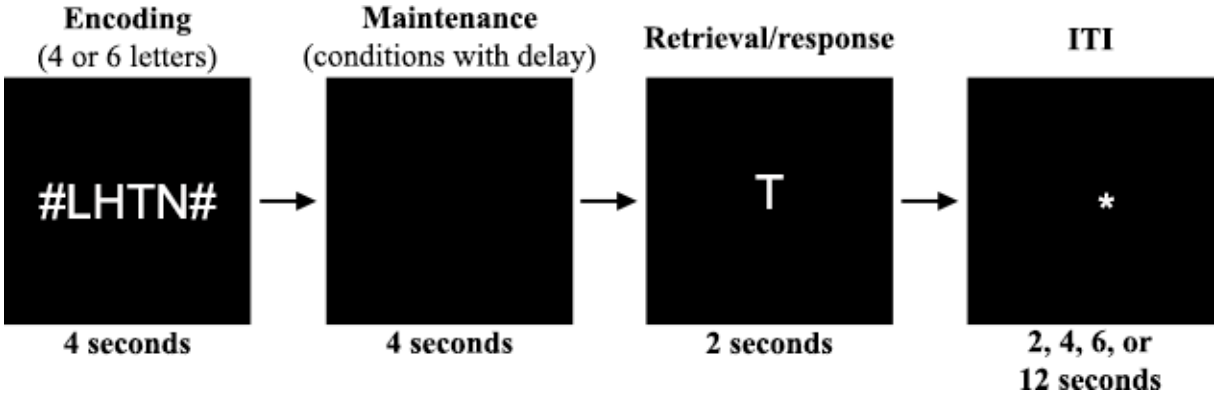

Figure 2.2. Spatial Capacity (SCAP) task design; stimuli downloaded from software developer's publicly available code library (https://poldracklab.stanford.edu/softwaredata). Participants are provided with the instructions: "You will see either 1, 3, 5, or 7 yellow dots on the screen. After these dots disappear, a green dot will appear. Press the FIRST button if the green dot is in the same place as one of the yellow dots. Press the SECOND button if the green dot is in a different place than one of the yellows."

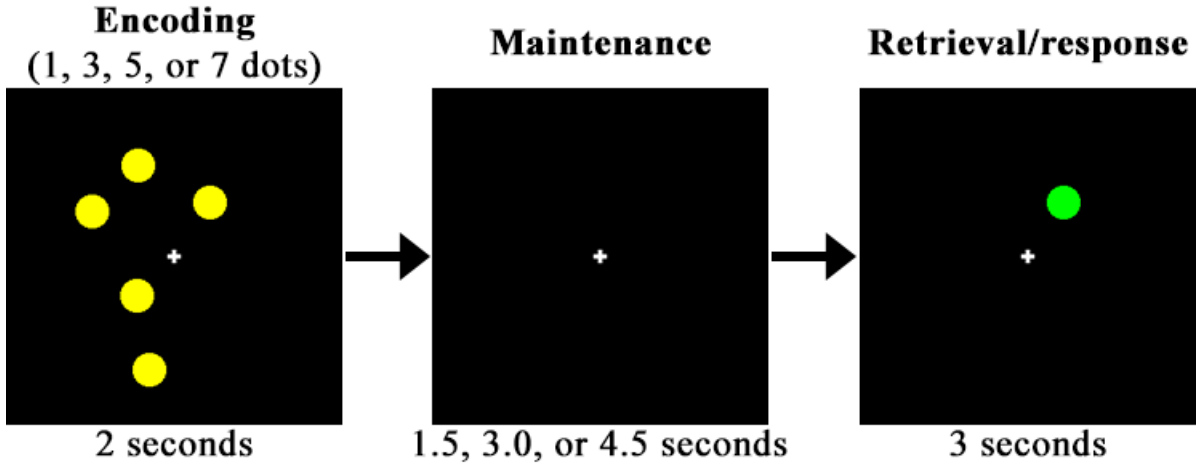

Figure 2.3. Task-Switch Inertia (TSI) task design. Task blocks began with the instructions "NAME THE COLOUR" or "NAME THE WORD", with reminders for which buttons to press at the bottom of the screen. Each block consisted of 10 trials, and a total of 12 blocks were completed (3 neutral colour-naming, 3 incongruent colour-naming, and 6 word-reading). Word-reading blocks consisted of 5 neutral and 5 incongruent stimuli pseudo-randomly distributed throughout the block so that no more than 3 of one type of stimulus appeared in the first 5 trials. cn = neutral colour-naming; ci = incongruent colour-naming; W = word-reading; ITI = inter-trial interval.

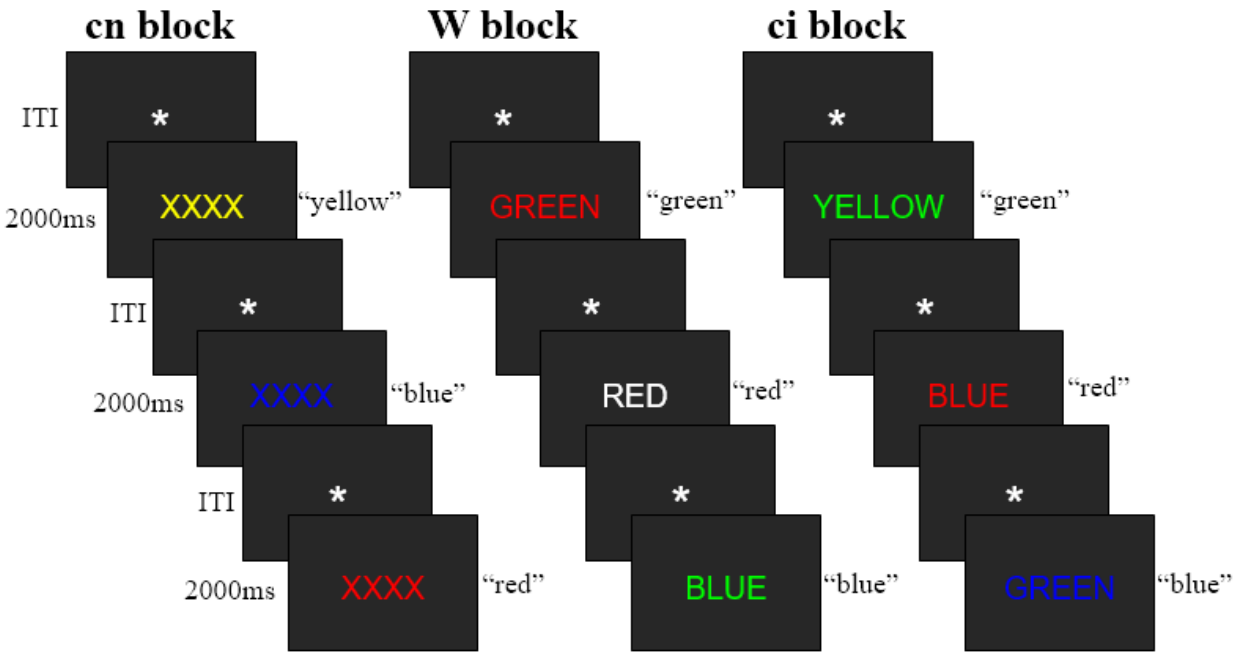

	Block 1	Block 2	Block 3	Block 4	Block 5	(Blocks 6-12)
Task	**10 colour-naming**	**10 word-reading**	**10 colour-naming**	**10 word-reading**	**10 colour-naming**	(etc.)
Stimulus	neutral	5 neutral + 5 incongruent	incongruent	5 neutral + 5 incongruent	neutral	

Figure 2.4. Thought Generation Task (TGT) design; examples of trials presented in a thought-generation block. Participants were instructed to either mentally generate (generating condition) or to listen to (hearing condition) a simple definition of a word (e.g., “Something you rest your head on when sleeping” for the word “pillow”). The conditions were cued with the words “something you…” or “listen…” presented under the images for the generating and hearing conditions, respectively. ITI = inter-trial interval.

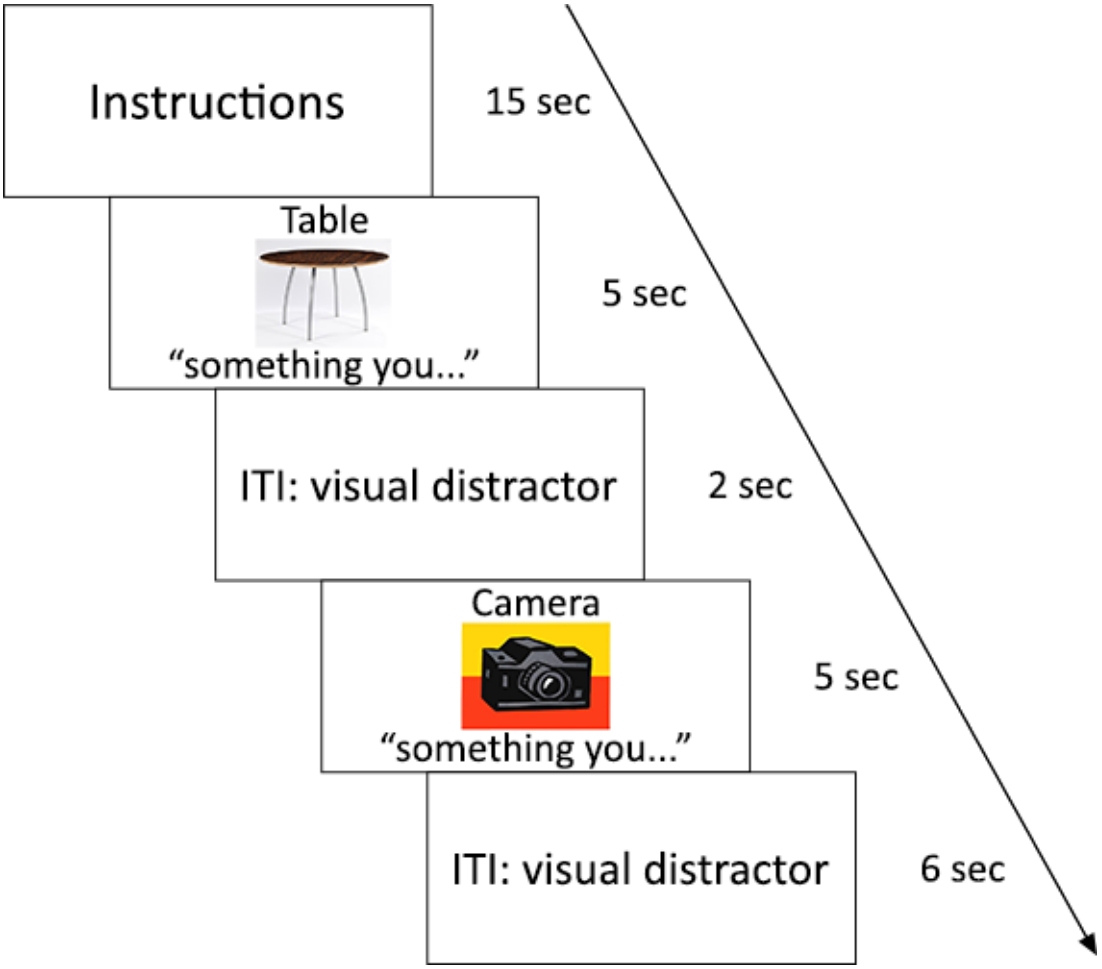

Figure 2.5. Schematic overview of fMRI-constrained principal component analysis (fMRI-CPCA). **Step 1**: Multivariate least-squares regression of blood oxygen level-dependent (BOLD) intensity values, *Z*, onto finite impulse response (FIR) basis set, *G* (performed for each participant). The *C* matrix comprises condition-specific regression weights. *GC* represents the variability in *Z* that is predictable from *G* (i.e., the task-related variability in BOLD signal). Individual participant *GC* matrices are concatenated to create the resulting *GC* matrix in the following step. **Step 2**: Singular value decomposition is used to extract components in *GC* that represent temporally orthogonal functional brain networks in which BOLD activity is directly related to the task timing. This produces a (rescaled) matrix, *VD*, containing the component loadings which are thresholded and overlaid on a brain template, and matrix *U*, containing the component scores for each participant. By convention, positive loadings are depicted in hot colours, and negative loadings are depicted in cool colours. **Step 3**: For each participant, component scores (*U*) are regressed onto *G* to produce predictor weights (*P*) estimating the intensity of the component at each time bin coded in *G*. Predictor weights should take the shape of a hemodynamic response (HDR) when plotted over post-stimulus time, and may be input to conventional statistical analyses such as a repeated measures analysis of variance (ANOVA).

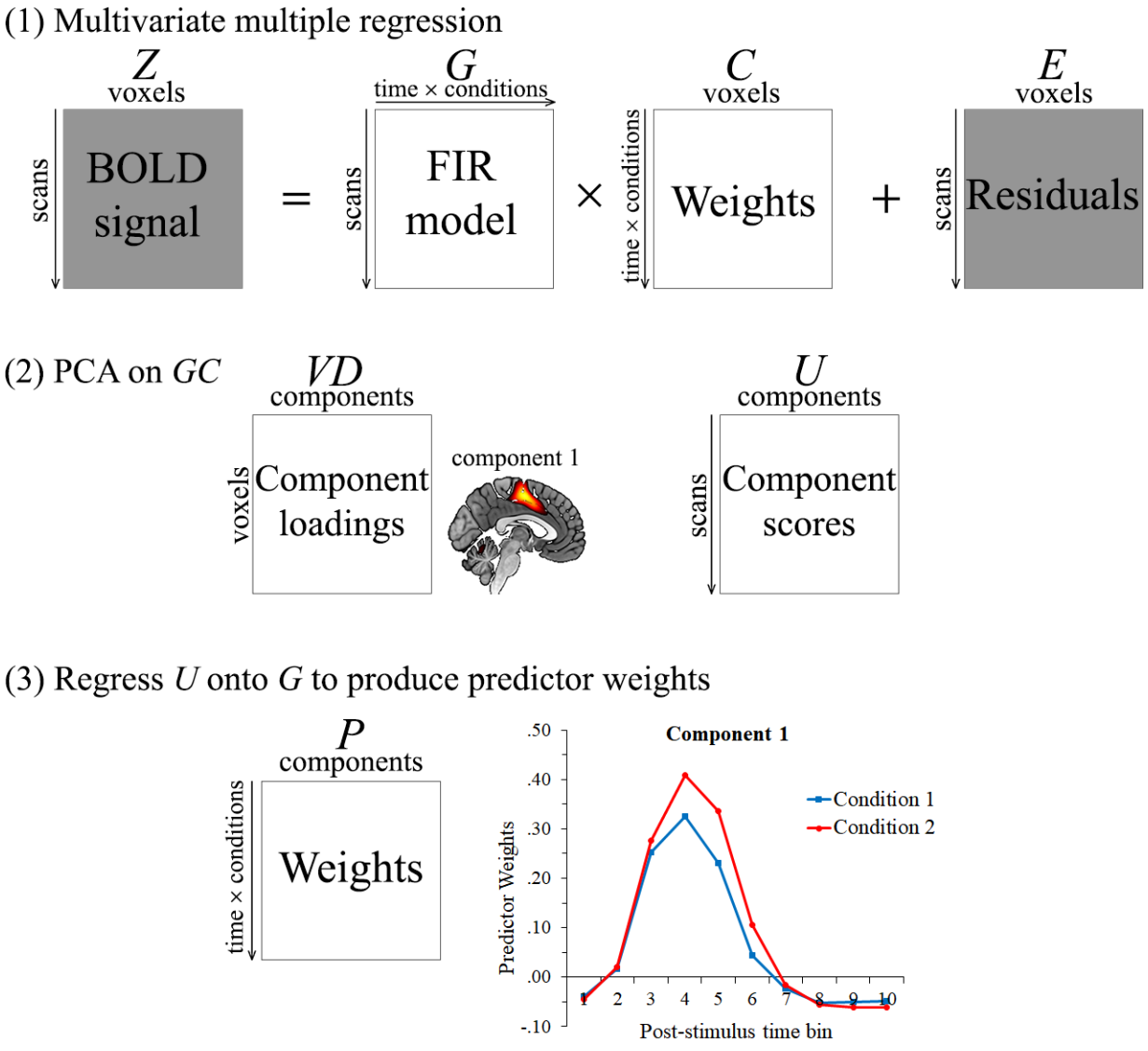

Chapter 3: Finer Separation of Working Memory Networks Using Multi-Experiment fMRI-CPCA

3.1. Background

Working memory (WM), defined as the ability to actively hold information in mind in order to guide behavior (Baddeley & Hitch, 1974), is a prevailing construct of interest in cognitive neuroscience (D'Esposito & Postle, 2015) and its neural circuitry may have implications in cognitive remediation for schizophrenia (Li et al., 2015). It has been proposed that there is a "core" network underlying WM processes, comprising dorsolateral prefrontal cortex (DLPFC), premotor cortex, anterior insula, supplementary motor area (SMA), and intraparietal sulcus (Rottschy et al., 2012). However, WM is not a unitary cognitive construct; distinct processes are expected to be involved in a WM task, including – at minimum – encoding external stimuli, maintaining internal representations, and selecting/executing a response. Although it is plausible for a given brain region to support a variety of cognitive operations (e.g., Cohen, Sreenivasan, & D'Esposito, 2014), a more refined characterization of functional brain networks underlying WM should be possible. However, given the limited temporal resolution of fMRI data, network decompositions derived from functionally correlated voxels could be confounded by coinciding/overlapping task demands such as internal maintenance of items in memory and preparation/execution of motor responses.

In a Sternberg item recognition paradigm (SIRP), one way to address the problem of low temporal resolution in fMRI data is to independently vary the degree of cognitive load (i.e., number of items to remember) and the duration of the delay period. With these manipulations, functional brain networks underlying encoding and maintenance should exhibit activity that increases with greater cognitive load, but those underlying motor responses should not. In addition,

functional brain networks underlying maintenance and retrieval/response should exhibit activity in which the timing depends on delay period length, but those underlying encoding should not. However, these experimental manipulations could affect multiple processes (e.g., increasing the number of items to remember may result in both an increase in encoding demands and an increase in perceptual processing), and the inability to randomize the order of task phases is a prevailing limitation, as the order must be: 1. encoding, 2. delay, and then 3. response.

In addition to utilizing strategic task designs, another way to delineate HDRs of networks underlying WM sub-processes is by treating the different task phases as distinct epochs (encoding, delay, and probe), and deriving spatial maps of connectivity by, for example, applying a seed-based approach (Gazzaley, Rissman, & D'Esposito, 2004; Rissman, Gazzaley, & D'Esposito, 2004) or independent component analysis (Meda et al., 2009; Steffener et al., 2012; Wong & Stevens, 2012). However, WM sub-processes may not fit neatly into one task phase or be elicited by the onset of a particular stimulus. For example, there could be preparatory activity that initiates within the maintenance phase but would be more accurately characterized as a response/retrieval process, or there could be encoding processes that extend into the delay period. It is also important to note that the actual cognitive processes engaged during a task may underlie a variety of different types of task demands, and demonstrating that a network is correlated with one particular task phase does not necessarily reveal what function that network serves per se.

3.2. Aims and Hypotheses

Two approaches were implemented to optimally separate and assign plausible cognitive processes to networks underlying a SIRP task involving memorizing letter strings: (1) independent manipulation of cognitive load and delay period length, and (2) multi-experiment fMRI-CPCA combining WM data with a different cognitive task, the Thought Generation Task (TGT;

Lavigne, Rapin, et al., 2015). A number of considerations were made in the decision to use the TGT as a comparison task. Firstly, the TGT task does not involve an overt response (button-press or otherwise), which offers a clear distinction to help separate motor response processes from cognitive processes involved in WM; that is, as motor response processes will be engaged in the WM task only, a response-based HDR should be elicited for the WM task but not the TGT task. Although a basic perceptual or motor task would provide a similar manipulation (e.g., visual fixation task without any motor response, or a motor response task without WM cognitive demands), the TGT task also entails some manipulation of higher-level cognitive demand which could be relevant to WM. For example, the TGT task's two conditions (silent thought generation and speech perception) provide a contrast between an internally-oriented cognitive process and an externally-oriented stimulus perception process, and this comparison could be analogous to the contrast between the WM process of internally rehearsing a sequence of letters in the absence of their external representation and encoding the letters presented on-screen. In summary, the purpose of utilizing the TGT data in the present study was to advance our understanding of networks engaged during the WM task, as separation of networks in the multi-experiment analysis was expected to be observed that were not separable in the WM dataset on its own; studies utilizing the TGT task as a construct of interest on its own have been previously published (Lavigne, Rapin, et al., 2015; Rapin et al., 2012), and it is analyzed in detail in Chapter 4, and so the TGT single-experiment fMRI-CPCA results are not discussed in the present chapter.

Previously published fMRI-CPCA results on WM and TGT tasks allowed for some general predictions to be made. First, in the WM task, frontoparietal connectivity coordinated with primary and association visual cortices was expected to emerge, with the magnitude of coordinated activation being dependent on cognitive load, and the activation initiating early in the post-

stimulus time series (Braunlich et al., 2015; Metzak et al., 2011; Metzak et al., 2012; Woodward et al., 2013). It was also expected that deactivation of the default mode network (DMN; Buckner, Andrews-Hanna, & Schacter, 2008) would be sustained throughout the WM trial phases, with the magnitude of deactivation also being dependent on cognitive load (Braunlich et al., 2015; Metzak et al., 2011; Metzak et al., 2012; Woodward et al., 2013). The respective activation and deactivation of these networks were expected to be similarly engaged in the TGT task (Lavigne, Rapin, et al., 2015). Finally, it was predicted that a third network would exhibit activation in regions involved in volitional control over motor responses, including the SMA, primary and premotor cortices contralateral to the response hand, basal ganglia, and cerebellar activations ipsilateral to the response hand. This "response" network was predicted to exhibit late, staggered onsets, dependent on the delay duration in the WM task (Braunlich et al., 2015; Woodward et al., 2013), but to produce a flat HDR in the TGT task since this task did not involve a motor response. Internally oriented WM processes related to maintenance and/or recall may temporally coincide with response anticipation and execution; therefore, in the current study, because internally oriented cognitive processes – but not response processes – are expected to overlap between the two tasks (i.e., in the thought generation condition for the TGT task), some separation of these processes onto distinct networks in the multi-experiment analysis was expected.

3.3. Methods

3.3.1. Participants

69 participants from two datasets were included in the present analysis, all of whom met the general inclusion criteria for healthy controls as detailed in Chapter 2 (Section 2.1). 37 participants completed the WM task and 32 non-overlapping participants completed the TGT task. Task performance on the fMRI WM task was examined to confirm participant engagement dur-

ing the task, and any runs in which a participant achieved < 60% correct responses were excluded from the analysis (note that participants had a 50% chance of guessing correctly on any given trial). A brief demographic questionnaire was administered to all participants to obtain their age, highest level of education, and any history of head injury, neurological conditions, drug use, and medication. In addition, visual acuity and color vision were assessed to ensure that participants were able to view the tasks on an fMRI presentation screen. Handedness was measured with the Annett Hand Preference Questionnaire (AHPQ; Annett, 1970), and IQ was estimated with the Quick IQ test (Mortimer & Bowen, 1999). Participants were recruited via posters on the University of British Columbia (UBC) campus, community bulletin boards, and on electronic bulletin boards such as Craigslist. Participants provided informed consent at the start of their testing sessions, and were compensated $10 per hour for time spent participating in the study plus $10 for travel expenses. Participants were also given a copy of their T1 MRI scan on a disc. Demographic information for each group of participants is provided in Table 3.1. Details regarding fMRI data acquisition and preprocessing are provided in Chapter 2 (Section 2.3 and Table 2.1)

3.3.2. Tasks

3.3.2.1. WM task design

Details regarding WM task design and administration are presented in Chapter 2 (Section 2.2.1 and Figure 2.1). In summary, a string of 4 or 6 upper case consonants was displayed for 4 seconds, and then a single probe letter was displayed for 2 seconds. Participants were asked to respond “yes” or “no” with a button-press as to whether this probe letter was part of the first string of letters. Both the cognitive load (4 or 6 letters in the item set) and delay period (0 or 4 seconds between the letter string and probe) were manipulated so as to facilitate identification of the functional brain networks distinctly involved in encoding, maintenance, and responding.

3.3.2.2. TGT task design

Details regarding TGT task design and administration are presented in Chapter 2 (Section 2.2.4 and Figure 2.4). Briefly, participants were presented with an object noun and its corresponding image (e.g., pillow) for five seconds and instructed to either mentally generate or listen to a simple definition of the word (e.g., "Something you rest your head on when sleeping"). The two experimental conditions (i.e., generating and hearing) were presented in alternating blocks of 15 trials.

3.3.3. Functional connectivity analysis

Multi-experiment fMRI-CPCA was carried out as described in detail in Chapter 2 (Section 2.4 and Figure 2.5). fMRI-CPCA combines multivariate multiple regression with PCA to reveal temporally orthogonal sources of post-stimulus BOLD activity, by employing PCA on the portion of variance in BOLD signal that is predictable from the task timing (as specified by a FIR model). In the present analysis, the time bins for which a FIR basis function was specified were scans 1-10 following trial onset (i.e., 20 seconds of post-stimulus time for the WM task with TR = 2,000ms, and 25 seconds of post-stimulus time for the TGT task with TR = 2,500ms). For the WM task, each level of cognitive load and delay duration was modelled, resulting in *G* matrices with 374 rows (scans) and 40 columns (4 conditions × 10 post-stimulus time bins) per task run. For the TGT task, both the generating and the hearing condition were modelled, resulting in *G* matrices with 176 rows (scans) and 20 columns (2 conditions × 10 post-stimulus time bins) per task run.

fMRI-CPCA produces predictor weights for each component (i.e., network) for each combination of post-stimulus time bin, task condition, and participant. Therefore, the estimated HDRs in each of the extracted networks was statistically examined by applying repeated

measures ANOVAs to the predictor weights to examine effects of post-stimulus time and experimental conditions in each task. For the WM task, a 2 (cognitive load; 4 vs. 6 letters) × 2 (delay duration; 0 vs. 4 seconds) × 10 (post-stimulus time bins) ANOVA was performed for each network. For the TGT task, a 2 (condition; hearing vs. generating) × 10 (post-stimulus time bins) ANOVA was performed for each network. Post hoc analyses of significant main effects and interactions were performed for networks extracted from the multi-experiment fMRI-CPCA only. For the WM task, post-hoc analyses were performed to examine effects of cognitive load, delay duration, load × delay, and delay × time. Main effects of load and delay were examined using polynomial contrasts. For the TGT task, post-hoc analyses were performed to examine effects of condition and condition × time. Effects of condition were examined using polynomial contrasts. In both tasks, interactions involving time were examined using repeated measures contrasts between adjacent time bins.

3.4. Results

3.4.1. WM task fMRI-CPCA results

A more extensive analysis of the WM task, with a larger sample size, is reported in Chapter 4. A brief summary is provided here for comparison with the subsequent multi-experiment results. Three components were extracted from the WM data, accounting for 16.83%, 9.70%, and 9.51% of the variance in task-related BOLD signal, respectively (after varimax rotation). These networks are referred to as (1) response/attention network, (2) default mode network (DMN), and (3) visual attention network.

The response/attention network (component 1) consisted of activation primarily in bilateral SMA, paracingulate gyrus, dorsal anterior cingulate, and insula, left somatomotor areas, and right cerebellum. The HDR onsets were staggered according to the delay length (Figure 3.1; ana-

tomical coordinates in Table 3.2). The 2 (load) × 2 (delay) × 10 (time) repeated measures ANOVA revealed significant main effects of cognitive load, $F(1, 36) = 21.053$, $p < .001$, $\eta_p^2 = .369$; delay, $F(1, 36) = 32.473$, $p < .001$, $\eta_p^2 = .474$; and time, $F(9, 324) = 25.336$, $p < .001$, $\eta_p^2 = .413$. Further, significant interactions emerged for load × time, $F(9, 324) = 8.400$, $p < .001$, $\eta_p^2 = .189$; and delay × time, $F(9, 324) = 78.078$, $p < .001$, $\eta_p^2 = .684$; but not for load × delay or load × delay × time (ps > .15). Together, these results indicate involvement of this network in retrieval/response, with the staggered somatomotor activity suggesting motor-response processes (i.e., the "yes"/"no" button-press); however, the main effect of cognitive load, due to greater engagement of this network in the 6-letter condition than in the 4-letter condition (mean predictor weights = 0.07 and 0.03, respectively), suggests a role in cognition/attention as well.

The DMN (component 2) consisted primarily of bilateral deactivation in known DMN regions, including precuneus, posterior cingulate gyrus, anterior paracingulate gyrus, superior lateral occipital cortex, and middle temporal gyrus (Figure 3.2; anatomical coordinates in Table 3.3). Component 2 is referred to as the DMN for consistency with fMRI literature convention (Buckner et al., 2008; Raichle, 2015; Yeo et al., 2011). Significant main effects emerged for load, $F(1, 36) = 16.320$, $p < .001$, $\eta_p^2 = .312$; delay, $F(1, 36) = 21.157$, $p < .001$, $\eta_p^2 = .370$; and time, $F(9, 324) = 36.854$, $p < .001$, $\eta_p^2 = .506$. Significant interactions emerged for load × delay, $F(1, 36) = 9.007$, $p = .005$, $\eta_p^2 = .200$; load × time, $F(9, 324) = 6.016$, $p < .001$, $\eta_p^2 = .143$; and delay × time, $F(9, 324) = 15.512$, $p < .001$, $\eta_p^2 = .301$; but not load × delay × time ($p > .08$). The load-dependence and extension of the HDR into late post-stimulus time points when a delay period was present suggests a cognitive process engaged throughout the trial.

The visual attention network (component 3) consisted primarily of bilateral activation in occipital cortex (extending dorsally into the superior parietal lobule), SMA, precentral gyrus, and thalamus, which peaked relatively early following trial onsets (Figure 3.3; anatomical coordinates in Table 3.4). Significant main effects emerged for load, $F(1, 36) = 22.020$, $p < .001$, $\eta_p^2 = .380$; delay, $F(1, 36) = 13.918$, $p = .001$, $\eta_p^2 = .279$; and time, $F(9, 324) = 129.140$, $p < .001$, $\eta_p^2 = .782$. Significant interactions emerged for load × time, $F(9, 324) = 13.983$, $p < .001$, $\eta_p^2 = .280$; and delay × time, $F(9, 324) = 20.250$, $p < .001$, $\eta_p^2 = .360$; but not for load × delay or load × delay × time (ps > .25). The activation of frontoparietal and primary/association visual cortices, as well as the dependence of HDR magnitude on cognitive load, suggest involvement of this network in visual attention; the absence of a second HDR peak in the 4-second delay conditions suggests that this activity underlies some cognitive process over and above basic visual perception.

3.4.2. Multi-experiment fMRI-CPCA results

3.4.2.1. Descriptive summary

Seven components were extracted from the combined WM and TGT data, accounting for 9.79%, 7.80%, 7.26%, 6.98%, 4.15%, 3.30%, and 2.54% of the variance in task-related BOLD signal, respectively (after varimax rotation). All components were interpretable and accorded with the event timing of both tasks; however, components 5-7 appeared to underlie basic sensory or vascular processes that were not of interest, and so are not discussed in detail in this chapter, but are presented in Figures 3.5 to 3.7, with statistical results listed in Table 3.5. Components 1-3 all exhibited some configuration of frontoparietal connectivity including activation in dorsomedial prefrontal cortex, and therefore merited further examination. Component 4 appeared to comprise DMN deactivation, which has been proposed to be important for WM and other cognitive

tasks (e.g., Santangelo & Bordier, 2019; Vatansever, Menon, Manktelow, Sahakian, & Stamatakis, 2015; Woodward et al., 2016). Components 1-4, which accounted for 34.53% of variance in task-related BOLD signal, are described below for clarity, followed by statistical results. These networks are referred to as (1) response network, (2) visual attention network, (3) internal attention network, and (4) DMN. Figure 3.4 presents a side-by-side comparison between these four components and the three components extracted in the single-experiment WM analysis, including surface representations and HDR plots for the WM task.

The response network (component 1), which overlapped with component 1 in the single-experiment WM analysis, consisted of activation primarily in the SMA, dorsal anterior cingulate, left somatomotor areas, cerebellum, and insula (Figure 3.8; anatomical coordinates in Table 3.6). Activation of this network was suppressed in the TGT task, but exhibited a pattern of activation in the WM task consistent with the timing of response processes (i.e., late initiation of the HDR, with the onsets in the 4-second delay conditions occurring approximately 4 seconds after the onsets in the 0-second delay conditions). Although this network was similar to component 1 in the single-experiment analysis, the prefrontal cortex and insula activation was slightly posterior to that of the single-experiment results (Figure 3.1), even in regions such as the medial prefrontal cortex that were common to the two analyses. Further, the HDR was less load-dependent than that of the single-experiment WM analysis, suggesting isolation of response processes. These observations suggest that this network underlies motor responses with the right hand.

The visual attention network (component 2), which was quite similar to the visual attention network in the single-experiment WM analysis (component 3), consisted of activation in visual cortex (extending dorsally into parietal regions), SMA, precentral gyrus, and thalamus (Figure 3.10; anatomical coordinates in Table 3.7). Unlike component 1, component 2 was active

in both the TGT and WM task. As in component 3 from the single-experiment WM analysis, activation was load-dependent and peaked early in the WM task, but did not exhibit a second peak when the probe stimulus was displayed after a 4-second delay. This suggests that the visual activity was related to some attentional process over and above primary visual perception, particularly during the encoding phase of the WM task.

Unlike the visual attention network (component 2), the internal attention network (component 3) was not identified in the single-experiment analysis, but emerged by way of combining the WM data with the TGT data. The internal attention network consisted of activation of paracingulate and superior frontal gyrus, DLPFC, frontal poles, anterior insula, and supramarginal gyrus (Figure 3.12; anatomical coordinates in Table 3.8). In the WM task, peak activation was strong for the maintenance phase of trials in which there was a 4-second delay before the probe was displayed, but modest for trials in which there was no delay, especially for the 4-letter condition. In the TGT task, activity was much greater in the generating condition than in the hearing condition. A possible explanation for this is that this network subserves volitional attention to internal stimuli representations.

The DMN, (component 4), similar to the DMN in the single-experiment analysis (component 3), primarily consisted of bilateral deactivation of the precuneus, posterior cingulate gyrus, anterior paracingulate gyrus, superior lateral occipital cortex, and middle temporal gyrus (Figure 3.14; anatomical coordinates in Table 3.9). As in the single-experiment analysis, this deactivation was load-dependent and sustained throughout the trials. Component 4 is referred to as the DMN for consistency with fMRI literature convention (Buckner et al., 2008; Raichle, 2015; Yeo et al., 2011).

3.4.2.2. Statistical results (WM task)

For the response network in the WM task, the 2 (load) × 2 (delay) × 10 (time) repeated measures ANOVA revealed a significant main effect of time, $F(2.77, 99.83) = 4.347$, $p = .008$, $\eta_p^2 = .108$; as well as significant interactions of load × time, $F(3.37, 121.33) = 3.899$, $p = .008$, $\eta_p^2 = .098$; and delay × time, $F(9, 324) = 63.435$, $p < .001$, $\eta_p^2 = .638$. No other main effects or interactions emerged for the response network (all *p*s > .08 for load, delay, load × delay, and load × delay × time). The delay × time interaction appeared to be driven by staggered onsets consistent with the probe timing (Figure 3.9).

For the visual attention network, significant main effects emerged for load, $F(1, 36) = 6.032$, $p = .019$, $\eta_p^2 = .144$; delay, $F(1, 36) = 35.197$, $p < .001$, $\eta_p^2 = .494$; and time, $F(9, 324) = 162.133$, $p < .001$, $\eta_p^2 = .818$. Significant interactions emerged for load × time, $F(9, 324) = 17.142$, $p < .001$, $\eta_p^2 = .323$; and delay × time, $F(9, 324) = 22.107$, $p < .001$, $\eta_p^2 = .380$; but not for load × delay or load × delay × time (both *p*s > .07). The main effect of load was due to greater mean activation in the 6-letter condition than in the 4-letter condition (mean predictor weights = 0.049 and 0.064 for the 4-letter and 6-letter conditions, respectively). The main effect of delay was due to greater mean activation in the 0s delay condition than in the 4s delay condition (mean predictor weights = 0.08 and 0.04 for 0s and 4s delay, respectively). Delay effects appeared to be driven by a more sustained HDR in the 0s delay condition, perhaps due to the appearance of the probe stimulus immediately after the encoding phase (Figure 3.11).

For the internal attention network, significant main effects emerged for cognitive load, $F(1, 36) = 69.448$, $p < .001$, $\eta_p^2 = .659$; delay, $F(1, 36) = 43.505$, $p < .001$, $\eta_p^2 = .547$; and time, $F(9, 324) = 22.954$, $p < .001$, $\eta_p^2 = .389$. Significant interactions emerged for load × delay,

$F(1, 36) = 4.625$, $p = .038$, $\eta_p^2 = .114$; load × time, $F(9, 324) = 15.451$, $p < .001$, $\eta_p^2 = .300$; delay × time, $F(9, 324) = 31.150$, $p < .001$, $\eta_p^2 = .464$; and load × delay × time, $F(4.34, 156.29) = 3.356$, $p = .009$, $\eta_p^2 = .085$. The main effect of load was due to greater mean activation in the 6-letter condition compared with the 4-letter condition (mean predictor weights = 0.023 and 0.106 for 4 letters and 6 letters, respectively). The main effect of delay was due to greater mean activation in the 4s delay condition than in the 0s delay condition (mean predictor weights = 0.03 and 0.10 for 0s and 4s delay, respectively). The effect of delay was greater in the 6-letter condition than in the 4-letter condition (Figure 3.13A). Delay effects were driven by not only a more sustained HDR in the 4s delay condition, but also a greater HDR peak compared with that of the 0s delay condition (Figure 3.13B).

Finally, for DMN deactivation, significant main effects emerged for cognitive load, $F(1, 36) = 22.033$, $p < .001$, $\eta_p^2 = .380$; delay, $F(1, 36) = 26.635$, $p < .001$, $\eta_p^2 = .425$; and time, $F(9, 324) = 42.880$, $p < .001$, $\eta_p^2 = .544$. Significant interactions emerged for load × delay, $F(1, 36) = 6.511$, $p = .015$, $\eta_p^2 = .153$; load × time, $F(9, 324) = 6.994$, $p < .001$, $\eta_p^2 = .163$; and delay × time, $F(9, 324) = 18.695$, $p < .001$, $\eta_p^2 = .342$. The main effect of load was driven by greater mean DMN deactivation in the 6-letter condition compared with the 4-letter condition (mean predictor weights = 0.140 and 0.190 for 4 letters and 6 letters, respectively). The main effect of delay was due to greater mean activation in the 4s delay condition than in the 0s delay condition (mean predictor weights = 0.14 and 0.19 for 0s and 4s delay, respectively). The effect of delay was greater in the 6-letter condition than in the 4-letter condition (Figure 3.15A). Effects related to delay appeared to be driven by a more sustained HDR in the 4s delay condition than in

the 0s delay condition, but not a greater *magnitude* of deactivation in the 4s delay condition per se (Figure 3.15B).

3.4.2.3. Statistical results (TGT task)

For the response network in the TGT task, the 2 (condition) × 10 (time) ANOVA revealed a main effect of time, $F(9, 279) = 32.778$, $p < .001$, $\eta_p^2 = .514$. Neither the condition nor the condition × time interaction were significant (both *p*s > .25).

For the visual attention network a significant main effect emerged for time, $F(9, 279) = 97.039$, $p < .001$, $\eta_p^2 = .758$, but not for condition or a condition × time interaction (both *p*s > .06).

For the internal attention network, significant main effects emerged for condition, $F(1, 31) = 11.157$, $p = .002$, $\eta_p^2 = .265$; and time, $F(9, 279) = 14.945$, $p < .001$, $\eta_p^2 = .325$. The condition × time interaction was also significant, $F(9, 279) = 9.851$, $p < .001$, $\eta_p^2 = .241$. Effects related to condition were due to greater mean activation in the generating condition compared with the hearing condition as a whole (mean predictor weights = 0.045 and 0.018 for generating and hearing, respectively), due to there being minimal response in the hearing condition (Figure 3.12B).

Finally, analysis of the DMN deactivation revealed a significant main effect of time, $F(9, 279) = 18.292$, $p < .001$, $\eta_p^2 = .371$, but no effect of condition or condition × time interaction (*p*s > .45).

3.5. Discussion of Multi-Experiment fMRI-CPCA

In the present analysis, a multi-experiment approach was demonstrated that helped delineate networks underlying a WM task. In addition to separation of task-based networks, the multi-experiment results extended previous analyses of brain networks involved in WM by allowing

the examination of temporal characteristics of these networks across different types of task demands. A particularly notable finding from the multi-experiment analysis was the emergence of a network exhibiting a plausible mechanism for attention to internal stimuli representations in both tasks, which is referred to as the "internal attention" network.

The results of the single-experiment WM analysis replicated previous findings using fMRI-CPCA and other methods, with somatomotor activity seemingly underlying the retrieval/response phase (based on its late, staggered peaks; component 1, Figure 3.1), visual, frontal, and thalamic activity initiating during encoding (having an early onset and return to baseline; component 3, Figure 3.3), and the DMN (component 2, Figure 3.2) exhibiting sustained, load-dependent deactivation (Braunlich et al., 2015; Metzak et al., 2011; Metzak et al., 2012; Woodward et al., 2006; Woodward et al., 2013). In previous studies, it was proposed that deactivation of the DMN supports WM maintenance, suggested from the observation that this load-dependent deactivation tends to peak intermediately between networks seeming to underlie encoding and retrieval/response. However, the current set of multi-experiment results suggests that the internal attention network is a better candidate for maintenance processes. First, the onset of DMN deactivation occurred quite early in the post-stimulus time series. Second, neither the present results nor a comparable previous study (Woodward et al., 2013) showed a meaningful decrease in magnitude of DMN deactivation when there was no delay before the probe stimulus. A functional brain network supporting maintenance-related processes would be expected to initiate activation several seconds into the post-stimulus time series – following networks activated from the trial onset – and show a strong increase in peak magnitude when the maintenance period is longer; both of these characteristics were observed in the internal attention network, but not in the DMN.

The response network that emerged from the multi-experiment analysis (component 1; Figure 3.8) was similar to the response/attention network in the single-experiment WM analysis (component 1; Figure 3.1) with respect to its spatial configuration and staggered activation patterns. However, in the single-experiment analysis, a main effect of cognitive load emerged for the response/attention network, suggesting that the network also supported cognitive/attentional processes; by contrast, the response network in the multi-experiment analysis appeared to be more specifically related to the motor response, supported in part by the observation that this network was suppressed in the TGT task (which did not require a response), and that it did not exhibit a main effect of cognitive load. Interestingly, insula and prefrontal activations in the response/attention network were situated more anteriorly in the single-experiment analysis than in the response network extracted from the multi-experiment analysis (compare Figures 3.1A and 3.8A, respectively), which may reflect meaningful anatomical differences with respect to higher-level cognition versus motor planning (Fuster, 2004). These findings suggest that the anatomical and functional characteristics of the response/attention network from the single-experiment analysis may comprise aspects of both the response network and internal attention network, as will be discussed below, while the multi-experiment version was a clearer delineation of the response network. This illustrates an advantage of simultaneously analyzing multiple tasks; that is, the combining of cognitive/behavioral processes into a single network was reduced when a task with relevant overlapping and non-overlapping cognitive demands was simultaneously analyzed.

The most striking result in the multi-experiment analysis was the emergence of a novel network (component 3, internal attention) that was considerably more engaged in the WM 4s delay condition than in the 0s delay condition (Figure 3.13B), and the onset of which followed that of the visual attention network, but preceded the response network (Figure 3.4D). Although pre-

vious research has identified networks underlying WM which spatially resemble this internal attention network (Emch, von Bastian, & Koch, 2019; Meda et al., 2009; Rottschy et al., 2012; Vasic, Walter, Sambataro, & Wolf, 2009; Wolf et al., 2008), the present study expands on this in providing the task-related time series, which strongly suggest engagement of this network not only during WM, but also during internal thought that is not required to be held in memory (in the TGT task). Moreover, the present results help clarify which aspect of a WM task this network underlies. Comparing the series of WM task HDRs across networks (as displayed in Figure 3.4D), it is possible that activation of the visual attention network supports visual attention to the to-be-encoded letter string at the trial onset, and its diminishing intensity reflects a coordinated shift from external to internal attention as the internal attention network becomes engaged; this may be required in order to maintain a mental representation of the stimuli. As to why this network is somewhat active in the 0s delay conditions despite the absence of the requirement to maintain items in memory, it could be the case that internal attention either (1) initiates during the late encoding phase of the task in anticipation of the possible maintenance phase, (2) overlaps with response anticipation and execution, or (3) some combination of both, as participants do not know until completion of the encoding phase whether or not there will be a delay period. Therefore, it is plausible that both internal (maintenance) processes and response anticipation processes become engaged before the end of the encoding phase and exhibit similar HDR shapes (when no delay actually occurs), particularly if sustaining internal attention into the response phase is required for accurate recall. This similarity in timing could explain why component 1 in the single-experiment analysis appeared to be comprised of both cognitive and motor response processes. The presence of an overlapping cognitive process between WM and TGT (i.e., internal representations of stimuli) and a non-overlapping process (i.e., motor response) may have al-

lowed these temporally correlated processes to separate onto different networks when the two datasets were analyzed simultaneously using multi-experiment fMRI-CPCA.

Although descriptive labels were assigned for the purposes of discussion ("response", "visual attention", etc.), the postulated function assigned to each network may not be the only function it may serve across the vast range of cognitive constructs examined in the wider cognitive neuroscience literature – the complexities of structure-function mapping are well-summarized by Poldrack (2010). For example, it cannot be determined from the present findings whether the internal attention network has a broad role of generating internal representations of task-relevant stimuli, or whether it underlies verbal tasks only. A larger set of tasks that, together, independently manipulate internal representations of various modalities, inner speech, cognitive control, memory demand, and a range of other constructs would ideally be combined in order to better infer the functional specificity of the internal attention network and other patterns of connectivity observed in the present study. However, the limited experimental design was appropriate for this relatively narrow, proof-of-concept study which aimed to demonstrate how the addition of even one carefully chosen task can provide valuable information that could be missed in the analysis of a single cognitive construct.

3.6. Chapter 3 Tables

Table 3.1. Demographic information for the WM task and the TGT task datasets (from WM-TGT multi-experiment analysis with healthy controls only). Standard deviations in parentheses.

	WM (n = 37)	TGT (n = 32)
Age	28.16 (8.70)	28.75 (8.58)
Years of education	15.86 (2.16)	15.58 (1.81)
Quick estimated IQ	99.59 (11.89)	97.09 (11.21)
Gender distribution (female/male)	27/10	13/19
Handedness (L/M/R)	3/2/32	3/1/28
Socioeconomic status factor score	58.24 (15.68)	65.75 (14.97)

Note. IQ = intelligence quotient; L = left-handed; M = mixed handedness; R = right-handed; WM = Working Memory; TGT = Thought Generation Task.

Table 3.2. WM task fMRI-CPCA, response/attention network (component 1): Clusters for the most extreme 10% of component loadings. Anatomical regions, Brodmann areas (BAs), and Montreal Neurological Institute (MNI) coordinates are listed for each cluster peak.

WM task response network (component 1) anatomical regions	Cluster volumes		BAs	MNI coordinates		
	voxels	mm^3		x	y	z
Positive loadings						
Cluster 1: left hemisphere	3,993	107,811				
Precentral gyrus			4	-36	-22	59
Postcentral gyrus			3	-45	-31	53
Postcentral gyrus			3	-51	-25	44
Central opercular cortex			48	-54	-19	20
Precentral gyrus			6	-33	-7	62
Supplementary motor area			6	-3	-4	53
Superior lateral occipital cortex			7	-12	-70	53
Parietal operculum cortex			48	-57	-40	23
Cluster 1: right hemisphere						
Paracingulate gyrus			32	3	17	47
Cluster 2: left hemisphere	1,456	39,312				
Cerebellum VI			n/a	-30	-55	-31
Lingual gyrus			18	-6	-73	-13
Cluster 2: bilateral						
Lingual gyrus			17	0	-79	2
Cluster 2: right hemisphere						
Cerebellum V			n/a	18	-52	-22
Cerebellum VIIIa			n/a	18	-64	-49
Cerebellum V			n/a	6	-61	-16
Cerebellum crus II			n/a	6	-73	-37
Cerebellum V			n/a	12	-58	-28
Cluster 3: left hemisphere	930	25,110				
Insular cortex			48	-30	20	5
Precentral gyrus			44	-54	8	29
Precentral gyrus			6	-54	8	23
Insular cortex			48	-39	-1	8
Middle frontal gyrus			46	-36	35	26
Frontal pole			46	-30	47	20
Temporal pole			48	-51	11	-4

(Table 3.2 continued on next page)

(Table 3.2, continued from previous page)

WM task response network (component 1) anatomical regions	Cluster volumes		BAs	MNI coordinates		
	voxels	mm^3		x	y	z
Putamen			48	-30	-16	2
Cluster 4: right hemisphere	549	14,823				
Postcentral gyrus			48	57	-16	26
Superior parietal lobule			40	39	-46	47
Postcentral gyrus			3	54	-19	38
Posterior supramarginal gyrus			2	45	-37	50
Cluster 5: right hemisphere	438	11,826				
Insular cortex			47	33	23	2
Inferior frontal gyrus, pars opercularis			6	57	11	20
Cluster 6: right hemisphere	227	6,129				
Frontal pole			46	36	41	26
Cluster 7: right hemisphere	177	4,779				
Middle frontal gyrus			6	33	-1	59
Cluster 8: left hemisphere	63	1,701				
Thalamus			n/a	-12	-19	8
Cluster 9: left hemisphere	54	1,458				
Inferior lateral occipital cortex			37	-48	-64	5
Middle temporal gyrus, temporooccipital part			21	-48	-52	8
Cluster 10: right hemisphere	39	1,053				
Thalamus			n/a	12	-16	8
Caudate			n/a	15	-1	14
Cluster 11: left hemisphere	16	432				
Cerebellum VIIb			n/a	-33	-58	-49
Cluster 12: right hemisphere	7	189				
Precuneus cortex			7	9	-70	50
Cluster 13: left hemisphere	2	54				
Intracalcarine cortex			18	-15	-70	2

Table 3.3. WM task fMRI-CPCA, default mode network (DMN, component 2): Clusters for the most extreme 10% of component loadings. Anatomical regions, Brodmann areas (BAs), and Montreal Neurological Institute (MNI) coordinates are listed for each cluster peak.

WM task default mode network (component 2) anatomical regions	Cluster volumes		BAs	MNI coordinates		
	voxels	mm^3		x	y	z
Positive loadings						
Cluster 1: left hemisphere	27	729				
Supplementary motor area			6	-3	8	56
Cluster 2: left hemisphere	9	243				
Precentral gyrus			6	-54	2	44
Negative loadings						
Cluster 1: left hemisphere	2,843	76,761				
Superior frontal gyrus			9	-21	35	44
Cluster 1: right hemisphere						
Frontal pole			10	3	56	11
Superior frontal gyrus			9	24	29	44
Frontal pole			9	15	47	38
Frontal pole			9	18	44	41
Cluster 2: left hemisphere	2,476	66,852				
Posterior cingulate gyrus			23	-3	-46	35
Cluster 2: bilateral						
Precuneus cortex			31	0	-70	29
Posterior cingulate gyrus			23	0	-16	38
Cluster 3: left hemisphere	853	23,031				
Superior lateral occipital cortex			39	-48	-70	29
Cluster 4: right hemisphere	848	22,896				
Superior lateral occipital cortex			39	48	-64	26
Middle temporal gyrus, temporooccipital part			21	60	-40	-4
Cluster 5: right hemisphere	269	7,263				
Anterior middle temporal gyrus			21	57	-4	-16
Temporal pole			38	42	20	-28

(Table 3.3 continued on next page)

(Table 3.3, continued from previous page)

WM task default mode network (component 2) anatomical regions	Cluster volumes		BAs	MNI coordinates		
	voxels	mm^3		x	y	z
Temporal pole			21	48	8	-31
Cluster 6: left hemisphere	237	6,399				
Anterior middle temporal gyrus			21	-54	-4	-19
Temporal pole			21	-48	11	-28
Frontal orbital cortex			38	-42	26	-16
Anterior inferior temporal gyrus			20	-51	-4	-37
Cluster 7: left hemisphere	106	2,862				
Cerebellum crus II			n/a	-21	-79	-37
Cluster 8: right hemisphere	92	2,484				
Cerebellum crus II			n/a	27	-76	-37
Cluster 9: right hemisphere	91	2,457				
Frontal orbital cortex			47	42	32	-10
Inferior frontal gyrus, pars triangularis			45	54	26	11
Inferior frontal gyrus, pars triangularis			45	51	29	8
Inferior frontal gyrus, pars triangularis			45	51	29	-1
Cluster 10: right hemisphere	27	729				
Planum temporale			42	60	-28	17
Cluster 11: right hemisphere	23	621				
Lingual gyrus			37	27	-40	-10
Cluster 12: left hemisphere	19	513				
Lingual gyrus			37	-27	-43	-10
Cluster 13: right hemisphere	12	324				
Heschl's gyrus			48	57	-10	5
Cluster 14: left hemisphere	9	243				
Middle temporal gyrus, temporooccipital part			37	-63	-55	2

(Table 3.3 continued on next page)

(Table 3.3, continued from previous page)

WM task default mode network (component 2) anatomical regions	Cluster volumes		BAs	MNI coordinates		
	voxels	mm^3		x	y	z
Cluster 15: right hemisphere	5	135				
Amygdala			n/a	21	-4	-19
Amygdala			n/a	30	2	-19
Cluster 16: right hemisphere	4	108				
Cerebellum IX			n/a	9	-52	-46
Cluster 17: left hemisphere	4	108				
Temporal pole			48	-33	2	-19

Table 3.4. WM task fMRI-CPCA, visual attention network (component 3): Clusters for the most extreme 10% of component loadings. Anatomical regions, Brodmann areas (BAs), and Montreal Neurological Institute (MNI) coordinates are listed for each cluster peak.

WM task visual attention network (component 3) anatomical regions	Cluster volumes		BAs	MNI coordinates		
	voxels	mm^3		x	y	z
Positive loadings						
Cluster 1: left hemisphere	3,364	90,828				
Occipital pole			18	-18	-91	-7
Superior lateral occipital cortex			19	-24	-70	32
Superior lateral occipital cortex			7	-21	-61	50
Temporal occipital fusiform cortex			37	-36	-49	-19
Cluster 2: bilateral	3,164	85,428				
Vermis crus II			n/a	0	-73	-28
Cluster 2: right hemisphere						
Occipital fusiform gyrus			18	21	-88	-4
Superior lateral occipital cortex			19	27	-67	35
Superior lateral occipital cortex			7	24	-61	56
Temporal occipital fusiform cortex			37	36	-46	-19
Cerebellum crus II			n/a	9	-76	-40
Cluster 3: left hemisphere	774	20,898				
Precentral gyrus			6	-51	-1	47
Precentral gyrus			44	-42	5	29
Precentral gyrus			6	-45	2	32
Precentral gyrus			6	-57	2	26
Middle frontal gyrus			6	-27	-1	50
Cluster 4: left hemisphere	224	6,048				
Supplementary motor area			6	-3	5	62
Cluster 5: right hemisphere	140	3,780				
Precentral gyrus			6	54	-4	47
Cluster 6: right hemisphere	57	1,539				
Precentral gyrus			6	33	-19	71
Precentral gyrus			4	42	-16	65

(Table 3.4 continued on next page)

(Table 3.4, continued from previous page)

WM task visual attention network (component 3) anatomical regions	Cluster volumes		BAs	MNI coordinates		
	voxels	mm^3		x	y	z
Cluster 7: right hemisphere	43	1,161				
Precentral gyrus			44	42	5	26
Cluster 8: left hemisphere	40	1,080				
Thalamus			n/a	-21	-28	-4
Cluster 9: right hemisphere	39	1,053				
Precentral gyrus			6	30	-1	47
Cluster 10: right hemisphere	35	945				
Thalamus			n/a	21	-28	-1
Cluster 11: bilateral	26	702				
Vermis IX			n/a	0	-58	-37
Cluster 12: left hemisphere	13	351				
Anterior supramarginal gyrus			40	-42	-37	41
Cluster 13: right hemisphere	9	243				
Cerebellum VIIb			n/a	24	-70	-49
Cluster 14: right hemisphere	5	135				
Anterior supramarginal gyrus			2	45	-34	44
Negative loadings						
Cluster 1: left hemisphere	19	513				
Lingual gyrus			17	-9	-76	-7
Cluster 2: right hemisphere	2	54				
Occipital pole			18	12	-88	20

Table 3.5. WM-TGT multi-experiment fMRI-CPCA, components 6 and 7 (occipital and auditory regions, respectively): Results of repeated measures analyses of variance (ANOVAs). Significant results are presented in bold font. Component 5 reflected artifact signal and was not analyzed.

Component 6 (occipital (de)activation)					
WM task	DF	DF_{error}	*F*	*p*	η_p^2
Load	**1**	**36**	**4.84**	**.034***	**.119**
Delay	**1**	**36**	**6.717**	**.014***	**.157**
Time	**9**	**324**	**6.691**	**< .001*****	**.157**
Load × delay	1	36	3.044	.090	.078
Load × time	**4.17**	**149.96**	**3.748**	**.006****	**.094**
Delay × time	**9**	**324**	**12.397**	**< .001*****	**.256**
Load × delay × time	5.30	190.86	2.073	.066	.054
TGT task	DF	DF_{error}	*F*	*p*	η_p^2
Condition	1	31	1.468	.235	.045
Time	**9**	**279**	**48.944**	**< .001*****	**.612**
Condition × time	3.22	99.95	0.758	.529	.024
Component 7 (auditory network)					
WM task[a]	DF	DF_{error}	*F*	*p*	η_p^2
-	-	-	-	-	-
TGT task	DF	DF_{error}	*F*	*p*	η_p^2
Condition	**1**	**31**	**39.018**	**< .001*****	**.557**
Time	**9**	**279**	**92.004**	**< .001*****	**.748**
Condition × time	**9**	**279**	**51.879**	**< .001*****	**.626**

[a]Analysis of the auditory network (component 7) was not performed for WM task due to absence of meaningful HDR shape (see Figure 3.7, WM conditions).
DF = degrees of freedom; * = $p < .05$; ** = $p < .01$; *** = $p < .001$.

Table 3.6. WM-TGT multi-experiment fMRI-CPCA, response network (component 1): Clusters for the most extreme 10% of component loadings. Anatomical regions, Brodmann areas (BAs), and Montreal Neurological Institute (MNI) coordinates are listed for each cluster peak.

WM-TGT response network (component 1) anatomical regions	Cluster volumes		BAs	MNI coordinates		
	voxels	mm^3		x	y	z
Positive loadings						
Cluster 1: left hemisphere	4,880	131,760				
Postcentral gyrus			3	-42	-22	56
Postcentral gyrus			3	-54	-22	44
Central opercular cortex			48	-51	-22	20
Supplementary motor area			6	-3	-7	53
Insular cortex			48	-39	-1	8
Precentral gyrus			6	-57	5	32
Cluster 1: right hemisphere						
Superior frontal gyrus			6	27	-4	62
Posterior cingulate gyrus			23	12	-22	41
Cluster 2: right hemisphere	1,982	53,514				
Postcentral gyrus			48	57	-19	35
Superior parietal lobule			2	36	-43	59
Precentral gyrus			6	57	8	23
Precentral gyrus			6	57	8	17
Insular cortex			48	39	-1	11
Precuneus cortex			5	12	-58	59
Precuneus cortex			31	12	-43	53
Cluster 3: left hemisphere	417	11,259				
Cerebellum VI			n/a	-30	-49	-31
Cluster 3: right hemisphere						
Cerebellum V			n/a	18	-52	-22
Cluster 4: right hemisphere	169	4,563				
Inferior lateral occipital cortex			37	45	-61	2
Cluster 5: right hemisphere	154	4,158				
Cerebellum VIIIb			n/a	18	-61	-52
Vermis VIIIa			n/a	3	-70	-37

(Table 3.6 continued on next page)

(Table 3.6, continued from previous page)

WM-TGT response network (component 1) anatomical regions	Cluster volumes		BAs	MNI coordinates		
	voxels	mm^3		x	y	z
Cluster 6: left hemisphere	153	4,131				
Inferior lateral occipital cortex			37	-48	-67	5
Cluster 7: left hemisphere	36	972				
Thalamus			n/a	-12	-19	5
Cluster 8: left hemisphere	31	837				
Frontal pole			46	-30	38	26
Cluster 9: right hemisphere	27	729				
Frontal pole			46	30	41	26
Cluster 10: left hemisphere	22	594				
Cerebellum VIIIa			n/a	-30	-55	-49
Cluster 11: right hemisphere	15	405				
Thalamus			n/a	12	-16	5
Cluster 12: left hemisphere	12	324				
Cerebellum VIIb			n/a	-15	-70	-49
Cerebellum VIIIa			n/a	-21	-64	-52

Table 3.7. WM-TGT multi-experiment fMRI-CPCA, visual attention network (component 2): Clusters for the most extreme 10% of component loadings. Anatomical regions, Brodmann areas (BAs), and Montreal Neurological Institute (MNI) coordinates are listed for each cluster peak.

WM-TGT visual attention network (component 2) anatomical regions	Cluster volumes		BAs	MNI coordinates		
	voxels	mm^3		x	y	z
Positive loadings						
Cluster 1: left hemisphere	6,388	172,476				
Occipital pole			18	-18	-91	-7
Temporal occipital fusiform cortex			37	-36	-49	-19
Superior lateral occipital cortex			19	-24	-70	32
Superior lateral occipital cortex			7	-21	-64	50
Cluster 1: bilateral						
Vermis crus II			n/a	0	-73	-28
Cluster 1: right hemisphere						
Occipital fusiform gyrus			18	21	-88	-4
Superior lateral occipital cortex			19	27	-70	32
Temporal occipital fusiform cortex			37	36	-46	-19
Superior lateral occipital cortex			7	24	-61	53
Cerebellum VI			n/a	9	-73	-22
Cluster 2: left hemisphere	755	20,385				
Precentral gyrus			6	-51	-1	47
Precentral gyrus			44	-42	5	29
Precentral gyrus			6	-57	2	23
Middle frontal gyrus			6	-27	-4	47
Cluster 3: right hemisphere	392	10,584				
Precentral gyrus			6	57	-1	47
Middle frontal gyrus			6	33	-1	47
Precentral gyrus			6	36	-19	71
Precentral gyrus			4	42	-16	65
Cluster 4: left hemisphere	218	5,886				
Supplementary motor area			6	-3	5	62
Cluster 5: right hemisphere	48	1,296				
Precentral gyrus			44	42	8	26

(Table 3.7 continued on next page)

(Table 3.7, continued from previous page)

WM-TGT visual attention network (component 2) anatomical regions	Cluster volumes		BAs	MNI coordinates		
	voxels	mm^3		x	y	z
Cluster 6: left hemisphere	43	1,161				
Thalamus			n/a	-21	-28	-1
Cluster 7: right hemisphere	32	864				
Thalamus			n/a	21	-28	-1
Cluster 8: bilateral	15	405				
Vermis IX			n/a	0	-58	-37
Negative loadings						
Cluster 1: left hemisphere	4	108				
Lingual gyrus			18	-9	-73	-7

Table 3.8. WM-TGT multi-experiment fMRI-CPCA, internal attention network (component 3): Clusters for the most extreme 10% of component loadings. Anatomical regions, Brodmann areas (BAs), and Montreal Neurological Institute (MNI) coordinates are listed for each cluster peak.

WM-TGT internal attention network (component 3) anatomical regions	Cluster volumes		BAs	MNI coordinates		
	voxels	mm^3		x	y	z
Positive loadings						
Cluster 1: bilateral	4,030	108,810				
Superior frontal gyrus			6	0	17	53
Cluster 1: left hemisphere						
Insular cortex			47	-30	23	2
Inferior frontal gyrus, pars opercularis			48	-48	14	29
Middle frontal gyrus			6	-36	-1	59
Middle frontal gyrus			45	-42	32	29
Frontal pole			46	-33	50	17
Superior frontal gyrus			6	-18	11	65
Caudate			n/a	-15	8	5
Thalamus			n/a	-12	-16	8
Cluster 2: right hemisphere	1,656	44,712				
Insular cortex			47	33	23	2
Middle frontal gyrus			45	42	35	29
Middle frontal gyrus			6	39	5	56
Inferior frontal gyrus, pars opercularis			44	54	14	17
Cluster 3: left hemisphere	932	25,164				
Superior parietal lobule			40	-33	-52	44
Superior lateral occipital cortex			7	-12	-73	53
Cluster 4: left hemisphere	548	14,796				
Occipital pole			17	-6	-97	5
Cluster 4: bilateral						
Lingual gyrus			17	0	-82	-4
Cluster 4: right hemisphere						
Cerebellum VI			n/a	9	-73	-25
Occipital pole			17	12	-94	11
Cerebellum VI			n/a	27	-61	-28

(Table 3.8 continued on next page)

(Table 3.8, continued from previous page)

WM-TGT internal attention network (component 3) anatomical regions	Cluster volumes		BAs	MNI coordinates		
	voxels	mm^3		x	y	z
Cluster 5: right hemisphere	304	8,208				
Superior parietal lobule			40	33	-52	41
Cluster 6: left hemisphere	132	3,564				
Cerebellum VI			n/a	-30	-58	-31
Cluster 7: right hemisphere	116	3,132				
Cerebellum VIIb			n/a	27	-70	-52
Cluster 8: left hemisphere	83	2,241				
Inferior temporal gyrus, temporooccipital part			37	-48	-55	-16
Cluster 9: right hemisphere	45	1,215				
Caudate			n/a	12	11	2
Caudate			n/a	15	5	11
Cluster 10: left hemisphere	28	756				
Posterior supramarginal gyrus			42	-60	-43	20
Cluster 11: left hemisphere	13	351				
Cerebellum crus I			n/a	-9	-76	-25
Cluster 12: left hemisphere	7	189				
Posterior middle temporal gyrus			21	-57	-31	-4
Cluster 13: left hemisphere	3	81				
Precentral gyrus			4	-33	-25	53

Table 3.9. WM-TGT multi-experiment fMRI-CPCA, default mode network (DMN, component 4): Clusters for the most extreme 10% of component loadings. Anatomical regions, Brodmann areas (BAs), and Montreal Neurological Institute (MNI) coordinates are listed for each peak.

WM-TGT default mode network (component 4) anatomical regions	Cluster volumes		BAs	MNI coordinates		
	voxels	mm^3		x	y	z
Positive loadings						
Cluster 1: left hemisphere	4	108				
Supplementary motor area			6	-3	8	56
Negative loadings						
Cluster 1: left hemisphere	3,729	100,683				
Superior frontal gyrus			9	-21	35	44
Cluster 1: right hemisphere						
Frontal pole			10	3	56	11
Superior frontal gyrus			9	24	29	44
Cluster 2: bilateral	1,749	47,223				
Posterior cingulate gyrus			23	0	-49	35
Cluster 2: right hemisphere						
Superior lateral occipital cortex			19	15	-85	41
Cluster 3: left hemisphere	932	25,164				
Superior lateral occipital cortex			39	-51	-70	29
Cluster 4: right hemisphere	840	22,680				
Superior lateral occipital cortex			39	51	-64	26
Cluster 5: right hemisphere	261	7,047				
Anterior middle temporal gyrus			21	57	-4	-19
Temporal pole			38	42	17	-28
Cluster 6: left hemisphere	229	6,183				
Anterior middle temporal gyrus			21	-54	-4	-19
Temporal pole			21	-48	8	-28
Cluster 7: right hemisphere	93	2,511				
Frontal orbital cortex			47	42	32	-10

(Table 3.9 continued on next page)

(Table 3.9, continued from previous page)

WM-TGT default mode network (component 4) anatomical regions	Cluster volumes		BAs	MNI coordinates		
	voxels	mm^3		x	y	z
Inferior frontal gyrus, pars triangularis			45	51	26	14
Frontal orbital cortex			47	30	32	-13
Cluster 8: left hemisphere	33	891				
Cerebellum crus I			n/a	-27	-76	-37
Cluster 9: right hemisphere	22	594				
Cerebellum crus II			n/a	27	-76	-37
Cluster 10: left hemisphere	4	108				
Frontal orbital cortex			38	-42	26	-13
Cluster 11: right hemisphere	2	54				
Frontal orbital cortex			48	27	20	-16

3.7. Chapter 3 Figures

Figure 3.1. WM task fMRI-CPCA, response/attention network (component 1): Anatomical and temporal characteristics. **A (top)**: dominant 10% of loadings (red/yellow = positive loadings, min = 0.21, max = 0.37; no negative loadings above threshold). Images are displayed in neurological orientation (left is left) with MNI coordinates. **B (bottom)**: predictor weights plotted over post-stimulus time for each task condition. 4L = 4 letters; 6L = 6 letters.

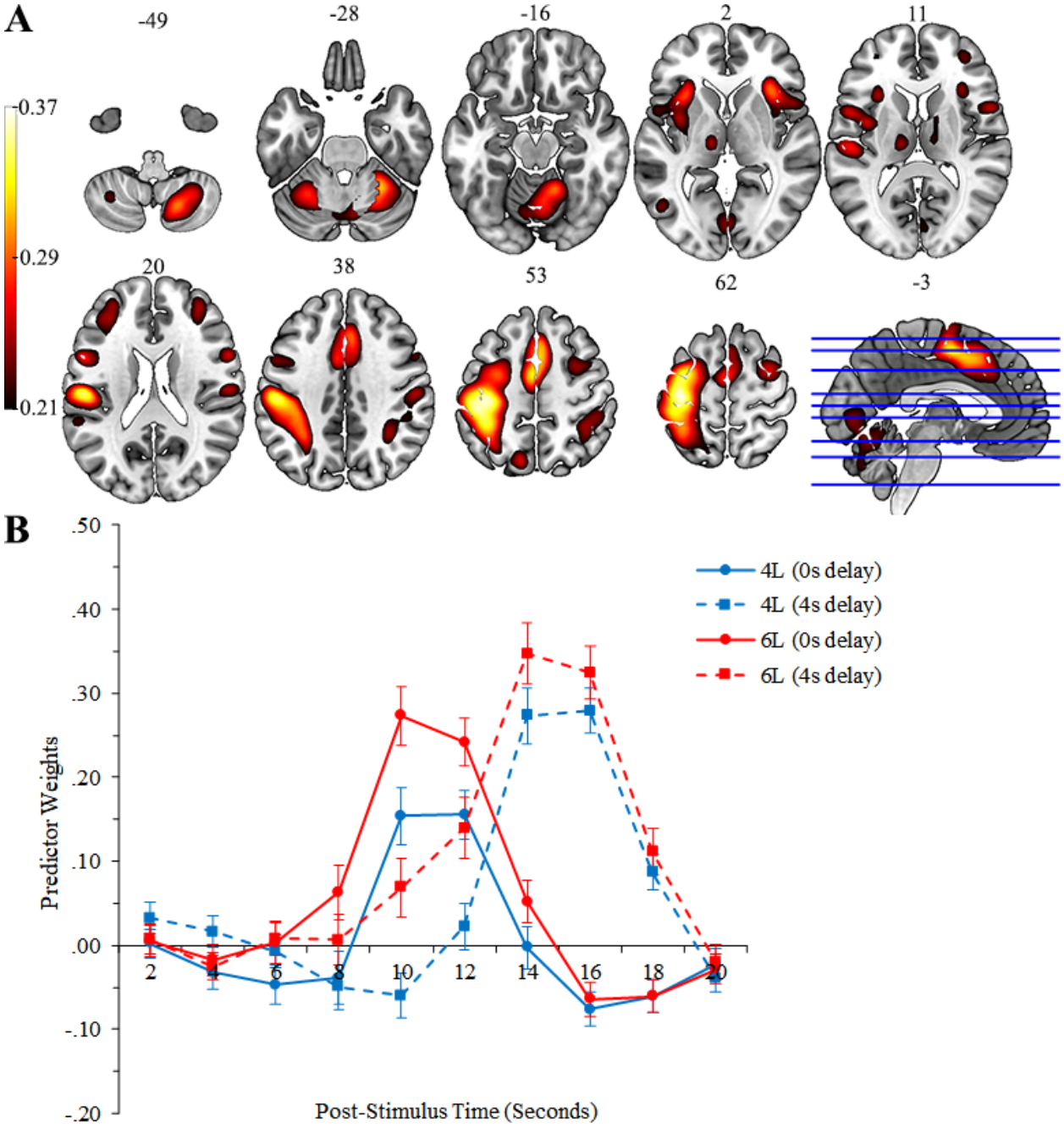

Figure 3.2. WM task fMRI-CPCA, default mode network (DMN, component 2): Anatomical and temporal characteristics. **A (top)**: dominant 10% of loadings (red/yellow = positive loadings, min = 0.16, max = 0.19; blue/green = negative loadings, min = -0.27, max = -0.16). Images are displayed in neurological orientation (left is left) with MNI coordinates. **B (bottom)**: predictor weights plotted over post-stimulus time for each task condition. Y axis is reversed (negative down, positive up) to facilitate interpretation (i.e., values above X axis reflect activation, and values below X axis reflect deactivation). 4L = 4 letters; 6L = 6 letters.

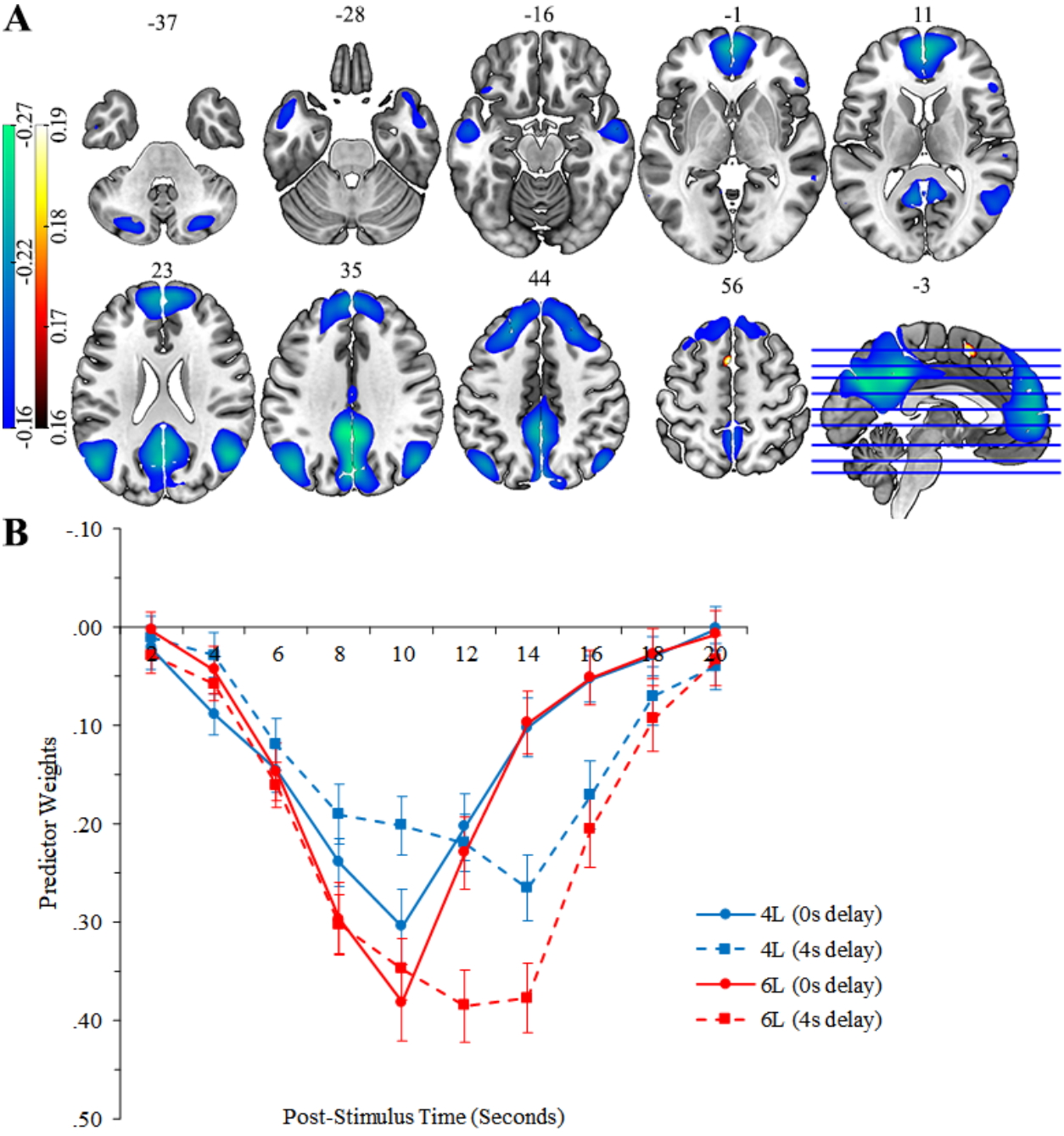

Figure 3.3. WM task fMRI-CPCA, visual attention network (component 3): Anatomical and temporal characteristics. **A (top)**: dominant 10% of loadings (red/yellow = positive loadings, min = 0.21, max = 0.37). Images are displayed in neurological orientation (left is left) with MNI coordinates. **B (bottom)**: predictor weights plotted over post-stimulus time for each task condition. 4L = 4 letters; 6L = 6 letters.

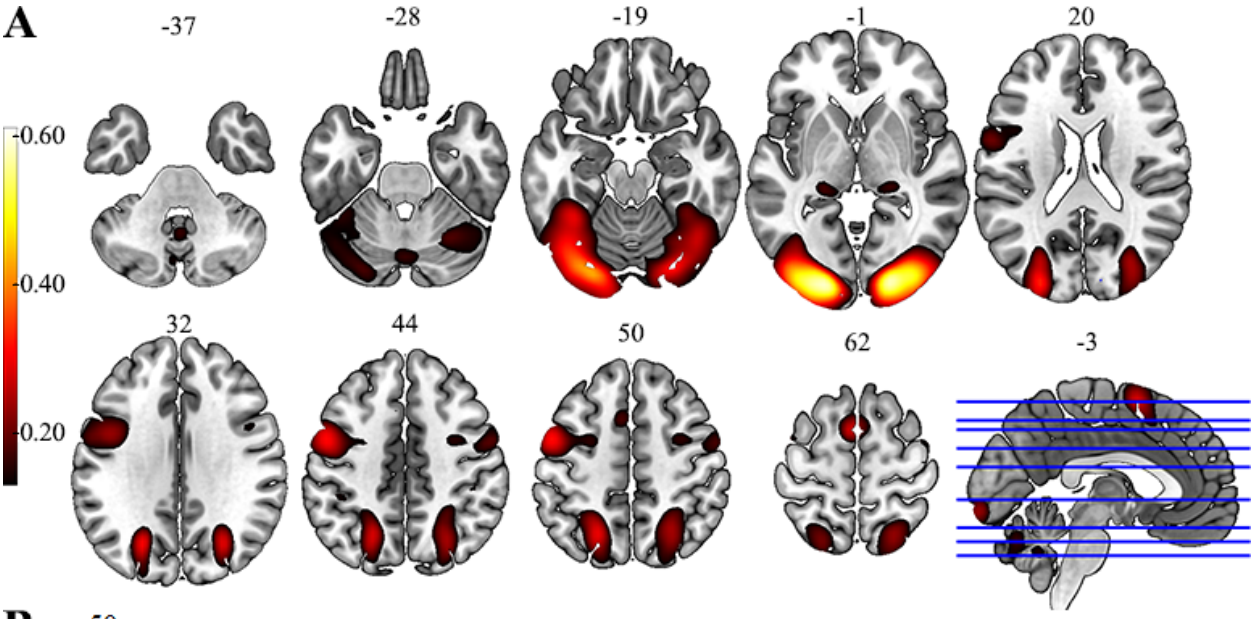

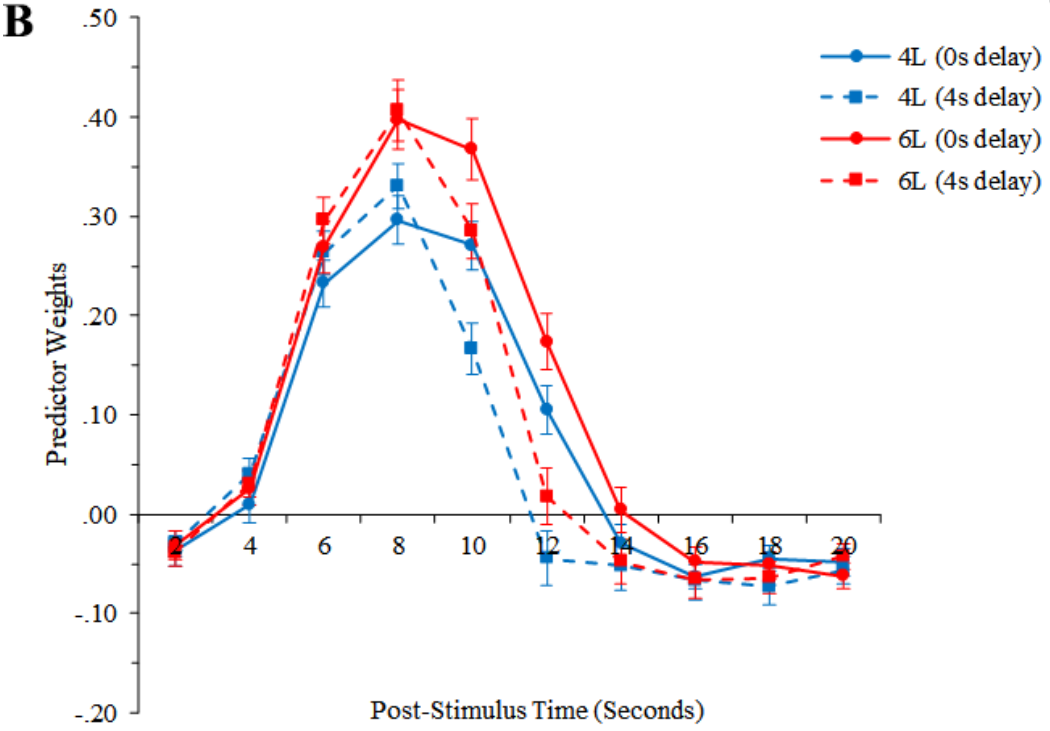

Figure 3.4. Surface representations and WM HDR shapes in the single-experiment vs. the multi-experiment fMRI-CPCA. **A (top left):** surface representations of components 1-3 from the single-experiment WM analysis. **B (bottom left):** predictor weights plotted over post-stimulus time for components 1-3 from the WM single-experiment analysis, averaged over load; component 2 predictor weights have been multiplied by -1 so that values above X axis reflect activation for all components. **C (top right):** surface representations of components 1-4 from the multi-experiment analysis (response, visual attention, internal attention, and default mode networks). **D (bottom right):** WM task predictor weights plotted over post-stimulus time for components 1-4 from the multi-experiment analysis (response, visual attention, internal attention, and default mode networks), averaged over load; DMN predictor weights have been multiplied by -1 so that values above X axis reflect activation for all components. Comp = component; DMN = default mode network.

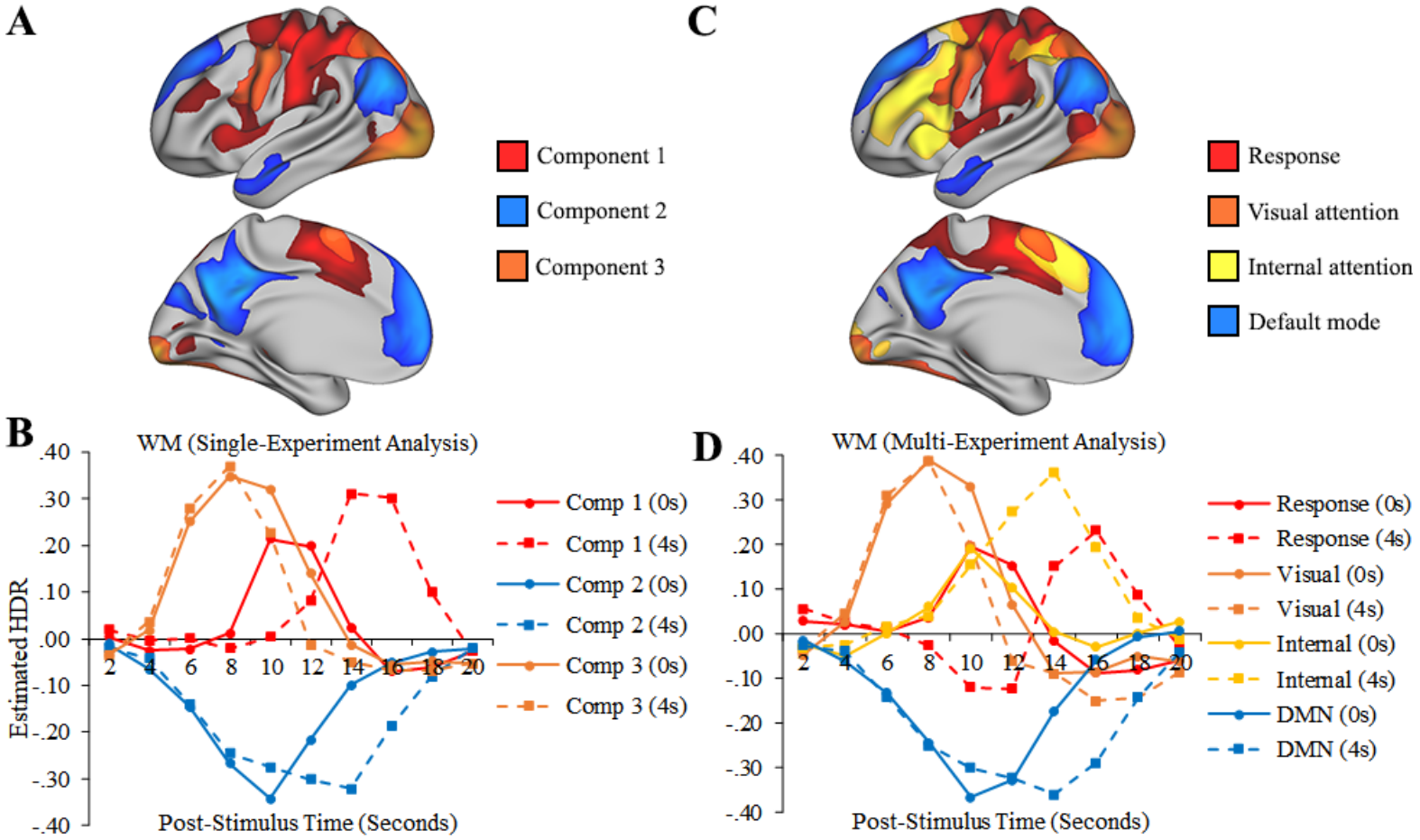

Figure 3.5. WM-TGT multi-experiment fMRI-CPCA, blood flow artifact (component 5): Anatomical and temporal characteristics. Many peak areas were outside of the brain, likely reflecting blood drainage after a neural response. **A (top):** dominant 10% of loadings (red/yellow = positive loadings, min = 0.10, max = 0.21; no negative loadings above threshold). Images are displayed in neurological orientation (left is left) with MNI z-axis coordinates. **B (bottom):** mean predictor weights plotted over post-stimulus time for each task and condition. 4L = 4 letters; 6L = 6 letters.

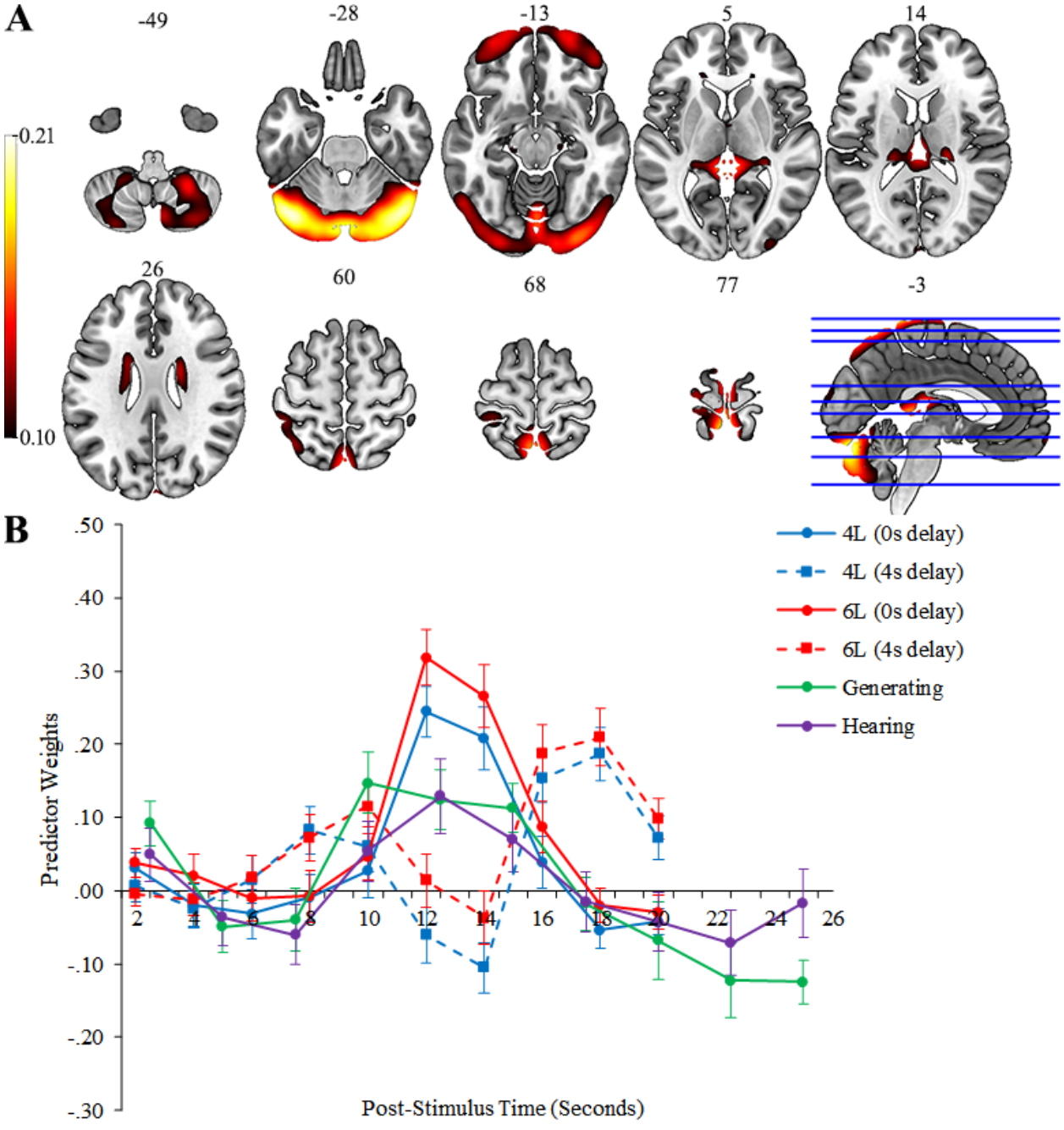

Figure 3.6. WM-TGT multi-experiment fMRI-CPCA, occipital (de)activation (component 6): Anatomical and temporal characteristics. **A (top):** dominant 10% of loadings (red/yellow = positive loadings, min = 0.08, max = 0.29; blue/green = negative loadings, min = -0.17, max = -0.08). Images are displayed in neurological orientation (left is left) with MNI z-axis coordinates. **B (bottom):** mean predictor weights plotted over post-stimulus time for each task and condition. 4L = 4 letters; 6L = 6 letters.

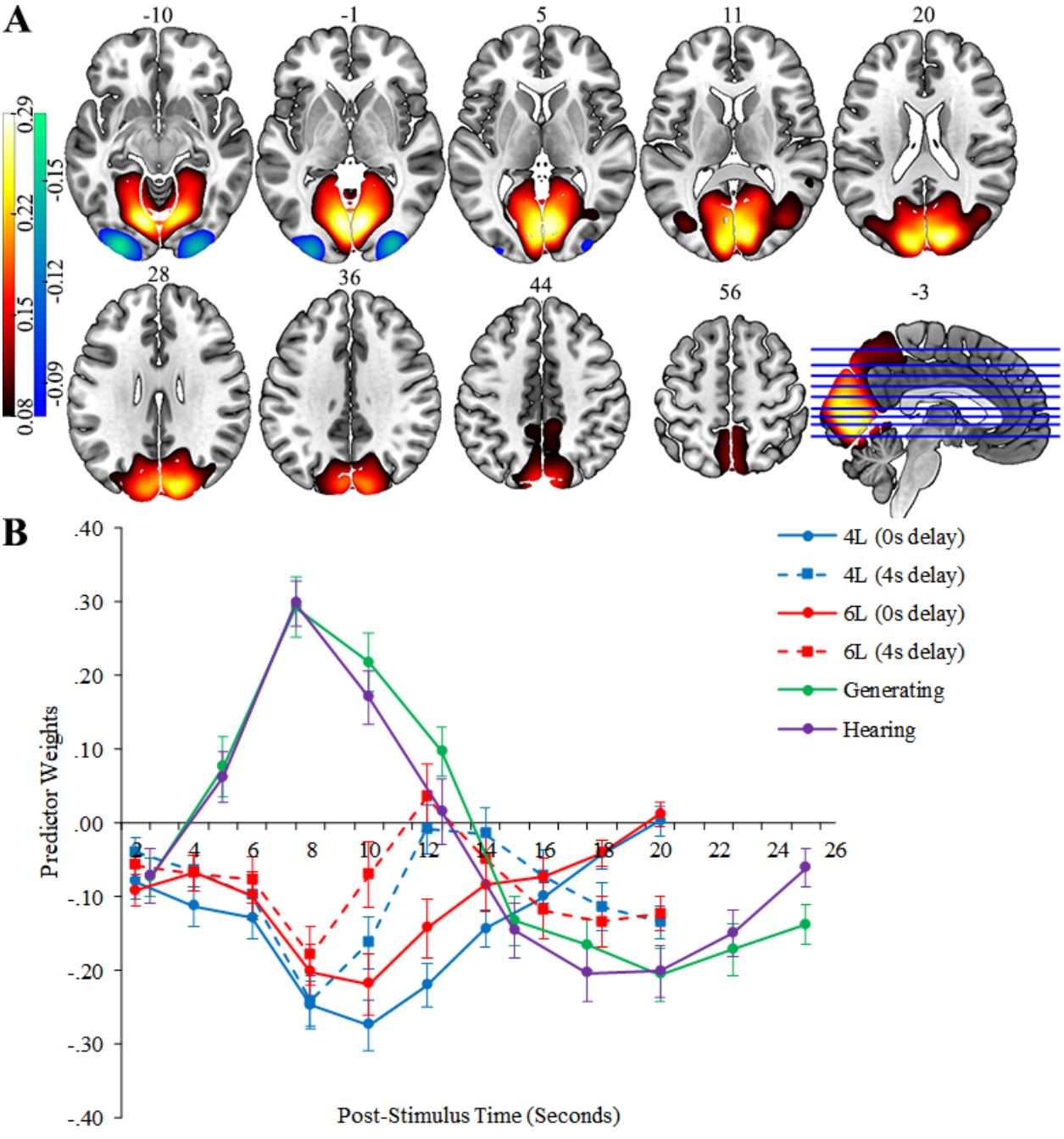

Figure 3.7. WM-TGT multi-experiment fMRI-CPCA, auditory network (component 7): Anatomical and temporal characteristics. **A (top):** dominant 10% of loadings (red/yellow = positive loadings, min = 0.07, max = 0.24; blue/green = negative loadings, min = -0.11, max = -0.07). Images are displayed in neurological orientation (left is left) with MNI z-axis coordinates. **B (bottom):** mean predictor weights plotted over post-stimulus time for each task and condition. 4L = 4 letters; 6L = 6 letters.

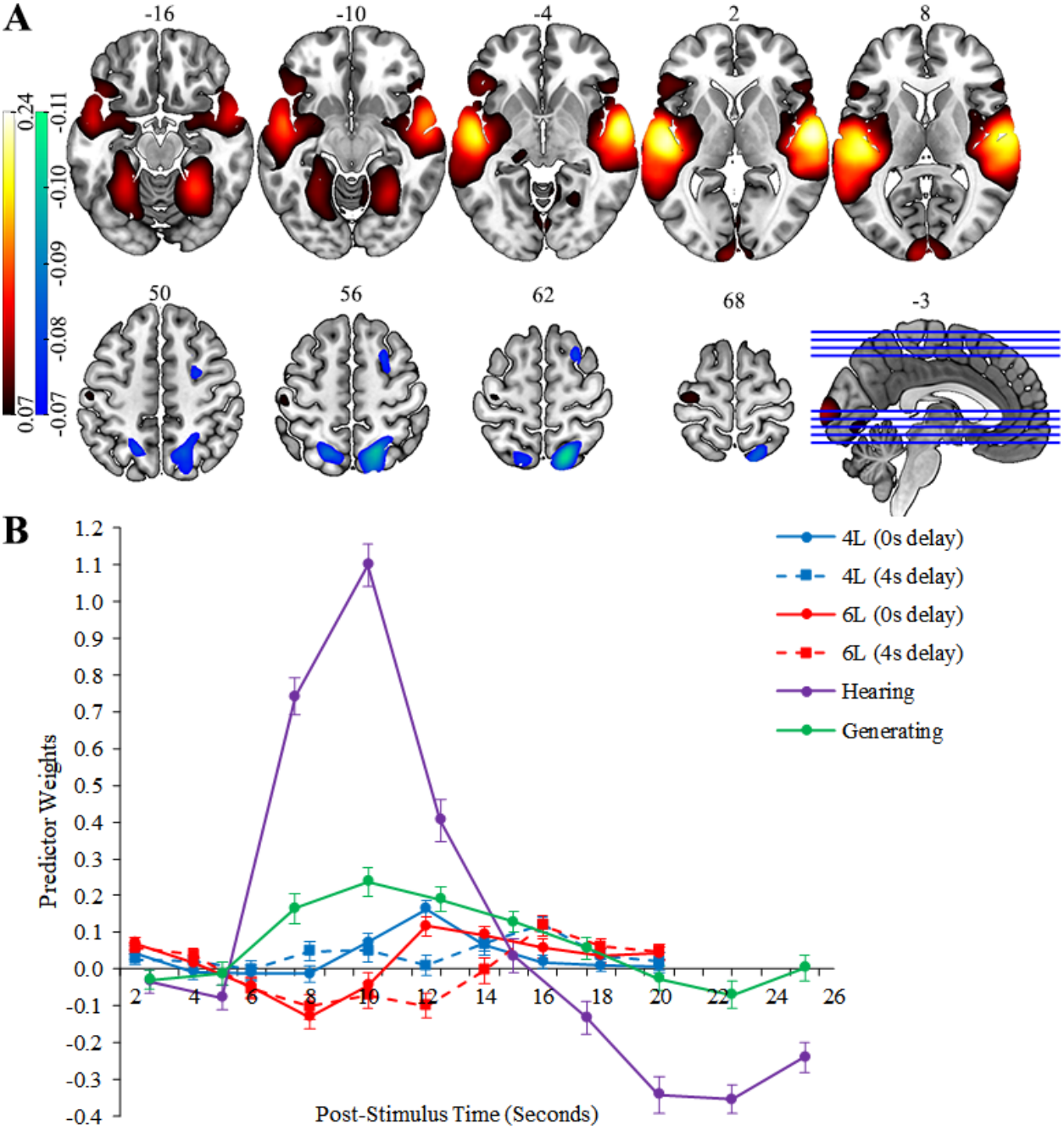

Figure 3.8. WM-TGT multi-experiment fMRI-CPCA, response network (component 1): Anatomical and temporal characteristics. **A (top)**: dominant 10% of loadings (red/yellow = positive loadings, min = 0.15, max = 0.30; no negative loadings above threshold). Images are displayed in neurological orientation (left is left) with MNI z-axis coordinates. **B (bottom)**: mean predictor weights plotted over post-stimulus time for each task and condition. 4L = 4 letters; 6L = 6 letters.

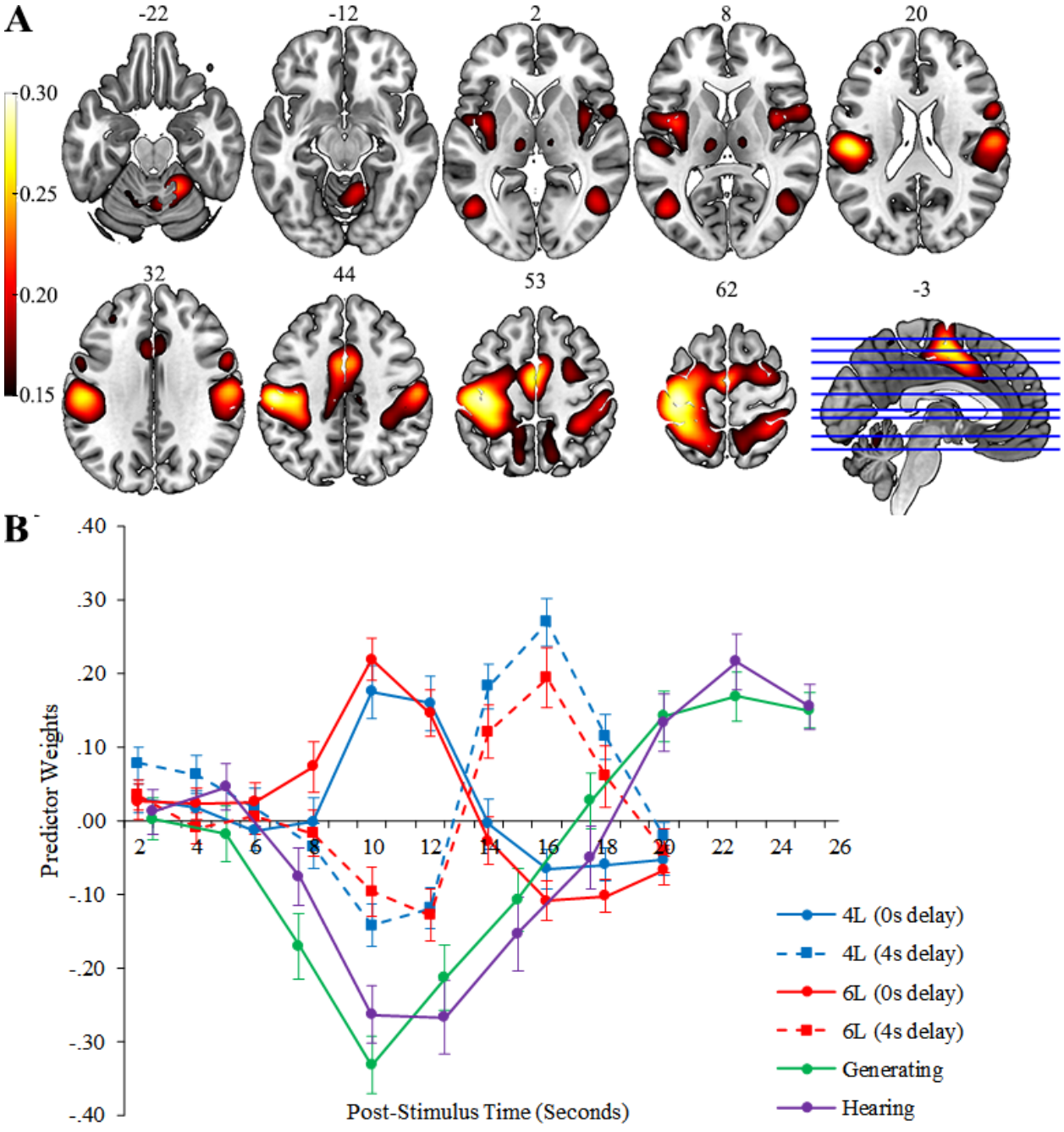

Figure 3.9. WM task from the WM-TGT multi-experiment fMRI-CPCA, response network (component 1): Estimated HDRs illustrating delay × time interaction. Asterisks indicate significant delay × time contrast between adjacent time bins. *** = $p < .001$.

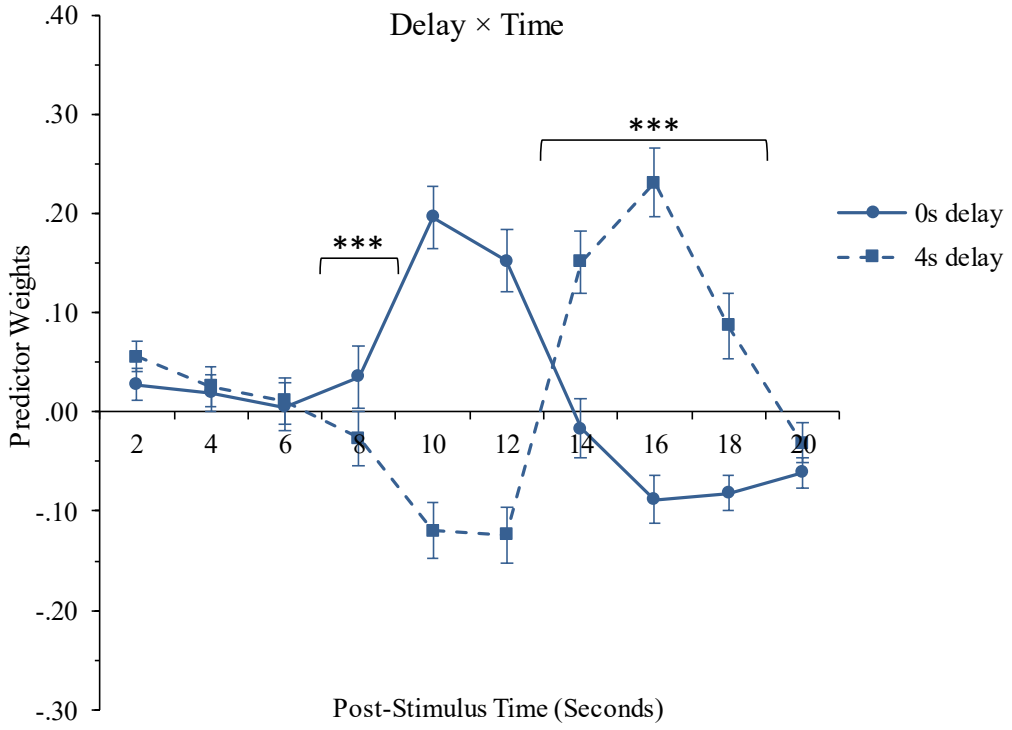

Figure 3.10. WM-TGT multi-experiment fMRI-CPCA, visual attention network (component 2): Anatomical and temporal characteristics. **A (top)**: dominant 10% of loadings (red/yellow = positive loadings, min = 0.11, max = 0.54; blue/green = negative loadings, min = -0.12, max = -0.11). Images are displayed in neurological orientation (left is left) with MNI z-axis coordinates. **B (bottom)**: mean predictor weights plotted over post-stimulus time for each task and condition. 4L = 4 letters; 6L = 6 letters.

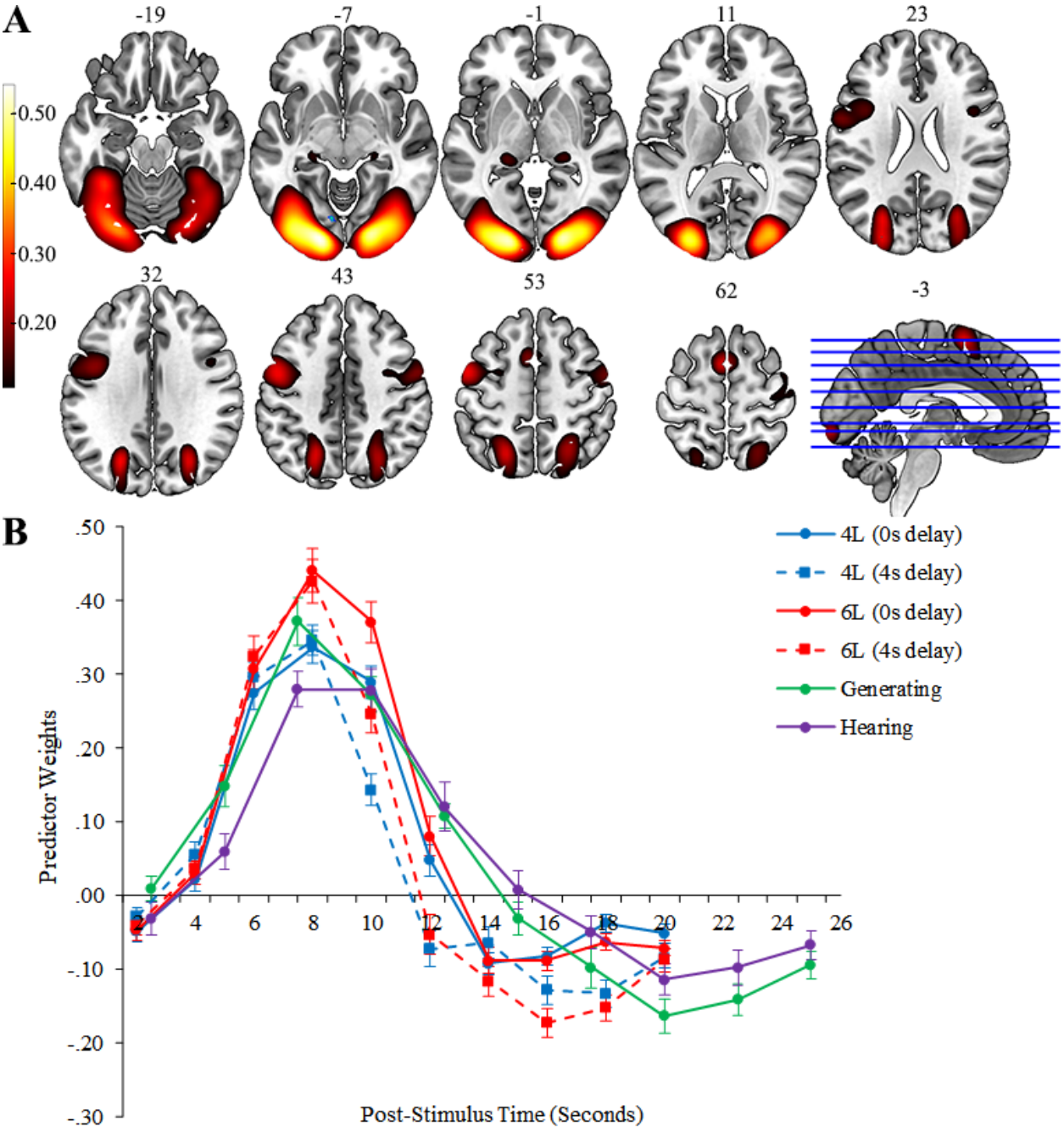

Figure 3.11. WM task from the WM-TGT multi-experiment fMRI-CPCA, visual attention network (component 2): Estimated HDRs illustrating delay × time interaction. Asterisks indicate significant delay × time contrast between adjacent time bins. * = $p < .05$; ** = $p < .01$; *** = $p < .001$.

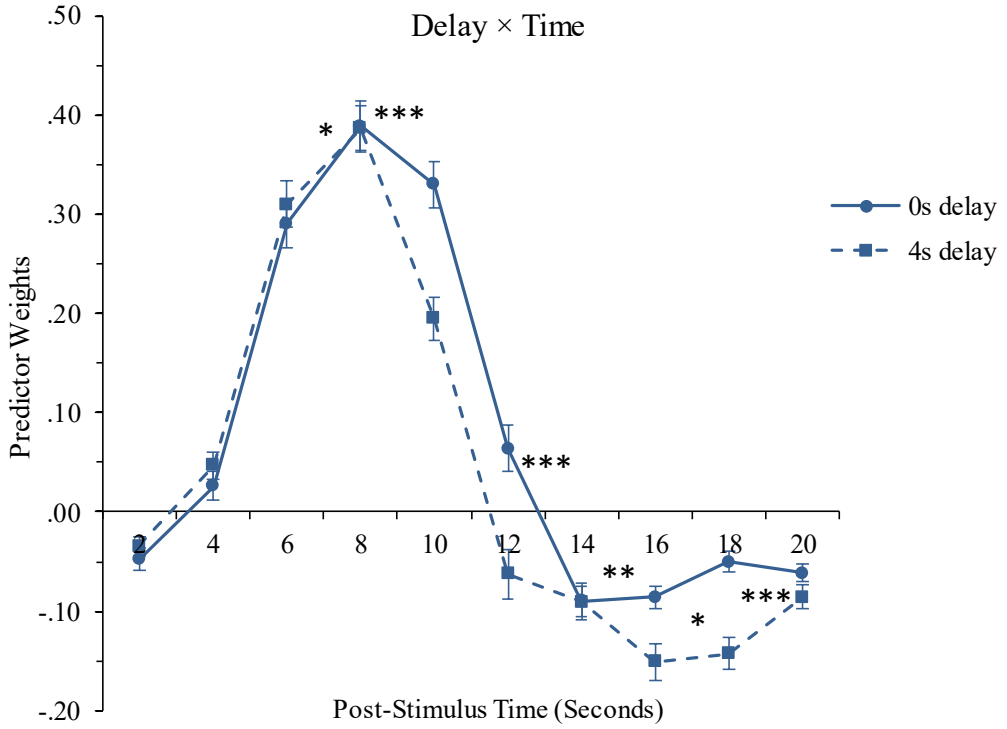

Figure 3.12. WM-TGT multi-experiment fMRI-CPCA, internal attention network (component 3): Anatomical and temporal characteristics. **A (top)**: dominant 10% of loadings (red/yellow = positive loadings, min = 0.14, max = 0.30; no negative loadings above threshold). Images are displayed in neurological orientation (left is left) with MNI z-axis coordinates. **B (bottom)**: mean predictor weights plotted over post-stimulus time for each task and condition. Asterisks indicate significant condition × time contrasts between adjacent time bins in the TGT task. 4L = 4 letters; 6L = 6 letters; * = $p < .05$; ** = $p < .01$; *** = $p < .001$.

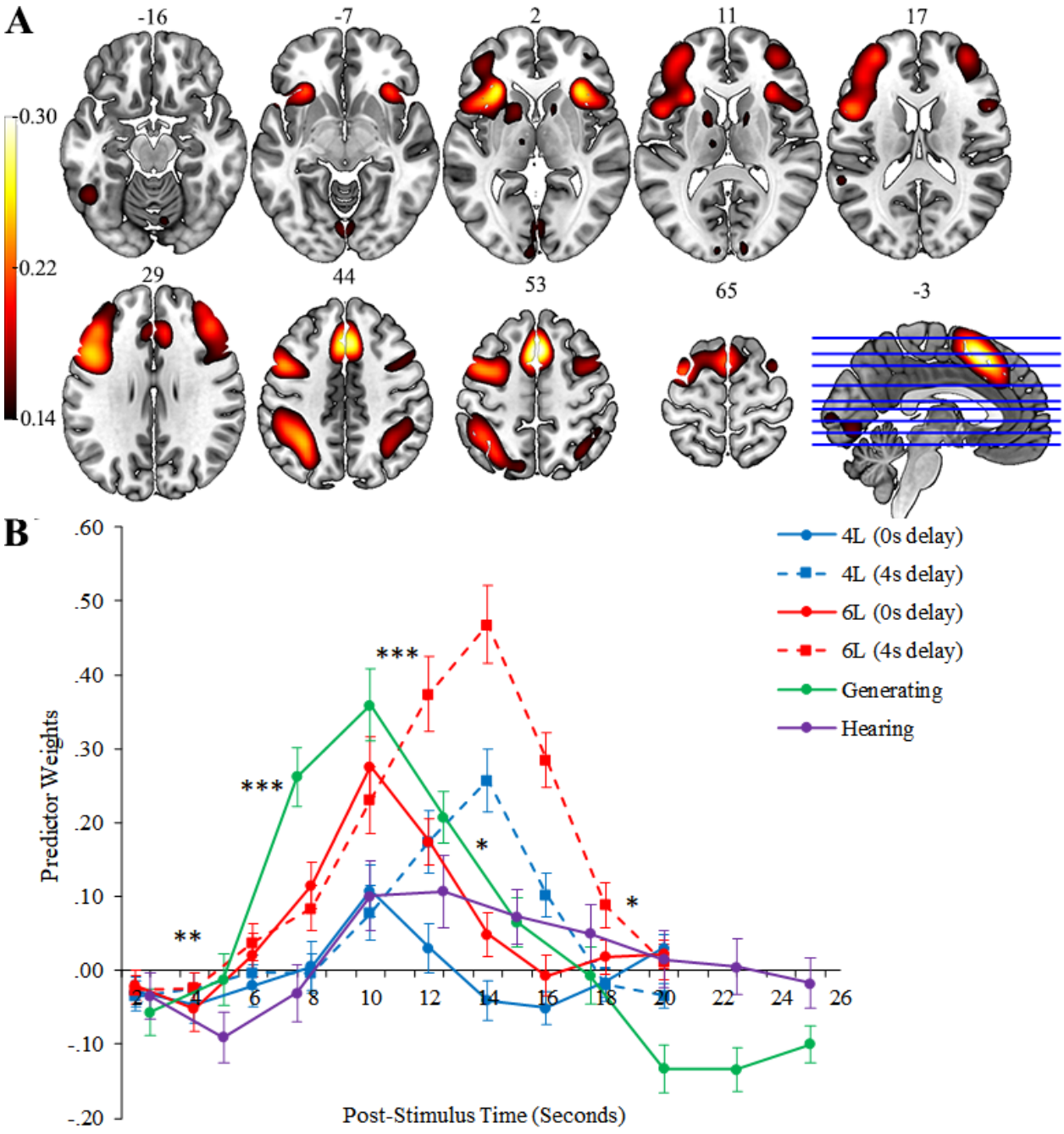

Figure 3.13. WM task from the WM-TGT multi-experiment fMRI-CPCA, internal attention network (component 3): Graphs illustrating effects of cognitive load and delay length. **A (top):** mean predictor weights illustrating load × delay interaction. **B (bottom):** estimated HDRs illustrating delay × time interaction (asterisks indicate significant delay × time contrast between adjacent time bins). * = $p < .05$; ** = $p < .01$; *** = $p < .001$.

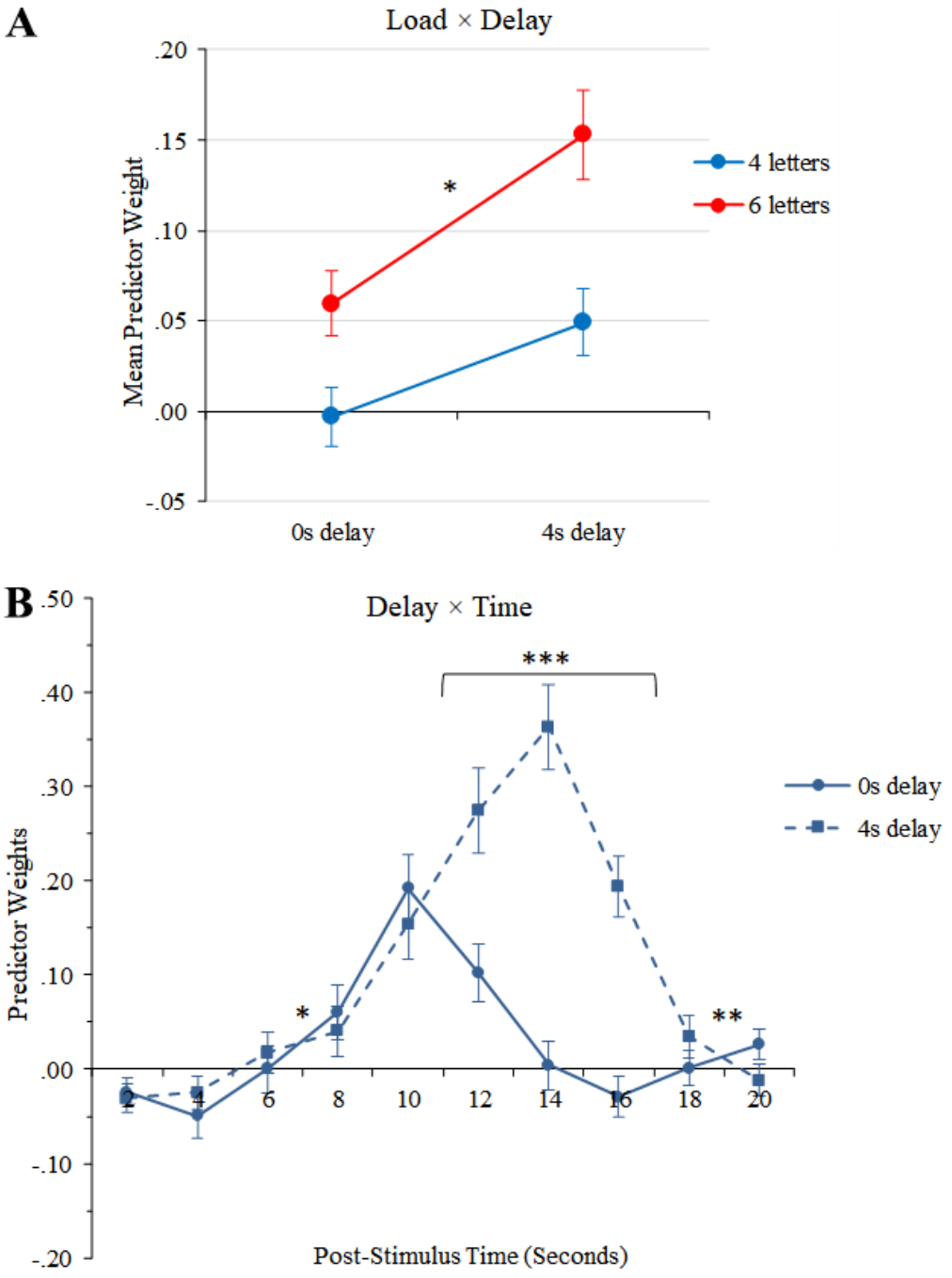

Figure 3.14. WM-TGT multi-experiment fMRI-CPCA, default mode network (DMN, component 4): Anatomical and temporal characteristics. **A (top)**: dominant 10% of loadings (red/yellow = positive loadings, min = 0.13, max = 0.14; blue/green = negative loadings, min = -0.24, max = -0.13). Images are displayed in neurological orientation (left is left) with MNI z-axis coordinates. **B (bottom)**: mean predictor weights plotted over post-stimulus time for each task and condition. Y axis has been reversed to facilitate interpretation (i.e., values above X axis indicate activation of blue/green voxels, and values below X axis indicate deactivation of blue/green voxels). 4L = 4 letters; 6L = 6 letters.

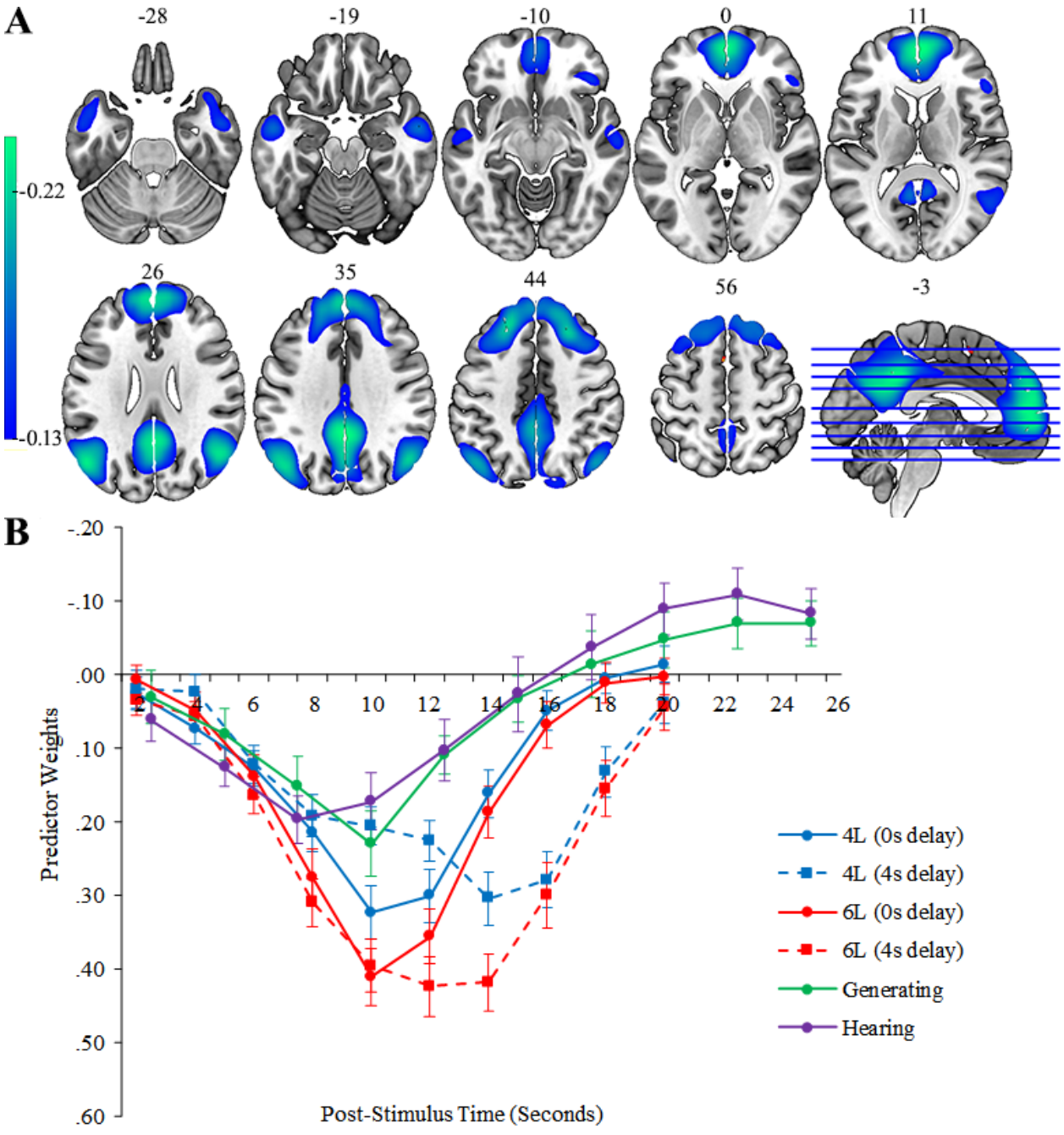

Figure 3.15. WM task from the WM-TGT multi-experiment fMRI-CPCA, default mode network (DMN, component 4): Graphs illustrating effects of cognitive load and delay length. Y axes are reversed (negative up, positive down) to facilitate interpretation (i.e., values above X axis reflect activation, and values below X axis reflect deactivation). **A (top):** mean predictor weights illustrating load × delay interaction. **B (bottom):** predictor weights plotted over post-stimulus time to illustrate delay × time interaction (asterisks indicate significant delay × time contrasts between adjacent time bins). * = $p < .05$; ** = $p < .01$; *** = $p < .001$.

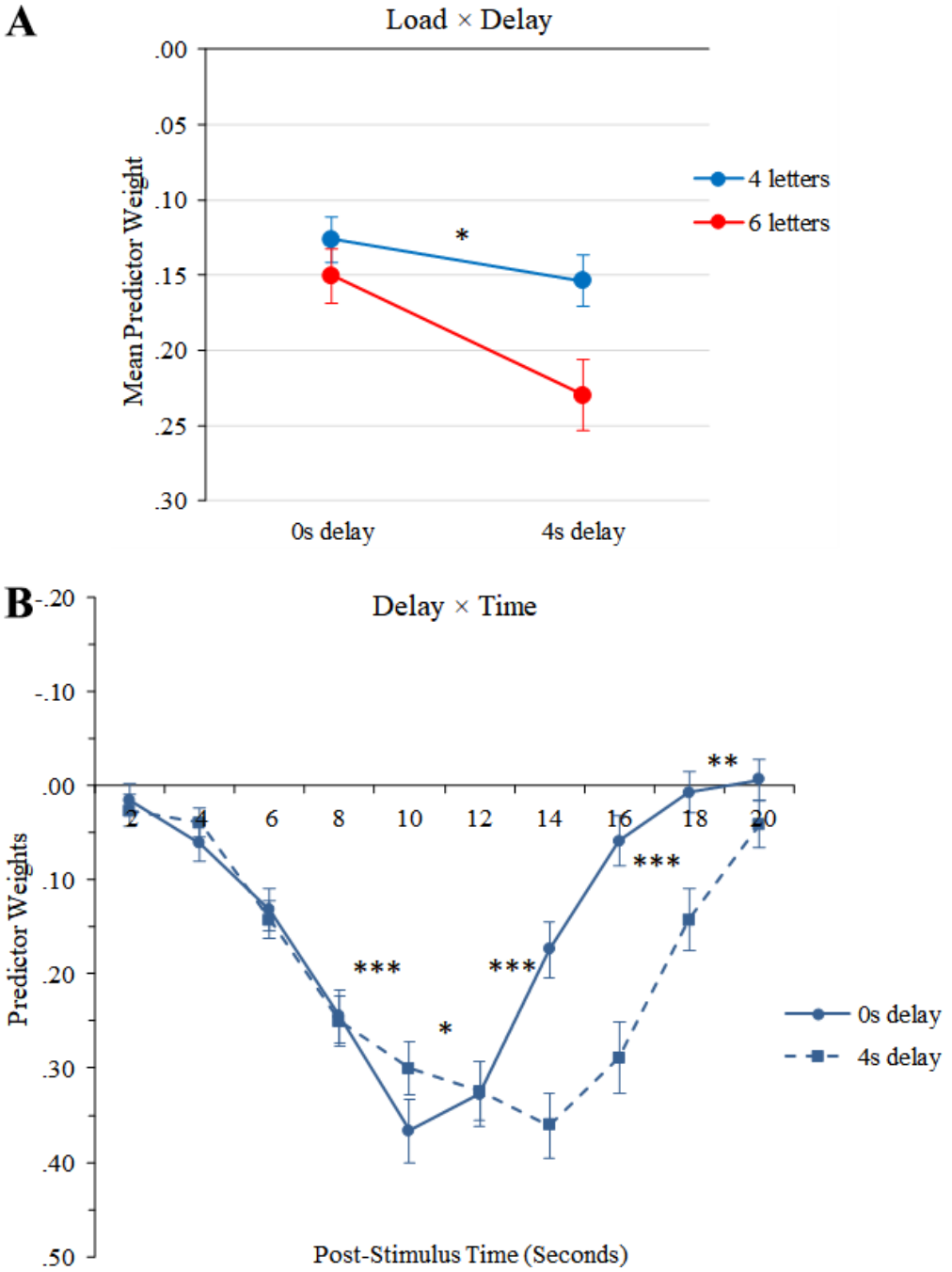

Chapter 4: Characterizing Dominant Networks Underlying Neurocognitive Tasks Using Single-Experiment fMRI-CPCA

4.1. Aims and Hypotheses

The previous chapter presented a preliminary multi-experiment fMRI-CPCA that was designed to obtain a more refined characterization of the functional brain networks underlying a Sternberg verbal WM task. Although the findings demonstrated that the addition of one task with relevant overlapping and non-overlapping cognitive processes can provide meaningful information that expands on a single-task analysis, a number of limitations should be noted. For example, the WM task and TGT are both highly verbal tasks; therefore, the addition of a visuospatial WM task, with a similar paradigm but non-verbal task content, would be valuable for determining the degree to which the observed networks are specific to tasks involving inner speech. Further, a more powerful manipulation may be required for dissociating internal versus external attention, as neither the WM task nor the TGT involve an externally-oriented task condition that is both challenging and not concurrent with memory encoding. The addition of a task that engages other executive function domains, such as inhibition and task-switching, could help determine whether the network tentatively described as "volitional internal attention" is specifically internally-oriented. Therefore, a 4-task fMRI-CPCA was designed, including the WM task and TGT task analysed in the previous chapter, with the addition of the Spatial Capacity (SCAP) task and the Task-Switch Inertia (TSI) task detailed in Chapter 2 (Sections 2.2.2 and 2.2.3, respectively). The main purpose of the present chapter was to describe the fundamental characteristics of the dominant networks underlying these tasks, as observed in healthy control participants. This includes a more detailed examination of the WM task with a larger sample size than the previous chapter (including participants who had also completed the TGT task, and so

had been excluded from the WM dataset so as not to have a mix of overlapping and non-overlapping participants in the TGT-WM analysis), although the same three networks were expected to emerge (i.e., frontoparietal network underlying the response phase of the task, a visual attention network underlying the encoding phase, and sustained DMN deactivation). It was predicted that these three networks would also emerge in the SCAP task, which encompasses the same WM task stages of encoding, maintenance, and recall/response. For the TSI task, it was expected that at least one bilateral, frontoparietal task-positive network and DMN deactivation would emerge, consistent with previous research of Stroop task-switching (Woodward et al., 2016). For the TGT data, it was predicted that, along with DMN deactivation, a left-dominant network comprising known language areas (pars opercularis of the inferior frontal gyrus and posterior superior temporal gyrus), SMA, and lateral occipital cortex would emerge and be more engaged in the thought generation condition than in the hearing condition, consistent with a previous analysis of this task (Lavigne, Rapin, et al., 2015). A number of factors were considered in the decision to carry out a new analysis of the TGT task rather than referring to published findings for comparison. First and foremost, the published analysis was carried out on a sample comprising healthy controls, schizophrenia patients, and bipolar disorder patients, whereas the intent of this chapter was to present "control" analyses derived from non-clinical participants. In addition, this work utilized more up-to-date preprocessing procedures (i.e., use of the SPM12 software package rather than SPM8), and although this may not necessarily result in meaningful differences between otherwise identical analyses, it would nevertheless add a confound to the present work.

4.2. Analysis 1: Working Memory Task

4.2.1. Methods

4.2.1.1. Participants

54 healthy participants who met all general inclusion criteria detailed in Chapter 2 (Section 2.1) were included in the present analysis. Task performance on the fMRI WM task was examined to confirm participant engagement during the task, and any runs in which a participant achieved < 60% correct responses were excluded from the analysis (note that participants had a 50% chance of guessing correctly on any given trial). Demographic information for this sample is provided in Table 4.1. A brief questionnaire was administered to all participants to obtain their age, highest level of education, and any history of head injury, neurological conditions, drug use, and medication. In addition, visual acuity and color vision were assessed to ensure that participants were able to view the task on an fMRI presentation screen. Handedness was measured with the AHPQ (Annett, 1970), and IQ was estimated with the Quick IQ test (Mortimer & Bowen, 1999). Participants were recruited via posters on the UBC campus, community bulletin boards, and on electronic bulletins such as Craigslist. Participants provided informed consent at the start of their testing sessions, and were compensated $10 per hour for time spent participating in the study plus $10 for travel expenses. Participants were also given a copy of their T1 MRI scan on a disc.

4.2.1.2. WM task design

Details regarding the WM task design and procedures are presented in Chapter 2 (task protocol described in Section 2.2.1 and Figure 2.1; fMRI data acquisition and preprocessing described in Section 2.3 and Table 2.1). In summary, a string of 4 or 6 upper case consonants was displayed for 4 seconds, and then a single probe letter was displayed for 2 seconds. Participants

responded “yes” or “no” with a right-handed button press as to whether this probe letter was part of the first string of letters. Both the cognitive load (4 or 6 letters in the item set) and delay period (0 or 4 seconds between the letter string and probe) were manipulated so as to facilitate identification of the functional brain networks distinctly involved in encoding, maintenance, and response/recall.

4.2.1.3. WM data analyses

WM task performance was measured as percentage of correct responses for each task condition. To examine effects of cognitive load and delay duration on task performance, these measures were entered into a 2 (load; 4 vs. 6 letters) × 2 (delay; 0s vs. 4s) repeated measures ANOVA, and significant effects were further examined with polynomial contrasts.

For the WM task functional connectivity analysis, a single-experiment fMRI-CPCA was carried out as described in Chapter 2 (Section 2.4). Each level of cognitive load and delay duration was specified in the design matrix (i.e., *G* matrix), and the time bins for which a FIR basis function was specified were scans 1-10 following trial onset (i.e., 20 seconds of post-stimulus time with TR = 2,000ms), resulting in *G* matrices with 374 rows (scans) and 40 columns (4 conditions × 10 post-stimulus time bins) per task run. After the regression and PCA steps, within-subject factors of cognitive load (4 vs. 6 letters), delay length (0s vs. 4s), and time (10 post-stimulus time bins) were examined with the resulting predictor weights, resulting in a 2 (load) × 2 (delay) × 10 (time) ANOVA for each component. Significant effects of load, delay, load × delay, and delay × time were further examined. Post hoc analyses of load and delay were carried out using polynomial contrasts, and interactions involving time were examined using repeated measures contrasts between adjacent time bins.

4.2.2. WM task performance results

WM task performance for the sample is listed in Table 4.2. The 2 (load) × 2 (delay) ANOVA revealed a significant main effect of load, $F(1, 53) = 51.851$, $p < .001$, $\eta_p^2 = .495$; and delay, $F(1, 53) = 10.319$, $p = .002$, $\eta_p^2 = .163$. The load × delay interaction was not significant ($p > .10$). The main effect of load was due to lower accuracy in the 6-letter condition compared with the 4-letter condition (mean correct = 93.68% and 87.00% for 4 letters and 6 letters, respectively). The main effect of delay was due to lower accuracy in the 4s delay condition compared with the 0s delay condition (mean correct = 91.80% and 88.89% for 0s delay and 4s delay, respectively).

4.2.3. WM functional connectivity results

Three components were extracted from the WM task-related variance in BOLD signal. After varimax rotation, the components accounted for 16.28%, 9.56%, and 9.14% of the variance, respectively. For the purpose of discussion, these components are referred to as (1) response/attention network, (2) visual attention network, and (3) DMN.

4.2.3.1. WM task, response/attention network (component 1)

Response/attention network (component 1) estimated HDR plots are presented in Figure 4.1B. This network consisted of activation in bilateral SMA, dorsal anterior cingulate/paracingulate gyrus, and insula, as well as left pre/postcentral gyri and slightly right-dominant cerebellum (see Figure 4.1A for anatomical visualization, and Table 4.3 for locations of cluster peaks). The 2 (load) × 2 (delay) × 10 (time) repeated measures ANOVA revealed significant main effects of cognitive load, $F(1, 53) = 24.062$, $p < .001$, $\eta_p^2 = .312$; delay, $F(1, 53) = 45.662$, $p < .001$, $\eta_p^2 = .463$; and time, $F(9, 477) = 40.996$, $p < .001$, $\eta_p^2 = .436$. Significant inter-

actions emerged for load × time, $F(9, 477) = 13.603$, $p < .001$, $\eta_p^2 = .204$; and delay × time, $F(9, 477) = 121.475$, $p < .001$, $\eta_p^2 = .696$.

The main effect of cognitive load was due to greater mean activation in the 6-letter condition than in the 4-letter condition (mean predictor weights = 0.036 and 0.074 for 4 letters and 6 letters, respectively). The main effect of delay was due to greater mean activation in the 4s delay condition than in the 0s delay condition (mean predictor weights = 0.030 and 0.080 for 0s delay and 4s delay, respectively). The delay × time interaction was due to the staggered onsets and peaks according to delay length, which occurred late in the post-stimulus time series (Figure 4.2).

4.2.3.2. WM task, visual attention network (component 2)

Visual attention network (component 2) estimated HDR plots are presented in Figure 4.3B. This network consisted of bilateral activation in the occipital poles (extending dorsally into superior lateral occipital cortex as well as ventrally into temporal-occipital fusiform cortex), SMA, precentral gyri, and thalamus (see Figure 4.3A for anatomical visualization, and Table 4.4 for locations of cluster peaks). The repeated measures ANOVA revealed significant main effects of load, $F(1, 53) = 19.054$, $p < .001$, $\eta_p^2 = .264$; delay, $F(1, 53) = 31.072$, $p < .001$, $\eta_p^2 = .370$; and time, $F(9, 477) = 222.024$, $p < .001$, $\eta_p^2 = .807$. Significant interactions emerged for load × time, $F(9, 477) = 23.689$, $p < .001$, $\eta_p^2 = .309$; and delay × time, $F(9, 477) = 33.278$, $p < .001$, $\eta_p^2 = .386$.

The main effect of load was due to greater mean activation in the 6-letter condition than in the 4-letter condition (mean predictor weights = 0.066 and 0.091 for 4 letters and 6 letters, respectively). The main effect of delay was due to greater mean activation in the 0s delay condition than in the 4s delay condition (mean predictor weights = 0.092 and 0.064 for 0s delay and 4s de-

lay, respectively). The delay × time interaction was due to a slightly more sustained HDR in the 0s delay condition than in the 4s delay condition, although the timing of onsets and peaks did not differ between conditions (Figure 4.4).

4.2.3.3. WM task, DMN (component 3)

DMN (component 3) estimated HDR plots are presented in Figure 4.5B. This network consisted primarily of deactivation in bilateral precuneus, posterior cingulate gyri, superior frontal gyri, frontal poles, superior lateral occipital cortex, middle temporal gyri, and cerebellar crus II, as well as small clusters of activation in the left precentral gyrus/SMA (see Figure 4.5A for anatomical visualization, and Table 4.5 for locations of cluster peaks). The repeated measures ANOVA revealed significant main effects of load, $F(1, 53) = 31.711$, $p < .001$, $\eta_p^2 = .374$; delay, $F(1, 53) = 21.821$, $p < .001$, $\eta_p^2 = .292$; and time, $F(9, 477) = 48.699$, $p < .001$, $\eta_p^2 = .479$. Significant interactions emerged for load × delay, $F(1, 53) = 5.509$, $p = .023$, $\eta_p^2 = .094$; load × time, $F(9, 477) = 7.627$, $p < .001$, $\eta_p^2 = .126$; delay × time, $F(9, 477) = 22.062$, $p < .001$, $\eta_p^2 = .294$; and load × delay × time, $F(4.43, 234.83) = 3.162$, $p = .012$, $\eta_p^2 = .056$.

The main effect of load was due to greater mean *deactivation* in the 6-letter condition than in the 4-letter condition (mean predictor weights = 0.111 and 0.164 for 4 letters and 6 letters, respectively). The main effect of delay was due to greater mean deactivation in the 4s delay condition than in the 0s delay condition (mean predictor weights = 0.120 and 0.155 for 0s delay and 4s delay, respectively). The load × delay interaction was due to this delay effect being more pronounced in the 6-letter condition than in the 4-letter condition (Figure 4.6A). The delay × time interaction was due to the staggered peaks corresponding to delay length, although the early onsets and initial HDR decreases were similar across delay conditions (Figure 4.6B).

4.2.4. Summary of WM task results

Unsurprisingly, WM task accuracy was higher in the 4-letter condition than in the 6-letter condition, and when no delay occurred between the encoding and recall phases; however, no load × delay interaction emerged. As in Chapter 3, three components emerged from the fMRI data. The response/attention network (component 1; Figure 4.1), replicating the response/attention network from the WM task analysis in Chapter 3 (see component 1, Figure 3.1), mainly comprised left-lateralized somatomotor regions as well as widespread activation in dorsal medial prefrontal cortex. Although the late, staggered onsets and the left-lateralized somatomotor activity suggest that this network underlies right-handed button-press responses, it is also important to note the substantial effect of cognitive load, with greater activity in the 6-letter condition than in the 4-letter condition. As discussed in Chapter 3, it is possible that this network reflects a blurring of maintenance and response processes. The visual attention network (component 2; Figure 4.3) comprised widespread activation in visual cortex as well as SMA and precentral gyri, which peaked early and was slightly more sustained in the 0s delay condition (likely due to the immediate appearance of the probe after the encoding phase); this replicates the visual attention network that emerged in the previous WM task analysis (see component 3, Figure 3.3) and in the multi-experiment WM-TGT analysis (see component 2, Figure 3.10) reported in Chapter 3. Finally, the DMN (component 3; Figure 4.5) exhibited early onsets but staggered peaks according to delay length; this replicates the DMN from the previous WM analysis (see component 2, Figure 3.2) and the multi-experiment WM-TGT analysis (see component 4, Figure 3.14). The main effect of delay appeared to be due to a more sustained HDR in the 4s delay condition rather than a greater magnitude of deactivation per se.

4.3. Analysis 2: Spatial Capacity (SCAP) Task

4.3.1. Methods

4.3.1.1. Participants

The data for the SCAP fMRI task were obtained from the OpenfMRI database (https://openfmri.org/dataset/ds000030/; accession number is ds000030). Complete details regarding this project are provided in Poldrack et al. (2016). Participants included in the present analysis consisted of 119 healthy adults who met all general inclusion criteria detailed in Section 2.1. Task performance on the fMRI SCAP task was examined to confirm participant engagement during the task, and any participants who achieved < 60% correct responses were excluded from the analysis (note that participants had a 50% chance of guessing correctly on any given trial). Demographic information is presented in Table 4.1, including age, gender distribution, handedness as measured with the Edinburgh Handedness Inventory (Oldfield, 1971), and educational achievement.

4.3.1.2. SCAP task design

Details regarding SCAP task design and procedures are provided in Chapter 2 (task protocol described in Section 2.2.2 and Figure 2.2; fMRI data acquisition and preprocessing described in Section 2.3 and Table 2.1). In summary, a target array of either 1, 3, 5, or 7 yellow dots, positioned pseudo-randomly around a central fixation, was presented during a 2-second encoding period. After a 1.5s, 3.0s, or 4.5s delay, a single green dot (probe) was displayed for 3 seconds. Participants were asked to respond with a button-press as to whether the probe dot was in the same position as one of the target dots. 4 load levels × 3 delay durations resulted in 12 task conditions.

4.3.1.3. SCAP data analyses

SCAP task performance was measured as percentage of correct responses for each condition. To examine effects of cognitive load and delay duration on task performance, these accuracy measures were entered into a 4 (cognitive load; 1, 3, 5, or 7 dots) × 3 (delay duration; 1.5s, 3.0s, or 4.5s) repeated measures ANOVA. As the load and delay factors comprised >2 levels, post-hoc polynomial analyses of significant main effects involved linear, quadratic, and (for load only) cubic contrasts, which allowed for the observation of ceiling and/or floor effects in manipulations of task difficulty.

For the SCAP task functional connectivity analysis, a single-experiment fMRI-CPCA was carried out as described in Chapter 2 (Section 2.4). Each level of cognitive load and delay duration was specified in the design, and the time bins for which a FIR basis function was specified were scans 1-10 following trial onset (i.e., 20 seconds of post-stimulus time with TR = 2,000ms), resulting in *G* matrices with 291 rows (scans) and 120 columns (12 conditions × 10 post-stimulus time bins) per participant. After the regression and PCA steps, within-subject factors of cognitive load (1, 3, 5, or 7 dots), delay length (1.5s, 3.0s, or 4.5s), and time (10 post-stimulus time bins) were examined with the resulting predictor weights, resulting in a 4 (load) × 3 (delay) × 10 (time) ANOVA for each component. Significant effects of load, delay, and delay × time were further examined. Post hoc analyses of load and delay effects were carried out using polynomial contrasts (as in the analysis of task performance), and interactions involving time were examined using repeated measures contrasts between adjacent time bins.

4.3.2. SCAP task performance results

SCAP task performance for the sample is listed in Table 4.2. The 4 (load) × 3 (delay) ANOVA revealed significant main effects of load, $F(3, 354) = 52.178$, $p < .001$, $\eta_p^2 = .307$; and

delay, $F(2, 236) = 7.324$, $p = .001$, $\eta_p^2 = .058$. The load × delay interaction was also significant, $F(5.15, 607.33) = 3.889$, $p = .002$, $\eta_p^2 = .032$.

The main effect of load was due to significant linear and cubic contrasts, with the linear contrast having the greater effect size (linear: $F(1, 118) = 145.055$, $p < .001$, $\eta_p^2 = .551$; cubic: $F(1, 118) = 7.893$, $p = .006$, $\eta_p^2 = .063$; quadratic $p > .10$). This was due to a general tendency for lower accuracy with higher cognitive load (mean correct = 92.65%, 84.03%, 82.63%, and 76.89% for 1, 3, 5, and 7 dots, respectively; see Figure 4.7A). Paired t-tests comparing adjacent load conditions revealed significant differences between 1 versus 3 dots (mean difference = 8.613, SEM = 1.181, $t(118) = 7.295$, $p < .001$) and 5 versus 7 dots (mean difference = 5.742, SEM = 1.296, $t(118) = 4.432$, $p < .001$), but not 3 versus 5 dots ($p > .25$). The main effect of delay was due to a significant linear contrast (linear: $F(1, 118) = 12.019$, $p = .001$, $\eta_p^2 = .092$; quadratic: $p > .30$). This was due to a general trend for decreasing accuracy with longer delay duration (mean correct = 86.34%, 83.51%, and 82.30% for 1.5s, 3.0s, and 4.5s delay, respectively; see Figure 4.7B). Paired t-tests comparing adjacent delay conditions revealed a significant difference between 1.5s versus 3.0s delay (mean difference = 2.836, SEM = 1.118, $t(118) = 2.536$, $p = .013$), but no difference between 3.0s versus 4.5s delay ($p > .20$).

4.3.3. SCAP functional connectivity results

Two components were extracted from the SCAP task-related variance in BOLD signal. After varimax rotation, the components accounted for 14.64% and 11.41% of the variance, respectively. For the purpose of discussion, these components are referred to as (1) external attention network and (2) DMN.

4.3.3.1. SCAP task, external attention network (component 1)

External attention network (component 1) estimated HDR plots are presented in Figure 4.8B. This network was primarily comprised of bilateral activation in the SMA/paracingulate gyri, precentral gyri, superior parietal lobules, superior and inferior lateral occipital cortex, and temporal-occipital fusiform cortex, as well as small clusters in anterior insula and thalamus (see Figure 4.8A for anatomical visualization and Table 4.6 for locations of cluster peaks). The 4 (load) × 3 (delay) × 10 (time) repeated measures ANOVA revealed main effects of load, $F(3, 354) = 24.016$, $p < .001$, $\eta_p^2 = .169$; delay, $F(2, 236) = 19.956$, $p < .001$, $\eta_p^2 = .145$; and time, $F(9, 1062) = 203.944$, $p < .001$, $\eta_p^2 = .633$. Significant interactions included load × delay, $F(6, 708) = 5.254$, $p < .001$, $\eta_p^2 = .043$; load × time, $F(27, 3186) = 11.973$, $p < .001$, $\eta_p^2 = .092$; delay × time, $F(18, 2124) = 54.033$, $p < .001$, $\eta_p^2 = .314$; and load × delay × time, $F(54, 6372) = 6.326$, $p < .001$, $\eta_p^2 = .051$.

Post-hoc analyses of the main effect of load revealed that both the linear and quadratic contrasts were significant, with the linear contrast having the greater effect size (linear: $F(1, 118) = 43.570$, $p < .001$, $\eta_p^2 = .270$; quadratic: $F(1, 118) = 3.938$, $p = .050$, $\eta_p^2 = .032$; cubic: $p > .45$). This was due to a tendency for greater mean activation with greater cognitive load (mean predictor weights = 0.034, 0.047, 0.060, and 0.064 for 1, 3, 5, and 7 dots, respectively; see Figure 4.9A). Paired t-tests between adjacent load conditions revealed that only the contrasts between 1 versus 3 dots and between 3 versus 5 dots were significant (1 vs. 3 dots: mean difference = 0.013, SEM = 0.004, $t(118) = 3.608$, $p < .001$; 3 vs. 5 dots: mean difference = 0.012, SEM = 0.004, $t(118) = 3.425$, $p = .001$; other $p > .15$). Post-hoc analyses of the main effect of delay revealed that only the quadratic contrast was significant ($F(1, 118) = 37.304$, $p < .001$, $\eta_p^2 =$

.240; linear $p > .10$). This was due to a tendency for greater mean activation with longer delay durations (mean predictor weights = 0.044, 0.049, and 0.062 for 1.5s, 3.0s, and 4.5s delay, respectively; see Figure 4.9B). Paired t-tests between adjacent delay conditions revealed that only the contrast between 3.0s delay versus 4.5s delay was significant (mean difference = 0.013, SEM = 0.003, $t(118) = 4.083$, $p < .001$; 1.5s vs. 3.0s $p > .05$). The delay × time interaction was due in part to HDR peaks occurring at later time bins with longer delay durations (Figure 4.9C). Further, the 3.0s and 4.5s delay conditions exhibited multiple peaks; the first peak occurred at 8 seconds for both delay conditions, and was followed by a later peak at 12 seconds in the 3.0s delay condition and at 14 seconds in the 4.5s delay condition. The 1.5s delay condition did not exhibit this pattern, possibly because the 1.5s delay was too brief for the HDR to exhibit a detectable decrease before the probe was displayed (see Figure 4.9C).

4.3.3.2. SCAP task, DMN (component 2)

DMN (component 2) estimated HDR plots are presented in Figure 4.10B. This network was primarily comprised of bilateral deactivation in regions of the DMN, including frontal poles/paracingulate gyri, superior frontal gyri, inferior frontal gyri (pars triangularis), frontal orbital cortex, posterior cingulate gyri, precuneus, superior lateral occipital cortex, angular gyri, planum temporale, middle temporal gyri, parahippocampal gyri, and cerebellar crus I (see Figure 4.10A for anatomical visualization and Table 4.7 for locations of cluster peaks). The repeated measures ANOVA revealed significant main effects of load, $F(3, 354) = 22.016$, $p < .001$, $\eta_p^2 = .157$; delay, $F(2, 236) = 15.859$, $p < .001$, $\eta_p^2 = .118$; and time, $F(9, 1062) = 128.499$, $p < .001$, $\eta_p^2 = .521$. Significant interactions included load × delay, $F(5.44, 641.42) = 2.812$, $p = .013$, $\eta_p^2 = .023$; load × time, $F(27, 3186) = 12.578$, $p < .001$, $\eta_p^2 = .096$; delay × time, $F(18, 2124) = 15.272$, $p < .001$, $\eta_p^2 = .115$; and load × delay × time, $F(54, 6372) = 3.529$, $p < .001$, $\eta_p^2 = .029$.

Post-hoc analyses of the main effect of load revealed that the linear and quadratic contrasts were both significant, with the linear contrast having the greater effect size (linear: $F(1, 118) = 49.137$, $p < .001$, $\eta_p^2 = .294$; quadratic: $F(1,118) = 10.331$, $p = .002$, $\eta_p^2 = .081$; cubic: $p > .35$). This was due to a general tendency for greater mean *deactivation* with greater cognitive load (mean predictor weights = 0.030, 0.050, 0.056, and 0.061 for 1, 3, 5, and 7 dots, respectively; see Figure 4.11A). Paired t-tests between adjacent load conditions revealed that only the contrast between 1 versus 3 dots was significant (mean difference = 0.020, SEM = 0.004, $t(118) = 5.168$, $p < .001$; other ps > .15). Post-hoc analyses of the main effect of delay revealed that both the linear and quadratic contrasts were significant, with the linear contrast having the greater effect size (linear: $F(1, 118) = 26.901$, $p < .001$, $\eta_p^2 = .186$; quadratic: $F(1, 118) = 4.395$, $p = .038$, $\eta_p^2 = .036$). This was due to a general tendency for greater mean deactivation with longer delay durations (mean predictor weights = 0.040, 0.053, and 0.055 for 1.5s, 3.0s, and 4.5s delay conditions, respectively; see Figure 4.11B). The delay × time interaction was due to more sustained HDRs with longer delay durations, and a later peak in the 4.5s delay condition compared with the 1.5s and 3.0s delay conditions (see Figure 4.11C).

4.3.4. Summary of SCAP task results

As in the verbal WM task, response accuracy was higher in low load conditions and in shorter delay conditions. Two components emerged from the fMRI data, which resembled patterns that would be expected for an external attention network (component 1; Figure 4.8) and deactivation of the DMN (component 2; Figure 4.10). Both of these networks were load-dependent (i.e., showing a greater degree of (de)activation with greater cognitive load), and both showed longer HDRs with longer trial durations. However, the external attention network appeared to respond separately to the target array and to the probe, as suggested by the presence of two peaks

(except in the 1.5s delay condition, which may be too brief for the HDR to exhibit a detectable decline). The decreases that emerged in the external attention network midway through the post-stimulus time series suggest that this network is unlikely to support WM maintenance. Although the DMN onsets and initial HDR decreases were similar across delay conditions, this deactivation did not exhibit multiple peaks within the post-stimulus time series despite being more sustained with longer trial durations. Neither network showed a greater magnitude of peak (de)activation with longer delay durations, suggesting that processes occurring after the encoding phase (e.g., maintenance and recognition) do not rely on further engagement of these networks over and above their initial responses.

4.4. Analysis 3: Task-Switch Inertia (TSI) Task

4.4.1. Methods

4.4.1.1. Participants

27 healthy participants who met all general inclusion criteria detailed in Chapter 2 (Section 2.1) were included in the present analysis. Task performance on the TSI task was examined to confirm participant engagement during the task, and any participants who achieved < 30% correct responses were excluded from the analysis (note that participants had a 25% chance of guessing correctly on any given trial). Demographic information for this sample is provided in Table 4.1. A brief questionnaire was administered to all participants to obtain their age, highest level of education, and any history of head injury, neurological conditions, drug use, and medication. In addition, visual acuity and color vision were assessed to ensure that participants were able to view the task on an fMRI presentation screen. Handedness was measured with the AHPQ (Annett, 1970), and IQ was estimated with the Quick IQ test (Mortimer & Bowen, 1999). Participants were recruited via posters on the UBC campus, community bulletin boards, and on elec-

tronic bulletins such as Craigslist. Participants provided informed consent at the start of their testing sessions, and were compensated $10 per hour for time spent participating in the study plus $10 for travel expenses. Participants were also given a copy of their T1 MRI scan on a disc.

4.4.1.2. TSI task design

Details regarding TSI task design and procedures are provided in Chapter 2 (task protocol described in Section 2.2.3 and Figure 2.3; fMRI data acquisition and preprocessing described in Section 2.3 and Table 2.1). In summary, the TSI task is a set-switching Stroop task that involves responding to Stroop stimuli in alternating blocks of colour-naming and word-reading of neutral and incongruent stimuli. A neutral word-reading stimulus is one in which a colour word ("GREEN", "RED", "YELLOW", or "BLUE") is displayed in white font against a black background, and a neutral colour-naming stimulus is one in which a string of Xs is displayed in green, red, yellow, or blue font. Incongruent stimuli are colour words ("GREEN", "RED", "YELLOW", or "BLUE") displayed in incongruent green, red, yellow, or blue font. In this version of the TSI task, each block consisted of 10 trials. Word-reading blocks consisted of an equal mixture of neutral and incongruent stimuli, whereas colour-naming blocks consisted of either 10 neutral *or* 10 incongruent stimuli. Therefore, word-reading trials may be further categorized as "colour-neutral task-switch" (where the preceding block of trials consisted of neutral colour-naming stimuli) and "colour-incongruent task-switch" (where the preceding block of trials consisted of incongruent colour-naming stimuli). Therefore, 4 word-reading conditions, each consisting of 15 trials, were examined in the present study: (1) neutral stimulus following a neutral colour-naming block (cn-WN), (2) neutral stimulus following an incongruent colour-naming block (ci-WN), (3) incongruent stimulus following a neutral colour-naming block (cn-WI), and

(4) incongruent stimulus following an incongruent colour-naming block (ci-WI). Colour-naming trials were not analysed in the present study.

4.4.1.3. TSI data analyses

TSI task performance was measured as either percentage of correct responses or mean reaction time (RT) for each condition. To examine effects of task condition, separate analyses were carried out on percent correct and RT measures, both of which were examined in a 2 (stimulus congruency; neutral vs. incongruent) × 2 (task-switch condition; preceding block = neutral vs. incongruent colour-naming) repeated measures ANOVA on word-reading trials only. Post-hoc analyses were carried out for significant effects of congruency, task-switch, and congruency × task-switch using polynomial contrasts.

For the TSI task functional connectivity analysis, a single-experiment fMRI-CPCA was carried out as described in Chapter 2 (Section 2.4). Each level of stimulus congruency and task-switch condition was specified in the design (but only for word-reading trials), and the time bins for which a FIR basis function was specified were scans 1-8 following trial onset (i.e., 16 seconds of post-stimulus time with TR = 2,000ms), resulting in *G* matrices with 330 rows (scans) and 32 columns (4 conditions × 8 post-stimulus time bins) per participant. After the regression and PCA steps, within-subject factors of stimulus congruency (neutral vs. incongruent stimulus), task-switch condition (preceding block = neutral vs. incongruent colour-naming), and time (8 post-stimulus time bins) were examined with the resulting predictor weights, resulting in a 2 (congruency) × 2 (task-switch) × 8 (time) repeated measures ANOVA for each component. Post-hoc analyses of significant effects of congruency, task-switch, congruency × task-switch, congruency × time, and task-switch × time were carried out, with effects of congruency and task-

switch examined using polynomial contrasts, and interactions involving time examined using repeated measures contrasts between adjacent time bins.

4.4.2. TSI task performance results

TSI task performance (i.e., percent correct and mean RT for each task condition) for the sample is listed in Table 4.2. Accuracy and RTs were analysed separately as reported below.

4.4.2.1. Response accuracy

Examining percentage of correct responses, the 2 (stimulus congruency) × 2 (task-switch condition) ANOVA revealed a significant main effect of congruency, $F(1, 26) = 48.098$, $p < .001$, $\eta_p^2 = .649$. Neither the main effect of task-switch nor the congruency × task-switch interaction were significant (both *p*s > .25). The main effect of congruency was due to greater mean accuracy in the neutral stimulus condition than in the incongruent condition (mean correct = 97.04% and 86.42% for neutral and incongruent stimuli, respectively).

4.4.2.2. Reaction time (RT)

Examining mean RTs, the 2 (congruency) × 2 (task-switch) ANOVA revealed significant main effects of congruency, $F(1, 26) = 154.452$, $p < .001$, $\eta_p^2 = .856$; and task-switch, $F(1, 26) = 11.649$, $p = .002$, $\eta_p^2 = .309$. The congruency × task-switch interaction was not significant ($p > .10$).

The main effect of congruency was due to longer RTs in the incongruent stimulus condition than in the neutral condition (mean RTs = 913.41ms and 1165.20ms for neutral and incongruent stimuli, respectively). The main effect of task-switch was due to longer RTs following an incongruent colour-naming block than following a neutral colour-naming block (mean RTs = 1014.57ms and 1064.04ms following neutral and incongruent colour-naming blocks, respective-

ly). The absence of a significant congruency × task-switch interaction suggests that the task-switch effect on RTs was the same for neutral as for incongruent word-reading trials.

4.4.3. TSI functional connectivity results

Three components were extracted from the TSI task-related variance in BOLD signal. After varimax rotation, the components accounted for 12.44%, 12.05%, and 7.92% of the variance, respectively. For the purpose of discussion, these components are referred to as (1) DMN/occipital network, (2) response network, and (3) evaluation network.

4.4.3.1. TSI task, DMN/occipital network (component 1)

DMN/occipital network (component 1) estimated HDR plots are presented in Figure 4.12B. This network was comprised of bilateral deactivation in regions of the DMN (including frontal poles, superior frontal gyri, precuneus, and posterior cingulate cortex) as well as broad occipital deactivation originating in the medial occipital lobes (including lingual gyri, intracalcarine cortex, occipital fusiform cortex, occipital poles, and superior lateral occipital cortex; see Figure 4.12A for anatomical visualization and Table 4.8 for locations of cluster peaks). The 2 (congruency) × 2 (task-switch) × 8 (time) repeated measures ANOVA revealed main effects of stimulus congruency, $F(1, 26) = 66.643$, $p < .001$, $\eta_p^2 = .719$; and time, $F(7, 182) = 39.834$, $p < .001$, $\eta_p^2 = .605$. Significant interactions emerged for congruency × task-switch, $F(1, 26) = 23.297$, $p < .001$, $\eta_p^2 = .473$; congruency × time, $F(7, 182) = 43.209$, $p < .001$, $\eta_p^2 = .624$; task-switch × time, $F(3.09, 80.42) = 6.219$, $p = .001$, $\eta_p^2 = .193$; and congruency × task-switch × time, $F(7, 182) = 6.936$, $p < .001$, $\eta_p^2 = .211$.

The main effect of stimulus congruency was due to greater mean *deactivation* in the incongruent condition compared with the neutral condition (mean predictor weights = -0.026 and 0.132 for neutral and incongruent stimuli, respectively). This was driven by the combination of

more extreme peak deactivation in the incongruent condition and a much greater post-HDR rise above baseline in the neutral condition (Figure 4.13A). Peak deactivation was also later in the incongruent colour-naming than the neutral colour-naming task-switch condition (Figure 4.13B). The congruency × task-switch interaction appeared to be due to a more pronounced effect of stimulus congruency following neutral colour-naming (Figure 4.13C).

4.4.3.2. TSI task, response network (component 2)

Response network (component 2) estimated HDR plots are presented in Figure 4.14B. This network was primarily comprised of bilateral activation in somatomotor regions including SMA, pre/postcentral gyri, and cerebellar regions, as well as bilateral superior parietal lobules, superior and inferior lateral occipital cortex, central opercular cortex, thalamus, and small clusters in the insula (see Figure 4.14A for anatomical visualization and Table 4.9 for locations of cluster peaks). The repeated measures ANOVA revealed significant main effects of stimulus congruency, $F(1, 26) = 11.399$, $p = .002$, $\eta_p^2 = .305$; and time, $F(7, 182) = 92.386$, $p < .001$, $\eta_p^2 = .780$. Significant interactions emerged for congruency × time, $F(7, 182) = 6.525$, $p < .001$, $\eta_p^2 = .201$; and congruency × task-switch × time, $F(7, 182) = 6.460$, $p < .001$, $\eta_p^2 = .199$.

The main effect of stimulus congruency was due to greater mean activation in the neutral stimulus condition than in the incongruent stimulus condition (mean predictor weights = 0.024 and -0.047 for neutral and incongruent stimuli, respectively). In addition, there was greater post-peak suppression in the incongruent stimulus condition than in the neutral stimulus condition (Figure 4.15).

4.4.3.3. TSI task, evaluation network (component 3)

Evaluation network (component 3) estimated HDR plots are presented in Figure 4.16B. This network was comprised primarily of bilateral activation in superior and middle frontal gyri,

frontal poles, frontal orbital cortex, inferior frontal gyri (pars opercularis), anterior insula, superior lateral occipital cortex, angular gyri, temporooccipital/posterior middle and inferior temporal gyri, and cerebellar crus I and II (see Figure 4.16A for anatomical visualization and Table 4.10 for locations of cluster peaks). The repeated measures ANOVA revealed significant main effects of congruency, $F(1, 26) = 8.773$, $p = .006$, $\eta_p^2 = .252$; and time, $F(2.88, 74.98) = 2.939$, $p = .041$, $\eta_p^2 = .102$. A significant interaction emerged for congruency × time, $F(7, 182) = 7.314$, $p < .001$, $\eta_p^2 = .220$.

The main effect of congruency was due to greater mean activation in the incongruent stimulus condition than in the neutral stimulus condition (mean predictor weights = -0.046 and 0.049 for neutral and incongruent stimuli, respectively). This was due to the HDR for the neutral stimulus condition being suppressed throughout the post-stimulus time series (Figure 4.17).

4.4.4. Summary of TSI task results

While both response accuracy and RT were affected by stimulus congruency (i.e., higher accuracy and shorter RTs for neutral stimuli than for incongruent stimuli), response accuracy was not affected by task-switch condition. However, RTs were slowed following a task-switch from an incongruent colour-naming block, and this effect was the same for neutral as for incongruent stimuli.

Three components were extracted from the TSI fMRI data. The DMN/occipital network (component 1; Figure 4.12) comprised a combination of DMN regions and widespread occipital deactivation, which was dependent on both stimulus congruency and task-switch condition. This network exhibited greater deactivation for incongruent stimuli than for neutral stimuli, and this effect was magnified following a task-switch from an incongruent colour-naming block. The response network (component 2; Figure 4.14) was dominated by bilateral activation of somatomo-

tor regions, such as the SMA, pre/postcentral gyri, and cerebellum. The bilateral distribution of somatomotor activity is consistent with the task design, which required both hands for button-press responses. This network peaked earlier than the other two networks, and exhibited greater activation for neutral stimuli than for incongruent stimuli. The evaluation network (component 3; Figure 4.16) was comprised of frontoparietal connectivity, with peaks in more anterior prefrontal cortex and more posterior parietal regions as compared to the response network. This evaluation network was only engaged in the incongruent stimulus condition, which could suggest that it underlies an externally-oriented salience or stimulus conflict detection process. However, this seems unlikely given its later onsets and peaks compared with those of the response network, as a bottom-up attention network would be expected to initiate at the trial onset. Therefore, a more plausible explanation for the effect of stimulus congruency is that this network subserves a process akin to reflecting on whether the response matched the current task rule (i.e., focus on the word rather than the font colour), which is ambiguous for incongruent but not neutral stimuli. Although no significant task-switch effect emerged in the evaluation network, it is possible that this may be due to insufficient statistical power (suggested by the large standard errors around the predictor weights), and it should be noted that the HDR shapes suggest a trend for greater engagement following an incongruent colour-naming block (Figure 4.16B).

4.5. Analysis 4: Thought Generation Task (TGT)

4.5.1. Methods

4.5.1.1. Participants

32 healthy participants who met all general inclusion criteria detailed in Chapter 2 (Section 2.1) were included in the present analysis. Demographic information for this sample is provided in Table 4.1. A brief questionnaire was administered to all participants to obtain their age,

highest level of education, and any history of head injury, neurological conditions, drug use, and medication. In addition, visual acuity and color vision were assessed to ensure that participants were able to view the task on an fMRI presentation screen. Handedness was measured with the AHPQ (Annett, 1970), and IQ was estimated with the Quick IQ test (Mortimer & Bowen, 1999). Participants were recruited via posters on the UBC campus, community bulletin boards, and on electronic bulletins such as Craigslist. Participants provided informed consent at the start of their testing sessions, and were compensated $10 per hour for time spent participating in the study plus $10 for travel expenses. Participants were also given a copy of their T1 MRI scan on a disc.

4.5.1.2. TGT task design

Details regarding the TGT task design and procedures are provided in Chapter 2 (task protocol described in Section 2.2.4 and Figure 2.4; fMRI data acquisition and preprocessing described in Section 2.3 and Table 2.1). In summary, participants were presented with an object noun and its corresponding image (e.g., pillow) for five seconds and instructed to either mentally generate or listen to a function of the noun (e.g., "Something you rest your head on when sleeping"). The two experimental conditions (i.e., generating and hearing) were presented in alternating blocks of 15 trials (30 trials total for each condition across two runs).

4.5.1.3. TGT data analysis

No overt behavioural responses are recorded in the TGT task, and so only functional connectivity was examined. A single-experiment fMRI-CPCA was carried out for the TGT task as described in Chapter 2 (Section 2.4). The generating and hearing conditions were both specified in the design, and the time bins for which a FIR basis function was specified were scans 1-8 following trial onset (i.e., 20 seconds of post-stimulus time with TR = 2,500ms). This resulted in *G* matrices with 176 rows (scans) and 16 columns (2 conditions × 8 post-stimulus time bins) per

task run. After the regression and PCA steps, within-subject factors of condition (generating vs. hearing) and time (8 post-stimulus time bins) were examined with the resulting predictor weights, resulting in a 2 (condition) × 8 (time) repeated measures ANOVA for each component. Post-hoc analyses of significant effects of condition and condition × time were carried out, with the interaction involving time examined using repeated measures contrasts between adjacent time bins.

4.5.2. TGT functional connectivity results

Four components were extracted from the TGT task-related variance in BOLD signal. After varimax rotation, the components accounted for 14.52%, 9.49%, 5.80%, and 5.33% of the variance, respectively. For the purpose of discussion, these components are referred to as (1) language network, (2) posterior-medial DMN, (3) anterior/posterior-lateral DMN, and (4) auditory network.

4.5.2.1. TGT task, language network (component 1)

Language network (component 1) estimated HDR plots are presented in Figure 4.18B. This network consisted of left-lateralized activation in posterior middle frontal gyrus, inferior frontal gyrus (pars opercularis and pars triangularis), frontal orbital cortex, and superior lateral occipital cortex, as well as bilateral (but slightly left-dominant) posterior superior temporal gyri, bilateral SMA/superior frontal gyrus, inferior lateral occipital cortex, occipital poles, and occipital fusiform cortex (see Figure 4.18A for anatomical visualization and Table 4.11 for locations of cluster peaks). The 2 (condition) × 8 (time) repeated measures ANOVA revealed significant main effects of condition, $F(1, 31) = 9.590$, $p = .004$, $\eta_p^2 = .236$; and time, $F(7, 217) = 85.500$, $p < .001$, $\eta_p^2 = .734$. A significant interaction emerged for condition × time, $F(2.44, 75.51) = 6.474$, $p = .001$, $\eta_p^2 = .173$.

The main effect of condition was due to greater mean activation in the generating condition than in the hearing condition (mean predictor weights = 0.129 and 0.100 for generating and hearing, respectively). The HDR shape for the generating condition also exhibited a steeper increase to peak and steeper post-peak decline as compared to the shape of the hearing condition HDR (Figure 4.18B).

4.5.2.2. TGT task, posterior-medial DMN (component 2)

Posterior-medial DMN (component 2) estimated HDR plots are presented in Figure 4.19B. This network primarily consisted of deactivation of posterior medial regions of the DMN including posterior cingulate gyrus, precuneus cortex, and cuneal cortex, as well as anterior cingulate cortex, SMA, pre/postcentral gyri, superior frontal gyri, superior and inferior lateral occipital cortex, anterior supramarginal gyri, and lingual gyri (see Figure 4.19A for anatomical visualization and Table 4.12 for locations of cluster peaks). The repeated measures ANOVA revealed a significant main effect of time, $F(7, 217) = 9.831$, $p < .001$, $\eta_p^2 = .241$. Neither the main effect of task condition nor the condition × time interaction were statistically significant (both ps > .20).

4.5.2.3. TGT task, anterior/posterior-lateral network (component 3)

Anterior/posterior-lateral DMN (component 3) estimated HDR plots are presented in Figure 4.20B. This network primarily consisted of bilateral deactivation in anterior and lateral posterior regions of the DMN including frontal poles, superior and middle frontal gyri, paracingulate gyri, superior lateral occipital cortex, and angular gyri, as well as middle temporal gyri and bilateral regions of the cerebellum including crus I and II. Small clusters of activation emerged as well in occipital fusiform cortex (see Figure 4.20A for anatomical visualizations and Table 4.13 for locations of cluster peaks). The repeated measures ANOVA revealed a significant

main effect of time, $F(7, 217) = 19.615$, $p < .001$, $\eta_p^2 = .388$. Neither the main effect of task condition nor the condition × time interaction were statistically significant (both *p*s > .60).

4.5.2.4. TGT task, auditory network (component 4)

Auditory network (component 4) estimated HDR plots are presented in Figure 4.21B. This network consisted of bilateral activation in primary auditory cortex and surrounding regions, including anterior superior temporal gyrus, temporal fusiform cortex, temporal-occipital fusiform cortex, inferior frontal gyrus (pars triangularis and pars opercularis), precentral gyrus, and thalamus, as well as small clusters of deactivation in inferior lateral occipital cortex (see Figure 4.21A for anatomical visualization and Table 4.14 for locations of cluster peaks). The repeated measures ANOVA revealed significant main effects of condition, $F(1, 31) = 107.394$, $p < .001$, $\eta_p^2 = .776$; and time, $F(7, 217) = 23.187$, $p < .001$, $\eta_p^2 = .428$. A significant interaction emerged for condition × time, $F(7, 217) = 83.205$, $p < .001$, $\eta_p^2 = .729$.

The main effect of condition was due to greater mean activation in the hearing condition than in the generating condition (mean predictor weights = -0.041 and 0.050 for generating and hearing conditions, respectively). This network was only engaged during the hearing condition, with onsets initiating at the 5-second post-stimulus time bin, and peaking at around 10 seconds (see Figure 4.21B).

4.5.3. Summary of TGT task results

Four components were extracted from the TGT data. The language network (component 1; Figure 4.18) comprised frontotemporal connectivity and widespread activity in occipital cortex. Several regions of this network were left-lateralized, including inferior frontal gyrus (pars triangularis), middle frontal gyrus, and superior lateral occipital cortex/superior parietal lobule, which, along with the activation in posterior superior temporal gyri, is consistent with known

language-related patterns of activity (i.e., Broca's area in the inferior frontal gyrus and Wernicke's area in posterior superior temporal gyrus; Flinker et al., 2015). This network was the only one that was more engaged in the generating condition than in the hearing condition. The posterior-medial DMN (component 2; Figure 4.19) consisted primarily of deactivation in posterior medial regions of the DMN – especially the precuneus – as well as in pre/postcentral gyri, and dorsal medial prefrontal regions including SMA and dorsal anterior cingulate. By contrast, the anterior/posterior-lateral DMN (component 3; Figure 4.20) consisted of deactivation of anterior portions of the DMN (frontal poles, superior frontal gyri) and the *lateral* posterior areas (superior lateral occipital cortex, temporooccipital part of the middle temporal gyri), and it peaked earlier than the posterior-medial DMN. Neither of these task-negative networks exhibited differences between task conditions. Finally, the auditory network (component 4; Figure 4.21) reflected activation of primary auditory cortex in response to the stimulus presented in the hearing condition.

4.6. Discussion of Single Experiment Analyses

Four single-experiment fMRI-CPCAs were carried out in the present study, consisting of verbal WM (WM task), visuospatial WM (SCAP task), Stroop task-switching (TSI task), and internal thought generation versus speech perception (TGT). Two to four components were extracted from each dataset. As expected, a commonality among all tasks was the involvement of at least one task-positive network including activation in dorsal medial prefrontal cortex and which was dependent on cognitive demand, and at least one task-negative network consisting of deactivation of the DMN (or particular sub-regions).

In both the WM task and the TSI task, two task-positive networks emerged that comprised dorsal medial prefrontal cortex and parietal regions, with one of the two appearing to un-

derlie response processes. Therefore, it is surprising that only one task-positive network emerged in the SCAP task, given its similarity to the verbal WM task with respect to the putative processes engaged (i.e., encoding, maintenance, and recall/response). The different component structures between these WM tasks could be due to the nature of the task design and/or cognitive demand – namely, verbal versus non-verbal memory store – but it is possible that additional networks emerge in the SCAP task when combined with other tasks, as observed in the verbal WM task in Chapter 3.

The TGT functional connectivity results were more distinct in that two task-negative networks emerged, each of which was dominated by different subdivisions of the DMN (posterior-medial and anterior/posterior-lateral; Figures 4.19 and 4.2, respectively). It has been suggested that language-related tasks are more likely to produce a decomposition of the DMN into sub-regions due to its partial overlap with language systems (Seghier, Fagan, & Price, 2010), and the impact of semantic processing may play contrasting roles on different sub-regions of the DMN (Seghier & Price, 2012). Although neither of the DMN sub-networks in the TGT task exhibited differences between task conditions, the networks did show differences in HDR shapes. Notably, the anterior/posterior-lateral DMN (component 3) was the first to peak of all four networks that emerged and exhibited a relatively brief response, while the posterior-medial DMN (component 2) peaked later and was slightly more sustained (compare Figures 4.19B and 4.20B).

Also unique to the TGT task was the presence of a left-lateralized task-positive network (i.e., the language network, component 1) that was more engaged in the thought generation condition than in the hearing condition (Figure 4.18), which is likely due to the language production and processing demands of the task. This raises the question as to why a similar network did not emerge in the TSI task, which is also intrinsically tied to language (i.e., making a semantic

judgement of a word presented on-screen). A possible explanation is that when a cognitive task – such as the TSI task – engages a more prepotent response to a highly familiar word, it does not elicit language-specific activity to the same degree as higher-level sentence production/comprehension.

Although meaningful insights may be gained from the individual analyses of these tasks, it is important to note the uncertainty of the degree to which any given network reflects task-specific activity rather than a more replicable pattern. Although this is not necessarily a limitation with respect to basic cognitive neuroscience research, in the context of schizophrenia research it may be important to identify networks that replicate across several cognitive tasks when the aim is to identify clinically meaningful patterns of brain activity. Therefore, the final analysis chapter involves combining these four tasks into a multi-experiment fMRI-CPCA with the overarching goal of characterizing networks that may underlie WM deficits in schizophrenia.

4.7. Chapter 4 Tables

Table 4.1. Demographic information for the WM task, SCAP task, TSI task, and TGT task datasets (from single-task analyses with healthy controls only). Standard deviations are in parentheses.

	WM (n = 54)	SCAP (n = 119)	TSI (n = 27)	TGT (n = 32)
Age	29.65 (9.41)	31.22 (8.80)	29.37 (8.63)	28.75 (8.58)
Years of education	15.79 (2.02)	15.03 (1.71)	16.31 (1.86)	15.58 (1.81)
Quick estimated IQ	100.06 (11.99)	-	101.22 (12.34)	97.09 (11.21)
Gender distribution (female/male)	36/18	64/55	20/7	13/19
Handedness (L/M/R)	5/2/47	0/0/119	1/1/25	3/1/28
Socioeconomic status factor score	59.63 (14.27)	-	54.89 (12.62)	65.75 (14.97)

Note. Years of education missing for 1 WM participant. IQ = intelligence quotient; L = left-handed; M = mixed handedness; R = right-handed; WM = Working Memory Task; SCAP = Spatial Capacity Task; TSI = Task-Switch Inertia Task; TGT = Thought Generation Task.

Table 4.2. Mean WM, SCAP, and TSI task performance results (percent correct and mean reaction time for each condition; standard deviations in parentheses).

Task/Condition	Percent correct	RT (milliseconds)[a]
WM task		
4 letters		
0s delay	94.64 (7.20)	1,035.83 (170.42)
4s delay	92.72 (7.18)	1,021.14 (157.92)
6 letters		
0s delay	88.96 (9.37)	1,108.63 (153.17)
4s delay	85.05 (12.00)	1,089.91 (180.02)
SCAP task		
1 dot		
1.5s delay	96.01 (11.27)	938.85 (226.01)
3.0s delay	92.86 (14.61)	902.74 (220.40)
4.5s delay	89.08 (19.43)	971.08 (271.09)
3 dots		
1.5s delay	84.87 (23.52)	1,097.02 (271.97)
3.0s delay	80.04 (24.05)	1,143.21 (292.22)
4.5s delay	87.18 (21.06)	1,041.19 (273.98)
5 dots		
1.5s delay	84.45 (19.80)	1,215.67 (297.27)
3.0s delay	84.66 (18.44)	1,129.39 (264.22)
4.5s delay	78.78 (25.34)	1,191.11 (315.12)
7 dots		
1.5s delay	80.04 (20.99)	1,281.85 (337.10)
3.0s delay	76.47 (19.34)	1,212.79 (283.01)
4.5s delay	74.16 (20.82)	1,201.38 (293.21)
TSI task		
Colour-naming[b]		
Neutral	95.56 (4.43)	884.21 (95.31)
Incongruent	87.65 (9.99)	1,120.85 (108.54)
Word-reading		
Neutral (*all)*	97.04 (3.38)	913.48 (104.37)
cn-WN	97.04 (3.85)	899.77 (103.00)
ci-WN	97.04 (5.01)	927.05 (120.95)
Incongruent (*all)*	86.42 (8.52)	1,164.92 (139.98)
cn-WI	87.90 (9.79)	1,129.36 (144.58)
ci-WI	84.94 (11.78)	1,201.03 (165.16)

[a]RT was not analyzed for the WM task or SCAP task, but is presented here for interest.
[b]Colour-naming trials were not analyzed, but task performance is presented here for interest.
RT = reaction time; cn = task-switch from neutral colour-naming block; ci = task-switch from incongruent colour-naming block; WN = neutral word-reading stimulus; WI = incongruent word-reading stimulus.

Table 4.3. WM task fMRI-CPCA, response/attention network (component 1): Clusters for the most extreme 10% of component loadings. Anatomical regions, Brodmann areas (BAs), and Montreal Neurological Institute (MNI) coordinates are listed for each cluster peak.

WM task response/attention network (component 1) anatomical regions	Cluster volumes		BAs	MNI coordinates		
	voxels	mm^3		x	y	z
Positive loadings						
Cluster 1: left hemisphere	4,036	108,972				
Precentral gyrus			4	-36	-22	59
Postcentral gyrus			3	-45	-28	53
Precentral gyrus			6	-33	-7	62
Postcentral gyrus			3	-51	-25	44
Central opercular cortex			48	-54	-19	20
Supplementary motor area			6	-3	-4	53
Superior lateral occipital cortex			7	-12	-70	53
Parietal operculum cortex			48	-57	-40	23
Cluster 1: right hemisphere						
Paracingulate gyrus			32	3	17	47
Cluster 2: left hemisphere	1,341	36,207				
Cerebellum VI			n/a	-33	-55	-31
Cluster 2: bilateral						
Lingual gyrus			17	0	-79	2
Cluster 2: right hemisphere						
Cerebellum VI			n/a	21	-52	-25
Cerebellum VIIIa			n/a	18	-64	-49
Cerebellum V			n/a	6	-64	-16
Cerebellum crus II			n/a	6	-73	-34
Cerebellum V			n/a	12	-58	-28
Cluster 3: left hemisphere	971	26,217				
Insular cortex			48	-30	20	5
Precentral gyrus			44	-54	8	29
Precentral gyrus			48	-51	5	11
Insular cortex			48	-39	-1	8
Frontal pole			46	-30	47	20
Middle frontal gyrus			46	-36	35	29
Inferior frontal gyrus, pars opercularis			45	-51	11	-1

(Table 4.3 continued on next page)

(Table 4.3, continued from previous page)

WM task response/attention network (component 1) anatomical regions	Cluster volumes		BAs	MNI coordinates		
	voxels	mm^3		x	y	z
Cluster 4: right hemisphere	529	14,283				
Postcentral gyrus			48	57	-16	26
Postcentral gyrus			3	54	-19	38
Posterior supramarginal gyrus			40	39	-46	44
Superior parietal lobule			2	42	-40	53
Anterior supramarginal gyrus			2	48	-34	50
Cluster 5: right hemisphere	471	12,717				
Insular cortex			47	33	23	2
Inferior frontal gyrus, pars opercularis			6	57	11	20
Inferior frontal gyrus, pars opercularis			48	54	11	8
Cluster 6: right hemisphere	227	6,129				
Frontal pole			46	36	44	26
Cluster 7: right hemisphere	186	5,022				
Middle frontal gyrus			6	33	-1	59
Cluster 8: left hemisphere	67	1,809				
Thalamus			n/a	-12	-19	8
Cluster 9: left hemisphere	58	1,566				
Inferior lateral occipital cortex			37	-51	-67	2
Middle temporal gyrus, temporooccipital part			21	-48	-52	8
Cluster 10: right hemisphere	33	891				
Thalamus			n/a	12	-16	8
Caudate			n/a	15	-1	14
Cluster 11: left hemisphere	16	432				
Cerebellum VIIb			n/a	-33	-58	-49
Cluster 12: right hemisphere	11	297				
Precuneus cortex			7	9	-70	50
Cluster 13: left hemisphere	7	189				
Cerebellum VIIb			n/a	-15	-70	-49

Table 4.4. WM task fMRI-CPCA, visual attention network (component 2): Clusters for the most extreme 10% of component loadings. Anatomical regions, Brodmann areas (BAs), and Montreal Neurological Institute (MNI) coordinates are listed for each cluster peak.

WM task visual attention network (component 2) anatomical regions	Cluster volumes		BAs	MNI coordinates		
	voxels	mm^3		x	y	z
Positive loadings						
Cluster 1: left hemisphere	6,617	178,659				
Occipital pole			18	-18	-91	-7
Superior lateral occipital cortex			7	-21	-64	50
Superior lateral occipital cortex			19	-24	-67	32
Cluster 1: bilateral						
Vermis crus II			n/a	0	-73	-28
Cluster 1: right hemisphere						
Occipital fusiform gyrus			18	21	-88	-4
Superior lateral occipital cortex			19	27	-67	35
Superior lateral occipital cortex			7	27	-61	53
Temporal occipital fusiform cortex			37	36	-46	-19
Cerebellum crus II			n/a	9	-76	-40
Cluster 2: left hemisphere	719	19,413				
Precentral gyrus			6	-51	-1	47
Precentral gyrus			6	-57	2	23
Middle frontal gyrus			6	-27	-1	50
Cluster 3: left hemisphere	220	5,940				
Supplementary motor area			6	-3	5	62
Cluster 4: right hemisphere	175	4,725				
Precentral gyrus			6	54	-1	44
Cluster 5: right hemisphere	39	1,053				
Precentral gyrus			44	42	8	26
Cluster 6: right hemisphere	36	972				
Precentral gyrus			6	30	-1	47
Cluster 7: right hemisphere	34	918				
Thalamus			n/a	21	-28	-1
Cluster 8: left hemisphere	32	864				
Thalamus			n/a	-21	-28	-4

(Table 4.4 continued on next page)

(Table 4.4, continued from previous page)

WM task visual attention network (component 2) anatomical regions	Cluster volumes		BAs	MNI coordinates		
	voxels	mm^3		x	y	z
Cluster 9: bilateral	23	621				
Vermis IX			n/a	0	-58	-37
Cluster 10: right hemisphere	14	378				
Precentral gyrus			6	33	-19	71
Cluster 11: right hemisphere	11	297				
Cerebellum VIIb			n/a	24	-70	-52
Cluster 12: right hemisphere	4	108				
Anterior supramarginal gyrus			2	42	-34	44
Cluster 13: left hemisphere	3	81				
Cerebellum X			n/a	-21	-40	-43
Cluster 14: left hemisphere	2	54				
Superior parietal lobule			40	-39	-40	44
Negative loadings						
Cluster 15: left hemisphere	17	459				
Lingual gyrus			18	-9	-73	-7
Cluster 16: left hemisphere	6	162				
Occipital pole			18	-9	-94	20
Cluster 17: right hemisphere	2	54				
Occipital pole			18	12	-88	23

Table 4.5. WM task fMRI-CPCA, default mode network (DMN, component 3): Clusters for the most extreme 10% of component loadings. Anatomical regions, Brodmann areas (BAs), and Montreal Neurological Institute (MNI) coordinates are listed for each cluster peak.

WM task default mode network (component 3)	Cluster volumes		BAs	MNI coordinates		
anatomical regions	voxels	mm^3		x	y	z
Positive loadings						
Cluster 1: left hemisphere	19	513				
Supplementary motor area			6	-3	8	56
Cluster 2: left hemisphere	5	135				
Precentral gyrus			6	-54	2	44
Negative loadings						
Cluster 3: left hemisphere	2,791	75,357				
Superior frontal gyrus			10	-6	56	29
Superior frontal gyrus			9	-21	35	44
Cluster 3: right hemisphere						
Frontal pole			10	3	56	14
Frontal pole			10	3	59	5
Superior frontal gyrus			9	24	32	47
Frontal pole			9	18	44	41
Middle frontal gyrus			46	39	20	44
Cluster 4: left hemisphere	2,565	69,255				
Posterior cingulate gyrus			23	-3	-46	35
Cluster 4: bilateral						
Precuneus cortex			31	0	-70	29
Posterior cingulate gyrus			23	0	-16	38
Cluster 5: left hemisphere	816	22,032				
Superior lateral occipital cortex			39	-45	-73	29
Cluster 6: right hemisphere	774	20,898				
Superior lateral occipital cortex			39	51	-64	23
Cluster 7: right hemisphere	422	11,394				
Anterior middle temporal gyrus			21	57	-4	-16
Temporal pole			38	42	20	-28
Inferior frontal gyrus, pars triangularis			45	54	26	11
Inferior frontal gyrus, pars triangularis			45	51	29	8
Temporal pole			21	48	8	-31

(Table 4.5 continued on next page)

(Table 4.5, continued from previous page)

WM task default mode network (component 3) anatomical regions	Cluster volumes		BAs	MNI coordinates		
	voxels	mm^3		x	y	z
Frontal orbital cortex			47	42	32	-10
Planum temporale			48	57	-10	5
Cluster 8: left hemisphere	224	6,048				
Anterior middle temporal gyrus			20	-54	-7	-16
Temporal pole			21	-48	11	-28
Frontal orbital cortex			38	-42	26	-16
Cluster 9: left hemisphere	150	4,050				
Cerebellum crus II			n/a	-21	-79	-37
Cluster 10: right hemisphere	115	3,105				
Cerebellum crus II			n/a	27	-76	-37
Cluster 11: left hemisphere	31	837				
Lingual gyrus			37	-27	-43	-10
Cluster 12: right hemisphere	18	486				
Lingual gyrus			37	27	-40	-10
Cluster 13: right hemisphere	11	297				
Temporal pole			38	30	5	-19
Cluster 14: right hemisphere	5	135				
Cerebellum IX			n/a	9	-52	-46
Cluster 15: left hemisphere	5	135				
Middle temporal gyrus, temporooccipital part			37	-63	-55	-1

Table 4.6. SCAP task fMRI-CPCA, external attention network (component 1): Clusters for the most extreme 10% of component loadings. Anatomical regions, Brodmann areas (BAs), and Montreal Neurological Institute (MNI) coordinates are listed for each cluster peak.

SCAP task external attention network (component 1) anatomical regions	Cluster volumes		BAs	MNI coordinates		
	voxels	mm^3		x	y	z
Positive loadings						
Cluster 1: left hemisphere	7,388	199,476				
Superior lateral occipital cortex			7	-18	-64	53
Superior parietal lobule			40	-33	-46	50
Superior lateral occipital cortex			19	-27	-73	29
Middle frontal gyrus			6	-27	-4	56
Inferior lateral occipital cortex			37	-48	-67	-7
Supplementary motor area			32	-3	8	50
Precentral gyrus			44	-51	5	32
Occipital fusiform gyrus			18	-9	-73	-19
Cluster 1: right hemisphere						
Superior lateral occipital cortex			7	24	-61	53
Superior lateral occipital cortex			7	21	-64	50
Superior parietal lobule			7	30	-52	53
Superior lateral occipital cortex			7	27	-70	38
Inferior temporal gyrus, temporooccipital part			37	48	-61	-10
Occipital pole			17	12	-91	11
Lingual gyrus			17	9	-88	-4
Cluster 2: right hemisphere	560	15,120				
Middle frontal gyrus			6	30	-1	59
Precentral gyrus			44	51	8	29
Cluster 3: left hemisphere	24	648				
Intracalcarine cortex			17	-12	-73	11
Cluster 4: right hemisphere	23	621				
Insular cortex			48	33	20	5
Cluster 5: left hemisphere	12	324				
Thalamus			n/a	-12	-19	8

(Table 4.6 continued on next page)

(Table 4.6, continued from previous page)

SCAP task external attention network (component 1) anatomical regions	Cluster volumes		BAs	MNI coordinates		
	voxels	mm^3		x	y	z
Cluster 6: right hemisphere	11	297				
Intracalcarine cortex			17	12	-67	11
Cluster 7: left hemisphere	5	135				
Insular cortex			48	-30	20	5
Cluster 8: right hemisphere	3	81				
Thalamus			n/a	12	-19	8

Table 4.7. SCAP task fMRI-CPCA, default mode network (DMN, component 2): Clusters for the most extreme 10% of component loadings. Anatomical regions, Brodmann areas (BAs), and Montreal Neurological Institute (MNI) coordinates are listed for each cluster peak.

SCAP task default mode network (component 2) anatomical regions	Cluster volumes		BAs	MNI coordinates		
	voxels	mm^3		x	y	z
Negative loadings						
Cluster 1: left hemisphere	3,431	92,637				
Frontal pole			10	-18	59	23
Superior frontal gyrus			8	-3	35	56
Middle frontal gyrus			9	-36	20	50
Cluster 1: bilateral						
Paracingulate gyrus			32	0	50	14
Frontal pole			9	0	62	17
Cluster 1: right hemisphere						
Frontal pole			9	18	47	41
Frontal pole			9	15	53	38
Superior frontal gyrus			8	6	41	53
Frontal pole			10	18	59	26
Middle frontal gyrus			9	42	20	47
Cluster 2: left hemisphere	1,255	33,885				
Precuneus cortex			30	-6	-55	11
Cluster 2: bilateral						
Posterior cingulate gyrus			31	0	-46	35
Posterior cingulate gyrus			23	0	-22	41
Precuneus cortex			31	0	-67	32
Cluster 3: right hemisphere	876	23,652				
Angular gyrus			39	51	-58	32
Posterior middle temporal gyrus			21	63	-22	-10
Posterior middle temporal gyrus			21	66	-28	-4
Cluster 4: left hemisphere	519	14,013				
Superior lateral occipital cortex			39	-48	-64	32
Cluster 5: left hemisphere	504	13,608				
Posterior middle temporal gyrus			21	-60	-22	-13
Posterior middle temporal gyrus			21	-63	-43	-1

(Table 4.7 continued on next page)

(Table 4.7, continued from previous page)

SCAP task default mode network (component 2) anatomical regions	Cluster volumes		BAs	MNI coordinates		
	voxels	mm^3		x	y	z
Planum temporale			22	-57	-25	11
Planum temporale			42	-60	-28	14
Central opercular cortex			48	-57	-7	5
Cluster 6: right hemisphere	339	9,153				
Cerebellum crus I			n/a	27	-82	-31
Cluster 7: left hemisphere	305	8,235				
Frontal orbital cortex			47	-48	26	-7
Cluster 8: left hemisphere	300	8,100				
Cerebellum crus I			n/a	-24	-82	-34
Cluster 9: right hemisphere	209	5,643				
Frontal orbital cortex			38	51	26	-7
Cluster 10: right hemisphere	205	5,535				
Planum temporale			48	54	-22	11
Central opercular cortex			48	57	-7	8
Central opercular cortex			48	60	-4	5
Insular cortex			48	39	-16	-4
Cluster 11: bilateral	26	702				
Thalamus			n/a	0	-13	8
Cluster 12: left hemisphere	25	675				
Posterior parahippocampal gyrus			20	-24	-22	-13
Cluster 13: left hemisphere	18	486				
Anterior parahippocampal gyrus			34	-24	-1	-16
Cluster 14: right hemisphere	11	297				
Hippocampus			n/a	24	-19	-13
Cluster 15: left hemisphere	3	81				
Planum polare			48	-42	-19	-1

Table 4.8. TSI task fMRI-CPCA, DMN/occipital network (component 1): Clusters for the most extreme 10% of component loadings. Anatomical regions, Brodmann areas (BAs), and Montreal Neurological Institute (MNI) coordinates are listed for each cluster peak.

TSI task DMN/occipital network (component 1) anatomical regions	Cluster volumes		BAs	MNI coordinates		
	voxels	mm^3		x	y	z
Negative loadings						
Cluster 1: left hemisphere	6,522	176,094				
Occipital pole			18	-9	-91	20
Lingual gyrus			18	-9	-79	-7
Precuneus cortex			17	-3	-61	11
Posterior cingulate gyrus			30	-3	-52	20
Superior lateral occipital cortex			39	-48	-67	23
Posterior cingulate gyrus			31	-3	-37	44
Posterior parahippocampal gyrus			37	-27	-34	-16
Posterior parahippocampal gyrus			30	-24	-40	-13
Anterior cingulate gyrus			23	-3	-13	41
Lingual gyrus			37	-21	-46	-10
Posterior parahippocampal gyrus			30	-24	-22	-16
Cluster 1: bilateral						
Lingual gyrus			17	0	-88	-1
Precuneus cortex			31	0	-73	29
Posterior cingulate gyrus			31	0	-49	32
Cluster 1: right hemisphere						
Superior lateral occipital cortex			19	21	-85	26
Lingual gyrus			18	15	-76	-7
Intracalcarine cortex			17	9	-85	2
Precuneus cortex			30	9	-52	5
Precuneus cortex			17	6	-58	11
Posterior cingulate gyrus			30	3	-52	20
Lingual gyrus			37	24	-52	-10
Precuneus cortex			5	3	-46	59
Cluster 2: left hemisphere	1,038	28,026				
Superior frontal gyrus			9	-24	35	44
Cluster 2: bilateral						
Frontal pole			10	0	59	2
Cluster 2: right hemisphere						
Frontal pole			9	24	38	44

(Table 4.8 continued on next page)

(Table 4.8, continued from previous page)

TSI task DMN/occipital network (component 1) anatomical regions	Cluster volumes		BAs	MNI coordinates		
	voxels	mm^3		x	y	z
Frontal pole			8	27	35	47
Frontal pole			9	15	53	41
Cluster 3: right hemisphere	289	7,803				
Anterior superior temporal gyrus			22	57	-4	-13
Temporal pole			38	42	20	-28
Cluster 4: left hemisphere	214	5,778				
Temporal pole			21	-51	8	-28
Anterior middle temporal gyrus			22	-57	-4	-13
Cluster 5: right hemisphere	14	378				
Amygdala			n/a	24	-4	-19
Cluster 6: left hemisphere	8	216				
Anterior parahippocampal gyrus			28	-21	-4	-19
Temporal pole			34	-30	2	-19

Table 4.9. TSI task fMRI-CPCA, response network (component 2): Clusters for the most extreme 10% of component loadings. Anatomical regions, Brodmann areas (BAs), and Montreal Neurological Institute (MNI) coordinates are listed for each cluster peak.

TSI task response network (component 2) anatomical regions	Cluster volumes		BAs	MNI coordinates		
	voxels	mm^3		x	y	z
Positive loadings						
Cluster 1: left hemisphere	5,979	161,433				
Postcentral gyrus			3	-51	-22	38
Postcentral gyrus			40	-39	-37	50
Superior parietal lobule			7	-30	-52	59
Middle frontal gyrus			6	-27	-4	59
Precentral gyrus			6	-54	5	32
Precentral gyrus			6	-36	-7	62
Superior lateral occipital cortex			7	-18	-61	56
Superior lateral occipital cortex			19	-24	-70	29
Central opercular cortex			48	-51	5	2
Insular cortex			48	-39	-1	8
Cluster 1: bilateral						
Supplementary motor area			6	0	-1	56
Cluster 1: right hemisphere						
Postcentral gyrus			3	45	-28	50
Superior frontal gyrus			6	30	-4	62
Superior parietal lobule			2	33	-46	59
Postcentral gyrus			4	51	-19	47
Precentral gyrus			6	39	-10	62
Postcentral gyrus			3	36	-37	59
Central opercular cortex			48	57	-16	20
Superior lateral occipital cortex			7	15	-67	56
Superior lateral occipital cortex			19	27	-67	35
Cluster 2: left hemisphere	1,785	48,195				
Cerebellum VI			n/a	-27	-55	-25
Inferior lateral occipital cortex			19	-45	-67	-4
Inferior temporal gyrus, temporooccipital part			37	-45	-58	-13
Cluster 2: bilateral						
Vermis VI			n/a	0	-67	-16
Vermis crus II			n/a	0	-73	-34

(Table 4.9 continued on next page)

(Table 4.9, continued from previous page)

TSI task response network (component 2) anatomical regions	Cluster volumes		BAs	MNI coordinates		
	voxels	mm^3		x	y	z
Cluster 2: right hemisphere						
Cerebellum VI			n/a	24	-55	-25
Cerebellum VI			n/a	30	-52	-28
Cerebellum VIIIa			n/a	27	-58	-52
Cerebellum VIIb			n/a	15	-70	-49
Inferior lateral occipital cortex			37	48	-67	-1
Inferior temporal gyrus, temporooccipital part			37	45	-58	-13
Inferior lateral occipital cortex			19	39	-79	-4
Cluster 3: right hemisphere	119	3,213				
Precentral gyrus			6	54	8	35
Cluster 4: left hemisphere	96	2,592				
Cerebellum VIIIa			n/a	-27	-61	-52
Cluster 5: left hemisphere	47	1,269				
Thalamus			n/a	-12	-19	8
Cluster 6: right hemisphere	35	945				
Thalamus			n/a	12	-16	8
Cluster 7: left hemisphere	13	351				
Insular cortex			48	-30	17	5
Cluster 8: right hemisphere	6	162				
Insular cortex			48	33	17	5
Cluster 9: right hemisphere	4	108				
Occipital fusiform gyrus			18	27	-85	2

Table 4.10. TSI task fMRI-CPCA, evaluation network (component 3): Clusters for the most extreme 10% of component loadings. Anatomical regions, Brodmann areas (BAs), and Montreal Neurological Institute (MNI) coordinates are listed for each cluster peak.

TSI task evaluation network (component 3) anatomical regions	Cluster volumes		BAs	MNI coordinates		
	voxels	mm^3		x	y	z
Positive loadings						
Cluster 1: left hemisphere	4,742	128,034				
Frontal pole			45	-42	47	5
Middle frontal gyrus			9	-45	17	44
Middle frontal gyrus			8	-30	17	56
Frontal orbital cortex			38	-48	26	-10
Inferior frontal gyrus, pars opercularis			38	-54	20	-1
Insular cortex			47	-36	20	-4
Frontal pole			46	-24	53	23
Cluster 1: bilateral						
Superior frontal gyrus			9	0	35	41
Superior frontal gyrus			8	0	26	50
Cluster 1: right hemisphere						
Middle frontal gyrus			44	45	20	41
Frontal pole			47	36	53	-1
Frontal pole			46	39	53	8
Middle frontal gyrus			8	33	14	56
Frontal pole			47	51	38	-7
Frontal orbital cortex			38	48	23	-7
Frontal orbital cortex			47	36	23	-7
Cluster 2: left hemisphere	1,171	31,617				
Cerebellum crus I			n/a	-42	-70	-34
Cerebellum crus II			n/a	-36	-70	-46
Cerebellum crus I			n/a	-30	-67	-31
Cerebellum crus I			n/a	-27	-70	-28
Cerebellum crus I			n/a	-9	-79	-28
Cluster 2: right hemisphere						
Cerebellum crus I			n/a	12	-79	-28
Cerebellum crus II			n/a	12	-82	-43
Cerebellum crus II			n/a	33	-73	-49
Cerebellum crus I			n/a	36	-67	-31

(Table 4.10 continued on next page)

(Table 4.10, continued from previous page)

TSI task evaluation network (component 3) anatomical regions	Cluster volumes		BAs	MNI coordinates		
	voxels	mm^3		x	y	z
Cluster 3: left hemisphere	942	25,434				
Angular gyrus			39	-42	-58	50
Angular gyrus			40	-42	-49	38
Cluster 4: right hemisphere	863	23,301				
Angular gyrus			40	42	-55	50
Superior lateral occipital cortex			7	36	-61	56
Cluster 5: left hemisphere	212	5,724				
Inferior temporal gyrus, temporooccipital part			37	-57	-55	-13
Posterior inferior temporal gyrus			20	-63	-40	-16
Posterior middle temporal gyrus			21	-63	-34	-7
Posterior middle temporal gyrus			21	-63	-28	-7
Cluster 6: right hemisphere	127	3,429				
Posterior middle temporal gyrus			21	63	-25	-10
Middle temporal gyrus, temporooccipital part			21	63	-46	-4
Inferior temporal gyrus, temporooccipital part			37	60	-55	-13
Cluster 7: left hemisphere	18	486				
Superior lateral occipital cortex			7	-9	-70	62
Precuneus cortex			7	-3	-67	50
Cluster 8: right hemisphere	10	270				
Frontal pole			9	24	44	38

Table 4.11. TGT task fMRI-CPCA, language network (component 1): Clusters for the most extreme 10% of component loadings. Anatomical regions, Brodmann areas (BAs), and Montreal Neurological Institute (MNI) coordinates are listed for each cluster peak.

TGT language network (component 1) anatomical regions	Cluster volumes		BAs	MNI coordinates		
	voxels	mm^3		x	y	z
Positive loadings						
Cluster 1: left hemisphere	6,280	169,560				
Temporal occipital fusiform cortex			19	-30	-61	-16
Inferior lateral occipital cortex			18	-27	-88	5
Posterior superior temporal gyrus			22	-57	-37	2
Superior lateral occipital cortex			7	-27	-67	44
Cluster 1: right hemisphere						
Temporal occipital fusiform cortex			37	33	-52	-19
Occipital pole			18	24	-91	8
Cluster 2: left hemisphere	1,015	27,405				
Middle frontal gyrus			6	-48	5	50
Inferior frontal gyrus, pars opercularis			48	-45	17	23
Inferior frontal gyrus, pars triangularis			45	-48	29	20
Inferior frontal gyrus, pars triangularis			47	-48	26	-1
Frontal orbital cortex			47	-36	29	-1
Cluster 3: right hemisphere	333	8,991				
Posterior superior temporal gyrus			22	54	-28	2
Planum temporale			22	57	-19	2
Posterior superior temporal gyrus			22	60	-16	-1
Cluster 4: left hemisphere	299	8,073				
Superior frontal gyrus			6	-3	11	59
Cluster 5: right hemisphere	47	1,269				
Cerebellum VIIb			n/a	24	-70	-52
Cluster 6: right hemisphere	38	1,026				
Middle frontal gyrus			6	51	5	53
Cluster 7: left hemisphere	19	513				
Thalamus			n/a	-24	-28	-4

Table 4.12. TGT task fMRI-CPCA, posterior-medial DMN (component 2): Clusters for the most extreme 10% of component loadings. Anatomical regions, Brodmann areas (BAs), and Montreal Neurological Institute (MNI) coordinates are listed for each cluster peak.

TGT posterior-medial DMN (component 2) anatomical regions	Cluster volumes		BAs	MNI coordinates		
	voxels	mm^3		x	y	z
Negative loadings						
Cluster 1: left hemisphere	7,287	196,749				
Precentral gyrus			4	-12	-37	47
Postcentral gyrus			2	-24	-40	62
Cuneal cortex			18	-12	-73	20
Cuneal cortex			18	-6	-79	29
Posterior cingulate gyrus			31	-12	-22	38
Anterior cingulate gyrus			24	-6	5	41
Precentral gyrus			4	-42	-16	50
Anterior supramarginal gyrus			2	-60	-28	32
Precentral gyrus			6	-24	-7	50
Superior lateral occipital cortex			7	-12	-73	47
Lingual gyrus			18	-15	-64	-4
Precentral gyrus			6	-24	-16	68
Superior frontal gyrus			6	-24	-4	62
Superior frontal gyrus			6	-24	-4	56
Anterior supramarginal gyrus			2	-48	-34	35
Postcentral gyrus			3	-57	-10	38
Cluster 1: bilateral						
Supplementary motor area			6	0	-10	59
Cluster 1: right hemisphere						
Precuneus cortex			5	6	-49	56
Precuneus cortex			7	9	-64	53
Superior parietal lobule			5	18	-46	68
Cuneal cortex			18	18	-67	20
Precuneus cortex			7	9	-76	35
Anterior cingulate gyrus			24	3	5	44
Middle frontal gyrus			9	27	32	41
Cuneal cortex			19	15	-82	23
Superior frontal gyrus			8	24	11	59
Precentral gyrus			6	6	-16	47
Superior parietal lobule			2	42	-37	56
Anterior supramarginal gyrus			2	57	-28	32

(Table 4.12 continued on next page)

(Table 4.12, continued from previous page)

TGT posterior-medial DMN (component 2) anatomical regions	Cluster volumes		BAs	MNI coordinates		
	voxels	mm^3		x	y	z
Postcentral gyrus			4	54	-16	44
Lingual gyrus			18	15	-67	-4
Anterior supramarginal gyrus			3	57	-22	41
Precentral gyrus			3	39	-13	41
Precentral gyrus			6	45	-10	44
Superior frontal gyrus			6	12	-10	71
Precentral gyrus			4	12	-22	74
Postcentral gyrus			48	60	-16	23
Postcentral gyrus			48	54	-13	26
Cluster 2: right hemisphere	420	11,340				
Inferior lateral occipital cortex			37	45	-64	14
Superior lateral occipital cortex			19	39	-70	32
Angular gyrus			22	48	-49	23
Cluster 3: left hemisphere	108	2,916				
Anterior cingulate gyrus			24	-6	38	11
Anterior cingulate gyrus			32	-12	44	8
Cluster 3: right hemisphere						
Frontal pole			10	9	59	14
Paracingulate gyrus			10	3	53	5
Anterior cingulate gyrus			32	6	41	8
Paracingulate gyrus			32	6	50	20
Cluster 4: left hemisphere	107	2,889				
Inferior lateral occipital cortex			37	-45	-67	11
Cluster 5: left hemisphere	34	918				
Frontal pole			46	-27	38	29
Cluster 6: left hemisphere	26	702				
Cerebellum VI			n/a	-30	-43	-40
Cluster 7: left hemisphere	23	621				
Cerebellum VIIIb			n/a	-15	-58	-55

(Table 4.12 continued on next page)

(Table 4.12, continued from previous page)

TGT posterior-medial DMN (component 2) anatomical regions	Cluster volumes		BAs	MNI coordinates		
	voxels	mm^3		x	y	z
Cluster 8: right hemisphere	13	351				
Cerebellum VIIIb			n/a	24	-52	-52
Cluster 9: right hemisphere	5	135				
Insular cortex			48	36	-7	-1
Cluster 10: right hemisphere	4	108				
Posterior supramarginal gyrus			40	39	-43	35
Cluster 11: left hemisphere	3	81				
Precentral gyrus			48	-60	-4	17

Table 4.13. TGT task fMRI-CPCA, anterior/posterior-lateral DMN (component 3): Clusters for the most extreme 10% of component loadings. Anatomical regions, Brodmann areas (BAs), and Montreal Neurological Institute (MNI) coordinates are listed for each cluster peak.

TGT anterior/posterior-lateral DMN (component 3) anatomical regions	Cluster volumes		BAs	MNI coordinates		
	voxels	mm^3		x	y	z
Positive loadings						
Cluster 1: right hemisphere	40	1,080				
Occipital fusiform gyrus			19	30	-67	-10
Temporal occipital fusiform cortex			37	33	-52	-13
Cluster 2: left hemisphere	19	513				
Occipital fusiform gyrus			19	-30	-67	-10
Cluster 3: left hemisphere	4	108				
Temporal occipital fusiform cortex			37	-36	-46	-16
Negative loadings						
Cluster 1: left hemisphere	4,227	114,129				
Frontal pole			46	-21	56	23
Frontal pole			10	-3	56	-1
Superior frontal gyrus			9	-24	35	44
Middle frontal gyrus			46	-39	23	41
Frontal pole			11	-21	56	-1
Paracingulate gyrus			32	-3	35	35
Frontal pole			47	-33	50	-7
Frontal pole			47	-42	41	-7
Frontal pole			47	-45	38	-10
Anterior cingulate gyrus			24	-3	26	23
Frontal pole			48	-30	35	14
Cluster 1: bilateral						
Frontal pole			10	0	59	-4
Superior frontal gyrus			8	0	32	56
Cluster 1: right hemisphere						
Middle frontal gyrus			9	30	29	47
Superior frontal gyrus			8	27	26	56
Frontal pole			10	6	62	5
Paracingulate gyrus			32	3	47	23
Frontal pole			10	6	56	11
Frontal pole			9	15	53	29

(Table 4.13 continued on next page)

(Table 4.13, continued from previous page)

TGT anterior/posterior-lateral DMN (component 3) anatomical regions	Cluster volumes		BAs	MNI coordinates		
	voxels	mm^3		x	y	z
Middle frontal gyrus			9	42	20	47
Frontal pole			9	18	50	32
Frontal pole			47	39	47	5
Frontal pole			47	33	56	-1
Frontal pole			11	18	59	-10
Frontal pole			45	48	38	-1
Frontal pole			47	42	50	-7
Frontal pole			47	45	44	-7
Frontal pole			47	48	38	-13
Cluster 2: left hemisphere	1,307	35,289				
Cerebellum crus I			n/a	-33	-76	-37
Cluster 2: right hemisphere						
Cerebellum crus II			n/a	24	-82	-37
Cerebellum crus I			n/a	48	-70	-37
Cluster 3: left hemisphere	1,191	32,157				
Angular gyrus			39	-54	-55	44
Superior lateral occipital cortex			19	-42	-79	35
Superior lateral occipital cortex			19	-39	-79	41
Superior lateral occipital cortex			39	-45	-67	50
Superior lateral occipital cortex			39	-57	-67	26
Superior lateral occipital cortex			39	-51	-73	29
Middle temporal gyrus, temporooccipital part			37	-66	-46	-7
Middle temporal gyrus, temporooccipital part			37	-63	-55	-7
Posterior middle temporal gyrus			21	-63	-22	-13
Middle temporal gyrus, temporooccipital part			37	-60	-61	-10
Inferior lateral occipital cortex			37	-60	-64	-1
Posterior middle temporal gyrus			20	-54	-16	-16
Cluster 4: right hemisphere	969	26,163				
Superior lateral occipital cortex			39	51	-73	35
Superior lateral occipital cortex			39	54	-61	41
Angular gyrus			39	60	-55	35
Superior lateral occipital cortex			39	48	-67	47
Superior lateral occipital cortex			39	60	-61	20
Inferior lateral occipital cortex			37	60	-67	8
Middle temporal gyrus, temporooccipital part			21	66	-55	5

(Table 4.13 continued on next page)

(Table 4.13, continued from previous page)

TGT anterior/posterior-lateral DMN (component 3) anatomical regions	Cluster volumes		BAs	MNI coordinates		
	voxels	mm^3		x	y	z
Cluster 5: right hemisphere	101	2,727				
Posterior middle temporal gyrus			21	66	-16	-16
Anterior middle temporal gyrus			21	54	-1	-28
Cluster 6: left hemisphere	74	1,998				
Superior lateral occipital cortex			7	-3	-70	68
Superior lateral occipital cortex			7	-6	-79	62
Cluster 7: left hemisphere	45	1,215				
Precuneus cortex			31	-3	-55	32
Cluster 7: bilateral						
Precuneus cortex			7	0	-67	47
Cluster 8: right hemisphere	23	621				
Frontal orbital cortex			47	33	20	-10
Cluster 9: left hemisphere	15	405				
Insular cortex			48	-33	17	-10
Cluster 10: right hemisphere	9	243				
Posterior middle temporal gyrus			21	72	-34	-7
Cluster 11: bilateral	5	135				
Posterior cingulate gyrus			23	0	-25	41
Cluster 12: right hemisphere	2	54				
Inferior temporal gyrus, temporooccipital part			20	66	-52	-13

Table 4.14. TGT task fMRI-CPCA, auditory network (component 4): Clusters for the most extreme 10% of component loadings. Anatomical regions, Brodmann areas (BAs), and Montreal Neurological Institute (MNI) coordinates are listed for each cluster peak.

TGT auditory network (component 4) anatomical regions	Cluster volumes		BAs	MNI coordinates		
	voxels	mm^3		x	y	z
Positive loadings						
Cluster 1: left hemisphere	3,130	84,510				
Heschl's gyrus			48	-54	-13	2
Cluster 2: right hemisphere	3,126	84,402				
Anterior superior temporal gyrus			48	60	-7	-1
Anterior temporal fusiform cortex			36	36	2	-37
Anterior temporal fusiform cortex			20	39	-7	-40
Cluster 3: left hemisphere	1,401	37,827				
Temporal occipital fusiform cortex			37	-30	-55	-13
Posterior temporal fusiform cortex			37	-30	-37	-19
Posterior temporal fusiform cortex			37	-27	-43	-16
Thalamus			n/a	-15	-28	-4
Cluster 3: right hemisphere						
Temporal occipital fusiform cortex			37	30	-52	-13
Posterior temporal fusiform cortex			37	30	-37	-19
Thalamus			n/a	15	-25	-4
Cluster 4: left hemisphere	192	5,184				
Inferior frontal gyrus, pars triangularis			45	-48	23	14
Inferior frontal gyrus, pars opercularis			48	-45	14	23
Cluster 5: right hemisphere	80	2,160				
Inferior frontal gyrus, pars opercularis			48	45	17	23
Inferior frontal gyrus, pars triangularis			45	48	26	17
Cluster 6: right hemisphere	44	1,188				
Precentral gyrus			6	54	2	47
Cluster 7: left hemisphere	28	756				
Precentral gyrus			6	-54	-7	50

(Table 4.14 continued on next page)

(Table 4.14, continued from previous page)

TGT auditory network (component 4) anatomical regions	Cluster volumes		BAs	MNI coordinates		
	voxels	mm^3		x	y	z
Cluster 8: left hemisphere	16	432				
Frontal orbital cortex			47	-36	32	-10
Negative loadings						
Cluster 1: left hemisphere	8	216				
Inferior lateral occipital cortex			37	-45	-70	5
Cluster 2: right hemisphere	6	162				
Inferior lateral occipital cortex			37	42	-64	2

4.8. Chapter 4 Figures

Figure 4.1. WM task fMRI-CPCA, response/attention network (component 1): Anatomical and temporal characteristics. **A (top)**: dominant 10% of loadings (red/yellow = positive loadings, min = 0.20, max = 0.37; no negative loadings above threshold). Images are displayed in neurological orientation (left is left) with MNI coordinates. **B (bottom)**: predictor weights plotted over post-stimulus time for each task condition. 4L = 4 letters; 6L = 6 letters.

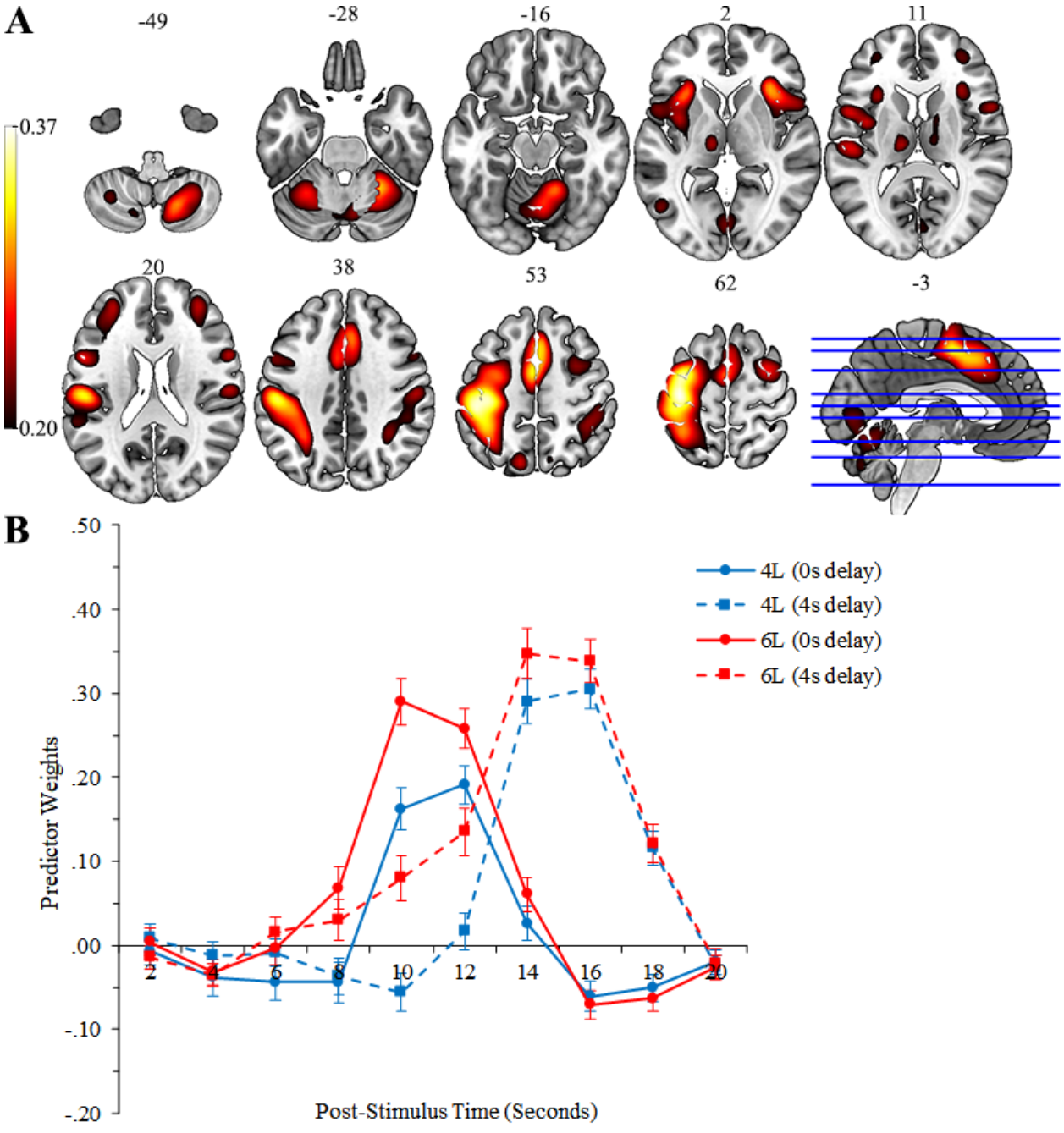

Figure 4.2. WM task fMRI-CPCA, response/attention network (component 1): Estimated HDRs illustrating delay × time interaction. Asterisks indicate significant delay × time contrast between adjacent time bins. ** = $p < .01$; *** = $p < .001$.

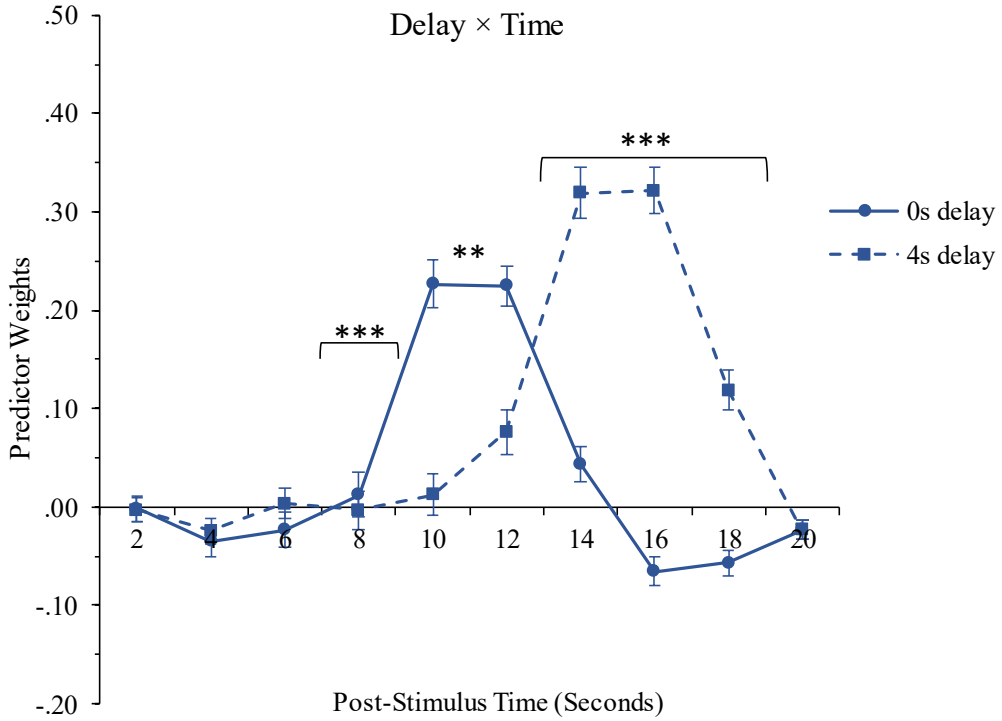

Figure 4.3. WM task fMRI-CPCA, visual attention network (component 2): Anatomical and temporal characteristics. **A (top)**: dominant 10% of loadings (red/yellow = positive loadings, min = 0.12, max = 0.62; blue/green = negative loadings, min = -0.16, max = -0.12). Images are displayed in neurological orientation (left is left) with MNI coordinates. **B (bottom)**: predictor weights plotted over post-stimulus time for each task condition. 4L = 4 letters; 6L = 6 letters.

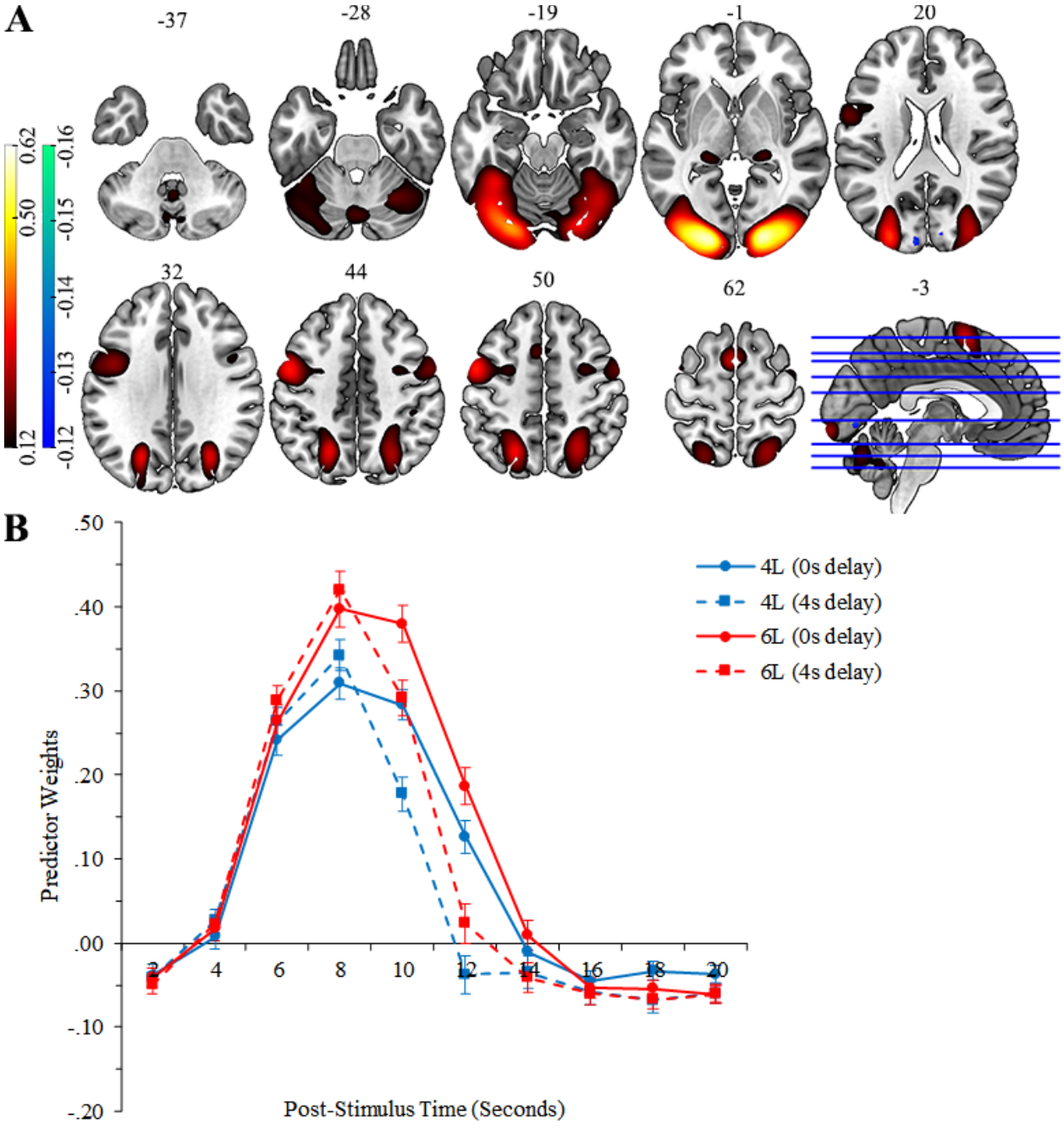

Figure 4.4. WM task fMRI-CPCA, visual attention network (component 2): Estimated HDRs illustrating delay × time interaction. Asterisks indicate significant delay × time contrast between adjacent time bins. * = $p < .05$; *** = $p < .001$.

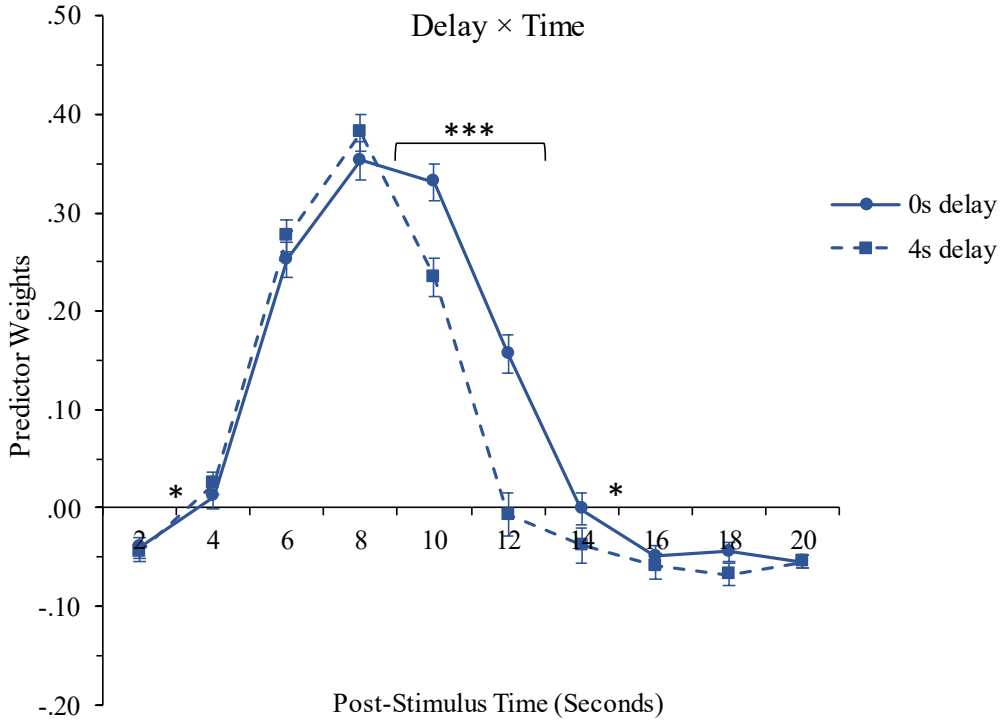

Figure 4.5. WM task fMRI-CPCA, default mode network (DMN, component 3): Anatomical and temporal characteristics. **A (top)**: dominant 10% of loadings (red/yellow = positive loadings, min = 0.15, max = 0.18; blue/green = negative loadings, min = -0.25, max = -0.15). Images are displayed in neurological orientation (left is left) with MNI coordinates. **B (bottom)**: predictor weights plotted over post-stimulus time for each task condition. Y axis has been reversed (negative up, positive down) to facilitate interpretation (i.e., values above X axis reflect activation of blue/green voxels, and values below X axis reflect deactivation of blue/green voxels). 4L = 4 letters; 6L = 6 letters.

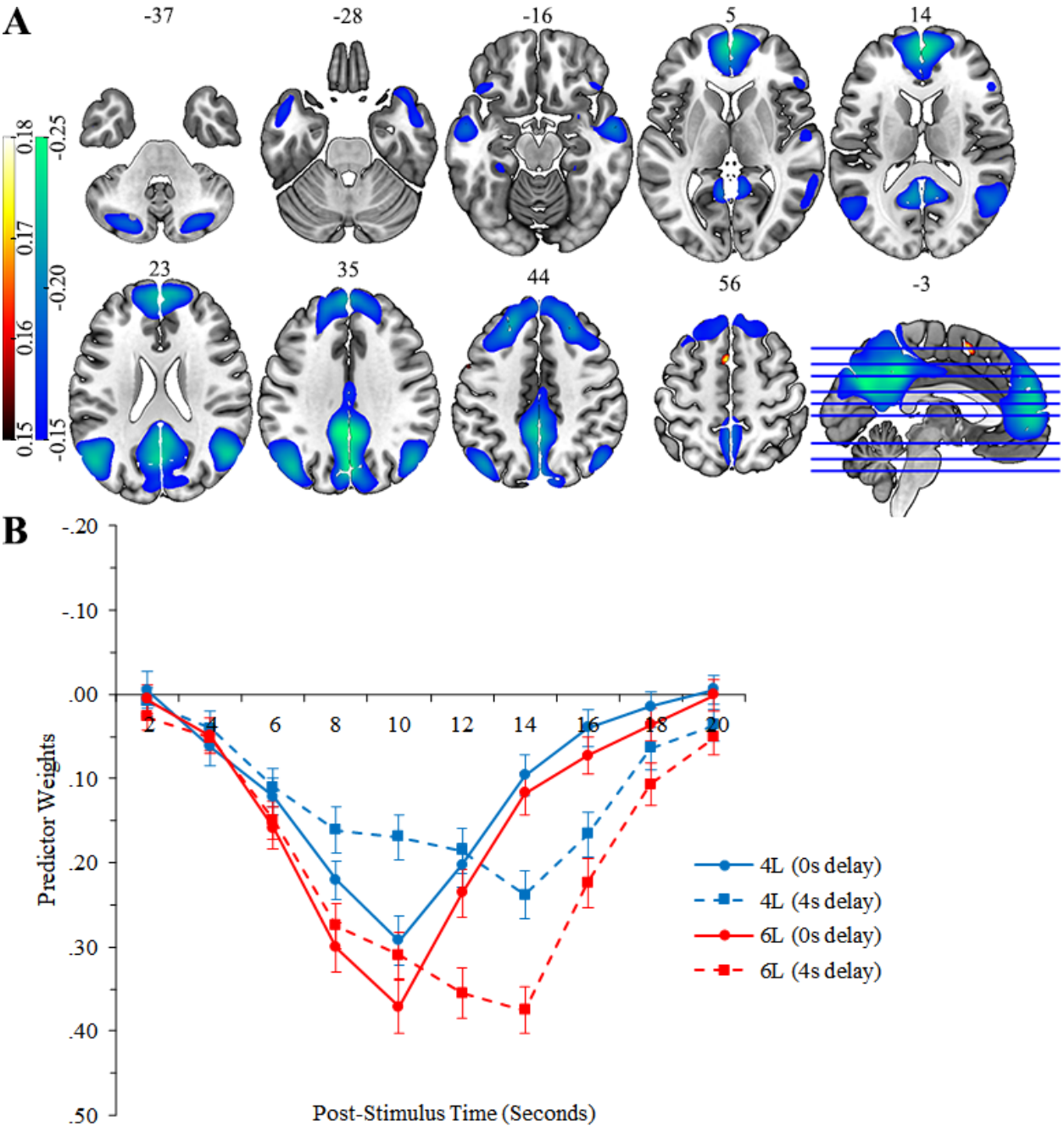

Figure 4.6. WM task fMRI-CPCA, default mode network (DMN, component 3): Graphs illustrating effects of cognitive load and delay length. **A (top)**: mean predictor weights illustrating significant load × delay interaction. **B (bottom)**: predictor weights averaged over load to illustrate delay × time interaction (asterisks indicate significant delay × time contrasts between adjacent time bins). Y axes are reversed (negative up, positive down) to facilitate interpretation (i.e., values above X axis reflect activation, and values below X axis reflect deactivation). * = $p < .05$; ** = $p < .01$; *** = $p < .001$.

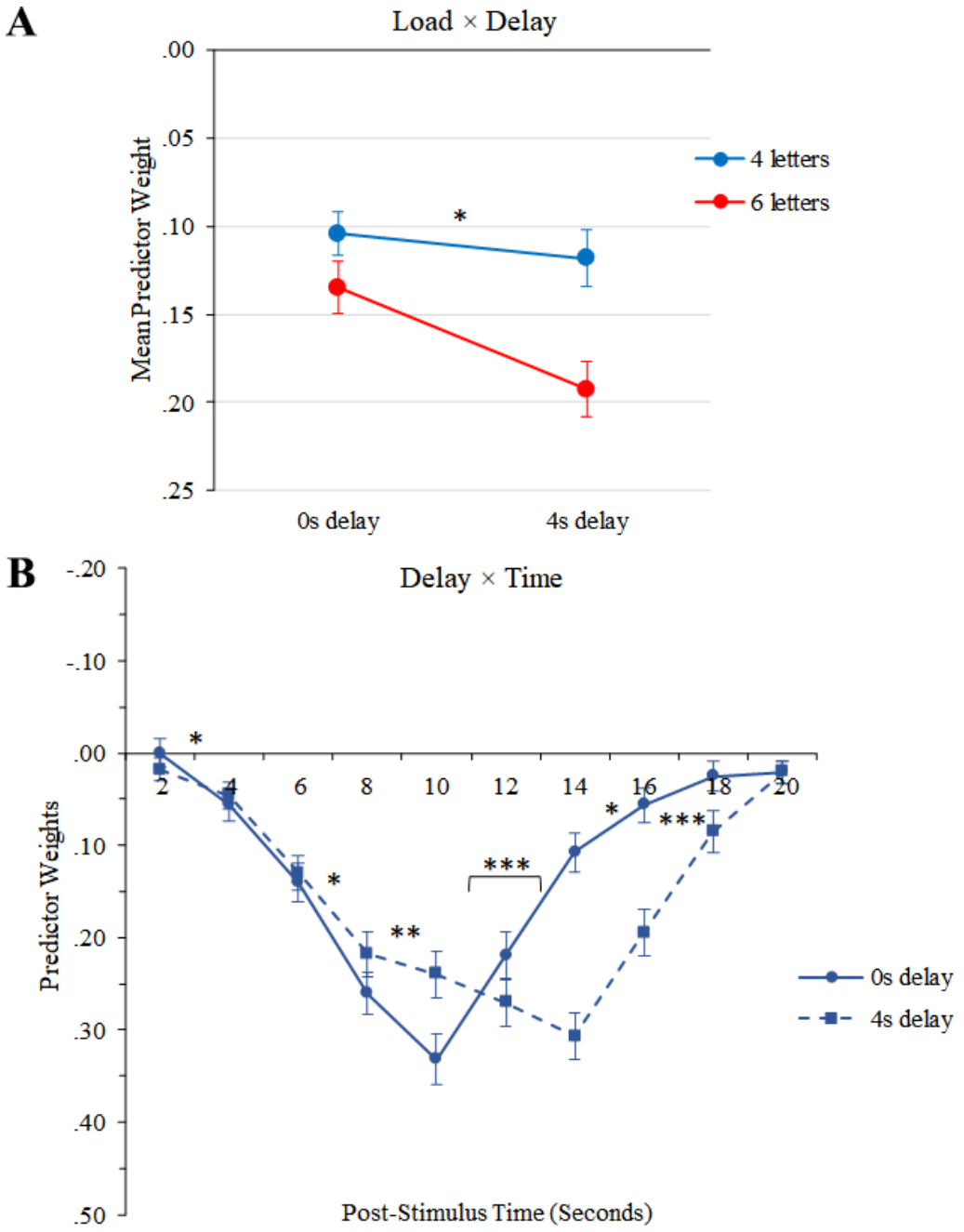

Figure 4.7. SCAP task performance results, graphs illustrating effects of cognitive load and delay length. **A (top)**: mean percentage of correct responses for each load level. **B (bottom)**: mean percentage of correct responses for each delay length. Asterisks indicate significant paired t-tests between adjacent conditions. * = $p < .05$; *** = $p < .001$.

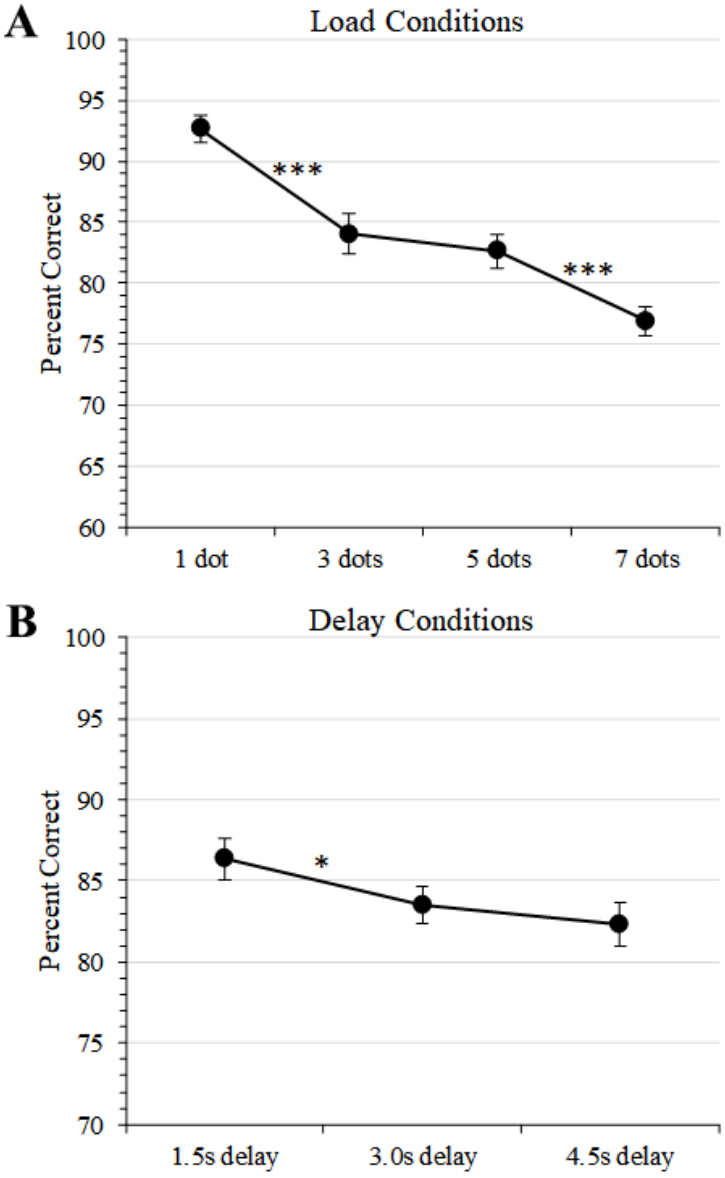

Figure 4.8. SCAP task fMRI-CPCA, external attention network (component 1): Anatomical and temporal characteristics. **A (top)**: dominant 10% of loadings (red/yellow = positive loadings, min = 0.39, max = 0.59; no negative loadings above threshold). Images are displayed in neurological orientation (left is left) with MNI coordinates. **B (bottom)**: predictor weights plotted over post-stimulus time (each load level displayed on a separate graph).

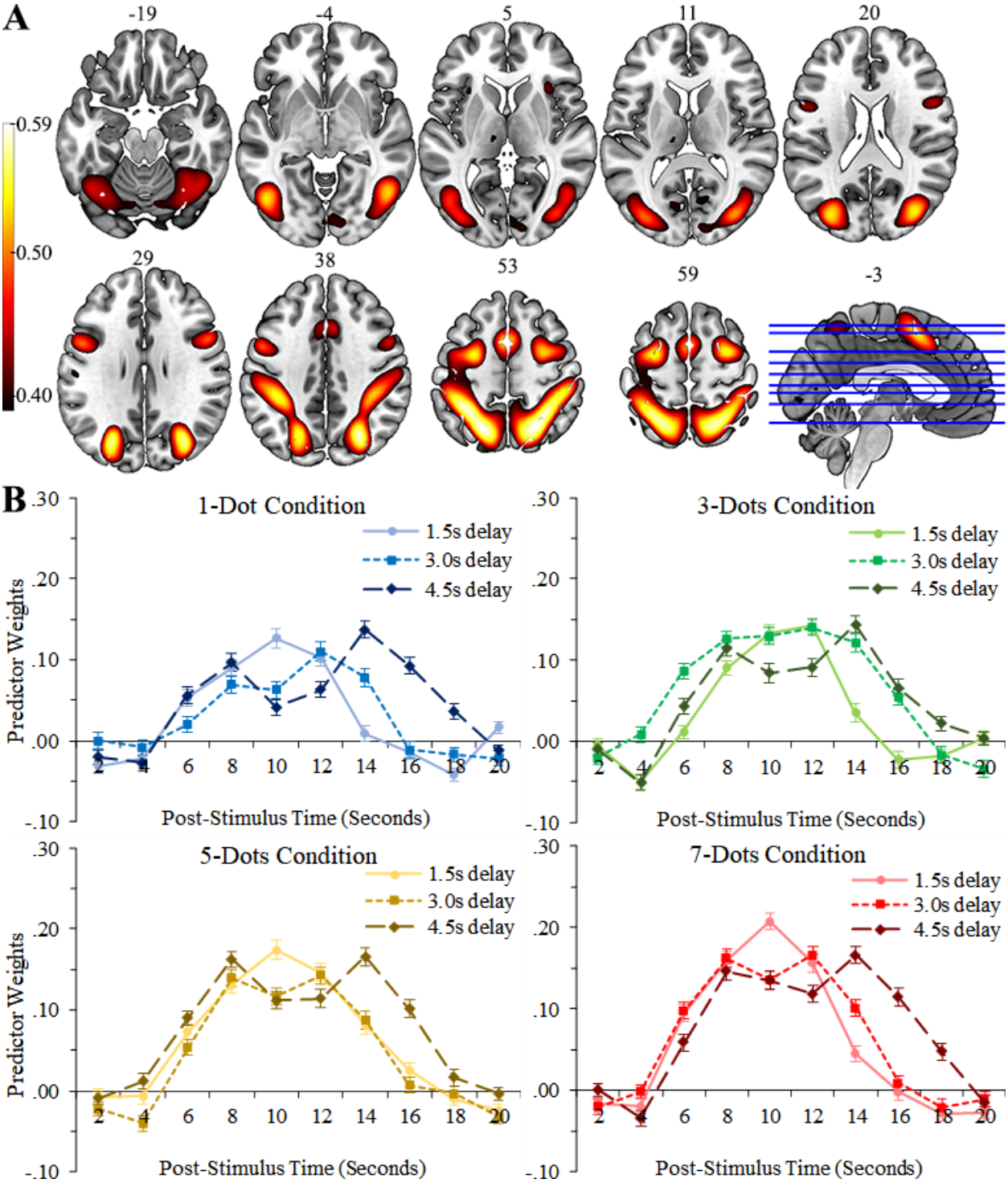

Figure 4.9. SCAP task fMRI-CPCA, external attention network (component 1): Graphs illustrating effects of cognitive load and delay length. **A (top left)**: mean predictor weights illustrating main effect of load (asterisks indicate significant paired t-tests between adjacent load conditions). **B (top right)**: mean predictor weights illustrating main effect of delay (asterisks indicate significant paired t-tests between adjacent delay conditions). **C (bottom)**: predictor weights averaged over load to illustrate delay × time interaction (asterisks indicate significant delay × time contrasts between adjacent time bins; contrast with greatest effect size is flagged). a = linear effect of delay; b = quadratic effect of delay; * = $p < .05$; ** = $p < .01$; *** = $p < .001$.

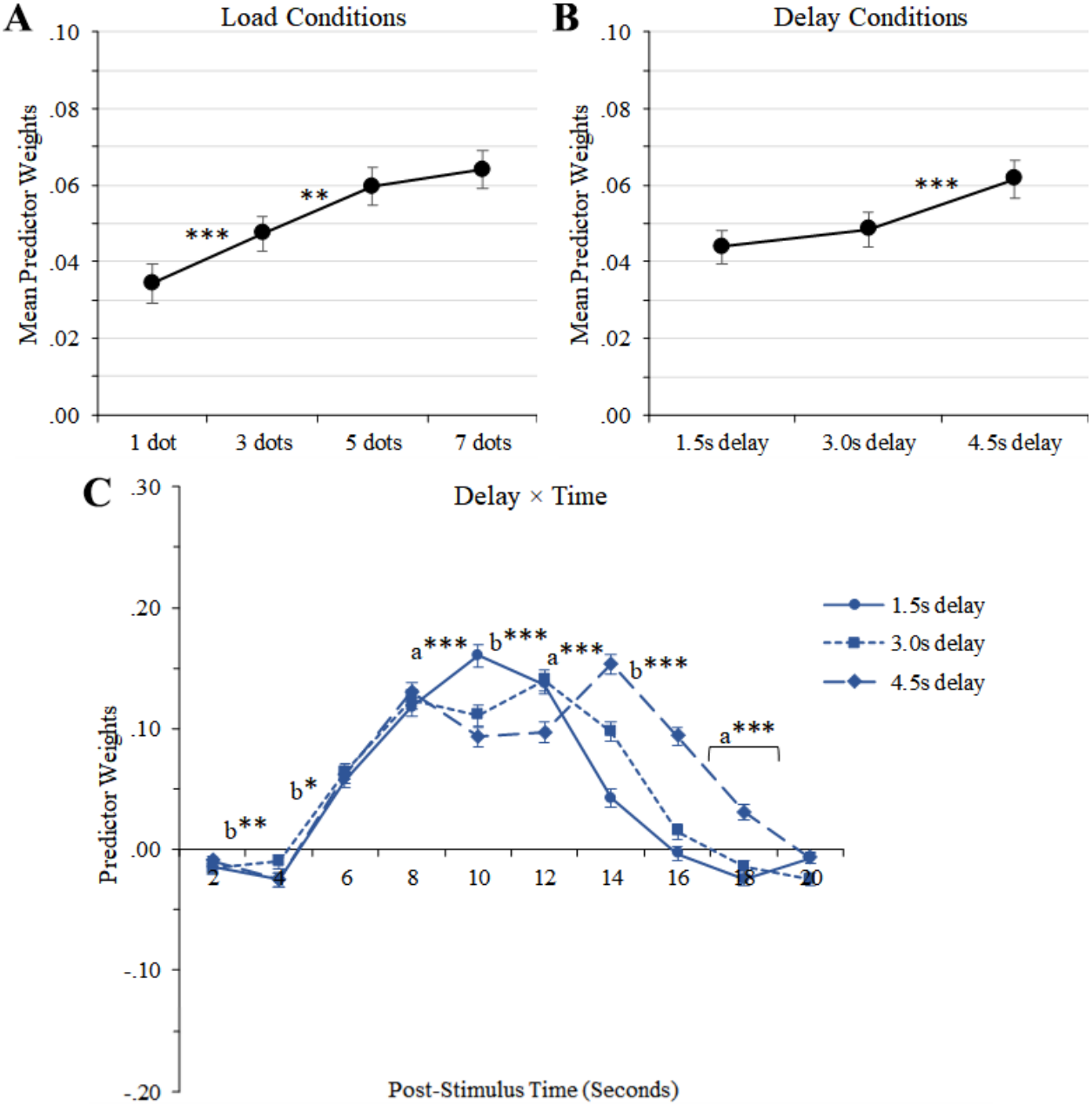

Figure 4.10. SCAP task fMRI-CPCA, DMN (component 2): Anatomical and temporal characteristics. **A (top)**: dominant 10% of loadings (blue/green = negative loadings, min = -0.50, max = -0.33; no positive loadings above threshold). Images are displayed in neurological orientation (left is left) with MNI coordinates. **B (bottom)**: predictor weights plotted over post-stimulus time (each load level displayed on a separate graph). Y axes are reversed to facilitate interpretation (i.e., values above X axis reflect activation, and values below X axis reflect deactivation).

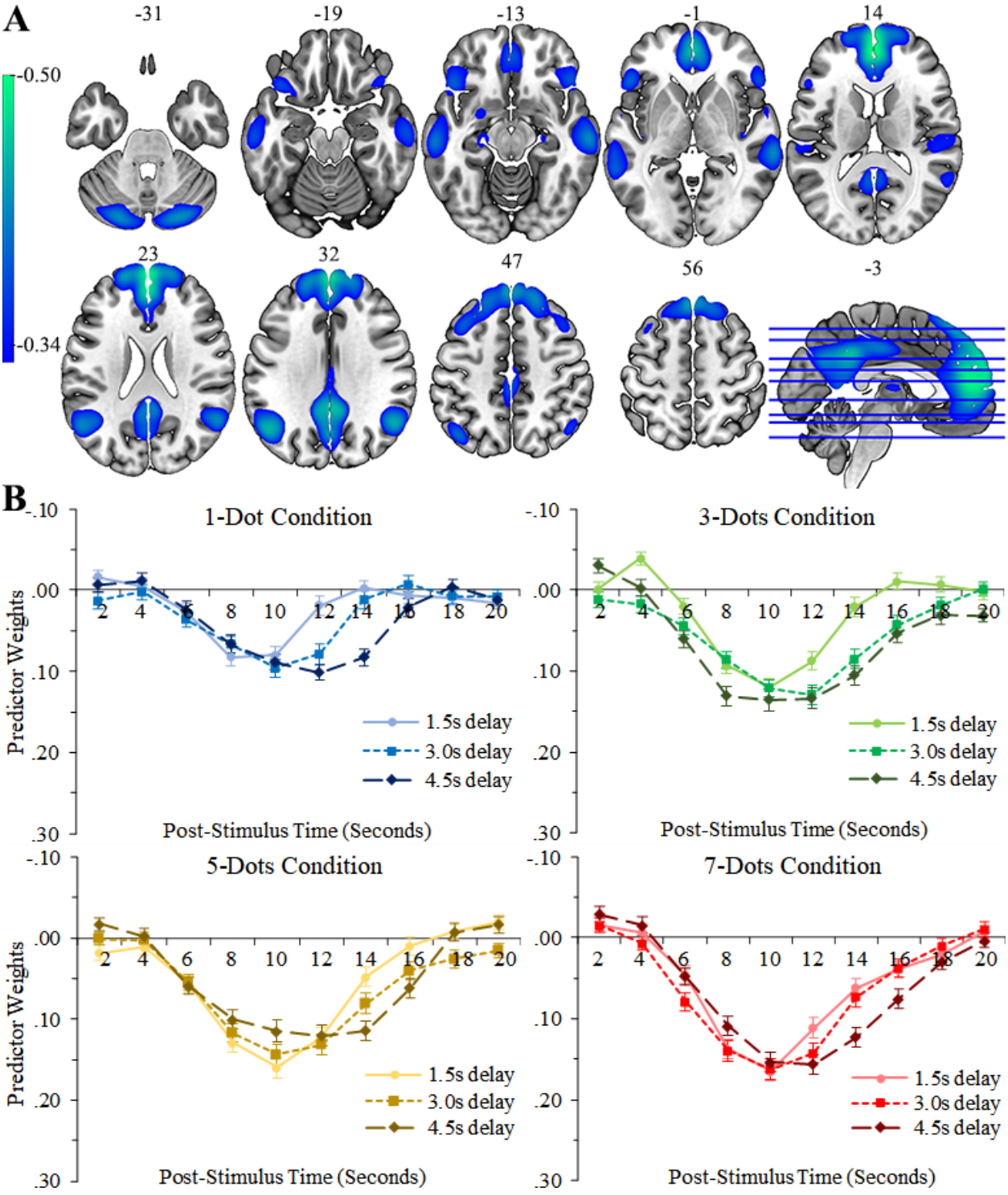

Figure 4.11. SCAP task fMRI-CPCA, default mode network (DMN, component 2): Graphs illustrating effects of cognitive load and delay length. Y axes are reversed (negative up, positive down) to facilitate interpretation (i.e., values above X axis reflect activation, and values below X axis reflect deactivation). **A (top left)**: mean predictor weights illustrating significant main effect of load (asterisks indicate significant paired t-tests between adjacent load conditions). **B (top right)**: mean predictor weights illustrating significant main effect of delay (asterisks indicate significant paired t-tests between adjacent delay conditions). **C (bottom)**: predictor weights averaged over load to illustrate delay × time interaction (asterisks indicate significant delay × time contrasts between adjacent time bins; contrast with greatest effect size is flagged). a = linear effect of delay; b = quadratic effect of delay; *** = $p < .001$.

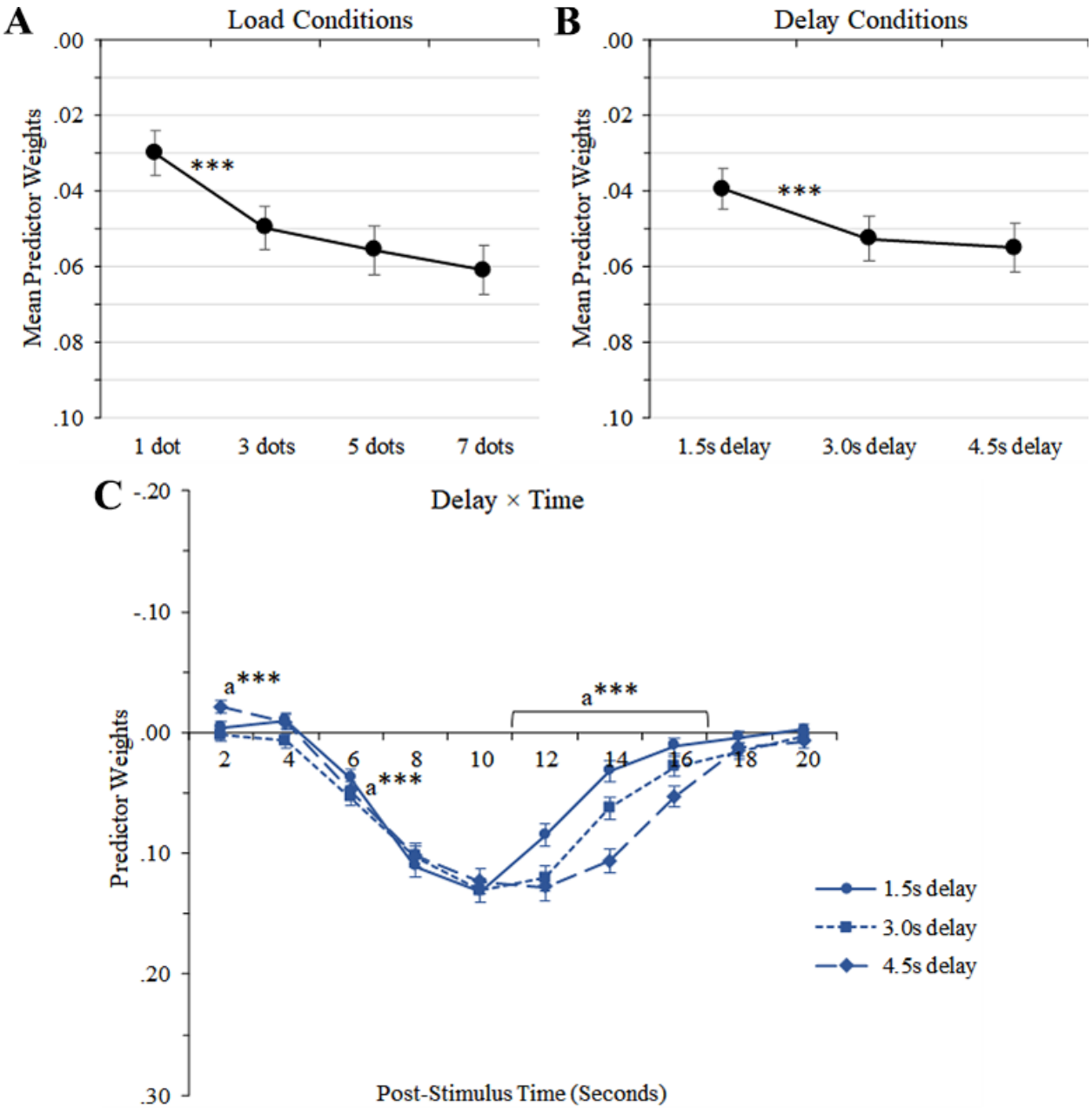

Figure 4.12. TSI task fMRI-CPCA, DMN/occipital network (component 1): Anatomical and temporal characteristics. **A (top)**: dominant 10% of loadings (blue/green = negative loadings, min = -0.34, max = -0.20; no positive loadings above threshold). Images are displayed in neurological orientation (left is left) with MNI coordinates. **B (bottom)**: predictor weights plotted over post-stimulus time for each word-reading condition. Y axis is reversed to facilitate interpretation (i.e., values above X axis reflect activation, and values below X axis reflect deactivation). cn = task-switch from neutral colour-naming block; ci = task-switch from incongruent colour-naming block; WN = neutral word-reading stimulus; WI = incongruent word-reading stimulus.

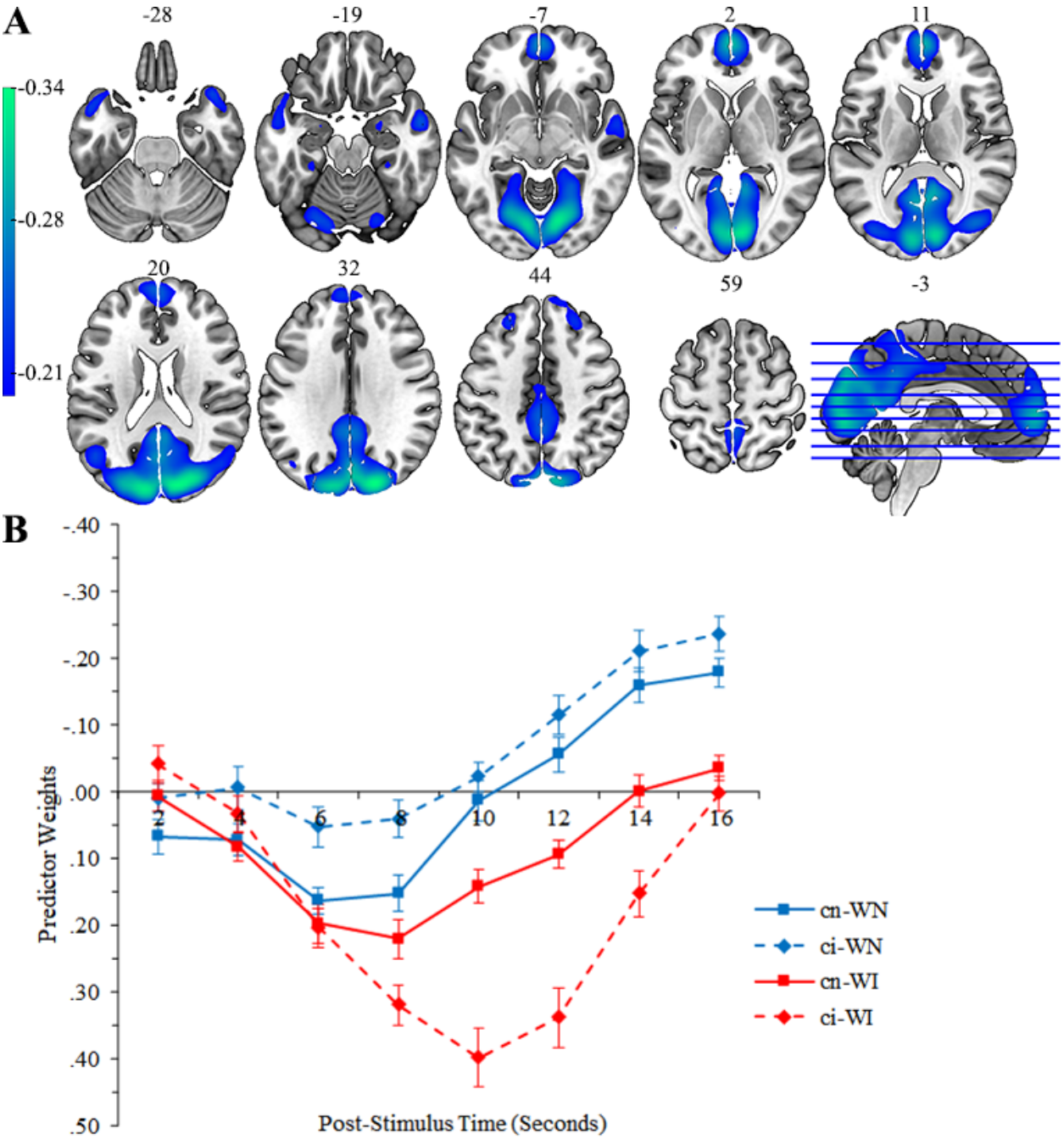

Figure 4.13. TSI task fMRI-CPCA, DMN/occipital network (component 1): Graphs illustrating effects of stimulus congruency and task-switch condition. Y axes are reversed (negative up, positive down) to facilitate interpretation (i.e., values above X axis reflect activation, and values below X axis reflect deactivation). **A (top left)**: predictor weights averaged over task-switch to illustrate congruency × time interaction (asterisks indicate significant congruency × time contrasts between adjacent time bins). **B (top right)**: predictor weights averaged over congruency to illustrate task-switch × time interaction (asterisks indicate significant task-switch × time contrasts between adjacent time bins). **C (bottom)**: mean predictor weights illustrating significant congruency × task-switch interaction. WN = neutral word-reading stimulus; WI = incongruent word-reading stimulus; cn = task-switch from neutral colour-naming block; ci = task-switch from incongruent colour-naming block; * = $p < .05$; ** = $p < .01$; *** = $p < .001$.

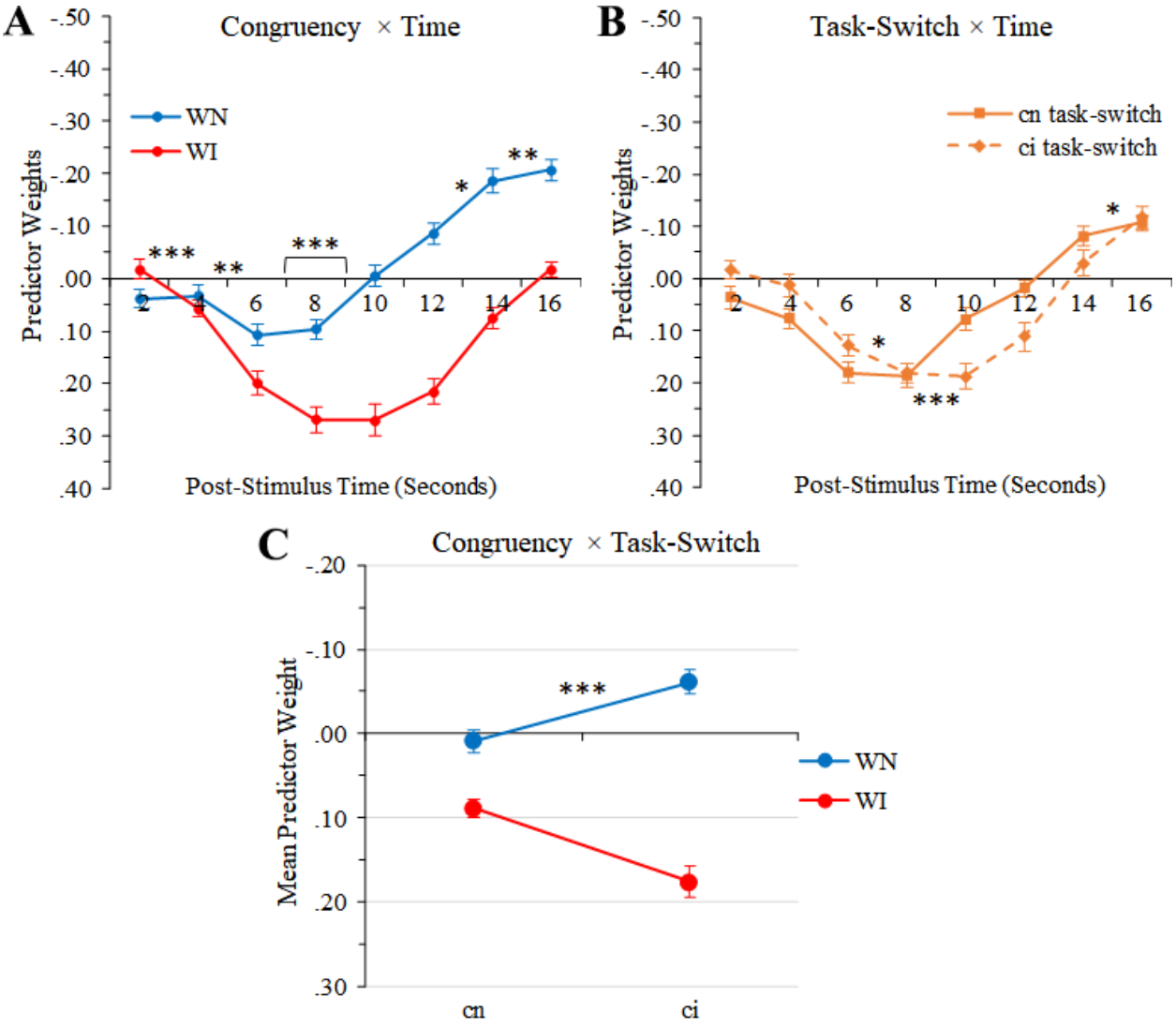

Figure 4.14. TSI task fMRI-CPCA, response network (component 2): Anatomical and temporal characteristics. **A (top)**: dominant 10% of loadings (red/yellow = positive loadings, min = 0.19, max = 0.32; no negative loadings above threshold). Images are displayed in neurological orientation (left is left) with MNI coordinates. **B (bottom)**: predictor weights for each word-reading condition plotted over post-stimulus time. cn = task-switch from neutral colour-naming block; ci = task-switch from incongruent colour-naming block; WN = neutral word-reading stimulus; WI = incongruent word-reading stimulus.

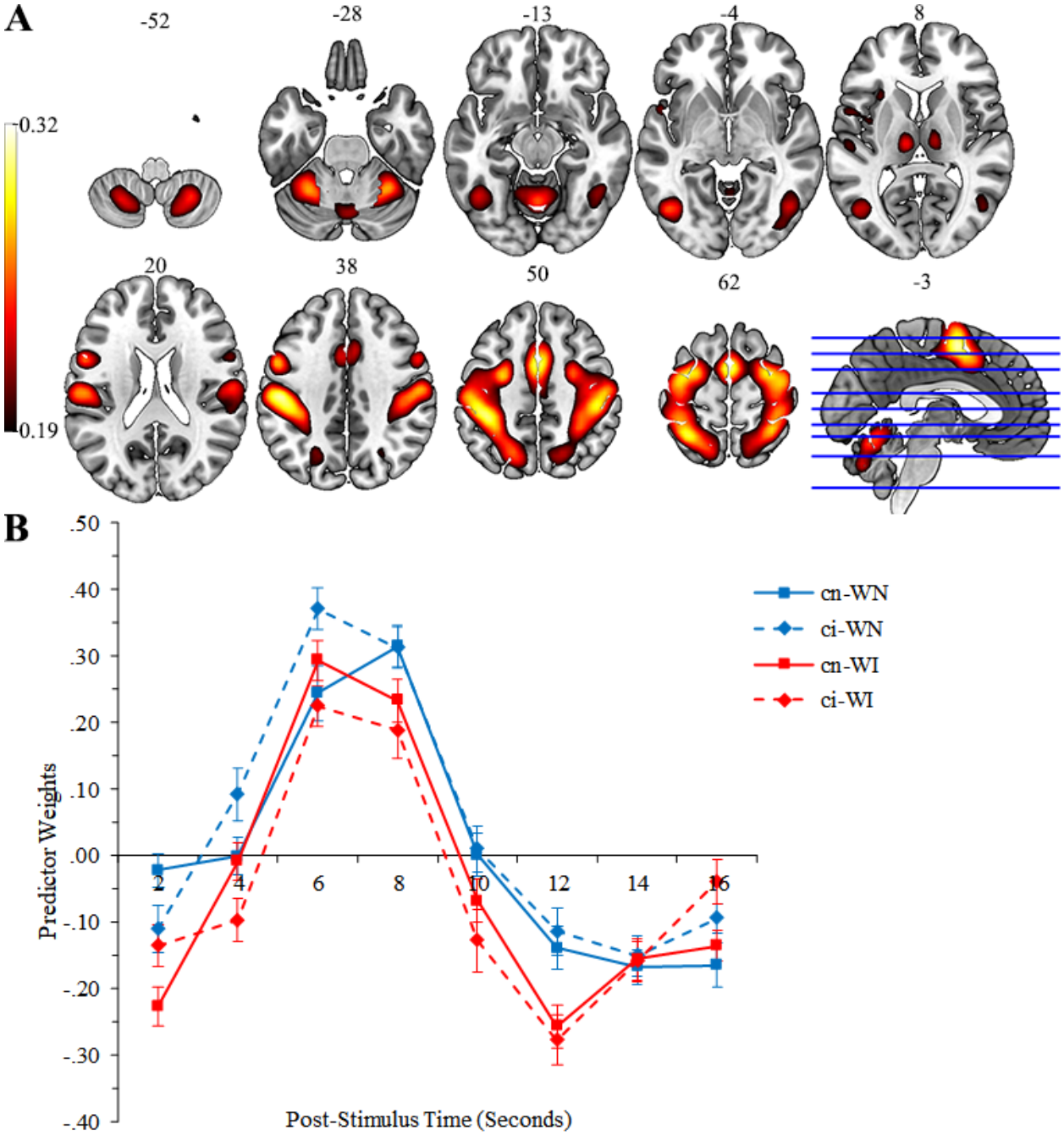

Figure 4.15. TSI task fMRI-CPCA, response network (component 2): Estimated HDRs illustrating congruency × time interaction. Asterisks indicate significant congruency × time contrasts between adjacent time bins. WN = neutral word-reading stimulus; WI = incongruent word-reading stimulus; *** = $p < .001$.

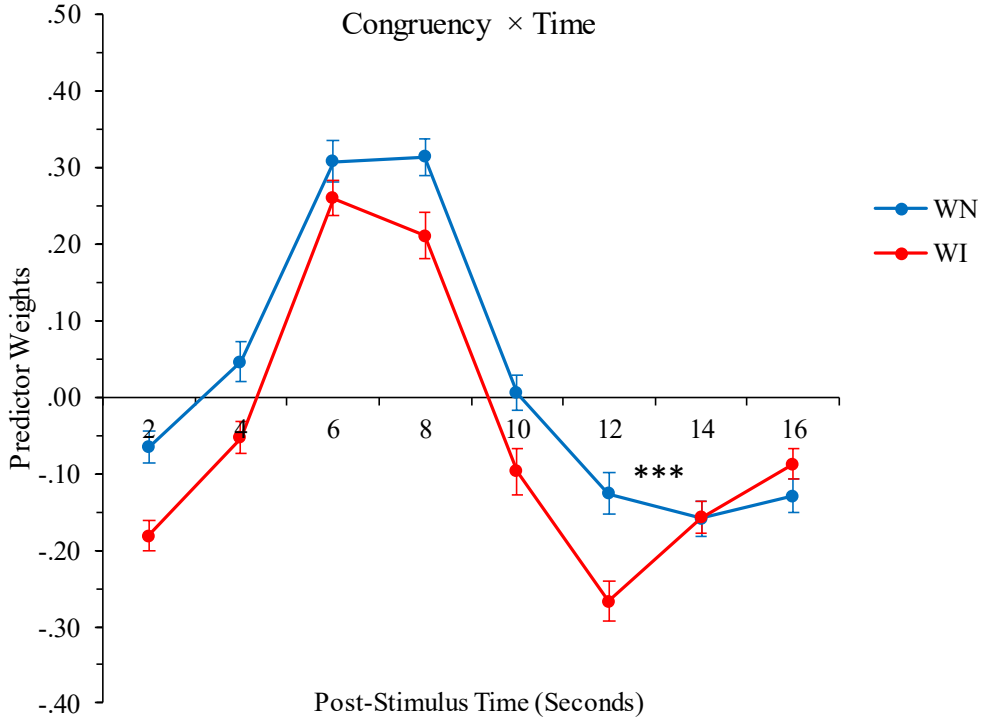

Figure 4.16. TSI task fMRI-CPCA, evaluation network (component 3): Anatomical and temporal characteristics. **A (top)**: dominant 10% of loadings (red/yellow = positive loadings, min = 0.16, max = 0.26; no negative loadings above threshold). Images are displayed in neurological orientation (left is left) with MNI coordinates. **B (bottom)**: predictor weights for each word-reading condition plotted over post-stimulus time. cn = task-switch from neutral colour-naming block; ci = task-switch from incongruent colour-naming block; WN = neutral word-reading stimulus; WI = incongruent word-reading stimulus.

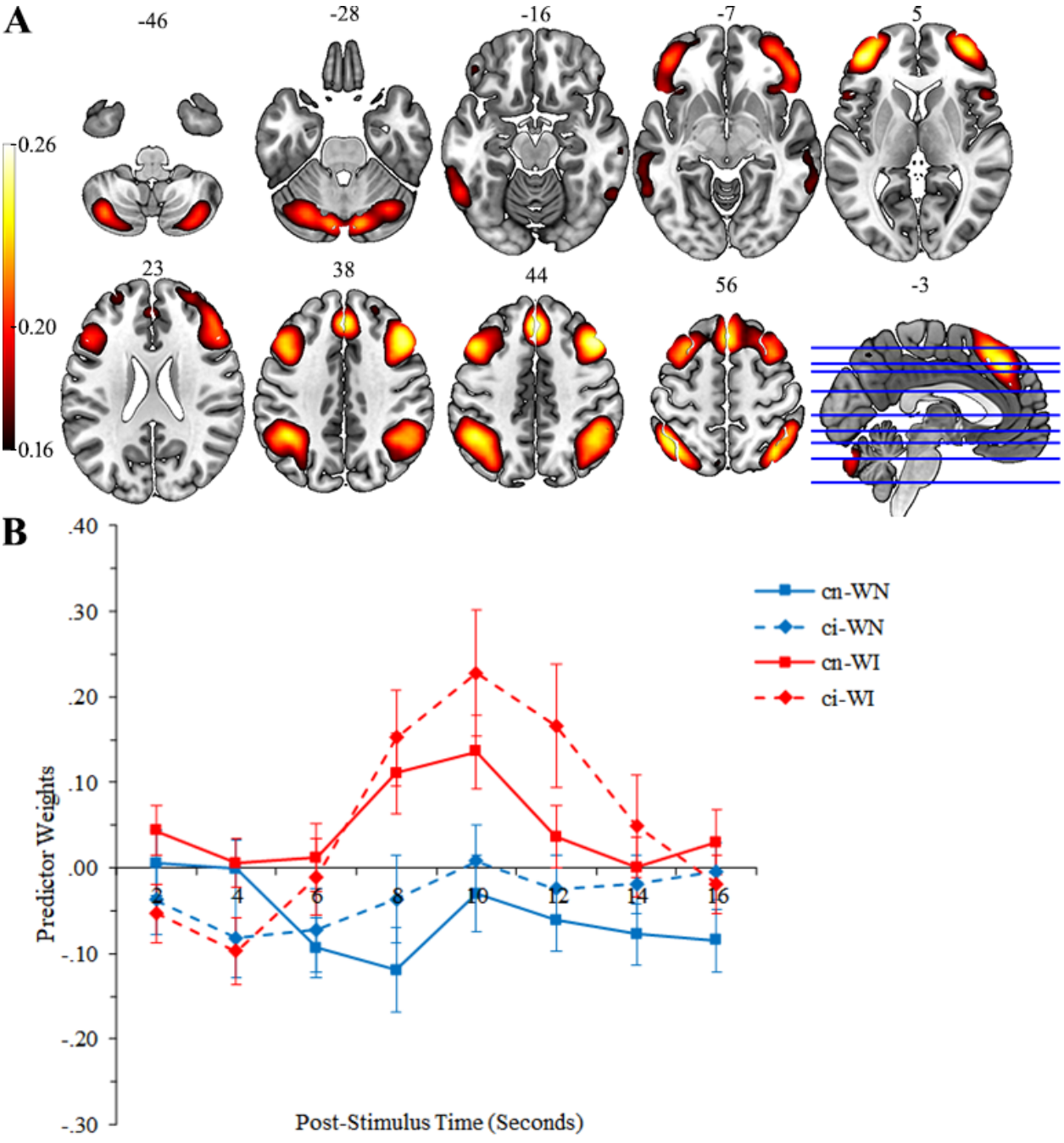

Figure 4.17. TSI task fMRI-CPCA, evaluation network (component 3): Estimated HDRs illustrating congruency × time interaction. Asterisks indicate significant congruency × time contrasts between adjacent time bins. WN = neutral word-reading stimulus; WI = incongruent word-reading stimulus; ** = $p < .01$; *** = $p < .001$.

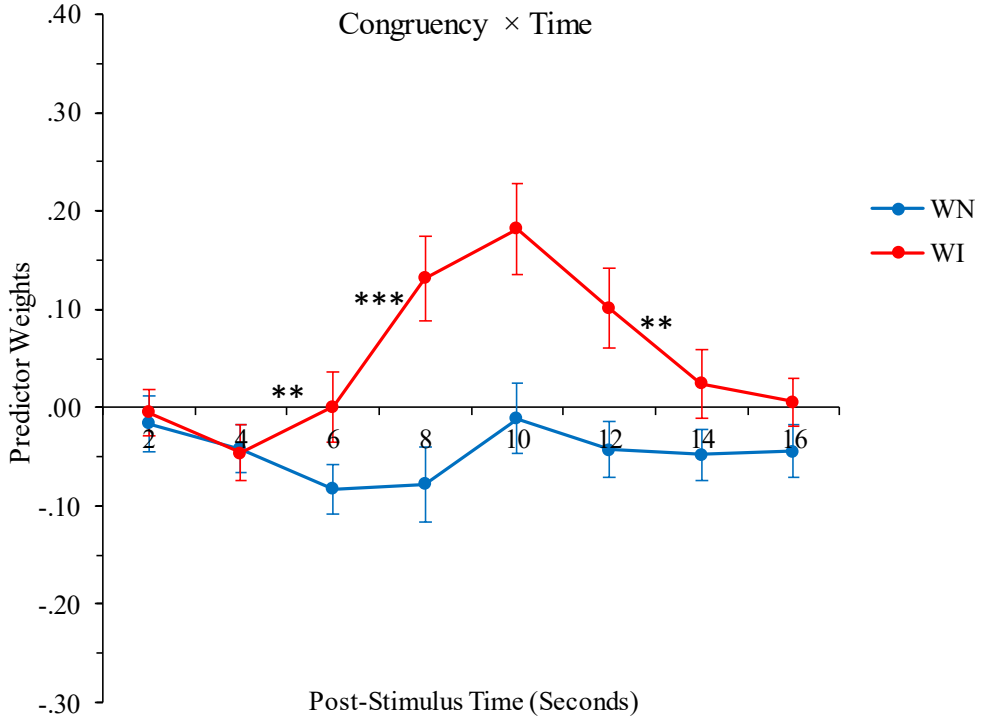

Figure 4.18. TGT task fMRI-CPCA, language network (component 1): Anatomical and temporal characteristics. **A (top)**: dominant 10% of loadings (red/yellow = positive loadings, min = 0.15, max = 0.35; no negative loadings above threshold). Images are displayed in neurological orientation (left is left) with MNI coordinates. **B (bottom)**: predictor weights plotted over post-stimulus time for each task condition. Asterisks indicate significant condition × time contrasts between adjacent time bins. * = $p < .05$; ** = $p < .01$; *** = $p < .001$.

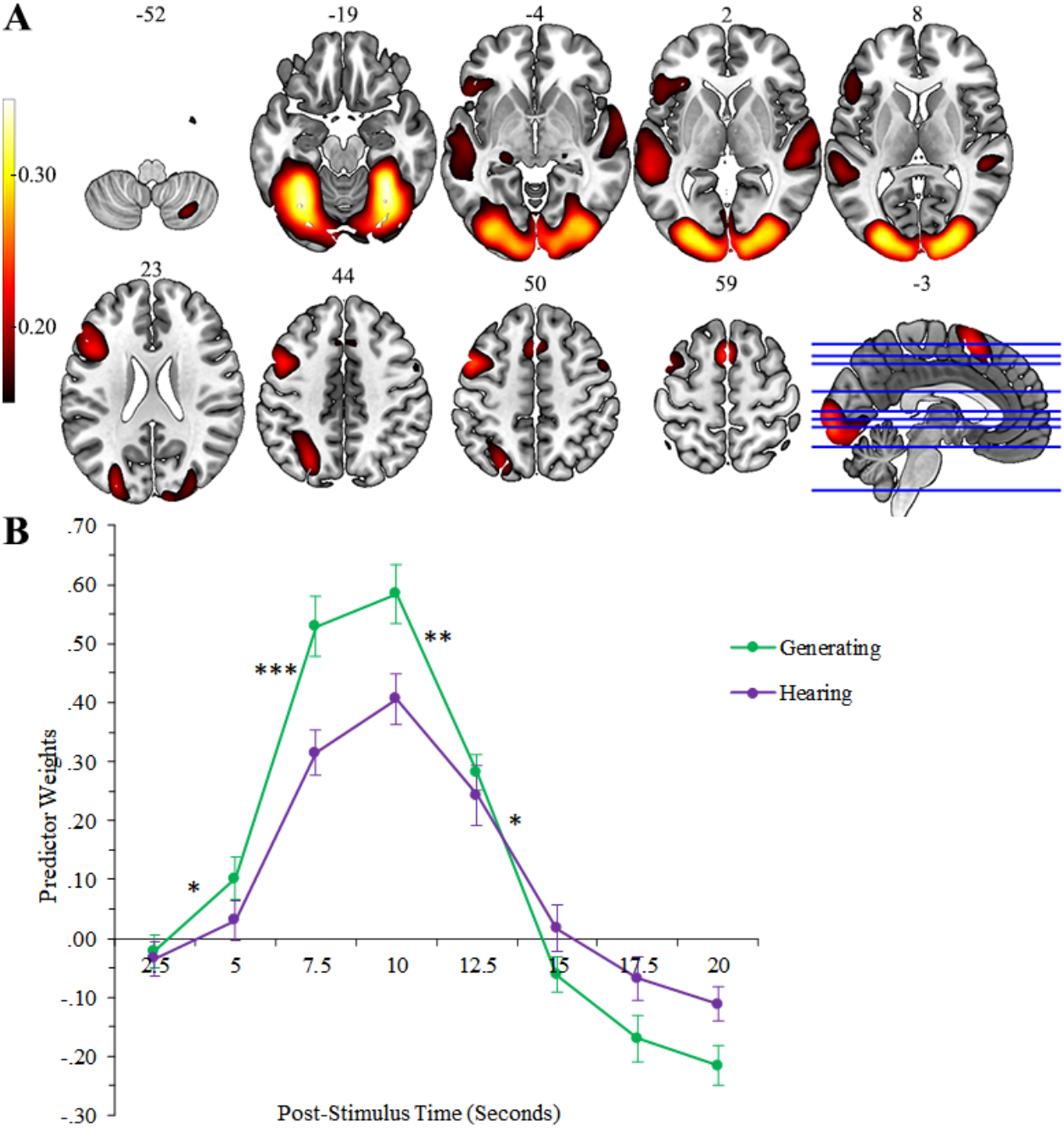

Figure 4.19. TGT task fMRI-CPCA, posterior-medial DMN (component 2): Anatomical and temporal characteristics. **A (top)**: dominant 10% of loadings (blue/green = negative loadings, min = -0.20, max = -0.12; no positive loadings above threshold). Images are displayed in neurological orientation (left is left) with MNI coordinates. **B (bottom)**: predictor weights for each task condition plotted over post-stimulus time. Y axis is reversed (negative up, positive down) to facilitate interpretation (i.e., values above X axis reflect activation, and values below X axis reflect deactivation).

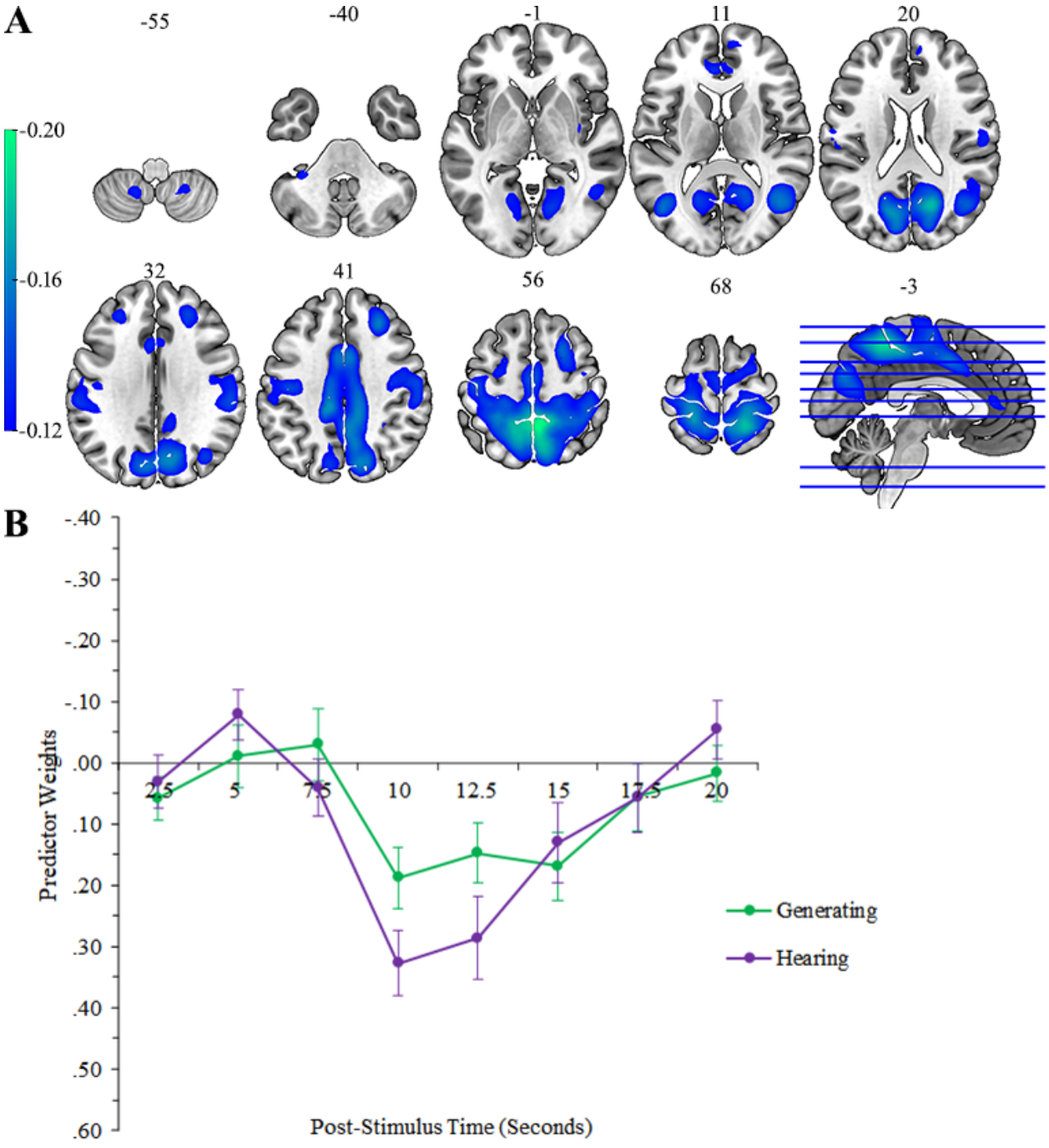

Figure 4.20. TGT task fMRI-CPCA, anterior/posterior-lateral DMN (component 3): Anatomical and temporal characteristics. **A (top)**: dominant 10% of loadings (red/yellow = positive loadings, min = 0.10, max = 0.12; blue/green = negative loadings, min = -0.15, max = -0.10). Images are displayed in neurological orientation (left is left) with MNI coordinates. **B (bottom)**: predictor weights for each task condition plotted over post-stimulus time. Y axis is reversed (negative up, positive down) to facilitate interpretation (i.e., values above X axis reflect activation in blue/green voxels, and values below X axis reflect deactivation in blue/green voxels).

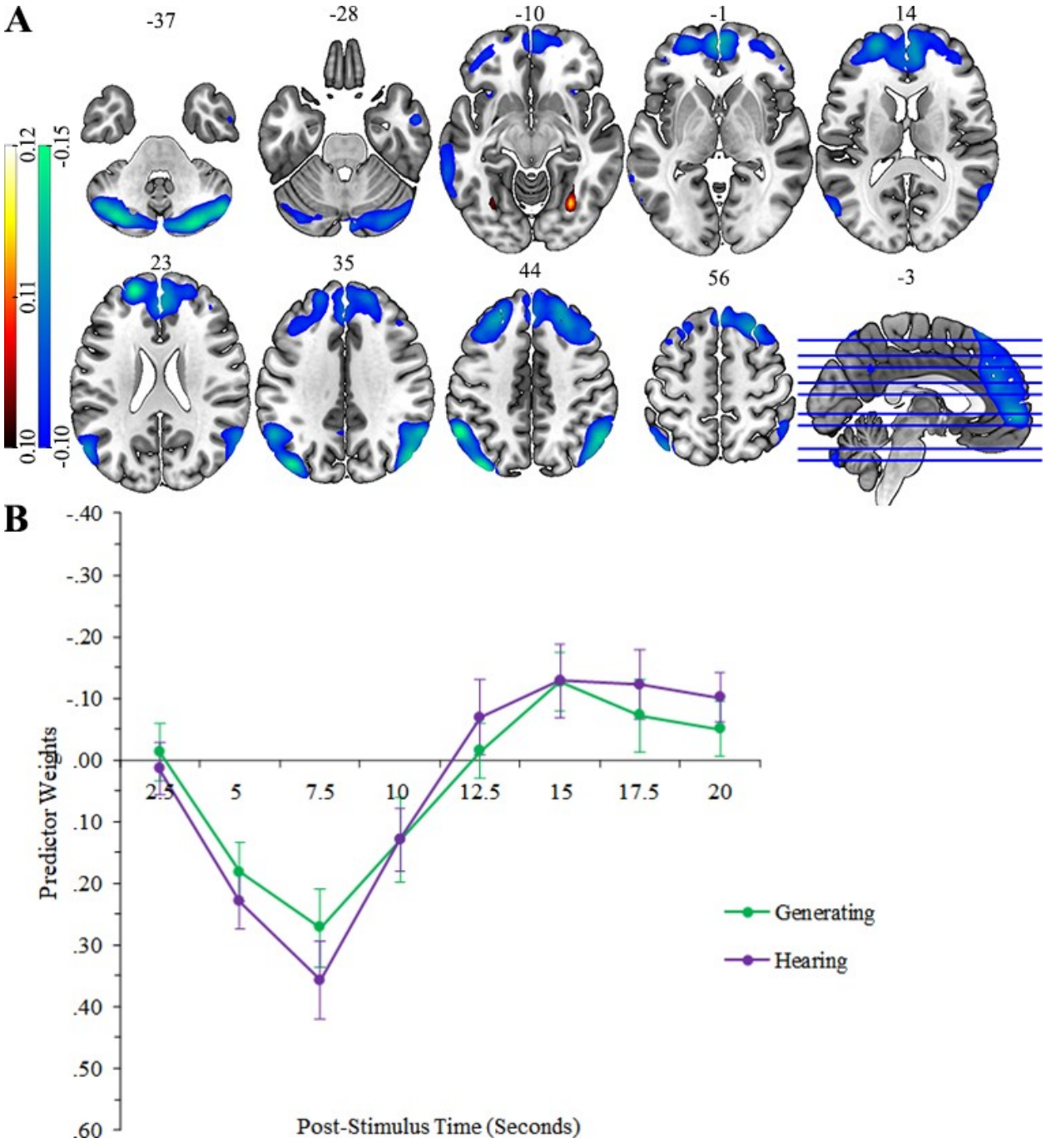

Figure 4.21. TGT task fMRI-CPCA, auditory network (component 4): Anatomical and temporal characteristics. **A (top)**: dominant 10% of loadings (red/yellow = positive loadings, min = 0.06, max = 0.39; blue/green = negative loadings, min = -0.07, max = -0.06). Images are displayed in neurological orientation (left is left) with MNI coordinates. **B (bottom)**: predictor weights for each task condition plotted over post-stimulus time. Asterisks indicate significant condition × time contrasts between adjacent time bins. *** = $p < .001$.

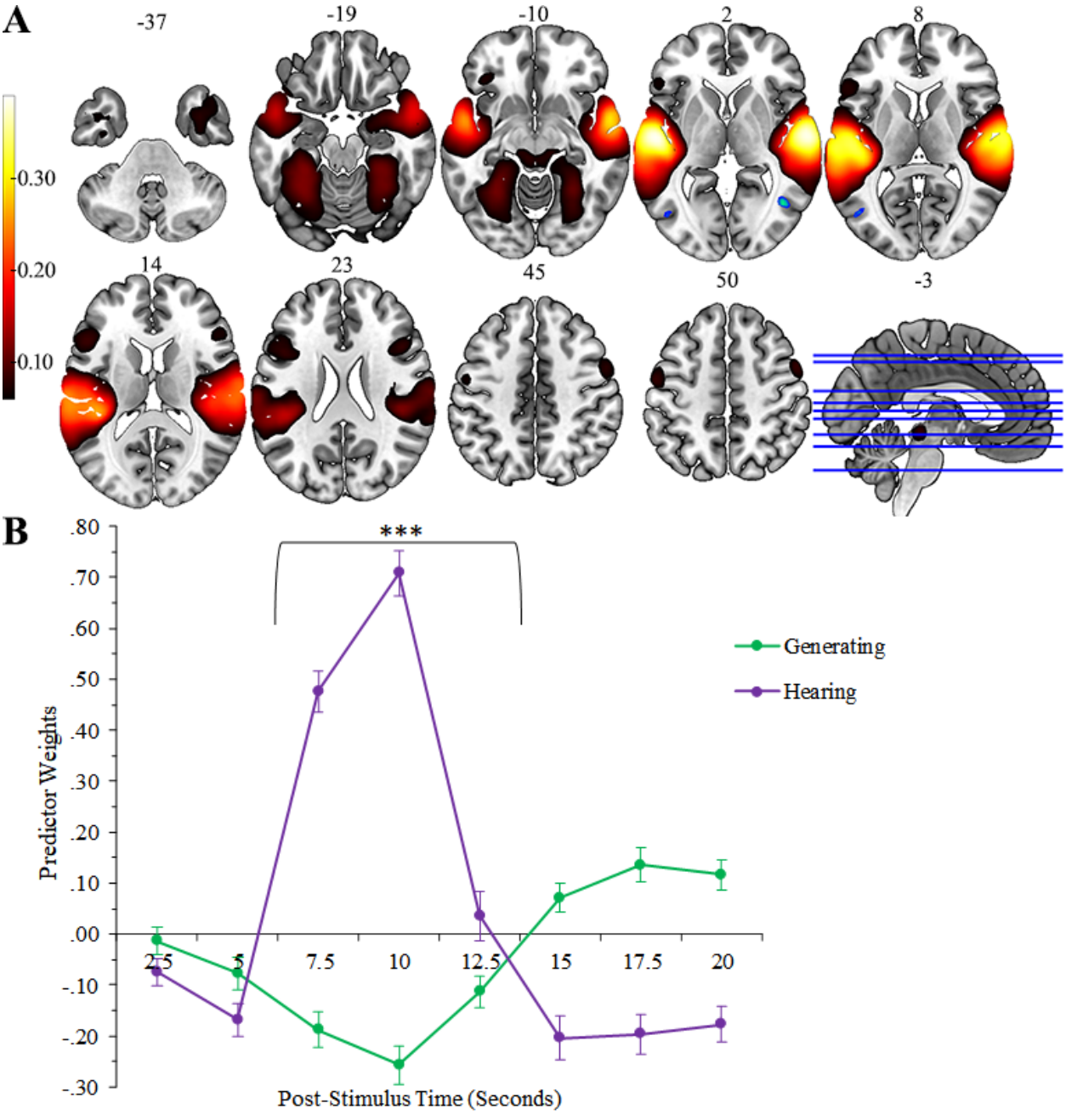

Chapter 5: Identifying Networks Underlying Working Memory Deficits in Schizophrenia Using Multi-Experiment fMRI-CPCA

5.1. Aims and Hypotheses

The overarching goal of this work was to characterize task-induced functional brain networks that may underlie WM deficits in schizophrenia. As demonstrated in Chapter 3, multi-experiment fMRI-CPCA may produce a more refined understanding of networks engaged during a cognitive task, and allows for the direct evaluation of the extent to which a given network is engaged across different tasks. However, limitations in interpreting the functions of networks observed in the verbal WM-TGT design were noted, which could be addressed in part with the addition of a visuospatial WM task and an externally-oriented, set-switching Stroop task. Each of these four tasks were analysed in the previous chapter. The aim of the following study was to characterize the functions of task-related networks simultaneously derived from all four tasks of interest, their relationships with task performance, and the nature of potentially suboptimal activity in schizophrenia patients.

Based on the results of the single-task fMRI-CPCAs (Chapter 4) and the preliminary 2-task fMRI-CPCA with the WM and TGT tasks (Chapter 3), it was hypothesized that networks underlying motor responses (dominated by activity in somatomotor cortex), internally-oriented attention (including DLPFC, dorsal anterior/paracingulate gyrus, and intraparietal sulcus), and visual attention (including SMA, lateral occipital activation extending dorsally into posterior parietal cortex, and thalamus) as well as DMN deactivation would emerge to varying degrees across all tasks. More basic visual and auditory sensory networks were expected to separate out as well, which was observed in the preliminary multi-experiment CPCA in Chapter 3, but the networks were not discussed in detail. The DMN sub-region networks observed in the TGT task

in the previous chapter (components 2 and 3) were not expected to emerge, as they did not emerge when the TGT data was combined only with the WM task, and neither the SCAP nor the TSI task exhibited decomposition of DMN regions either. Based on previous research suggesting a link between the DLPFC and cognitive deficits in schizophrenia (Barch & Ceaser, 2012; Glausier & Lewis, 2018; Potkin et al., 2009), suboptimal patterns of activity were expected to emerge in a network resembling the internal attention network (component 3 from the WM-TGT analysis in Chapter 3), reflecting cognitive inefficiency (i.e., hyperactivity at low levels of cognitive load) and/or hypoactivity as a whole compared with healthy controls.

5.2. Methods

5.2.1. Datasets

The WM task, SCAP task, TSI task, and the TGT task analysed in the previous chapter were entered into a 4-task fMRI-CPCA. The task paradigms and information regarding data acquisition and preprocessing for each dataset are detailed in Chapter 2 (Sections 2.2 and 2.3 for tasks and fMRI data information, respectively). Each dataset comprised a healthy control group and a schizophrenia patient group. Although the healthy control participants largely overlapped with those included in the respective single-task CPCAs reported in Chapter 4, in some cases they only comprised sub-samples as described below.

5.2.1.1. WM and TSI participants

Participants for the WM and TSI tasks were drawn from the same dataset, and so only participants who completed both the WM and TSI tasks were included in this analysis. This resulted in a sample size of 54 for both tasks (26 healthy controls and 28 schizophrenia patients). Demographic and neuropsychological information for these participants is presented in Table 5.1, including age, Quick estimated IQ (Mortimer & Bowen, 1999), scaled digit span score from

the Wechsler Adult Intelligence Scale subtest (WAIS; Wechsler, 2008), gender distribution, handedness as measured with the AHPQ (Annett, 1970), socioeconomic status (SES), educational achievement, and clinical information (patients only). The participant groups differed in age (mean age greater in patients; mean difference = 11.624 years, SEM = 2.56, $t(50.50) = 4.539$, $p < .001$), scaled digit span score (digit span higher in controls; mean difference = 1.319 digits, SEM = 0.607, $t(52) = 2.174$, $p = .034$), SES factor scores (mean factor score lower in controls; mean difference = 19.462, SEM = 4.674, $t(46) = 4.232$, $p < .001$), and years of education (mean years of education greater in controls; mean difference = 1.658 years, SEM = 0.603, $t(52) = 2.750$, $p = .008$).

The patient group consisted of outpatients with a diagnosis of schizophrenia or related disorder (i.e., schizoaffective or psychotic disorder not otherwise specified) being followed by a mental health care provider at the time of participation. Diagnoses were confirmed for each participant using the Mini International Neuropsychiatric Interview (MINI; Sheehan et al., 1998), which was also used to screen healthy controls for psychiatric illness. Symptom severity in patients was assessed with the Signs and Symptoms of Psychotic Illness semi-structured interview (SSPI; Liddle, Ngan, Duffield, & Warren, 2002). All patients reported taking antipsychotic medication at the time of testing, but one patient did not have up-to-date medication information. Of the 27 patients with complete medication information, 25 patients reported taking atypical antipsychotics (e.g., clozapine, olanzapine, risperidone) and 2 patients reported taking typical antipsychotic medication (e.g., loxapine, fluphenazine) as their primary medication. 9 patients reported taking an additional antipsychotic, 7 of which were atypical, and 2 of which were typical antipsychotics. 4 patients reported taking antianxiety medication, 9 reported taking an antidepressant, 3 reported taking lithium, 2 reported taking an anticonvulsant, and 5 reported taking an

anticholinergic as secondary medication. Further information regarding illness duration and severity is provided in Table 5.1.

5.2.1.2. SCAP participants

The original study from which these data were downloaded comprised a considerably greater number of healthy controls than schizophrenia patients (119 controls and 44 patients with useable fMRI data), and this dataset as a whole was larger than the other sample sizes for the tasks included in the present study (163 vs. 54-60). Therefore, to avoid over-representing the SCAP healthy controls in the component solution extracted from the combined datasets, as well as to reduce computing time, 44 controls were randomly selected from the larger sample included in Chapter 4, which had similar demographic characteristics to the full sample from which they were drawn (compare Tables 4.1 and 5.2). This resulted in the SCAP dataset comprising a sample size of $n = 88$ (44 healthy controls and 44 schizophrenia patients). Demographic and neuropsychological information for the controls and patients included in this chapter is presented in Table 5.2, including age, raw digit span score as measured with the Wechsler Memory Scale (WMS-IV; Wechsler, 2009), gender distribution, handedness as measured with the Edinburgh Handedness Inventory (Oldfield, 1971), educational achievement, and clinical information (patients only). The participant groups differed in age (mean age greater in patients; mean difference = 5.477 years, SEM = 1.912, $t(86) = 2.864$, $p = .005$), gender distribution (greater proportion of males in the patient group; $\chi^2(1) = 8.017$, $p = .005$), and years of education (mean years of education greater in controls; mean difference = 2.341 years, SEM = 0.383, $t(86) = 6.108$, $p < .001$), which was also the case when patients were compared with the full sample of healthy controls (all ps $< .05$). Participants also differed in WMS total raw digit span score

(higher digit span in controls; mean difference = 7.636 digits, SEM = 1.131, $t(86) = 6.753$, $p < .001$); however, standard scaled scores were not available for this dataset.

The patient group consisted of outpatients with a primary diagnosis of schizophrenia or schizoaffective disorder, based on the Structured Clinical Interview for DSM-IV Axis I Disorders (SCID-I; First, Spitzer, Gibbon, & Williams, 2002). Symptom severity was assessed with the Scale for the Assessment of Negative Symptoms (SANS; Andreasen, 1984a) and the Scale for the Assessment of Positive Symptoms (SAPS; Andreasen, 1984b). Medication information was not available for 4 patients. Of the 40 patients with available medication history, 39 reported taking at least one atypical antipsychotic. 4 patients reported taking both an atypical and a typical antipsychotic; no patients reported taking only a typical antipsychotic. 1 patient did not report taking any antipsychotic medication. 18 patients reported taking an antidepressant, 11 reported taking an anticonvulsant, 5 reported taking an anticholinergic, and 3 reported taking lithium. Further information regarding illness duration and severity is provided in Table 5.2.

5.2.1.3. TGT participants

The healthy controls included in this chapter were the same participants as those included in the previous TGT analyses in chapters 3 and 4, resulting in a total sample size of $n = 60$ (32 healthy controls and 28 schizophrenia patients). Demographic and neuropsychological information for the two groups is provided in Table 5.3, including age, Quick IQ (Mortimer & Bowen, 1999), WAIS scaled digit span (Wechsler, 2008), gender distribution, AHPQ handedness (Annett, 1970), SES, educational achievement, and clinical information (patients only). The groups differed in age (mean age greater in patients; mean difference = 4.786 years, SEM = 2.376, $t(58) = 2.014$, $p = .049$), years of education (mean years of education greater in controls; mean difference = 1.257 years, SEM = 0.566, $t(58) = 2.220$, $p = .030$), and scaled digit span

scores (higher digit span in controls; mean difference = 1.887 digits, SEM = 0.726, $t(57) = 2.598$, $p = .012$).

The patient group consisted of outpatients with a diagnosis of schizophrenia or related disorder (i.e., schizoaffective or psychotic disorder not otherwise specified) being followed by a mental health care provider at the time of participation. Diagnoses were confirmed for each participant using the MINI (Sheehan et al., 1998), which was also used to screen healthy controls for psychiatric illness. Symptom severity in patients was assessed using the SSPI semi-structured interview (Liddle et al., 2002). All patients but three reported taking antipsychotic medication at the time of testing, and medication details were missing for one participant. Of the 24 patients with current medication information, 22 patients reported taking atypical antipsychotics and 2 patients reported taking typical antipsychotic medication as their primary medication. 11 patients reported taking an additional antipsychotic, 8 of which were atypical, and 3 of which were typical antipsychotics. 8 patients reported taking antianxiety medication, 10 reported taking an antidepressant, 2 reported taking lithium, 3 reported taking an anticonvulsant, and 2 reported taking an anticholinergic as secondary medication. Further information regarding illness duration and severity is provided in Table 5.3.

5.2.2. Analysis

5.2.2.1. Task performance

Task performance was examined in the WM task, SCAP task, and TSI task only, as no overt behavioural response was recorded in the TGT task. For the WM task, task performance was calculated as percentage of correct responses for each condition. To examine effects of task condition and differences between healthy controls and schizophrenia patients, these accuracy measures were entered into a 2 (cognitive load; 4 vs. 6 letters) × 2 (delay duration; 0s vs. 4s) ×

2 (group) mixed-model ANOVA. As age was a potential confound in this sample, group effects were further examined in a follow-up ANOVA with the same factors, but performed on the residuals obtained from regressing out variance in accuracy predicted by age. Digit span and years of education were not statistically controlled for because these variables are likely to be intrinsically tied to differences between healthy individuals and people with a diagnosis of schizophrenia in the general population.

For the SCAP task, task performance was also calculated as percentage of correct responses for each condition. To examine effects of task condition and differences between healthy controls and schizophrenia patients, these accuracy measures were entered into a 4 (cognitive load; 1, 3, 5, or 7 dots) × 3 (delay duration; 1.5s, 3.0s, or 4.5s) × 2 (group) ANOVA. As age and gender were potential confounds in this sample, group effects were further examined in a follow-up ANOVA performed on the residuals obtained from regressing out variance predicted by age and gender. Educational achievement and digit span were not statistically controlled.

For the TSI task, task performance was measured as either percentage of correct responses or mean reaction time (RT) for each condition. To examine effects of task condition and differences between controls and patients, separate analyses were carried out on percent correct and RT measures, both of which were examined in a 2 (stimulus congruency; neutral vs. incongruent) × 2 (task-switch condition; preceding block = neutral vs. incongruent colour-naming) × 2 (group) ANOVA. As in the WM task (which comprised the same sample of participants), group effects were further examined in follow-up ANOVAs performed on the residuals obtained from regressing out variance predicted by age.

5.2.2.2. Functional connectivity analyses

Multi-experiment fMRI-CPCA was carried out as described in Chapter 2 (Section 2.4 and Figure 2.5). To examine effects of task condition and group differences on HDRs, a mixed-model ANOVA was performed for each component extracted and for each task as described below.

For the WM task, each level of cognitive load and delay duration was specified in the design matrix (i.e., *G* matrix), and the time bins for which a FIR basis function was specified were scans 1-10 following trial onset (i.e., 20 seconds of post-stimulus time with TR = 2,000ms), resulting in *G* matrices with 374 rows (scans) and 40 columns (4 conditions × 10 post-stimulus time bins) per task run. After the regression and PCA steps, within-subject factors of cognitive load (4 vs. 6 letters), delay length (0s vs. 4s), and time (10 post-stimulus time bins) were examined with the resulting predictor weights, resulting in a 2 (load) × 2 (delay) × 10 (time) × 2 (group) ANOVA for each component. Significant effects of load, delay, load × delay, delay × time, and any effects/interactions involving group differences were further examined. Post hoc analyses of load and delay were carried out using polynomial contrasts, and interactions involving time were examined using repeated measures contrasts between adjacent time bins. To verify whether group effects remained after accounting for age, a follow-up ANOVA was carried out for each component with the same factors entered into the model, but performed on the residuals obtained from regressing out variance predicted by age.

For the SCAP task, each level of cognitive load and delay duration was specified in the design, and the time bins for which a FIR basis function was specified were scans 1-10 following trial onset (i.e., 20 seconds of post-stimulus time with TR = 2,000ms), resulting in *G* matrices with 291 rows (scans) and 120 columns (12 conditions × 10 post-stimulus time bins) per partici-

pant. After the regression and PCA steps, within-subject factors of cognitive load (1, 3, 5, or 7 dots), delay length (1.5s, 3.0s, or 4.5s), and time (10 post-stimulus time bins) were examined with the resulting predictor weights, resulting in a 4 (load) × 3 (delay) × 10 (time) × 2 (group) ANOVA for each component. Significant effects of load, delay, delay × time, and any effects/interactions involving group differences were further examined. Post hoc analyses of load and delay effects were carried out using polynomial contrasts, and interactions involving time were examined using repeated measures contrasts between adjacent time bins. To verify whether group effects remained after accounting for differences in age and gender distribution, a follow-up ANOVA was performed with the same factors entered into the model, but computed on the residuals obtained from regressing out variance predicted by age and gender.

For the TSI task, each level of stimulus congruency and task-switch condition was specified in the design (but only for word-reading trials), and the time bins for which a FIR basis function was specified were scans 1-10 following trial onset (i.e., 20 seconds of post-stimulus time with TR = 2,000ms), resulting in *G* matrices with 330 rows (scans) and 40 columns (4 conditions × 10 post-stimulus time bins) per participant. After the regression and PCA steps, within-subject factors of stimulus congruency (neutral vs. incongruent stimulus), task-switch condition (preceding block = neutral vs. incongruent colour-naming), and time (10 post-stimulus time bins) were examined with the resulting predictor weights, resulting in a 2 (congruency) × 2 (task-switch) × 10 (time) × 2 (group) ANOVA for each component. Post-hoc analyses of significant effects of congruency, task-switch, congruency × task-switch, congruency × time, task-switch × time, and any effects/interactions involving group differences were carried out, with effects of congruency and task-switch examined using polynomial contrasts, and interactions involving time examined using repeated measures contrasts between adjacent time bins. To verify whether

group effects remained after accounting for differences in age, a follow-up ANOVA was performed with the same factors entered into the model, but computed on the residuals obtained from regressing out variance predicted by age.

Finally, for the TGT task, the generating and hearing conditions were both specified in the design, and the time bins for which a FIR basis function was specified were scans 1-10 following trial onset (i.e., 25 seconds of post-stimulus time with TR = 2,500ms). This resulted in *G* matrices with 176 rows (scans) and 20 columns (2 conditions × 10 post-stimulus time bins) per task run. After the regression and PCA steps, within-subject factors of condition (generating vs. hearing) and time (10 post-stimulus time bins) were examined with the resulting predictor weights, resulting in a 2 (condition) × 10 (time) × 2 (group) ANOVA for each component. Post-hoc analyses of significant effects of condition, condition × time, and any effects/interactions involving group differences were carried out, with interactions involving time examined using repeated measures contrasts between adjacent time bins. To verify whether group effects remained after accounting for differences in age, a follow-up ANOVA was performed with the same factors entered into the model, but performed on the residuals obtained from regressing out variance predicted by age.

5.2.2.3. Correlations between task performance and brain activity

Correlations between task performance and HDR shapes were examined for the WM, SCAP, and TSI tasks. Past work has shown that the HDR increase and the subsequent return to baseline can reflect separable cognitive/behavioural processes (Lavigne, Menon, & Woodward, 2016); therefore, in all three of these tasks, HDR increase-to-peak (ITP) and return-to-baseline (RTB) measures were computed separately by averaging across time bins that were selected by examining HDR shapes. For ITP measures, time bins included the HDR peak and the time bins

preceding it up to (but not including) the baseline point. For RTB measures, time bins included the time bin immediately following the peak and the subsequent time bins down to the lowest point (or highest, in cases where the HDR reflected deactivation rather than activation). In cases where the onset and/or termination of the HDR was ambiguous, contrasts were performed between adjacent time bins to determine whether there was a significant increase/decrease from one time bin to the next; for example, if there was no significant difference between pre-peak time points 1 and 2, then the second time point would be marked as the baseline point. As the purpose of this analysis was to gain a general sense of patterns predicting task performance, predictor weights were averaged across task conditions where appropriate. Due to the large number of statistical tests being carried out for this section, a threshold of $p < .01$ was set as the significance threshold, and results with a p value higher than this but $< .05$ are noted as trend correlations.

To examine relationships between task performance and brain activity in the WM task, two-tailed Pearson correlations were performed between accuracy (averaged over load conditions) and the corresponding ITP/RTB for each delay condition. The delay conditions were separated out because the difference in timing of the task phases results in correspondingly different timing of HDR phases. Participants' WAIS digit span scores were examined as an additional behavioural measure of WM capacity. WAIS digit span scores are scaled according to an individual's age, and so it is a practical measure of WM capacity that is not confounded by age (and was verified to not be directly correlated with age in this sample, $p > .18$).

For the SCAP task, two-tailed Pearson correlations were performed between accuracy (averaged over load conditions) and the corresponding ITP/RTB for each delay condition, as in the WM task. As standard WMS scores were not available for this dataset, but digit span was

nevertheless a neuropsychological measure of interest, partial correlations were performed between raw digit span and HDR ITPs/RTBs while controlling for age.

For the TSI task, two-tailed Pearson correlations were performed between task performance (percent correct or mean RTs) and HDR ITP/RTB for each component. Task performance and HDRs were averaged across all task conditions for this analysis. Although WAIS digit span was not expected to be correlated with the TSI task, it was included as a behavioural measure of interest for comparison with results from the WM task (which was completed by the same participants).

5.3. Task Performance Results

5.3.1. WM task performance

WM task performance (i.e., percent correct in each task condition) for each participant group and the total sample is listed in Table 5.4. The 2 (load) × 2 (delay) × 2 (group) ANOVA revealed a significant main effect of load, $F(1, 52) = 31.166$, $p < .001$, $\eta_p^2 = .375$, due to greater accuracy in the 4-letter condition than in the 6-letter condition (means = 92.66% correct and 87.37% correct for 4 letters and 6 letters, respectively); all other ps > .06. After removing variance predicted by age, a significant load × group interaction emerged, $F(1, 52) = 4.417$, $p = .040$, $\eta_p^2 = .078$. This interaction appeared to be due to healthy controls showing greater improvement in accuracy at the lower cognitive load (see Figure 5.1).

5.3.2. SCAP task performance

SCAP task performance (i.e., percent correct in each task condition) for each participant group and the total sample is listed in Table 5.5. The 4 (load) × 3 (delay) × 2 (group) ANOVA revealed significant main effects of load, $F(3, 258) = 44.075$, $p < .001$, $\eta_p^2 = .339$; and group, $F(1, 86) = 31.397$, $p < .001$, $\eta_p^2 = .267$, which remained significant after removing variance pre-

dicted by age and gender ($p < .001$). Significant interactions emerged for load × delay, $F(6, 516) = 3.401$, $p = .003$, $\eta_p^2 = .038$; and, initially, load × group, $F(3, 258) = 2.742$, $p = .044$, $\eta_p^2 = .031$. However, the load × group interaction did not remain significant after removing variance predicted by age and gender ($p > .25$).

The main effect of load was due to both linear and quadratic effects, with the linear effect having the greater effect size (linear: $F(1, 86) = 132.270$, $p < .001$,$\eta_p^2 = .606$; quadratic: $F(1, 86) = 7.103$, $p = .009$, $\eta_p^2 = .076$; cubic: $p > .40$). This was due to a general tendency for lower accuracy with higher cognitive load (mean correct = 89.96%, 81.82%, 74.62%, and 72.82% for 1, 3, 5, and 7 dots, respectively; see Figure 5.2). Paired t-tests comparing adjacent load conditions revealed significant differences between 1 versus 3 dots (mean difference = 8.144, SEM = 1.444, $t(87) = 5.639$, $p < .001$) and 3 versus 5 dots (mean difference = 7.197, SEM = 1.689, $t(87) = 4.262$, $p < .001$), but not 5 versus 7 dots ($p > .35$). The main effect of group was due to controls having greater mean accuracy than patients (mean correct = 86.27% and 73.34% for controls and patients, respectively).

5.3.3. TSI task performance

TSI task performance (i.e., percent correct and mean RT for each task condition) for each participant group and the total sample is listed in Table 5.6. Accuracy and RTs were analysed separately as reported below.

5.3.3.1. Response accuracy

Examining percent correct in each task condition, the 2 (stimulus congruency) × 2 (task-switch condition) × 2 (group) ANOVA revealed significant main effects of congruency, $F(1, 52) = 89.808$, $p < .001$, $\eta_p^2 = .633$; task-switch, $F(1, 52) = 10.105$, $p = .002$, $\eta_p^2 = .163$; and

group, $F(1, 52) = 14.074$, $p < .001$, $\eta_p^2 = .213$. Significant interactions emerged for congruency × task-switch, $F(1, 52) = 15.190$, $p < .001$, $\eta_p^2 = .226$; task-switch × group, $F(1, 52) = 5.021$, $p = .029$, $\eta_p^2 = .088$; and congruency × task-switch × group, $F(1, 52) = 7.736$, $p = .008$, $\eta_p^2 = .130$. However, neither the task-switch × group interaction nor the congruency × task-switch × group interaction remained significant after removing variance predicted by age (*p*s > .06).

The main effect of congruency was due to greater mean accuracy in the neutral stimulus condition than in the incongruent condition (mean correct = 93.02% and 80.74% for neutral and incongruent stimuli, respectively). The main effect of task-switch was due to greater mean accuracy following a neutral colour-naming block than following an incongruent colour-naming block (mean correct = 88.89% and 84.88% following neutral and incongruent colour-naming, respectively). The congruency × task-switch interaction was due to a more pronounced congruency effect following an incongruent colour-naming block; that is, while accuracy on neutral stimulus trials was similar regardless of whether the preceding colour-naming block consisted of neutral or incongruent stimuli, accuracy on incongruent stimulus trials was much lower when preceded by an incongruent rather than neutral colour-naming block (Figure 5.3). The main effect of group was due to controls having greater mean accuracy compared with patients (mean correct = 91.99% and 82.14% for controls and patients, respectively).

5.3.3.2. Reaction time (RT)

Examining mean RTs, the 2 (congruency) × 2 (task-switch) × 2 (group) ANOVA revealed significant main effects of congruency, $F(1, 52) = 245.043$, $p < .001$, $\eta_p^2 = .825$; task-switch, $F(1, 52) = 18.067$, $p < .001$, $\eta_p^2 = .258$; and group, $F(1, 52) = 5.367$, $p = .024$, $\eta_p^2 = .094$. A significant congruency × group interaction initially emerged, $F(1, 52) = 7.308$, $p = .009$, $\eta_p^2 =$

.123. However, neither the main effect of group nor the congruency × group interaction remained significant after removing variance predicted by age (both *p*s > .08).

The main effect of congruency was due to longer RTs in the incongruent stimulus condition than in the neutral condition (mean RTs = 970.10ms and 1180.25ms for neutral and incongruent stimuli, respectively). The main effect of task-switch was due to longer RTs following an incongruent colour-naming block than following a neutral colour-naming block (mean RTs = 1048.42ms and 1102.67ms following neutral and incongruent colour-naming blocks, respectively).

5.4. Overview of fMRI-CPCA Results

Although the scree plot suggested that either a 4-component or 8-component solution may be appropriate, the less conservative option was selected to allow for the examination of small components that may only be engaged in one task. Therefore, 8 components were extracted, which after varimax rotation accounted for 5.83%, 5.80%, 5.55%, 4.83%, 4.41%, 4.21%, 3.08%, and 2.76% of the task-related variance in BOLD signal, respectively. Components 1, 2, 3, 4, 5, and 7 appeared to originate primarily in grey matter and exhibited plausible HDR shapes in all tasks, and therefore were selected for further examination. Figure 5.4 presents a visual summary of components 1-5 and 7 for all tasks, including surface representations and HDR shapes. Components 6 and 8 appeared to reflect artifacts originating from non-cortical sources, and so are not discussed further but are presented in Figures 5.5 and 5.6, respectively. The following sections report the anatomical characteristics and the mixed-model ANOVA results for each of these six components. For the purpose of discussion, each component was assigned a descriptive label following extensive evaluation of its anatomical and functional characteristics; therefore, the following labels are used hereafter to refer to each component: (1) default mode network

(DMN), (2) internal attention network, (3) sensorimotor network, (4) motor response network, (5) visual attention network, and (7) occipital network.

5.5. Default Mode Network (Component 1)

5.5.1. Anatomical characteristics

The DMN (component 1) was primarily characterized by bilateral deactivation in the medial frontal cortex (frontal poles, superior frontal gyri, and anterior paracingulate gyri), middle frontal gyri, medial parietal cortex (posterior cingulate gyri and precuneus), superior lateral occipital cortex, middle temporal gyri, and temporal poles. See Figure 5.7 for anatomical visualization and Table 5.7 for locations of cluster peaks.

5.5.2. DMN: WM task results

DMN (component 1) estimated HDR plots for the WM task are presented in Figure 5.8. The 2 (load; 4 vs. 6 letters) × 2 (delay; 0s vs. 4s) × 10 (time) × 2 (group) ANOVA revealed significant main effects of load, $F(1, 52) = 39.858$, $p < .001$, $\eta_p^2 = .434$; delay, $F(1, 52) = 15.108$, $p < .001$, $\eta_p^2 = .225$; and time, $F(9, 468) = 61.987$, $p < .001$, $\eta_p^2 = .544$. Significant interactions emerged for load × delay, $F(1, 52) = 6.654$, $p = .013$, $\eta_p^2 = .113$; load × time, $F(9, 468) = 17.185$, $p < .001$, $\eta_p^2 = .248$; and delay × time, $F(9, 468) = 39.697$, $p < .001$, $\eta_p^2 = .433$. No significant effects related to group differences emerged (all ps > .05). Although a delay × time × group trend interaction initially appeared to be worth examining ($p = .053$), this interaction was concluded to be non-significant after removing variance predicted by age ($p > .20$).

Post-hoc analyses of the main effects of load and delay revealed that there was a greater degree of mean *deactivation* in the 6-letter load condition compared with the 4-letter load condition (mean predictor weights = 0.135 and 0.090, respectively), and a greater degree of mean deactivation in the 4s delay condition compared with the 0s delay condition (mean predictor

weights = 0.128 and 0.097, respectively). Delay effects appeared to be driven by the presence of a more sustained HDR in the 4s delay conditions rather than the magnitude of suppression being greater per se (Figure 5.9A). The load × delay interaction was due to the effect of delay length being greater within the 6-letter condition than within the 4-letter condition (Figure 5.9B).

5.5.3. DMN: SCAP task results

DMN (component 1) estimated HDR plots for the SCAP task are presented in Figure 5.10. The 4 (load; 1, 3, 5, or 7 dots) × 3 (delay; 1.5s, 3.0s, or 4.5s) × 10 (time) × 2 (group) ANOVA revealed significant main effects of load, $F(3, 258) = 13.372$, $p < .001$, $\eta_p^2 = .135$; delay, $F(2, 172) = 5.770$, $p = .004$, $\eta_p^2 = .063$; and time, $F(9, 774) = 77.063$, $p < .001$, $\eta_p^2 = .473$. Significant interactions emerged for load × time, $F(27, 2322) = 6.174$, $p < .001$, $\eta_p^2 = .067$; delay × time, $F(18, 1548) = 10.187$, $p < .001$, $\eta_p^2 = .106$; and load × delay × time, $F(19.66, 1690.61) = 2.207$, $p = .002$, $\eta_p^2 = .025$. No significant effects emerged involving group differences (all *p*s > .09).

Post-hoc analyses of the main effect of load revealed that the linear and quadratic contrasts were both significant, with the linear contrast having the greater effect size (linear: $F(1, 86) = 27.824$, $p < .001$, $\eta_p^2 = .244$; quadratic: $F(1, 86) = 14.666$, $p < .001$, $\eta_p^2 = .146$; cubic: $p > .90$). This was due to a general tendency for increasing *deactivation* with increasing cognitive load, except for the change from 5 dots to 7 dots (mean predictor weights = 0.041, 0.067, 0.080, and 0.078 for 1, 3, 5, and 7 dots, respectively; see Figure 5.11A). Further examination of differences between adjacent conditions showed that only the contrast between 1 and 3 dots was significant (mean difference = 0.026, SEM = 0.007, $t(87) = 3.764$, $p < .001$; other *p*s > .10). Examination of the main effect of delay revealed that the linear and quadratic contrasts were both

significant, with the linear contrast having the greater effect size (linear: $F(1, 86) = 6.686$, $p = .011$, $\eta_p^2 = .072$; quadratic: $F(1, 86) = 4.808$, $p = .031$, $\eta_p^2 = .053$). This was due to a general tendency for increasing deactivation with increasing delay duration, except for the change from 3.0s delay to 4.5s delay conditions (mean predictor weights = 0.057, 0.073, and 0.070 for 1.5s, 3.0s, and 4.5s delay, respectively; see Figure 5.11B). Further examination of differences between adjacent conditions showed that only the difference between 1.5s delay and 3.0s delay was significant (mean difference = 0.016, SEM = 0.005, $t(87) = 3.304$, $p = .001$; other $p > .50$). Similar to the pattern observed in the verbal WM task, delay effects appeared to be due to DMN deactivation being more sustained in trials with longer delay periods rather than exhibiting a greater magnitude of deactivation per se (see Figure 5.11C).

5.5.4. DMN: TSI task results

DMN (component 1) estimated HDR plots for the TSI task are presented in Figure 5.12. The 2 (stimulus congruency; neutral vs. incongruent) × 2 (task-switch condition; following neutral vs. incongruent colour-naming) × 10 (time) × 2 (group) ANOVA revealed significant main effects of congruency, $F(1, 52) = 7.163$, $p = .010$, $\eta_p^2 = .121$; and time, $F(9, 468) = 50.062$, $p < .001$, $\eta_p^2 = .491$. Significant interactions emerged for congruency × task-switch, $F(1, 52) = 16.987$, $p < .001$, $\eta_p^2 = .246$; congruency × time, $F(4.18, 217.18) = 3.746$, $p = .005$, $\eta_p^2 = .067$; task-switch × time, $F(3.88, 201.89) = 2.959$, $p = .022$, $\eta_p^2 = .054$; and congruency × task-switch × time, $F(4.63, 241.01) = 3.722$, $p = .004$, $\eta_p^2 = .067$. No significant effects emerged involving group differences before or after removing variance predicted by age (all ps > .30).

The main effect of congruency was due to there being a greater degree of mean *deactivation* in the incongruent stimulus condition compared with the neutral stimulus condition (mean

predictor weights = -0.010 and 0.030 for neutral and incongruent stimuli, respectively), which emerged during the HDR increase (Figure 5.13A). The congruency × task-switch interaction was due to there being a significant effect of stimulus congruency following an incongruent colour-naming block (mean difference between neutral and incongruent stimuli = 0.090, SEM = 0.021, $t(53) = 4.215$, $p < .001$) but not following a neutral colour-naming block ($p > .50$; see Figure 5.13B). The task-switch × time interaction appeared to be due to there being a less extreme response in the incongruent task-switch condition as compared to the neutral task-switch condition after averaging across stimulus congruency (i.e., less peak deactivation *and* less post-peak activation); however, this was a result of the congruency × task-switch × time interaction apparent in Figure 5.12, whereby the HDR peak deactivation is dampened in the neutral condition but not the incongruent condition, and the post-peak rise above baseline is dampened in the incongruent stimulus condition but not the neutral stimulus condition.

5.5.5. DMN: TGT task results

DMN (component 1) estimated HDR plots for the TGT task are presented in Figure 5.14. The 2 (condition; generating vs. hearing) × 10 (time) × 2 (group) ANOVA revealed a significant main effect of time, $F(9, 522) = 35.652$, $p < .001$, $\eta_p^2 = .381$. A significant interaction emerged for condition × time, $F(3.17, 184.03) = 2.600$, $p = .050$, $\eta_p^2 = .043$. No significant effects involving group differences emerged before or after removing variance predicted by age (all ps > .25). The condition × time interaction was due to the later HDR peak observed in the thought generation condition than in the hearing condition (Figure 5.14).

5.5.6. Summary of DMN results

The DMN (component 1; Figures 5.7 to 5.14) exhibited deactivation that was dependent on cognitive demand in all tasks. In the WM and SCAP tasks, deactivation was greater in condi-

tions of higher load. In the TSI task, the DMN exhibited a greater degree of deactivation for incongruent stimuli than for congruent stimuli, and this effect was magnified when the preceding colour-naming block consisted of incongruent stimuli (Figure 5.13B). In the WM and SCAP tasks, HDRs initiated early in the post-stimulus time series, and peaks were staggered according to delay duration (Figures 5.9A and 5.11C for WM and SCAP, respectively). However, the *magnitude* of the peaks did not continually increase with longer delays, suggesting that the cognitive processes that occur later in the trial (e.g., maintenance and recall) do not rely on further deactivation in this network over and above its initial decline from the trial onset. In the TGT task, deactivation peaked later and to a slightly greater degree in the generating condition than in the hearing condition (Figure 5.14), which may reflect the greater cognitive demand required for volitional internal thought generation than for passive speech perception. No group differences emerged for this network in any of the tasks examined.

5.6. Internal Attention Network (Component 2)

5.6.1. Anatomical characteristics

The internal attention network (component 2) was primarily characterized by bilateral activation in prefrontal cortex (middle frontal gyri, frontal poles, dorsal paracingulate gyrus), anterior insula, parietal regions peaking in posterior supramarginal gyri and right superior parietal lobule, cerebellum (especially right lobe VI), and subcortical regions including bilateral caudate and thalamus. See Figure 5.15 for anatomical visualization and Table 5.8 for coordinates of peak locations.

5.6.2. Internal attention network: WM task results

Internal attention network (component 2) estimated HDR plots for the WM task are presented in Figure 5.16. The 2 (load; 4 vs. 6 letters) × 2 (delay; 0s vs. 4s) × 10 (time) × 2 (group)

ANOVA revealed significant main effects of load, $F(1, 52) = 129.511$, $p < .001$, $\eta_p^2 = .714$; delay, $F(1, 52) = 59.859$, $p < .001$, $\eta_p^2 = .535$; and time; $F(9, 468) = 52.562$, $p < .001$, $\eta_p^2 = .503$. Significant interactions emerged for load × delay, $F(1, 52) = 9.358$, $p = .004$, $\eta_p^2 = .153$; load × time, $F(9, 468) = 24.996$, $p < .001$, $\eta_p^2 = .325$; delay × time, $F(9, 468) = 84.202$, $p < .001$, $\eta_p^2 = .618$; delay × time × group, $F(3.37, 175.18) = 3.321$, $p = .017$, $\eta_p^2 = .060$; and load × delay × time, $F(4.78, 248.49) = 2.513$, $p = .033$, $\eta_p^2 = .046$. However, the delay × time × group interaction did not remain significant after removing variance predicted by age ($p > .10$).

The main effect of load was due to greater engagement of this network in 6-letter condition compared with 4-letter condition (mean predictor weights = 0.043 and 0.119 for 4 letters and 6 letters, respectively). The main effect of delay was due to greater engagement in 4s delay condition compared with 0s delay condition (mean predictor weights = 0.053 and 0.109 for 0s and 4s delays, respectively). The load × delay interaction was due to the effect of delay length being more pronounced in the 6-letter condition than in the 4-letter condition (Figure 5.17B). Notably, the delay × time interaction was not only due to the staggered peaks corresponding to delay length, but also there appeared to be a continual increase in activation throughout the 4-second delay (Figure 5.17A).

5.6.3. Internal attention network: SCAP task results

Internal attention network (component 2) estimated HDR plots for the SCAP task are presented in Figure 5.18. The 4 (load; 1, 3, 5, or 7 dots) × 3 (delay; 1.5s, 3.0s, or 4.5s) × 10 (time) × 2 (group) ANOVA revealed significant main effects of load, $F(2.66, 229.10) = 6.449$, $p = .001$, $\eta_p^2 = .070$; delay, $F(2, 172) = 16.816$, $p < .001$, $\eta_p^2 = .164$; and time, $F(9, 774) = 65.446$, $p < .001$, $\eta_p^2 = .432$. Significant interactions emerged for time × group, $F(2.97, 255.41) =$

3.404, $p = .019$, $\eta_p^2 = .038$; load × delay, $F(6, 516) = 2.184$, $p = .043$, $\eta_p^2 = .025$; load × time, $F(27, 2322) = 3.498$, $p < .001$, $\eta_p^2 = .039$; load × time × group, $F(14.21, 1221.97) = 1.709$, $p = .047$, $\eta_p^2 = .019$; delay × time, $F(18, 1548) = 20.137$, $p < .001$, $\eta_p^2 = .190$; delay × time × group, $F(18, 1548) = 3.230$, $p < .001$, $\eta_p^2 = .036$; and load × delay × time, $F(54, 4644) = 4.131$, $p < .001$, $\eta_p^2 = .046$.

Follow-up analyses of the main effect of load revealed that the linear and quadratic contrasts were both significant, with the linear contrast having the greater effect size (linear: $F(1, 86) = 9.819$, $p = .002$, $\eta_p^2 = .102$; quadratic: $F(1, 86) = 9.422$, $p = .003$, $\eta_p^2 = .099$; cubic: $p > .80$). This was due to a general trend for greater activation with greater cognitive load, except for the change from 1 dot to 3 dots (mean predictor weights = 0.048, 0.046, 0.052, and 0.071 for 1, 3, 5, and 7 dots, respectively; see Figure 5.19A). Paired t-tests between adjacent load conditions revealed a significant difference only between the 5-dots and 7-dots conditions (mean difference = 0.020, SEM = 0.006, $t(87) = 3.231$, $p = .002$). Examination of the main effect of delay revealed that the linear and quadratic contrasts were both significant, with the linear contrast having the greater effect size (linear: $F(1, 86) = 25.341$, $p < .001$, $\eta_p^2 = .228$; quadratic: $F(1, 86) = 4.388$, $p = .039$, $\eta_p^2 = .049$). This was due to a tendency for increasing activation with increasing delay duration (mean predictor weights = 0.038, 0.059, and 0.065 for 1.5s, 3.0s, and 4.5s delay, respectively; see Figure 5.19B), and further examination of differences between adjacent conditions showed that only the difference between 1.5s delay and 3.0s delay was significant (mean difference = 0.022, SEM = 0.004, $t(87) = 4.986$, $p < .001$). The delay × time interaction was due to the progressively later *and* higher peaks with longer delay durations (Figure 5.19C).

The time × group and delay × time × group interactions remained significant after removing variance predicted by age and gender (both *p*s < .05), but the load × time × group interaction did not ($p > .10$). Post-hoc analysis of the time × group interaction revealed that group differences were largely due to a greater increase and steeper decrease of HDRs in healthy controls as compared to schizophrenia patients (Figure 5.20A). Further, differences between HDR peaks across delay conditions appeared to be more pronounced in controls as compared to patients, as evident from an apparently greater peak in the 4.5s delay condition than in the other conditions being exhibited in healthy controls but not in schizophrenia patients (Figure 5.20B, see HDR shapes from 12-18 seconds in particular).

5.6.4. Internal attention network: TSI task results

Internal attention network (component 2) estimated HDR plots for the TSI task are presented in Figure 5.21. The 2 (stimulus congruency; neutral vs. incongruent) × 2 (task-switch condition; following neutral vs. incongruent colour-naming) × 10 (time) × 2 (group) ANOVA revealed significant main effects of congruency, $F(1, 52) = 24.651$, $p < .001$, $\eta_p^2 = .322$; task-switch, $F(1, 52) = 5.209$, $p = .027$, $\eta_p^2 = .091$; and time, $F(9, 468) = 16.938$, $p < .001$, $\eta_p^2 = .246$. Significant interactions emerged for congruency × time, $F(9, 468) = 13.732$, $p < .001$, $\eta_p^2 = .209$; congruency × time × group, $F(3.85, 200.20) = 2.498$, $p = .046$, $\eta_p^2 = .046$; task-switch × time, $F(9, 468) = 6.476$, $p < .001$, $\eta_p^2 = .111$; and congruency × task-switch × time, $F(9, 468) = 6.423$, $p < .001$, $\eta_p^2 = .110$. The congruency × time × group interaction did not remain significant after removing variance predicted by age ($p > .50$).

The main effect of congruency was due to there being greater mean activity in the incongruent condition than in the neutral condition (mean predictor weights = -0.030 and 0.041 for

neutral and incongruent stimuli, respectively), due to the minimal response elicited in the neutral stimulus condition (Figure 5.22A). The main effect of task-switch condition was due to there being greater mean activity following an incongruent colour-naming block than following a neutral colour-naming block (mean predictor weights = 0.001 and 0.010 for neutral and incongruent task-switch conditions, respectively). Further, activity following an incongruent colour-naming block was more sustained (Figure 5.22B), particularly during incongruent stimulus trials (Figure 5.21).

5.6.5. Internal attention network: TGT task results

Internal attention network (component 2) estimated HDR plots for the TGT task are presented in Figure 5.23. The 2 (condition; generating vs. hearing) × 10 (time) × 2 (group) ANOVA revealed significant main effects of condition, $F(1, 58) = 39.113$, $p < .001$, $\eta_p^2 = .403$; and time, $F(9, 522) = 10.800$, $p < .001$, $\eta_p^2 = .157$. A significant interaction emerged for condition × time, $F(9, 522) = 21.131$, $p < .001$, $\eta_p^2 = .267$. No significant effects involving group differences emerged before or after removing variance predicted by age (all ps > .40). The condition effects were evidently due to the engagement of this network being exclusive to the generating condition (no main effect of time emerged when the hearing condition was examined in isolation; $p > .20$).

5.6.6. Summary of internal attention network results

The internal attention network (component 2; Figures 5.15 to 5.23) was comprised of frontoparietal activity including dorsal paracingulate gyrus, DLPFC, and intraparietal sulcus as well as anterior insula. Activity in this network was dependent on cognitive load and exhibited staggered peaks in the WM and SCAP tasks, and showed greater magnitude of activation with longer delay durations (Figures 5.17A and 5.19C for WM and SCAP, respectively). The internal attention network responded minimally to neutral stimuli in the TSI task (Figure 5.22A), and ex-

hibited a more sustained HDR following an incongruent colour-naming block (Figure 5.22B). In the TGT task, this network was engaged during thought generation but not the hearing condition (Figure 5.23). Group differences emerged in the SCAP task which suggested that activity in this network is relatively attenuated in schizophrenia patients (Figure 5.20A), and does not exhibit as pronounced increases with longer delay durations as in healthy controls (Figure 5.20B). Group effects also initially emerged in the WM task and TSI task, but these differences did not remain significant after accounting for age differences.

5.7. Sensorimotor Network (Component 3)

5.7.1. Anatomical characteristics

The sensorimotor network (component 3) was primarily characterized by (de)activation in auditory cortex and surrounding areas, including bilateral central opercular cortex, posterior insula, postcentral gyri, SMA/dorsal anterior cingulate, and lingual gyri, as well as left precentral gyrus, left temporal occipital fusiform cortex, and right cerebellum VI. See Figure 5.24 for anatomical visualization and Table 5.9 for coordinates of peak locations.

5.7.2. Sensorimotor network: WM task results

Sensorimotor network (component 3) estimated HDR plots for the WM task are presented in Figure 5.25. The 2 (load; 4 vs. 6 letters) × 2 (delay; 0s vs. 4s) × 10 (time) × 2 (group) ANOVA revealed significant main effects of load, $F(1, 52) = 4.011$, $p = .050$, $\eta_p^2 = .072$; delay, $F(1, 52) = 8.836$, $p = .004$, $\eta_p^2 = .145$; and time, $F(9, 468) = 42.390$, $p < .001$, $\eta_p^2 = .449$. Significant interactions emerged for delay × time, $F(9, 468) = 66.551$, $p < .001$, $\eta_p^2 = .561$; and delay × time × group, $F(4.13, 214.96) = 2.993$, $p = .018$, $\eta_p^2 = .054$. However, the delay × time × group interaction was no longer significant after removing variance predicted by age ($p > .40$).

The main effect of load was due to greater mean activation in the 4-letter condition than in the 6-letter condition (mean predictor weights = 0.034 and 0.022 for 4 letters and 6 letters, respectively). The main effect of delay was due to greater mean activation in the 4s delay condition than in the 0s delay condition (mean predictor weights = 0.020 and 0.036 for 0s and 4s delay, respectively), which could be due to the 4s delay condition exhibiting a later HDR as well as a slightly higher peak than the 0s delay condition (Figure 5.26B). The delay × time interaction was due to the staggered time courses consistent with delay length, with both the onsets and the peaks occurring later in the 4s delay condition (Figure 5.26A).

5.7.3. Sensorimotor network: SCAP task results

Sensorimotor network (component 3) estimated HDR plots for the SCAP task are presented in Figure 5.27. Unlike in the verbal WM task, HDRs in the SCAP task reflected deactivation rather than activation. The 4 (load; 1, 3, 5, or 7 dots) × 3 (delay; 1.5s, 3.0s, or 4.5s) × 10 (time) × 2 (group) ANOVA revealed significant main effects of load, $F(3, 258) = 12.159$, $p < .001$, $\eta_p^2 = .124$; delay, $F(2, 172) = 8.203$, $p < .001$, $\eta_p^2 = .087$; and time, $F(9, 774) = 27.779$, $p < .001$, $\eta_p^2 = .244$. Significant interactions emerged for load × delay, $F(6, 516) = 3.496$, $p = .002$, $\eta_p^2 = .039$; load × time, $F(27, 2322) = 5.167$, $p < .001$, $\eta_p^2 = .057$; delay × time, $F(18, 1548) = 12.217$, $p < .001$, $\eta_p^2 = .124$; and load × delay × time, $F(54, 4644) = 2.408$, $p < .001$, $\eta_p^2 = .027$. Initially, no significant effects involving group differences emerged (all ps > .05); however, the load × group interaction became significant after removing variance predicted by age and gender, $F(2.51, 215.64) = 3.018$, $p = .039$, $\eta_p^2 = .034$.

Post-hoc analyses of the main effect of load revealed that both the linear and quadratic contrasts were significant, with the linear contrast having the greater effect size (linear:

$F(1, 86) = 20.392$, $p < .001$, $\eta_p^2 = .192$; quadratic: $F(1, 86) = 10.268$, $p = .002$, $\eta_p^2 = .107$; cubic: $p > .07$). This was due to a tendency for more extreme negative predictor weights with increasing load, except for the change from 3 dots to 5 dots (mean predictor weights = -0.015, -0.047, -0.046, and -0.053 for 1, 3, 5, and 7 dots, respectively; Figure 5.28A). Paired t-tests between adjacent conditions revealed that this difference was significant only for the contrast between the 1-dot and 3-dots conditions (mean difference = 0.032, SEM = 0.007, $t(87) = 4.560$, $p < .001$; other ps > .20). Post-hoc analyses of the main effect of delay revealed that both the linear and quadratic contrasts were significant, with the quadratic contrast having the greater effect size (linear: $F(1, 86) = 6.856$, $p = .010$, $\eta_p^2 = .074$; quadratic: $F(1, 86) = 9.551$, $p = .003$, $\eta_p^2 = .100$). This was due to a tendency for more extreme negative predictor weights with increasing delay length, except for the change from 3.0s to 4.5s delay conditions (mean predictor weights = -0.029, -0.049, and -0.042 for 1.5s, 3.0s, and 4.5s delay, respectively; Figure 5.28B). Paired t-tests between adjacent conditions revealed that only the change from 1.5s delay to 3.0s delay was significant (mean difference = 0.020, SEM = 0.005, $t(87) = 4.001$, $p < .001$; other $p > .10$). The delay × time interaction was due to the difference in timing of peak deactivation across delay conditions, with largely similar initial HDR decreases but an increasingly delayed return to baseline with increasing delay length (Figure 5.28C). The load × group interaction appeared to be primarily due to patients exhibiting greater suppression in the 1-dot condition compared with controls (Figure 5.29), although independent t-tests for each load level were non-significant (all ps > .08).

5.7.4. Sensorimotor network: TSI task results

Sensorimotor network (component 3) estimated HDR plots for the TSI task are presented in Figure 5.30. The 2 (stimulus congruency; neutral vs. incongruent) × 2 (task-switch condition; neutral vs. incongruent colour-naming) × 10 (time) × 2 (group) ANOVA revealed significant

main effects of congruency, $F(1, 52) = 15.862$, $p < .001$, $\eta_p^2 = .234$; and time, $F(9, 468) = 5.548$, $p < .001$, $\eta_p^2 = .096$. Significant interactions emerged for time × group, $F(4.29, 222.87) = 2.807$, $p = .024$, $\eta_p^2 = .051$; congruency × task-switch, $F(1, 52) = 10.427$, $p = .002$, $\eta_p^2 = .167$; congruency × time, $F(9, 468) = 12.586$, $p < .001$, $\eta_p^2 = .195$; task-switch × time, $F(4.10, 213.27) = 3.683$, $p = .006$, $\eta_p^2 = .066$; and congruency × task-switch × time, $F(9, 468) = 9.354$, $p < .001$, $\eta_p^2 = .152$. The time × group interaction did not remain significant after removing variance predicted by age ($p > .25$).

The main effect of congruency was due to greater mean activation in trials with neutral stimuli (mean predictor weights = 0.024 and -0.027 for neutral and incongruent stimulus conditions, respectively), an effect which emerged early in the HDR but then diminished towards the end of the post-stimulus time series (Figure 5.31A). This congruency effect was much more pronounced following incongruent colour-naming blocks than following neutral colour-naming blocks (Figure 5.31B). The task-switch × time interaction was due to a small difference between task-switch conditions in the contrast between the first two post-stimulus time bins ($p = .032$; change from the first to second time bin = 0.030 and -0.014 following neutral and incongruent colour-naming blocks, respectively).

5.7.5. Sensorimotor network: TGT task results

Sensorimotor network (component 3) estimated HDR plots for the TGT task are presented in Figure 5.32. The 2 (condition; generating vs. hearing) × 10 (time) × 2 (group) ANOVA revealed significant main effects of condition, $F(1, 58) = 45.638$, $p < .001$, $\eta_p^2 = .440$; and time, $F(9, 522) = 58.533$, $p < .001$, $\eta_p^2 = .502$. A significant interaction emerged for condition × time,

$F(9, 522) = 34.763$, $p < .001$, $\eta_p^2 = .375$. No significant effects involving group emerged before or after removing variance predicted by age (all ps > .20).

The main effect of condition was due to greater engagement of this network in the hearing condition than in the generating condition (mean predictor weights = 0.015 and 0.043 for generating and hearing, respectively). Along with peak activation being considerably greater in the hearing condition, the HDR also exhibited greater post-peak suppression than that of the generating condition (Figure 5.32).

5.7.6. Summary of sensorimotor network results

The sensorimotor network (component 3; Figures 5.24 to 5.32) largely comprised auditory cortex, left-lateralized somatomotor areas, and insula and dorsal anterior cingulate just posterior to the insula and dorsal anterior cingulate peaks located in the internal attention network (component 2; Figure 5.15). In the TGT task, this network was engaged during the hearing condition but showed little activation in the generating condition (Figure 5.32), which is in line with the activation of auditory cortex. In the WM, SCAP, and TSI tasks, there was a greater degree of activation (or lower degree of suppression) in conditions of lower task difficulty, and in the TSI task, this effect was magnified following an incongruent colour-naming block (Figure 5.31B). A load × group interaction emerged in the SCAP task which appeared to be due to a trend of patients exhibiting greater suppression of this network compared with controls in the 1-dot load condition but not at the higher load conditions (Figure 5.29). Group differences in the WM task and TSI task did not remain significant after accounting for age differences.

5.8. Motor Response Network (Component 4)

5.8.1. Anatomical characteristics

The motor response network (component 4) was characterized by bilateral (de)activation in somatomotor regions (pre/postcentral gyri and SMA), superior frontal gyri, superior parietal lobules, and lateral occipital cortex. See Figure 5.33 for anatomical visualization and Table 5.10 for coordinates of peak locations.

5.8.2. Motor response network: WM task results

Motor response network (component 4) estimated HDR plots for the WM task are presented in Figure 5.34. The 2 (load; 4 vs. 6 letters) × 2 (delay; 0s vs. 4s) × 10 (time) × 2 (group) ANOVA revealed significant main effects of load, $F(1, 52) = 12.471$, $p = .001$, $\eta_p^2 = .193$; and time, $F(9, 468) = 8.360$, $p < .001$, $\eta_p^2 = .138$. Significant interactions emerged for load × group, $F(1, 52) = 4.933$, $p = .031$, $\eta_p^2 = .087$; time × group, $F(2.47, 128.63) = 6.074$, $p = .001$, $\eta_p^2 = .105$; load × delay × group, $F(1, 52) = 5.359$, $p = .025$, $\eta_p^2 = .093$; load × time, $F(9, 468) = 8.047$, $p < .001$, $\eta_p^2 = .134$; delay × time, $F(9, 468) = 67.358$, $p < .001$, $\eta_p^2 = .564$; delay × time × group, $F(3.92, 203.95) = 3.256$, $p = .013$, $\eta_p^2 = .059$; and a trend-level interaction of load × delay × time, $F(5.53, 287.68) = 2.161$, $p = .052$, $\eta_p^2 = .040$.

Effects of load were driven in part by greater mean activation in the 4-letter condition than in the 6-letter condition (mean predictor weights = 0.041 and 0.021, respectively). Load effects were particularly pronounced at or following HDR peaks, and there appeared to be greater post-response suppression in the 6-letter condition than in the 4-letter condition (Figure 5.34). The delay × time interaction was due to the staggered time courses according to delay length, with both the onsets and the peaks occurring later in the 4s delay condition (Figure 5.35).

The load × group interaction was due to the load effect (4 letters > 6 letters) being more pronounced in healthy controls than in schizophrenia patients (mean difference = 0.034 and 0.008 in controls and patients, respectively; see Figure 5.36). This interaction remained after removing variance predicted by age, $F(1, 52) = 5.919$, $p = .018$, $\eta_p^2 = .102$. Neither the time × group, load × delay × group, nor the delay × time × group interactions remained significant after removing variance predicted by age (all *p*s > .08).

5.8.3. Motor response network: SCAP task results

Motor response network (component 4) estimated HDR plots for the SCAP task are presented in Figure 5.37. The 4 (load; 1, 3, 5, or 7 dots) × 3 (delay; 1.5s, 3.0s, or 4.5s) × 10 (time) × 2 (group) ANOVA revealed significant main effects of delay, $F(2, 172) = 14.063$, $p < .001$, $\eta_p^2 = .141$; and time, $F(9, 774) = 49.754$, $p < .001$, $\eta_p^2 = .366$. Significant interactions emerged for delay × group, $F(2, 172) = 3.791$, $p = .024$, $\eta_p^2 = .042$; time × group, $F(3.03, 260.45) = 3.206$, $p = .023$, $\eta_p^2 = .036$; load × time, $F(27, 2322) = 2.870$, $p < .001$, $\eta_p^2 = .032$; delay × time, $F(18, 1548) = 15.352$, $p < .001$, $\eta_p^2 = .151$; and load × delay × time, $F(24.99, 2149.38) = 1.913$, $p = .004$, $\eta_p^2 = .022$.

Post-hoc analyses of the main effect of delay revealed that only the linear contrast was significant, $F(1, 86) = 29.953$, $p < .001$, $\eta_p^2 = .258$ (quadratic: $p > .90$). This effect was due to consistently greater mean activation with longer delay duration (mean predictor weights = 0.044, 0.057, and 0.070 for 1.5s, 3.0s, and 4.5s delay conditions, respectively; Figure 5.38B). Paired t-tests between adjacent delay conditions were both significant (1.5s vs. 3.0s: mean difference = 0.013, SEM = 0.005, $t(87) = 2.923$, $p = .004$; 3.0s vs. 4.5s: mean difference = 0.013, SEM = 0.006, $t(87) = 2.288$, $p = .025$). However, this effect appeared to be due to the pattern of more

sustained HDRs with longer delays rather than greater magnitude of activation per se (Figure 5.38B).

Both the delay × group and time × group interactions remained significant after removing variance predicted by age and gender (both *p*s < .05). Post-hoc analyses of the delay × group interaction showed that the groups exhibited different degrees of change from one condition to the next; while patients showed a steeper increase from 1.5s delay to 3.0s delay and little additional increase for 4.5s delay, controls showed a steep increase from 3.0s delay to 4.5s delay (Figure 5.39A); however, independent t-tests for each delay condition were non-significant (all *p*s > .10). Averaging across task conditions, controls showed a greater HDR increase compared with patients, but a similar post-peak return to baseline (Figure 5.39B).

5.8.4. Motor response network: TSI task results

Motor response network (component 4) estimated HDR plots for the TSI task are presented in Figure 5.40. The 2 (stimulus congruency; neutral vs. incongruent) × 2 (task-switch condition; neutral vs. incongruent colour-naming block) × 10 (time) × 2 (group) ANOVA revealed significant main effects of congruency, $F(1, 52) = 12.851$, $p = .001$, $\eta_p^2 = .198$; time, $F(9, 468) = 53.319$, $p < .001$, $\eta_p^2 = .506$; and group, $F(1, 52) = 5.040$, $p = .029$, $\eta_p^2 = .088$. Significant interactions emerged for time × group, $F(9, 468) = 7.271$, $p < .001$, $\eta_p^2 = .123$; congruency × time, $F(9, 468) = 20.166$, $p < .001$, $\eta_p^2 = .279$; task-switch × time, $F(4.64, 241.32) = 2.613$, $p = .029$, $\eta_p^2 = .048$; and congruency × task-switch × time, $F(5.07, 263.64) = 3.950$, $p = .002$, $\eta_p^2 = .071$.

The main effect of congruency was due to greater mean activation in the neutral condition than in the incongruent condition (mean predictor weights = 0.024 and -0.031 for neutral and incongruent stimuli, respectively), which emerged early in the HDR (Figure 5.41A). Alt-

hough the initial HDR increase and peak was similar between task-switch conditions, the task-switch × time interaction appeared to be driven by a steeper post-peak return-to-baseline and a greater degree of subsequent suppression in the neutral colour-naming task-switch condition compared with the incongruent colour-naming task-switch condition (Figure 5.41B).

The main effect of group did not remain significant after removing variance predicted by age ($p > .09$). However, the time × group interaction remained significant ($p < .05$) and was due to patients exhibiting a more gradual return to baseline rather than a greater magnitude of activation per se, as the initial HDR increase and peak was similar between groups (Figure 5.42).

5.8.5. Motor response network: TGT task results

Motor response network (component 4) estimated HDR plots for the TGT task are presented in Figure 5.43. Unlike all other tasks in this analysis, this network exhibited deactivation rather than activation in the TGT task. The 2 (condition; generating vs. hearing) × 10 (time) × 2 (group) ANOVA revealed only a significant main effect of time, $F(9, 522) = 101.098$, $p < .001$, $\eta_p^2 = .635$.

5.8.6. Summary of motor response network results

The motor response network (component 4; Figures 5.33 to 5.43) primarily comprised bilateral somatomotor regions, evidently underlying motor responses (or suppression thereof, in the TGT task). In both the WM and the SCAP task, onsets were staggered – consistent with the timing of button presses – and activity diminished or plateaued midway through the post-stimulus time series before increasing again in conditions with a long delay (Figures 5.35 and 5.38B for WM and SCAP, respectively). In the TSI task, activation was greater for neutral stimuli than for incongruent stimuli (Figure 5.41A), and post-peak activation was slightly more sustained following an incongruent colour-naming block (Figure 5.41B). Group differences

emerged in all tasks except TGT. In the WM task, a load × group interaction emerged that was due to controls exhibiting lower mean activation in the 6-letter condition than in the 4-letter condition, while patients showed little of this effect and thus exhibited greater activation than controls in the 6-letter condition (Figure 5.36). In the TSI task, patients sustained activity in this network considerably longer than did controls (Figure 5.42). In the SCAP task, patients showed less activation during the increase-to-peak phase of the HDR (Figure 5.39B).

5.9. Visual Attention Network (Component 5)

5.9.1. Anatomical characteristics

The visual attention network (component 5) was primarily characterized by bilateral (de)activation in occipital cortex (occipital poles, lateral occipital cortex, and occipital fusiform gyri), precentral gyri, middle frontal gyri, SMA/superior frontal gyrus, and thalamus. See Figure 5.44 for anatomical visualization and Table 5.11 for coordinates of peak locations.

5.9.2. Visual attention network: WM task results

Visual attention network (component 5) estimated HDR plots for the WM task are presented in Figure 5.45. The 2 (load; 4 letters vs. 6 letters) × 2 (delay; 0s vs. 4s) × 10 (time) × 2 (group) ANOVA revealed significant main effects of load, $F(1, 52) = 13.512$, $p = .001$, $\eta_p^2 = .206$; delay, $F(1, 52) = 68.578$, $p < .001$, $\eta_p^2 = .569$; and time, $F(9, 468) = 361.523$, $p < .001$, $\eta_p^2 = .874$. Significant interactions emerged for load × time, $F(9, 468) = 29.900$, $p < .001$, $\eta_p^2 = .365$; and delay × time, $F(9, 468) = 38.746$, $p < .001$, $\eta_p^2 = .427$. Initially, no significant effects emerged involving group differences (all ps > .07).

Post-hoc analyses revealed that there was greater mean activation in the 6-letter load condition than in the 4-letter load condition (mean predictor weights = 0.076 and 0.090 for 4 letters and 6 letters, respectively), and greater mean activation in the 0s delay condition than in the

4s delay condition (mean predictor weights = 0.103 and 0.064, respectively). Although the increase-to-peak phase of the HDR was the same across delay conditions, the 0s delay condition exhibited a more gradual return to baseline, most likely due to the immediate presentation of the probe stimulus following the encoding period (Figure 5.46). In the 4s delay condition, however, there was no presence of a second peak that would correspond with the presentation of the probe after a delay, suggesting that this activation was more important during the encoding phase of the task.

Contrary to the initial ANOVA, the load × time × group interaction became significant only after removing variance predicted by age, $F(4.79, 249.08) = 2.656$, $p = .025$, $\eta_p^2 = .049$. This interaction was due to patients exhibiting less activation in this network and a slightly more gradual return to baseline that was statistically significant from 10 to 12 seconds (see Figure 5.47).

5.9.3. Visual attention network: SCAP task results

Visual attention network (component 5) estimated HDR plots for the SCAP task are presented in Figure 5.48. The 4 (load; 1, 3, 5, or 7 dots) × 3 (delay; 1.5s, 3.0s, or 4.5s) × 10 (time) × 2 (group) ANOVA revealed significant main effects of load, $F(3, 258) = 48.089$, $p < .001$, $\eta_p^2 = .359$; delay, $F(2, 172) = 15.610$, $p < .001$, $\eta_p^2 = .154$; and time, $F(9, 774) = 124.160$, $p < .001$, $\eta_p^2 = .591$. Significant interactions emerged for time × group, $F(2.95, 253.39) = 4.311$, $p = .006$, $\eta_p^2 = .048$; load × delay, $F(6, 516) = 3.785$, $p = .001$, $\eta_p^2 = .042$; load × time, $F(27, 2322) = 39.679$, $p < .001$, $\eta_p^2 = .316$; load × time × group, $F(13.20, 1134.91) = 1.854$, $p = .031$, $\eta_p^2 = .021$; delay × time, $F(18, 1548) = 10.548$, $p < .001$, $\eta_p^2 = .109$; and load × delay × time, $F(54, 4644) = 9.550$, $p < .001$, $\eta_p^2 = .100$.

Post-hoc analyses of the main effect of load revealed that the linear and quadratic contrasts were significant, with the linear contrast having the greater effect size (linear: $F(1, 86) = 88.975$, $p < .001$, $\eta_p^2 = .509$; quadratic: $F(1, 86) = 41.258$, $p < .001$, $\eta_p^2 = .324$; cubic $p > .90$). This was due to a tendency for greater activation with increasing load (mean predictor weights = -0.020, 0.008, 0.023, and 0.023 for 1, 3, 5, and 7 dots, respectively; Figure 5.49A). Paired t-tests between adjacent load conditions were significant for 1 versus 3 dots (mean difference = 0.028, SEM = 0.004, $t(87) = 7.218$, $p < .001$) and 3 versus 5 dots (mean difference = 0.015, SEM = 0.004, $t(87) = 3.359$, $p = .001$), but not 5 versus 7 dots ($p > .90$). Post-hoc analyses of the main effect of delay revealed a significant quadratic contrast, $F(1, 86) = 30.480$, $p < .001$, $\eta_p^2 = .262$ (linear $p > .50$). This was due to mean activation in the 3.0s delay condition being lower than both the 1.5s delay condition (mean difference = 0.012, SEM = 0.003, $t(87) = 4.444$, $p < .001$) and the 4.5s delay condition (mean difference = 0.013, SEM = 0.003, $t(87) = 5.074$, $p < .001$; Figure 5.49B). Although the initial HDR increase was the same across delay conditions, the delay × time effect appeared to be due to a more gradual return to baseline with *shorter* delay periods, as observed in the WM task (Figure 5.49C).

Both the time × group and load × time × group interactions remained significant after removing variance predicted by age and gender (both ps $< .05$). Across task conditions, the time × group interaction appeared to be due to an attenuated response in schizophrenia patients (i.e., less increase-to-peak and less extreme post-peak suppression; Figure 5.50A). The load × time × group interaction appeared to be due to differences in the post-peak return to baseline phase of the HDR, which may amount to controls exhibiting a steeper decrease below baseline particularly for conditions of higher cognitive load (Figure 5.50B).

5.9.4. Visual attention network: TSI task results

Visual attention network (component 5) estimated HDR plots for the TSI task are presented in Figure 5.51. The 2 (stimulus congruency: neutral vs. incongruent) × 2 (task-switch condition: following neutral vs. incongruent colour-naming block) × 10 (time) × 2 (group) ANOVA revealed significant main effects of congruency, $F(1, 52) = 96.571$, $p < .001$, $\eta_p^2 = .650$; task-switch, $F(1, 52) = 4.218$, $p = .045$, $\eta_p^2 = .075$; and time, $F(9, 468) = 39.661$, $p < .001$, $\eta_p^2 = .433$. Significant interactions emerged for congruency × time, $F(9, 468) = 82.180$, $p < .001$, $\eta_p^2 = .612$; task-switch × time, $F(9, 468) = 5.007$, $p < .001$, $\eta_p^2 = .088$; and congruency × task-switch × time, $F(9, 468) = 32.732$, $p < .001$, $\eta_p^2 = .386$. No significant effects emerged involving group differences before or after removing variance predicted by age (all *p*s > .10).

The main effect of congruency was due to greater mean activation in trials with neutral stimuli than with incongruent stimuli (mean predictor weights = 0.032 and -0.055 for neutral and incongruent stimuli, respectively). Further, activation in the neutral stimulus condition was somewhat sustained throughout the post-stimulus time series, whereas activity in the incongruent condition was brief and was followed by a substantial suppression below baseline (Figure 5.52A). The main effect of task-switch was due to greater mean activation following incongruent colour-naming blocks than following neutral colour-naming blocks (mean predictor weights = -0.012 and -0.009 for neutral and incongruent colour-naming, respectively), and the peak activation was followed by greater post-peak suppression in the incongruent task-switch condition (Figure 5.52B). Differences in HDR shapes between stimulus congruency conditions were particularly pronounced following an incongruent colour-naming block (Figure 5.51).

5.9.5. Visual attention network: TGT task results

Visual attention network (component 5) estimated HDR plots for the TGT task are presented in Figure 5.53. The 2 (condition; generating vs. hearing) × 10 (time) × 2 (group) ANOVA revealed significant main effects of time, $F(9, 522) = 302.867$, $p < .001$, $\eta_p^2 = .839$; and group, $F(1, 58) = 4.926$, $p = .030$, $\eta_p^2 = .078$. Significant interactions emerged for time × group, $F(2.62, 151.71) = 6.259$, $p = .001$, $\eta_p^2 = .097$; and condition × time, $F(3.50, 202.92) = 2.995$, $p = .025$, $\eta_p^2 = .049$.

The condition × time interaction was due to the steeper HDR increase and earlier peak in the generating condition than in the hearing condition (Figure 5.53). Both the main effect of group and the time × group interaction remained significant after removing variance predicted by age (both *p*s < .05). The main effect of group was due to greater mean activation in schizophrenia patients than in healthy controls (mean predictor weights = 0.057 and 0.081 for controls and patients, respectively). Patients also exhibited a steeper HDR increase and decrease compared with controls (Figure 5.54).

5.9.6. Summary of visual attention network results

The visual attention network (component 5; Figures 5.44 to 5.54) comprised activation in visual cortex, SMA, precentral gyri, and thalamus, but it did not appear to underlie primary visual perception per se. A substantial effect of cognitive load emerged in the WM task, despite the fact that the number of items on-screen was the same regardless of whether 4 or 6 letters were displayed, as the 4-letter string was flanked by pound ('#') signs. Moreover, this network did not exhibit a second peak corresponding to the presentation of the probe stimulus in the 4s delay condition. An effect of task condition emerged in the TGT task (i.e., greater peak in the generating condition; Figure 5.53) despite the fact that stimulus size and duration was identical between

conditions, and stimuli were randomly assigned to task conditions across participants. Similarly, the effect of task-switching in the TSI task, in which a greater response and greater post-peak suppression was exhibited following an incongruent colour-naming block (Figure 5.52B), cannot be explained by basic visual perception demands, as the proportion of neutral versus incongruent stimuli was the same regardless of task-switch condition. Group differences in the WM and SCAP tasks amounted to attenuated and/or more gradual responses in patients which, given the early onset of this network, may reflect impaired encoding into memory (Figures 5.47 and 5.50 for WM and SCAP, respectively). However, patients exhibited greater activation than controls in the TGT task (Figure 5.54).

5.10. Occipital Network (Component 7)

5.10.1. Anatomical characteristics

The occipital network (component 7) was primarily characterized by widespread bilateral (de)activation in occipital cortex (especially medial areas), including lingual gyrus, intracalcarine cortex, cuneal cortex, and superior lateral occipital cortex, as well as precuneus and right angular gyrus. See Figure 5.55 for anatomical visualization and Table 5.12 for coordinates of peak locations.

5.10.2. Occipital network: WM task results

Occipital network (component 7) estimated HDR plots for the WM task are presented in Figure 5.56, reflecting deactivation in this network. The 2 (load; 4 vs. 6 letters) × 2 (delay; 0s vs. 4s) × 10 (time) × 2 (group) ANOVA revealed a significant main effect of time, $F(9, 468) = 32.195$, $p < .001$, $\eta_p^2 = .382$; and a significant interaction emerged for delay × time, $F(9, 468) = 14.881$, $p < .001$, $\eta_p^2 = .223$. No significant effects involving group differences emerged before or after removing variance predicted by age (all ps > .07).

While the decrease-to-peak phases of the HDRs were the same between delay conditions, the 0s delay condition showed a more gradual return to baseline (Figure 5.57), mirroring the pattern observed in the visual attention network (component 5; Figure 5.46). However, the 0s delay condition also showed a continual increase following peak deactivation, whereas the post-peak increase in the 4s delay condition plateaued from the 12-second post-stimulus time bin onwards (Figure 5.57).

5.10.3. Occipital network: SCAP task results

Occipital network (component 7) estimated HDR plots for the SCAP task are presented in Figure 5.58, reflecting activation rather than deactivation in this network. The 4 (load; 1, 3, 5, or 7 dots) × 3 (delay; 1.5s, 3.0s, or 4.5s) × 10 (time) × 2 (group) ANOVA revealed significant main effects of load, $F(3, 258) = 17.176$, $p < .001$, $\eta_p^2 = .166$; delay, $F(2, 172) = 6.536$, $p = .002$, $\eta_p^2 = .071$; and time, $F(9, 774) = 22.094$, $p < .001$, $\eta_p^2 = .204$. Significant interactions emerged for load × delay, $F(6, 516) = 5.586$, $p < .001$, $\eta_p^2 = .061$; load × time, $F(27, 2322) = 4.895$, $p < .001$, $\eta_p^2 = .054$; delay × time, $F(18, 1548) = 12.186$, $p < .001$, $\eta_p^2 = .124$; and load × delay × time, $F(54, 4644) = 5.950$, $p < .001$, $\eta_p^2 = .065$. No significant effects involving group differences emerged before or after removing variance predicted by age and gender (all ps > .10).

Post-hoc analyses of the main effect of load revealed significant linear and cubic contrasts, with the linear contrast having the greater effect size (linear: $F(1, 86) = 33.879$, $p < .001$, $\eta_p^2 = .283$; cubic: $F(1, 86) = 8.301$, $p = .005$, $\eta_p^2 = .088$; quadratic: $p > .80$). This was due to a general tendency for greater activation with greater cognitive load (mean predictor weights = 0.001, 0.001, -0.027, and -0.028 for 1, 3, 5, and 7 dots, respectively; see Figure 5.59A), and specifically in the change from 3 to 5 dots (mean difference = 0.027, SEM = 0.006, $t(87) = 4.378$,

$p < .001$; ps for 1 vs. 3 dots and 5 vs. 7 dots contrasts > .70). Post-hoc analyses of the main effect of delay revealed a significant linear contrast only (linear: $F(1, 86) = 10.724$, $p = .002$, $\eta_p^2 = .111$; quadratic: $p > .10$). This was due to less activation with longer delay conditions (mean predictor weights = -0.022, -0.011, and -0.008 for 1.5s, 3.0s, and 4.5s delay, respectively; see Figure 5.59B). Paired t-tests between adjacent delay conditions revealed that the 1.5s versus 3.0s delay contrast was significant (mean difference = 0.011, SEM = 0.004, $t(87) = 3.183$, $p = .002$; other $p > .60$). The 1.5s delay condition exhibited continual activation to a later peak as compared with the 3.0s and 4.5s delay conditions, following a slight plateau occurring at around the same time as when peak activation occurs in the 3.0s and 4.5s delay conditions. A possible explanation for this is that the peak in the 1.5s delay condition is actually a secondary response – perhaps elicited by the probe stimulus – that ends up being higher than the first because the delay is too brief for a full return to baseline in the 1.5s delay condition. By contrast, the longer delay conditions exhibit a full decline and then a much smaller second peak later on in the post-stimulus time series (Figure 5.59C).

5.10.4. Occipital network: TSI task results

Occipital network (component 7) estimated HDR plots are presented in Figure 5.60, reflecting deactivation in this network. The 2 (stimulus congruency; neutral vs. incongruent) × 2 (task-switch condition; following neutral vs. incongruent colour-naming) × 10 (time) × 2 (group) ANOVA revealed significant main effects of congruency, $F(1, 52) = 33.411$, $p < .001$, $\eta_p^2 = .391$; task-switch, $F(1, 52) = 6.649$, $p = .013$, $\eta_p^2 = .113$; time, $F(9, 468) = 71.731$, $p < .001$, $\eta_p^2 = .580$; and group, $F(1, 52) = 4.822$, $p = .033$, $\eta_p^2 = .085$. Significant interactions emerged for congruency × task-switch, $F(1, 52) = 52.272$, $p < .001$, $\eta_p^2 = .501$; congruency × time, $F(9, 468) = 53.568$, $p < .001$, $\eta_p^2 = .507$; task-switch × time, $F(9, 468) = 10.229$, $p < .001$, $\eta_p^2 =$

.164; and congruency × task-switch × time, $F(9, 468) = 4.428$, $p < .001$, $\eta_p^2 = .078$. The main effect of group did not remain significant after removing variance predicted by age ($p > .10$).

The main effect of stimulus congruency was due to greater mean deactivation in the incongruent condition compared with the neutral condition (mean predictor weights = -0.022 and 0.047 for neutral and incongruent stimuli, respectively). This was driven by the combination of more extreme peak deactivation in the incongruent condition and a much greater post-HDR rise above baseline in the neutral condition (Figure 5.61A). The main effect of task-switch was due to greater mean deactivation following incongruent colour-naming compared with neutral colour-naming blocks (mean predictor weights = 0.008 and 0.017 following neutral and incongruent colour-naming, respectively). Peak deactivation occurred later in the incongruent colour-naming than the neutral colour-naming task-switch condition (Figure 5.61B). Overall, the effect of stimulus congruency was only pronounced following an incongruent colour-naming block rather than a neutral colour-naming block (Figure 5.61C).

5.10.5. Occipital network: TGT task results

Occipital network (component 7) estimated HDR plots for the TGT task are presented in Figure 5.62, reflecting activation in this network. The 2 (condition; generating vs. hearing) × 2 (time) × 2 (group) ANOVA revealed a significant main effect of time, $F(9, 522) = 39.128$, $p < .001$, $\eta_p^2 = .403$. Significant interactions emerged for condition × group, $F(1, 58) = 11.107$, $p = .002$, $\eta_p^2 = .161$; and time × group, $F(3.89, 225.53) = 2.970$, $p = .021$, $\eta_p^2 = .049$.

Both the condition × group and time × group interactions remained significant after removing variance predicted by age (both ps $< .05$). The condition × group interaction was due to the groups showing opposite effects of task condition (Figure 5.63). While healthy controls showed greater mean activation in the generating condition than in the hearing condition (mean

difference = 0.013, SEM = 0.005, $t(31) = 2.479$, $p = .019$), schizophrenia patients showed greater mean activation in the hearing condition than in the generating condition (mean difference = 0.012, SEM = 0.005, $t(27) = 2.266$, $p = .032$). Although initial activation and HDR peaks were similar between groups, a more prolonged post-peak response emerged in patients (Figure 5.63).

5.10.6. Summary of occipital network results

The occipital network (component 7; Figures 5.55 to 5.63) comprised visual cortex (de)activation originating in the medial occipital lobes, which activated in the SCAP task and TGT (Figures 5.58 and 5.62, respectively), but deactivated in the WM task and TSI task (Figures 5.56 and 5.60, respectively). No main effect of cognitive load emerged in the WM task, and although there was greater activity with increasing load in the SCAP task, this is confounded by there being more complex visual stimuli at high load levels due to the greater number of dots displayed on-screen. A condition × group interaction emerged in the TGT task which reflected contrasting effects of condition between groups; that is, healthy controls exhibited lower mean activation of this network in the hearing condition than in the generating condition, whereas patients exhibited lower mean activation of this network in the generating condition than in the hearing condition (Figure 5.63A). The basis of this effect was in the post-peak return to baseline and suppression below baseline, as patients exhibited more sustained activation following the peak as well as greater post-peak suppression towards the end of the time series (Figure 5.63B).

5.11. Correlations Between Task Performance and HDR Increases/Decreases

5.11.1. WM task performance and HDRs

5.11.1.1. Computations of WM HDR measures

Due to the difference in trial lengths and event timing between 0s delay trials and 4s delay trials, predictor weights and fMRI task performance were averaged across load condition but

not delay condition, resulting in four HDR measures per component (increase-to-peak and return-to-baseline for the 0s delay and 4s delay conditions). Correlations between HDR measures and WM task performance were only examined between the corresponding delay conditions; for example, a correlation between accuracy in the 0s delay condition and HDR measures in the 4s delay condition would not be performed. WAIS scaled digit span was included in the analysis as an additional behavioural WM measure.

For the DMN (component 1; Figure 5.9A), the 0s delay increase-to-peak (ITP) measure was computed by averaging across time bins from 6-10 seconds, and the return-to-baseline (RTB) measure was computed by averaging across time bins from 12-18 seconds. The DMN 4s delay ITP was computed by averaging time bins from 6-14 seconds, and RTB was computed by averaging time bins from 16-20 seconds. For the internal attention network (component 2; Figure 5.17A), the 0s delay ITP was computed by averaging time bins from 6-10 seconds, and RTB was computed by averaging time bins from 12-16 seconds. The internal attention network 4s delay ITP was computed by averaging time bins from 6-14 seconds, and RTB was computed by averaging time bins from 16-20 seconds. For the sensorimotor network (component 3; Figure 5.26), the 0s delay ITP was computed by averaging time bins from 10-12 seconds, and RTB was computed by averaging time bins from 14-18 seconds. The sensorimotor network 4s delay ITP was computed by averaging time bins from 14-16 seconds, and RTB was computed by averaging time bins from 18-20 seconds. For the motor response network (component 4; Figure 5.35), the 0s delay ITP was computed by averaging time bins from 8-10 seconds, and RTB was computed by averaging time bins from 12-16 seconds. The motor response network 4s delay ITP was computed by averaging time bins from 14-16 seconds, and RTB was computed by averaging time bins from 18-20 seconds. For the visual attention network (component 5; Figure 5.46), the 0s de-

lay ITP was computed by averaging time bins from 4-8 seconds, and RTB was computed by averaging time bins from 10-16 seconds. The visual attention network 4s delay ITP was computed by averaging time bins from 4-8 seconds, and RTB was computed by averaging time bins from 10-16 seconds. Finally, for the occipital network (component 7, Figure 5.57), the 0s delay ITP was computed by averaging time bins from 4-8 seconds, and RTB was computed by averaging time bins from 10-20 seconds. The occipital network 4s delay ITP was computed by averaging time bins from 4-8 seconds, and RTB was computed by averaging time bins from 10-12 seconds.

5.11.1.2. Results

Although no correlations reached a statistical threshold of $p < .01$, some trend correlations emerged in the visual attention network (component 5) with a more liberal threshold of $p < .05$. Of the fMRI WM task measures, only the 4s delay condition showed a small correlation between the visual attention network ITP and response accuracy ($r(52) = .270$, $p = .048$). Interestingly, digit span also showed small correlations with component 5 ITP in both the 0s delay and 4s delay conditions (0s delay: $r(52) = .307$, $p = .024$; 4s delay: $r(52) = .313$, $p = .021$). Although these correlations should be interpreted with caution given the potentially inflated risk of Type I error, it is noteworthy that both the fMRI WM task performance and the out-of-scanner neuropsychological measure of WM capacity showed the same relationship with the same network underlying this task.

5.11.2. SCAP task performance and HDRs

5.11.2.1. Computations of SCAP HDR measures

A similar approach as taken in the WM task analysis above was applied to the SCAP task HDRs; that is, predictor weights and task performance were averaged across load conditions but not delay. This resulted in six HDR measures per component (ITP and RTB for 1.5s, 3.0s, and

4.5s delay conditions). WMS digit span was analysed as well, but as standard scores were not available for this dataset, partial correlations between HDR measures and digit span were performed while controlling for age.

For the DMN (component 1; Figure 5.11C), the 1.5s delay ITP was computed by averaging time bins from 6-12 seconds, and the RTB was computed by averaging time bins from 14-20 seconds. The DMN 3.0s delay ITP was computed by averaging time bins from 6-12 seconds, and RTB was computed by averaging time bins from 14-20 seconds. The DMN 4.5s delay ITP was computed by averaging time bins from 6-14 seconds, and RTB was computed by averaging time bins from 16-20 seconds. For the internal attention network (component 2; Figure 5.19C), the 1.5s delay ITP was computed by averaging time bins from 6-10 seconds, and the RTB was computed by averaging time bins from 12-18 seconds. The internal attention network 3.0s delay ITP was computed by averaging time bins from 6-12 seconds, and RTB was computed by averaging time bins from 14-18 seconds. The internal attention 4.5s delay ITP was computed by averaging time bins from 6-14 seconds, and RTB was computed by averaging time bins from 16-20 seconds. For the sensorimotor network (component 3; Figure 5.28C), the 1.5s delay ITP was computed by averaging time bins from 6-8 seconds, and the RTB was computed by averaging time bins from 10-12 seconds. The sensorimotor network 3.0s delay ITP was computed by averaging time bins from 6-10 seconds, and RTB was computed by averaging time bins from 12-14 seconds. The sensorimotor network 4.5s delay ITP was computed by averaging time bins from 6-12 seconds, and RTB was computed by averaging time bins from 14-16 seconds. For the motor response network (component 4; Figure 5.38B), the 1.5s delay ITP was computed by averaging time bins from 6-10 seconds, and the RTB was computed by averaging time bins from 12-16 seconds. The motor response network 3.0s delay ITP was computed by averaging time bins from

6-12 seconds, and RTB was computed by averaging time bins from 14-16 seconds. The motor response network 4.5s delay ITP was computed by averaging time bins from 6-14 seconds, and RTB was computed by averaging time bins from 16-20 seconds. For the visual attention network (component 5; Figure 5.49C), the 1.5s delay ITP was computed by averaging time bins from 6-8 seconds, and the RTB was computed by averaging time bins from 10-14 seconds. The visual attention network 3.0s delay ITP was computed by averaging time bins from 6-8 seconds, and RTB was computed by averaging time bins from 10-16 seconds. The visual attention network 4.5s delay ITP was computed by averaging time bins from 6-8 seconds, and RTB was computed by averaging time bins from 10-12 seconds. The occipital network (component 7; Figure 5.59C) was not examined due to the ambiguity and inconsistency of HDR shapes across delay conditions.

5.11.2.2. Results

The correlations between behavioural measures and HDR ITPs/RTBs in the SCAP task were similar to those observed in the WM task. Significant correlations emerged for the visual attention network (component 5), including a correlation between the 1.5s delay ITP and 1.5s delay accuracy ($r(86) = .280$, $p = .008$); and between the 3.0s delay ITP and 3.0s delay accuracy ($r(86) = .284$, $p = .007$). At a more liberal threshold of $p < .05$, trend correlations also emerged in the visual attention network between the 4.5s delay ITP and 4.5s delay accuracy ($r(86) = .267$, $p = .012$), and between 4.5s delay ITP and digit span while controlling for age ($r(85) = .225$, $p = .036$). Trend correlations also emerged for the motor response network (component 4) between the 4.5s delay ITP and 4.5s delay accuracy($r(86) = .260$, $p = .014$); and between the 4.5s delay ITP and digit span while controlling for age ($r(85) = .240$, $p = .025$). No correlations emerged for RTBs with either SCAP task accuracy or digit span (all ps > .15).

5.11.3. TSI task performance and HDRs

5.11.3.1. Computations of TSI HDR measures

TSI task performance measures (accuracy and RTs) and HDR ITP/RTB measures were averaged across all conditions for the following analysis (averaged time courses for all components are shown in Figure 5.4D). Digit span was also included as a behavioural measure of interest for comparison with the above results from the WM task. For the DMN (component 1), the ITP measure was computed by averaging across time bins from 4-8 seconds, and the RTB measure was computed by averaging across time bins from 10-16 seconds. For the internal attention network (component 2), the ITP measure was computed by averaging across time bins from 4-6 seconds, and the RTB measure was computed by averaging across time bins from 8-16 seconds. For the sensorimotor network (component 3), the ITP measure was computed by averaging across time bins from 6-8 seconds, and the RTB measure was computed by averaging across time bins from 10-12 seconds. For the motor response network (component 4), the ITP measure was computed by averaging across time bins from 4-6 seconds, and the RTB measure was computed by averaging across time bins from 8-12 seconds. For the visual attention network (component 5), the ITP measure was computed by averaging across time bins from 4-6 seconds, and the RTB measure was computed by averaging across time bins from 8-12 seconds. Finally, for the occipital network (component 7), the ITP measure was computed by averaging across time bins from 4-8 seconds, and the RTB measure was computed by averaging across time bins from 10-18 seconds.

5.11.3.2. Results

With a threshold of $p < .01$, a significant negative correlation emerged between the motor response network (component 4) RTB and TSI task accuracy ($r(52) = -.375$, $p = .005$). At a more

liberal threshold of $p < .05$, trend correlations emerged between task accuracy and the sensorimotor network (component 3) ITP ($r(52) = .328$, $p = .015$), and a negative trend correlation emerged between accuracy and the internal attention network (component 2) RTB ($r(52) = -.290$, $p = .034$). No correlations emerged with mean RT or digit span (all ps $> .05$).

5.12. Discussion of 4-Task fMRI-CPCA Results

Eight components were extracted from the 4-task fMRI-CPCA. Components 1-5 and 7 (i.e., the DMN, internal attention, sensorimotor, motor response, visual attention, and occipital networks) reflected task-related functional brain networks engaged in the four tasks to varying degrees, while components 6 and 8 reflected artifacts arising from non-cortical sources. Results of these networks with respect to each task are discussed below, followed by a discussion of functions that may be attributed to the networks, and then the group differences that emerged.

5.12.1. WM task

Most of the networks that emerged in this analysis were similar to those of the WM-TGT multi-experiment fMRI-CPCA in Chapter 3 – with the notable exception of the sensorimotor network, component 3 – and showed correspondingly similar HDR shapes consistent with earlier interpretations. Comparing the series of HDR onsets across networks (Figure 5.4B), activation of the visual attention network (component 5, replicating the "visual attention" network previously observed in Chapter 3) may support encoding of the letter string at the trial onset, and its diminishing intensity could reflect a coordinated shift from external attention to internal attention as the internal attention network (component 2, replicating the "internal attention" network previously observed) becomes engaged, which may be required so as to maintain a mental representation of the stimuli. Components 1-4 (i.e., DMN, internal attention, sensorimotor, and motor response networks) all exhibited staggered peaks consistent with delay length, suggesting that

they underlie processes that initiate after or extend beyond the encoding phase of the task. However, HDRs in components 1 and 2 (DMN and internal attention) also showed similar *onsets* across delay conditions (Figures 5.9A and 5.17A for the DMN and internal attention network, respectively), while HDRs in component 3 and 4 (sensorimotor and motor response) showed staggered onsets that initiated later in the post-stimulus time series (suggesting that they underlie processes that initiate after the probe appears; Figures 5.26 and 5.35 for the sensorimotor and motor response networks, respectively). The visual attention network (component 5) was the most highly correlated with task performance (and with digit span), but only in the 4s delay condition; that is, the condition with a greater requirement to encode items into memory store. The internal attention network (component 2) appeared to support and/or coincide with WM maintenance, but may not directly underlie the encoding of items into memory, as it was not correlated with task performance or digit span. The occipital network (component 7) displayed a similar time course as the visual attention network, but reflected deactivation rather than activation (Figure 5.4B), and was not dependent on cognitive load.

5.12.2. SCAP task

For the most part, the networks exhibited similar patterns in the SCAP task as in the WM task, with the exceptions of the sensorimotor and occipital networks (components 3 and 7; compare Figure 5.4B and C). The sensorimotor network was much more suppressed during the SCAP task, with deactivation peaking just before the motor response (component 4) HDR peak. Nevertheless, its initial suppression followed by disinhibition later in the post-stimulus time series is not entirely inconsistent with the pattern observed in the verbal WM task. The occipital network, however, was active in the SCAP task rather than being suppressed, and in the 3.0s and 4.5s delay conditions, exhibited multiple peaks that were consistent with the timing of visual

stimuli appearing on the screen (Figure 5.59C). Further, component 7 was more engaged in conditions of higher cognitive load in the SCAP task but not the WM task; this may be due to greater visual processing demands (e.g., searching/saccades) with larger target arrays in the SCAP task. Otherwise, brain activity in the SCAP task exhibited similar patterns as the WM task in the DMN (component 1; early onsets and sustained, load-dependent deactivation), the internal attention network (component 2; more gradual increases, with greater magnitude of load-dependent activation with longer delay duration), the motor response network (component 4; late, staggered onsets and peaks consistent with the timing of motor responses), and the visual attention network (component 5; early onsets and load-dependent peaks, and the most highly correlated with response accuracy and digit span).

5.12.3. TSI task

Remarkably, the networks showed clearly separable HDR shapes in the TSI task despite trials being only 2 seconds in duration (see Figure 5.4D). The DMN (component 1) initiated early and was somewhat sustained as observed in other tasks, but not to the same degree as the occipital network (component 7), which exhibited a substantial and sustained suppression for most of the post-stimulus time series before rising well above baseline (presumably during the ITI). The internal attention network (component 2) not only showed considerably greater engagement for incongruent stimuli than for neutral stimuli (Figure 5.22A), but it also exhibited a task-switch effect whereby the HDR was more sustained when the preceding colour-naming block consisted of incongruent stimuli than when it consisted of neutral stimuli (Figure 5.22B). In addition, a trend correlation emerged in which the degree of sustained activation in the RTB phase of the HDR was negatively correlated with response accuracy in the TSI task (i.e., higher accuracy correlated with lower post-peak HDR values), despite activation in this network appearing to extend

beyond the button-press responses (based on its HDR timing relative to the motor response network, component 4; see Figure 5.4D). It could be the case that performance in the TSI task relies on the brain's ability to rapidly switch between states from trial to trial, and that a rapid post-peak decline in this network reflects more efficient switching between networks, improving accuracy on the subsequent trial. Alternatively, it could be that the HDR for the internal attention network is more sustained following an incorrect response due to an error monitoring/evaluation process, and so individuals who produce more incorrect responses have on average higher RTB activity. Both explanations are possible, but the latter is further supported by the finding of a much more sustained HDR in trials with an incongruent word-reading stimulus following an incongruent colour-naming block (i.e., the condition with the lowest accuracy; Figure 5.21), which may be explained by a post-response evaluation process such as reflecting on the current task rules. This is also consistent with existing literature linking post-response error processing (but not necessarily response conflict per se) to dorsal anterior cingulate–anterior insula connectivity and/or co-activation (e.g., Bastin et al., 2016; Edwards, Calhoun, & Kiehl, 2012; Hoffmann, Labrenz, Themann, Wascher, & Beste, 2014; Iannaccone et al., 2015). However, this explanation cannot be tested without a more direct comparison of brain activity during correct-response trials versus incorrect-response trials, which would not necessarily be appropriate with the present dataset given the large disparity in the number of correct versus incorrect responses in these participants. The sensorimotor network (component 3) exhibited a similar pattern in the TSI task as in the WM task, having relatively late onsets and being more engaged in the (easier) neutral stimulus condition than in the incongruent stimulus condition (Figure 5.31A). Although a trend positive correlation emerged between the sensorimotor network ITP and task accuracy, it is important to note that this phase of the HDR occurs late in the post-stimulus time series as a

whole as compared to the other networks (Figure 5.4D), and so activation is unlikely to *produce* correct responses. A possible explanation is that activation of this network is greater following correct responses. Unlike in the WM and SCAP tasks, the motor response network (component 4) initiated and peaked fairly early in the TSI task, which is consistent with participants having to make more rapid responses. The motor response network also exhibited a significant negative correlation between degree of sustained activation in the RTB phase of the HDR and response accuracy, which, as mentioned above with respect to the similar (trend) relationship that was observed between the internal attention network RTB and response accuracy, could indicate that rapid deactivation of this network is important for accuracy on the subsequent trial (e.g., reflecting a "reset" of motor response inhibition) or that this network deactivates quicker following a correct response, or some combination of both. The visual attention network (component 5) exhibited a similarly early and brief response as in the WM and SCAP tasks, although it was much less engaged in the TSI task – especially for incongruent stimuli – and was not correlated with task performance.

5.12.4. TGT task

Although no overt behavioural response was recorded in the TGT task, variability in shapes and timing between networks emerged as observed in the other three tasks. The DMN (component 1) peaked slightly earlier in the hearing condition than in the generating condition (Figure 5.14), perhaps because deactivation of DMN is not as important for passive speech perception. The internal attention network (component 2) was engaged in the generating condition, but showed a completely flat HDR in the hearing condition (i.e., neither activated nor deactivated in response to the trial onset; Figure 5.23). This was the only network that exhibited such a striking difference between conditions, demonstrating that it does not support any bottom-up,

externally-oriented attention processes that would be involved in the hearing condition. Conversely, the sensorimotor network (component 3) was considerably more engaged in the hearing condition than in the generating condition – presumably underlying auditory perception – although it may play some role in attention as well, considering it was not completely suppressed in the generating condition (Figure 5.32). The motor response network (component 4) was suppressed for both conditions, consistent with the notion of it underlying motor responses (which are not involved in the TGT task), although it is noteworthy that it was actively suppressed below baseline rather than showing a flat HDR (Figure 5.43). This could be a result of participants being instructed to remain still during scanning, and this sample in particular may have been primed to respond, as these participants completed other tasks during the same scanning session. In summary, the DMN, internal attention, and visual attention networks showed greater engagement in the generating condition to some degree, although this was relatively slight in the DMN and visual attention network, and seemed to be more due to differences in timing of peaks rather than magnitude per se (with the generating condition peaking later in the DMN and earlier in the visual attention network). The sensorimotor network showed considerably more engagement in the hearing condition than in the generating condition, and the motor response network and occipital network (component 7) showed no effects of condition. Like the SCAP task, the occipital network was activated rather than deactivated in the TGT, although its response was relatively brief compared with the other networks (Figure 5.4E).

5.12.5. Task-related network functions

Deactivation in the DMN (component 1; Figures 5.7 to 5.14), comprising anterior medial frontal cortex, medial parietal cortex (posterior cingulate gyri and precuneus), superior lateral occipital cortex, middle temporal gyri, and temporal poles, is widely observed in task-state fMRI

literature (Raichle, 2015), and so this terminology is used for consistency with fMRI convention. As expected for the DMN, the degree of deactivation tended to be greater with more demanding conditions in all tasks, and HDRs initiated early and were usually more sustained than other networks.

The internal attention network (component 2; Figures 5.15 to 5.23) consisted of connectivity typically associated with WM, including the DLPFC, dorsal anterior cingulate cortex, anterior insula, and intraparietal sulcus (Rottschy et al., 2012). Findings from the WM and SCAP tasks are consistent with this characterization in that it was more engaged with longer maintenance periods, and was dependent on cognitive load. However, the TSI results are not necessarily consistent with such a characterization, as a WM network would not be expected to remain activated following the button-press response, which is what was exhibited in the TSI task (Figure 5.4D, compare components 2 and 4). This pattern is consistent with a more abstract process akin to error monitoring and/or keeping in mind the current task rules (i.e., focus on the word rather than the font colour), especially considering that activation was much greater for incongruent stimuli than for neutral stimuli. Further, this network was engaged during the thought generation condition (but not hearing condition) in the TGT task, despite no requirement to maintain or manipulate information in mind. It seems likely that this network underlies internally-oriented attention processes across all four tasks rather than WM per se, and as such is referred to as the "internal attention" network. Although its role could be even more abstract, this may be an appropriate interpretation based on the findings in this particular set of tasks.

The sensorimotor network (component 3; Figures 5.24 to 5.32) was primarily comprised of auditory perception regions, particularly responding to the hearing condition in the TGT; as such, it is surprising that this network displayed such marked responses in the WM and TSI tasks

(Figures 5.25 and 5.30, respectively). As the onsets were quite late, it is possible that the activation that emerged in these tasks reflects disinhibition of attention to extraneous stimuli (e.g., awareness of scanner noise), and/or a salience-orienting process with the appearance of the ITI fixation image. Its connectivity between posterior insula and the sensorimotor regions observed here, as well as its functional differentiation from an anterior insula-DLPFC network (i.e., the internal attention network), replicates patterns of insula connectivity observed in resting-state research (Cauda et al., 2011). Considering the broad connectivity of auditory cortex with somatomotor and anterior cingulate cortex, this network is referred to as the "sensorimotor" network rather than strictly "auditory".

The motor response network (component 4; Figures 5.33 to 5.43) is referred to as such largely due to its somatomotor activity and the timing of HDR onsets, which were consistent with button-press responses in the WM, SCAP, and TSI tasks, and were suppressed during the TGT task (which does not involve a motor response). Moreover, this network did not show greater engagement in more demanding task conditions, and in fact tended to show the opposite effect where differences between conditions emerged (e.g., greater mean activation in the 4-letter condition than in the 6-letter condition in the WM task).

In the visual attention network (component 5; Figures 5.44 to 5.54), which resembled the previously observed visual attention network in Chapter 3 (Figure 3.10), a particularly notable finding was that relationships between HDR ITP and task performance/digit span were consistent between the WM and SCAP tasks. That is, in both tasks, the ITP phase of the HDR was positively correlated with response accuracy and with digit span measured in a separate testing session. Although some of these correlations were small (only trend relationships in the WM task, and for digit span in both tasks), it is quite compelling that these relationships emerged in non-

overlapping datasets and in tasks with different types of stimuli but similar WM paradigms, and yet activity in this network during the TSI task was *not* correlated with task performance or digit span (which was carried out by the same participants within the same scanning session as the verbal WM task). Although it is likely that this network supports encoding of the memory set in the WM and SCAP tasks, it is given the more generic description of "visual attention" due to its engagement in the other tasks as well (though to a lesser degree in the TSI task; Figure 5.51). In all four tasks, this network was among the earliest to initiate in the post-stimulus time series (Figure 5.4). Consistent with the early HDR, it has been suggested that activation in the superior region of dorsomedial prefrontal cortex (which emerged in this network) underlies energization of the required response set for a cognitive task (Stuss, 2006), and it could be the case that there is a less intense trial-by-trial energization in tasks in which trials are relatively rapid, such as the TSI task.

Finally, the occipital network (component 7; Figures 5.55 to 5.63) comprised visual cortex (de)activation originating in the medial occipital lobes, which activated in the SCAP task and TGT (Figure 5.4C and E), but deactivated in the WM task and TSI task (Figure 5.4B and D). Although the observed discrepancy between activation versus suppression across tasks is somewhat difficult to explain, one possibility is that activity in this network is dependent on the degree to which bottom-up visual processing of stimulus features is tied to the task. In the WM and TSI tasks, in which the stimuli comprise letters or words to be rehearsed/read, the basic visual characteristics are either not relevant or must be actively ignored (in the TSI task). By contrast, in the SCAP task, encoding of basic visual features (namely, spatial location) is directly tied to the task demands, and the dependence on cognitive load may be explained by the greater complexity of the visual display and more saccades being required with more dots to encode. Alth-

ough visual processing is not a requirement of the TGT task, each trial began with a colourful image that was likely to elicit a visual response regardless of the task instructions, and the response was brief and peaked early. As activity primarily originated in the occipital lobes with little connectivity to remote brain regions, this network is simply referred to as the "occipital" network.

5.12.6. Group differences in network activity

Summaries of the mixed model ANOVA results for group differences in each network are presented in Tables 5.13 (DMN), 5.14 (internal attention), 5.15 (sensorimotor network), 5.16 (motor response network), 5.17 (visual attention network), and 5.18 (occipital network). No significant group differences emerged in the DMN (component 1) for any of the tasks examined. This is somewhat surprising given previous research suggesting that the DMN may exhibit altered connectivity in schizophrenia (Hu et al., 2017). However, Hu and colleagues do note from their review of DMN research in schizophrenia (Hu et al., 2017) that findings of hyper- or hypoactivity in the DMN in schizophrenia vary considerably across task-state studies of medicated patients with chronic schizophrenia, and suggest that connectivity in the DMN may be modulated by treatment and/or symptom severity. Therefore, a more comprehensive analysis of relationships with symptom severity, duration of illness, and other clinical factors may be more relevant for the DMN.

In the internal attention network (component 2), significant group differences emerged in the SCAP task only, although the WM task participants showed a similar pattern prior to removing variance predicted by age. In the SCAP task, patients exhibited a relatively attenuated response, which was especially pronounced in the 4.5s delay condition (Figure 5.20). This is consistent with the view that hypoactivity of DLPFC (or networks in which it is connected) con-

tributes to or underlies WM deficits in schizophrenia (Barch & Ceaser, 2012; Glausier & Lewis, 2018). However, this network was not correlated with task performance or digit span in either the WM or the SCAP task. Therefore, although there is evidence of impaired engagement of this network in schizophrenia patients as expected (at least in the SCAP task), it may not be the primary basis of WM deficits in schizophrenia.

In the sensorimotor network (component 3), a significant load × group interaction emerged in the SCAP task which appeared to be due to a trend of schizophrenia patients exhibiting greater suppression of this network compared with controls in the 1-dot load condition but not at the higher load conditions (Figure 5.29). The greater suppression exhibited by schizophrenia patients at low overt cognitive load could reflect a compensatory mechanism in line with the inefficiency hypothesis of cognitive deficits in schizophrenia (Liddle et al., 2013; Metzak et al., 2012).

In the motor response network (component 4), group differences emerged in all tasks except TGT. In the WM task, healthy controls exhibited less activation in the 6-letter condition than in the 4-letter condition, while schizophrenia patients showed little of this effect and thus exhibited greater activation than controls in the 6-letter condition (Figure 5.36). In the TSI task, patients sustained activity in this network considerably longer than did controls (Figure 5.42). This effect cannot be explained by differences in reaction times, as mean RT did not differ between groups in any TSI task condition, and RT was not correlated with either the ITP or RTB phase of the HDR. In both the WM and the TSI task, the group differences amounted to a pattern in which patients exhibited greater activation than healthy controls. Somewhat contradictory to this was that in the SCAP task, patients showed less activation during the initial HDR increase (Figure 5.39B). As there was a small (trend) positive correlation between the ITP part of this

network and SCAP task accuracy in the 4.5s delay condition, this could be due to controls producing more responses than patients. However, it may also be noted that the groups' similarity in the post-peak return to baseline despite patients' initially attenuated response may suggest that patients sustain activation of the network for longer than would be expected given their initial level of activation. As this response network, and in particular the RTB phase of the HDR, was the most highly correlated with task performance in the TSI task, it is possible that this lack of post-response suppression between task trials could explain performance deficits in schizophrenia patients, as motor control and response inhibition is directly tied to the TSI task demands. A similar effect has been observed in schizophrenia patients during an auditory oddball task, which also requires increased control over motor responses (Lavigne et al., 2016).

In the visual attention network (component 5), which was the most clearly related to WM capacity in both the WM task and SCAP task data, some load-related group effects emerged (see Figures 5.47 and 5.50 for WM and SCAP, respectively). Group differences in the WM and SCAP tasks amounted to attenuated and/or more gradual responses in schizophrenia patients – especially in conditions of high cognitive load – which may reflect impaired encoding into memory, given the early onset of this network. By contrast, patients exhibited greater HDRs than controls in the TGT task, regardless of task condition (Figure 5.54). However, it is unclear how this may relate to behaviour, as there is no overt measure of task performance in the TGT task.

Finally, in the occipital network (component 7), a condition × group interaction emerged in the TGT task which reflected contrasting effects of condition between groups. That is, healthy controls exhibited lower mean activation of this network in the hearing condition than in the generating condition, whereas patients exhibited lower mean activation of this network in the generating condition than in the hearing condition (Figure 5.63A). The basis of this effect was in

the post-peak return to baseline and suppression below baseline, as patients exhibited more sustained activation following the peak as well as greater post-peak suppression towards the end of the time series (Figure 5.63B). Given that the initial HDR increase did not differ between groups, this may reflect differences in the degree to which visual fixation is maintained during the TGT task.

5.12.7. Clinical implications

While schizophrenia patients exhibited differences from healthy controls in at least one task in almost all networks examined (except the DMN), the clearest link to WM deficits emerged in the visual attention network. As noted above, this is supported by the replication of its relationships with task performance and digit span in both the verbal WM and the SCAP datasets. Given the visual attention network's early onset in all tasks, the reduced engagement in schizophrenia patients suggests that the source of WM deficits may lie in the energization of processes required for successful encoding of items into temporary store. As such, patients with WM deficits may benefit from treatments that focus on improving initial cognitive energization. In treatments that aim to modulate brain activity directly, the visual attention network (or specific clusters within the network) could be a promising target. The next and final chapter expands on these conclusions and presents comparisons of findings across chapters.

5.13. Chapter 5 Tables

Table 5.1. Demographic information for healthy controls and schizophrenia patients in the WM and TSI tasks dataset (4-task fMRI-CPCA study). Standard deviations are in parentheses.

	Patients (n = 28)	Controls (n = 26)	All (n = 54)	Test for group differences	p-value for group differences
Age	40.39 (10.54)	28.77 (8.20)	34.80 (11.08)	$t(50.5) = 4.539$	**< .001**
Quick estimated IQ	96.54 (12.12)	101.12 (12.57)	98.74 (12.44)	$t(52) = 1.363$	.179
WAIS scaled digit span	9.14 (2.16)	10.46 (2.30)	9.78 (2.30)	$t(52) = 2.174$	**.034**
Gender (female/male)	15/13	19/7	34/20	$\chi^2(1) = 2.000$	.138
Handedness (L/M/R)	4/1/23	1/1/24	5/2/47	$\chi^2(2) = 1.750$	.417
Socioeconomic status factor score	74.50 (20.36)	55.04 (12.85)	65.13 (19.63)	$t(46) = 4.232$	**< .001**
Years of education	14.55 (2.53)	16.21 (1.81)	15.35 (2.35)	$t(52) = 2.750$	**.008**
Highest education completed					
Doctorate degree	0	2	2	-	-
Master's degree	3	2	5	-	-
Bachelor's degree	7	15	22	-	-
Associate degree	1	1	2	-	-
Other post-secondary	1	1	2	-	-
High school diploma	15	5	20	-	-
High school not completed	1	0	1	-	-
Age at first diagnosis	25.11 (9.57)	-	-	-	-
Illness duration in years	20.29 (12.32)	-	-	-	-
SSPI factor scores					
Anxiety (max = 4)	1.32 (1.25)	-	-	-	-
Depression (max = 4)	1.04 (1.26)	-	-	-	-
Psychomotor poverty (max = 16)	2.82 (3.01)	-	-	-	-
Psychomotor excitation (max = 24)	1.96 (1.64)	-	-	-	-
Disorganization (max = 16)	2.36 (1.45)	-	-	-	-
Reality distortion (max = 8)	2.71 (2.27)	-	-	-	-
Poor insight (max = 4)	0.86 (1.18)	-	-	-	-
SSPI total score	13.14 (6.96)	-	-	-	-
CPZ equivalent dose (mg)	1,317.85 (1,760.22)	-	-	-	-

Note. Illness duration unknown for 4 participants. IQ = intelligence quotient; WAIS = Wechsler Adult Intelligence Scale; L = left; M = mixed; R = right; SSPI = Signs and Symptoms of Psychotic Illness; SSPI psychomotor poverty = sum of scores for anhedonia, underactivity, flattened affect, and poverty of speech; SSPI psychomotor excitation = sum of scores for elated mood, insomnia, overactivity, pressured speech, peculiar behaviour, and irritability/hostility; SSPI disorganization = sum of scores for attentional impairment, disorientation, inappropriate affect, and disordered form of thought; SSPI reality distortion = sum of global scores for delusions and hallucinations; CPZ = chlorpromazine (equivalent doses calculated for 26 patients, according to guidelines from the *Clinical Handbook of Psychotropic Drugs, 22nd Edition*; Procyshyn, Bezchlibnyk-Butler, & Jeffries, 2017).

Table 5.2. Demographic information for healthy controls and schizophrenia patients in the SCAP task dataset (4-task fMRI-CPCA study). Standard deviations are in parentheses.

	Patients (n = 44)	Controls (n = 44)	All (n = 88)	Test for group differences	p-value for group differences
Age	37.09 (9.09)	31.61 (8.84)	34.35 (9.33)	$t(86) = 2.864$	**.005**
WMS raw digit span	22.89 (4.94)	30.52 (5.64)	26.70 (6.52)	$t(86) = 6.753$	**< .001**
Gender (female/male)	11/33	24/20	35/53	$\chi^2(1) = 8.017$	**.005**
Handedness	all right	all right	all right	-	-
Years of education	12.66 (1.83)	15.00 (1.77)	13.83 (2.14)	$t(86) = 6.108$	**< .001**
Highest education completed					
Doctorate degree	0	0	0	-	-
Master's degree	0	2	2	-	-
Bachelor's degree	5	24	29	-	-
Associate degree	1	1	2	-	-
Some college	8	9	17	-	-
High school	19	6	25	-	-
High school not completed	8	1	9	-	-
Other	2	1	3	-	-
SAPS global scores					
Bizarre behaviour	0.98 (1.39)	-	-	-	-
Delusions	2.64 (1.43)	-	-	-	-
Hallucinations	2.32 (1.78)	-	-	-	-
Inappropriate affect	0.41 (0.92)	-	-	-	-
Formal thought disorder	1.52 (1.53)	-	-	-	-
SANS global scores					
Alogia	0.95 (1.12)	-	-	-	-
Anhedonia	2.34 (1.48)	-	-	-	-
Attention	2.11 (1.37)	-	-	-	-
Avolition	2.77 (1.55)	-	-	-	-
Blunted affect	1.23 (1.27)	-	-	-	-
CPZ equivalent dose (mg)	615.95 (827.90)	-	-	-	-

Note. Education information missing for 1 schizophrenia patient. IQ = intelligence quotient; WMS = Wechsler Memory Scale; SAPS = Scale for the Assessment of Positive Symptoms; SANS = Scale for the Assessment of Negative Symptoms; CPZ = chlorpromazine (equivalent doses calculated for 35 patients, according to guidelines from the *Clinical Handbook of Psychotropic Drugs, 22nd Edition*; Procyshyn et al., 2017). Max score for all SAPS/SANS measures = 5.

Table 5.3. Demographic and clinical information for healthy controls and schizophrenia patients in the TGT dataset (4-task fMRI-CPCA study). Standard deviations are in parentheses.

	Patients (n = 28)	Controls (n = 32)	All (n = 60)	Test for group differences	p-value for group differences
Age	33.54 (9.83)	28.75 (8.58)	30.98 (9.42)	$t(58) = 2.014$	**.049**
Quick estimated IQ	96.57 (11.28)	97.09 (11.21)	96.85 (11.15)	$t(58) = 0.180$	.858
WAIS scaled digit span	10.50 (2.67)	12.39 (2.88)	11.49 (2.92)	$t(57) = 2.598$	**.012**
Gender (female/male)	14/14	13/19	27/33	$\chi^2(1) = 0.530$	.466
Handedness (L/M/R)	1/1/26	3/1/28	4/2/54	$\chi^2(2) = 0.811$	.667
Socioeconomic status factor score	69.71 (28.42)	65.75 (14.97)	67.60 (22.17)	$t(40) = 0.662$	0.512
Years of education	14.32 (2.55)	15.58 (1.81)	14.99 (2.26)	$t(58) = 2.220$	**.030**
Highest education completed					
Doctorate degree	0	0	0	-	-
Master's degree	3	3	6	-	-
Bachelor's degree	4	10	14	-	-
Some post-secondary	15	18	33	-	-
High school diploma	3	1	4	-	-
High school not completed	3	0	3	-	-
Age at first diagnosis	23.26 (6.24)	-	-	-	-
Illness duration in years	16.65 (12.79)	-	-	-	-
SSPI factor scores					
Anxiety (max = 4)	1.26 (1.10)	-	-	-	-
Depression (max = 4)	1.00 (1.24)	-	-	-	-
Psychomotor poverty (max = 16)	4.11 (2.47)	-	-	-	-
Psychomotor excitation (max = 24)	3.56 (3.53)	-	-	-	-
Disorganization (max = 16)	2.19 (1.98)	-	-	-	-
Reality distortion (max = 8)	3.70 (2.52)	-	-	-	-
Poor insight (max = 4)	1.41 (1.34)	-	-	-	-
SSPI total score	17.41 (7.96)	-	-	-	-
CPZ equivalent dose (mg)	731.60 (891.93)	-	-	-	-

Note. Digit span score is missing for 1 healthy control; age at first diagnosis is missing for 1 patient; illness duration in years is missing for 2 patients; all SSPI scores are missing for 1 patient. IQ = intelligence quotient; WAIS = Wechsler Adult Intelligence Scale; L = left; M = mixed; R = right; SSPI = Signs and Symptoms of Psychotic Illness; SSPI psychomotor poverty = sum of scores for anhedonia, underactivity, flattened affect, and poverty of speech; SSPI psychomotor excitation = sum of scores for elated mood, insomnia, overactivity, pressured speech, peculiar behaviour, and irritability/hostility; SSPI disorganization = sum of scores for attentional impairment, disorientation, inappropriate affect, and disordered form of thought; SSPI reality distortion = sum of global scores for delusions and hallucinations; CPZ = chlorpromazine (equivalent doses calculated for 23 patients, according to guidelines from the *Clinical Handbook of Psychotropic Drugs, 22nd Edition*; Procyshyn et al., 2017).

Table 5.4. Mean Working Memory (WM) task performance for each participant group and full sample (percent correct and mean reaction time for each task condition; standard deviations in parentheses). Reaction time (RT) values are in milliseconds.

	Patients		Controls		All	
Condition	% correct	RT[a]	% correct	RT[a]	% correct	RT[a]
4 letters						
0s delay	91.33 (8.66)	1,122.56 (149.98)	96.43 (5.71)	981.45 (132.29)	93.78 (7.76)	1,054.62 (157.42)
4s delay	88.90 (9.98)	1,046.31 (127.66)	94.37 (5.73)	965.01 (119.97)	91.53 (8.59)	1,007.16 (129.51)
6 letters						
0s delay	86.61 (10.94)	1,177.05 (144.95)	89.29 (8.33)	1,065.36 (124.36)	87.90 (9.77)	1,123.27 (145.50)
4s delay	85.97 (11.04)	1,127.96 (132.87)	87.77 (10.84)	1,031.77 (132.82)	86.84 (10.88)	1,081.64 (140.25)

[a]RT was not analyzed, but is presented here for interest.

Table 5.5. Mean Spatial Capacity (SCAP) task performance for each participant group and full sample (percent correct and mean reaction time for each task condition; standard deviations in parentheses). Reaction time (RT) values are in milliseconds.

	Patients		Controls		All	
Condition	% correct	RT[a]	% correct	RT[a]	% correct	RT[a]
1 dot						
1.5s delay	85.23 (20.40)	1,088.27 (250.33)	98.86 (5.27)	951.87 (194.63)	92.05 (16.32)	1,020.07 (233.24)
3.0s delay	86.36 (17.43)	1,062.80 (299.51)	95.45 (11.14)	921.58 (189.76)	90.91 (15.25)	992.19 (259.19)
4.5s delay	82.95 (21.41)	1,069.30 (330.80)	90.91 (15.34)	1,033.02 (262.89)	86.93 (18.94)	1,051.16 (297.62)
3 dots						
1.5s delay	73.86 (25.26)	1,213.70 (310.31)	92.05 (15.97)	1,120.01 (214.87)	82.95 (22.91)	1,166.31 (268.95)
3.0s delay	73.86 (22.85)	1,300.35 (323.55)	81.25 (23.58)	1,195.70 (296.74)	77.56 (23.38)	1,248.02 (313.10)
4.5s delay	78.98 (22.84)	1,202.01 (287.29)	90.91 (15.34)	1,035.26 (250.30)	84.94 (20.25)	1,118.63 (280.69)
5 dots						
1.5s delay	61.93 (25.57)	1,365.54 (360.86)	82.95 (20.01)	1,273.61 (296.15)	72.44 (25.15)	1,319.57 (331.43)
3.0s delay	71.02 (26.93)	1,275.69 (313.31)	85.23 (18.14)	1,130.00 (263.30)	78.13 (23.92)	1,202.85 (296.90)
4.5s delay	63.07 (22.55)	1,404.20 (353.65)	83.52 (20.13)	1,241.21 (328.00)	73.30 (23.61)	1,322.70 (348.87)
7 dots						
1.5s delay	68.18 (27.68)	1,484.50 (306.39)	82.39 (18.35)	1,403.50 (362.73)	75.28 (24.42)	1,444.00 (336.28)
3.0s delay	62.50 (25.57)	1,412.03 (364.59)	76.70 (19.73)	1,272.11 (311.94)	69.60 (23.81)	1,342.07 (344.59)
4.5s delay	72.16 (21.71)	1,406.74 (304.13)	75.00 (19.44)	1,252.09 (313.23)	73.58 (20.54)	1,329.41 (316.63)

[a]RT was not analyzed, but is presented here for interest.

Table 5.6. Mean TSI task performance for each participant group and full sample (percent correct and mean reaction time for each condition; standard deviations in parentheses).

	Patients		Controls		All	
Condition	% correct	RT	% correct	RT	% correct	RT
Colour-naming[a]						
Neutral	89.17 (11.39)	994.38 (137.18)	95.64 (4.50)	885.54 (96.94)	92.28 (9.29)	941.97 (130.51)
Incongruent	65.83 (22.91)	1258.51 (111.25)	87.82 (10.15)	1113.82 (104.24)	76.42 (20.95)	1188.84 (129.44)
Word-reading						
Neutral (*all)*	89.17 (9.41)	1020.93 (106.01)	97.18 (3.36)	915.35 (105.97)	93.02 (8.17)	970.10 (117.72)
cn-WN	89.05 (11.07)	990.23 (106.29)	97.18 (3.85)	901.07 (104.82)	92.96 (9.29)	947.30 (113.84)
ci-WN	89.29 (10.79)	1053.45 (134.20)	97.18 (5.05)	929.49 (122.66)	93.09 (9.34)	993.77 (142.06)
Incongruent (*all)*	75.12 (16.69)	1195.89 (125.76)	86.79 (8.46)	1163.40 (142.52)	80.74 (14.50)	1180.25 (133.82)
cn-WI	81.90 (16.91)	1165.11 (141.47)	87.95 (9.98)	1132.77 (146.33)	84.81 (14.21)	1149.53 (143.39)
ci-WI	68.33 (19.51)	1228.32 (149.41)	85.64 (11.42)	1193.55 (163.70)	76.67 (18.21)	1211.58 (155.95)

[a]Colour-naming trials were not analyzed, but task performance is presented here for interest. RT = reaction time (in milliseconds); cn = task-switch from neutral colour-naming block; ci = task-switch from incongruent colour-naming block; WN = neutral word-reading stimulus; WI = incongruent word-reading stimulus.

Table 5.7. 4-task fMRI-CPCA, default mode network (DMN, component 1): Clusters for the most extreme 10% of component loadings. Anatomical regions, Brodmann areas (BAs), and Montreal Neurological Institute (MNI) coordinates are listed for each cluster peak.

DMN (component 1) anatomical regions	Cluster volumes		BAs	MNI coordinates		
	voxels	mm^3		x	y	z
Negative loadings						
Cluster 1: left hemisphere	4,161	112,347				
Frontal pole			9	-18	41	44
Middle frontal gyrus			8	-33	23	50
Cluster 1: right hemisphere						
Frontal pole			10	0	56	11
Frontal pole			9	18	41	47
Cluster 2: left hemisphere	1,124	30,348				
Posterior cingulate gyrus			23	-3	-46	35
Cluster 3: left hemisphere	819	22,113				
Superior lateral occipital cortex			39	-48	-67	35
Cluster 4: right hemisphere	637	17,199				
Superior lateral occipital cortex			39	54	-61	29
Cluster 5: left hemisphere	390	10,530				
Anterior middle temporal gyrus			21	-57	-7	-16
Posterior middle temporal gyrus			21	-60	-16	-13
Posterior middle temporal gyrus			21	-63	-43	-4
Cluster 6: right hemisphere	275	7,425				
Posterior middle temporal gyrus			21	60	-10	-16
Posterior middle temporal gyrus			21	66	-34	-4
Temporal pole			21	51	5	-31
Cluster 7: left hemisphere	173	4,671				
Frontal orbital cortex			47	-48	29	-10
Cluster 8: right hemisphere	101	2,727				
Frontal orbital cortex			47	45	32	-10
Inferior frontal gyrus, pars triangularis			45	54	26	8

(Table 5.7 continued on next page)

(Table 5.7, continued from previous page)

DMN (component 1) anatomical regions	Cluster volumes		BAs	MNI coordinates		
	voxels	mm^3		x	y	z
Cluster 9: right hemisphere	76	2,052				
Cerebellum crus I			n/a	30	-79	-37
Cluster 10: left hemisphere	60	1,620				
Cerebellum crus I			n/a	-30	-79	-37

Table 5.8. 4-task fMRI-CPCA, internal attention network (component 2): Clusters for the most extreme 10% of component loadings. Anatomical regions, Brodmann areas (BAs), and Montreal Neurological Institute (MNI) coordinates are listed for each cluster peak.

Internal attention network (component 2) anatomical regions	Cluster volumes		BAs	MNI coordinates		
	voxels	mm^3		x	y	z
Positive loadings						
Cluster 1: left hemisphere	5,588	150,876				
Insular cortex			47	-30	20	2
Middle frontal gyrus			44	-45	8	32
Middle frontal gyrus			48	-45	26	29
Middle frontal gyrus			6	-33	-1	59
Middle frontal gyrus			6	-30	2	56
Frontal pole			46	-33	50	14
Cluster 1: right hemisphere						
Paracingulate gyrus			8	3	20	47
Insular cortex			47	33	23	-1
Middle frontal gyrus			45	45	32	26
Middle frontal gyrus			44	48	14	32
Middle frontal gyrus			8	33	5	56
Frontal pole			46	36	47	17
Inferior frontal gyrus, pars opercularis			48	51	14	11
Cluster 2: left hemisphere	1,008	27,216				
Posterior supramarginal gyrus			40	-36	-49	44
Superior lateral occipital cortex			7	-12	-70	50
Cluster 3: right hemisphere	730	19,710				
Superior parietal lobule			40	36	-49	44
Posterior supramarginal gyrus			40	45	-43	47
Precuneus cortex			7	12	-67	50
Cluster 4: right hemisphere	138	3,726				
Cerebellum VI			n/a	30	-61	-28
Cerebellum VI			n/a	9	-73	-25
Cluster 5: right hemisphere	100	2,700				
Caudate			n/a	15	8	8
Thalamus			n/a	12	-10	8

(Table 5.8 continued on next page)

(Table 5.8, continued from previous page)

Internal attention network (component 2) anatomical regions	Cluster volumes		BAs	MNI coordinates		
	voxels	mm^3		x	y	z
Cluster 6: left hemisphere	96	2,592				
Caudate			n/a	-12	8	5
Cluster 7: left hemisphere	76	2,052				
Cerebellum crus I			n/a	-30	-61	-31
Cluster 8: left hemisphere	25	675				
Inferior temporal gyrus, temporooccipital part			37	-48	-58	-10
Cluster 9: left hemisphere	24	648				
Thalamus			n/a	-12	-16	8
Cluster 10: left hemisphere	21	567				
Cerebellum crus I			n/a	-9	-76	-28
Cluster 11: right hemisphere	10	270				
Cerebellum VIIb			n/a	27	-70	-49

Table 5.9. 4-task fMRI-CPCA, sensorimotor network (component 3): Clusters for the most extreme 10% of component loadings. Anatomical regions, Brodmann areas (BAs), and Montreal Neurological Institute (MNI) coordinates are listed for each cluster peak.

Sensorimotor network (component 3) anatomical regions	Cluster volumes voxels	mm^3	BAs	MNI coordinates x	y	z
Positive loadings						
Cluster 1: left hemisphere	3,501	94,527				
Central opercular cortex			48	-54	-22	14
Central opercular cortex			48	-51	-7	5
Postcentral gyrus			4	-54	-19	47
Precentral gyrus			3	-45	-16	56
Postcentral gyrus			6	-33	-28	68
Cluster 2: right hemisphere	3,043	82,161				
Central opercular cortex			42	60	-19	17
Central opercular cortex			48	54	-7	5
Insular cortex			48	39	5	5
Insular cortex			48	39	-16	2
Postcentral gyrus			3	57	-13	41
Cluster 3: bilateral	481	12,987				
Supplementary motor area			6	0	-4	47
Cluster 4: right hemisphere	453	12,231				
Cerebellum VI			n/a	21	-52	-19
Lingual gyrus			18	15	-58	2
Cluster 5: left hemisphere	292	7,884				
Lingual gyrus			18	-15	-55	-4
Temporal occipital fusiform cortex			37	-21	-55	-19
Cluster 6: left hemisphere	38	1,026				
Thalamus			n/a	-12	-19	5
Cluster 7: right hemisphere	8	216				
Thalamus			n/a	9	-16	5

Table 5.10. 4-task fMRI-CPCA, motor response network (component 4): Clusters for the most extreme 10% of component loadings. Anatomical regions, Brodmann areas (BAs), and Montreal Neurological Institute (MNI) coordinates are listed for each cluster peak.

Motor response network (component 4) anatomical regions	Cluster volumes		BAs	MNI coordinates		
	voxels	mm^3		x	y	z
Positive loadings						
Cluster 1: left hemisphere	7,593	205,011				
Superior parietal lobule			40	-33	-40	56
Precentral gyrus			6	-27	-10	62
Precentral gyrus			6	-54	2	35
Superior lateral occipital cortex			19	-24	-73	35
Cluster 1: right hemisphere						
Postcentral gyrus			40	36	-37	53
Postcentral gyrus			3	42	-31	50
Superior frontal gyrus			6	27	-7	59
Supplementary motor area			6	0	-7	56
Cluster 2: right hemisphere	94	2,538				
Inferior lateral occipital cortex			37	51	-64	2
Cluster 3: left hemisphere	90	2,430				
Inferior lateral occipital cortex			37	-48	-70	5
Cluster 4: right hemisphere	39	1,053				
Precentral gyrus			6	54	5	32

Table 5.11. 4-task fMRI-CPCA, visual attention network (component 5): Clusters for the most extreme 10% of component loadings. Anatomical regions, Brodmann areas (BAs), and Montreal Neurological Institute (MNI) coordinates are listed for each cluster peak.

Visual attention network (component 5) anatomical regions	Cluster volumes		BAs	MNI coordinates		
	voxels	mm^3		x	y	z
Positive loadings						
Cluster 1: left hemisphere	6,720	181,440				
Occipital pole			18	-27	-91	8
Occipital pole			18	-18	-91	-4
Inferior lateral occipital cortex			19	-36	-82	-7
Superior lateral occipital cortex			7	-21	-61	50
Cluster 1: right hemisphere						
Superior lateral occipital cortex			18	30	-88	8
Occipital fusiform gyrus			18	21	-88	-4
Inferior lateral occipital cortex			18	33	-85	5
Superior lateral occipital cortex			7	24	-58	53
Cluster 2: left hemisphere	585	15,795				
Precentral gyrus			6	-51	-1	47
Precentral gyrus			44	-42	5	29
Precentral gyrus			6	-57	2	23
Middle frontal gyrus			6	-27	-4	50
Cluster 3: right hemisphere	240	6,480				
Precentral gyrus			6	54	2	44
Cluster 4: left hemisphere	215	5,805				
Supplementary motor area			6	-3	8	59
Cluster 5: left hemisphere	23	621				
Thalamus			n/a	-21	-31	-1
Cluster 6: right hemisphere	19	513				
Thalamus			n/a	21	-28	-1
Cluster 7: right hemisphere	14	378				
Middle frontal gyrus			6	30	-1	50

Table 5.12. 4-task fMRI-CPCA, occipital network (component 7): Clusters for the most extreme 10% of component loadings. Anatomical regions, Brodmann areas (BAs), and Montreal Neurological Institute (MNI) coordinates are listed for each cluster peak.

Occipital network (component 7) anatomical regions	Cluster volumes		BAs	MNI coordinates		
	voxels	mm^3		x	y	z
Negative loadings						
Cluster 1: left hemisphere	7,816	211,032				
Lingual gyrus			17	-6	-79	-1
Intracalcarine cortex			17	-3	-82	2
Intracalcarine cortex			18	-6	-88	11
Superior lateral occipital cortex			19	-36	-79	20
Cluster 1: right hemisphere						
Cuneal cortex			18	12	-85	20
Lingual gyrus			17	9	-76	-1
Superior lateral occipital cortex			39	42	-70	20
Precuneus cortex			7	6	-49	47
Angular gyrus			41	48	-46	20

Table 5.13. 4-task fMRI-CPCA, default mode network (DMN, component 1): Mixed model ANOVA results for effects/interactions involving group differences for each task after regressing out variance predicted by confounding variables. No results were statistically significant.

Default mode network (component 1)					
WM task[a]	DF	DF_{error}	*F*	*p*	η_p^2
Group	1	52	0.038	.845	.001
Load × group	1	52	0.020	.888	.000
Delay × group	1	52	1.660	.203	.031
Time × group	2.62	136.39	1.625	.192	.030
Load × delay × group	1	52	0.258	.613	.005
Load × time × group	3.96	205.81	1.477	.211	.028
Delay × time × group	3.34	173.51	1.384	.247	.026
Load × delay × time × group	4.85	252.01	0.577	.713	.011
SCAP task[b]	DF	DF_{error}	*F*	*p*	η_p^2
Group	1	86	0.079	.779	.001
Load × group	2.62	225.46	0.128	.926	.001
Delay × group	2	172	1.081	.342	.012
Time × group	2.52	217.09	0.754	.500	.009
Load × delay × group	6	516	0.846	.534	.010
Load × time × group	12.25	1,053.10	1.117	.342	.013
Delay × time × group	8.33	716.79	1.789	.073	.020
Load × delay × time × group	19.54	1,680.14	1.191	.254	.014
TSI task[a]	DF	DF_{error}	*F*	*p*	η_p^2
Group	1	52	0.463	.499	.009
Congruency × group	1	52	0.002	.966	.000
Task-switch × group	1	52	0.055	.815	.001
Time × group	4.10	212.94	0.456	.773	.009
Congruency × task-switch × group	1	52	0.908	.345	.017
Congruency × time × group	4.20	218.49	0.336	.862	.006
Task-switch × time × group	3.81	198.00	0.919	.450	.017
Congruency × task-switch × time × group	4.55	236.37	0.185	.959	.004
TGT task[a]	DF	DF_{error}	*F*	*p*	η_p^2
Group	1	58	0.066	.798	.001
Condition × group	1	58	0.116	.734	.002
Time × group	3.57	206.95	1.351	.255	.023
Condition × time × group	3.17	183.68	0.609	.619	.010

[a]Statistical results after removing variance predicted by age (WM, TSI, and TGT tasks).
[b]Statistical results after removing variance predicted by age and gender (SCAP task).
DF = degrees of freedom; WM = Working Memory; SCAP = Spatial Capacity; TSI = Task-Switch Inertia; TGT = Thought Generation Task.

Table 5.14. 4-task fMRI-CPCA, internal attention network (component 2): Mixed model ANOVA results for effects/interactions involving group differences for each task after regressing out variance predicted by confounding variables. Significant results are presented in bold.

Internal attention network (component 2)					
WM task[a]	DF	DF_{error}	*F*	*p*	η_p^2
Group	1	52	0.045	.832	.001
Load × group	1	52	0.409	.525	.008
Delay × group	1	52	0.422	.519	.008
Time × group	2.57	133.86	0.589	.598	.011
Load × delay × group	1	52	0.014	.905	.000
Load × time × group	3.90	202.83	0.812	.516	.015
Delay × time × group	3.33	173.16	2.058	.101	.038
Load × delay × time × group	4.81	249.92	0.545	.735	.010
SCAP task[b]	DF	DF_{error}	*F*	*p*	η_p^2
Group	1	86	0.476	.492	.006
Load × group	2.66	229.04	2.015	.120	.023
Delay × group	2	172	0.609	.545	.007
Time × group	**2.99**	**257.27**	**3.052**	**.029***	**.034**
Load × delay × group	6	516	1.495	.178	.017
Load × time × group	14.18	1,219.05	1.435	.128	.016
Delay × time × group	**10.05**	**864.71**	**2.272**	**.012***	**.026**
Load × delay × time × group	22.11	1,901.06	0.923	.564	.011
TSI task[a]	DF	DF_{error}	*F*	*p*	η_p^2
Group	1	52	0.000	.994	.000
Congruency × group	1	52	0.000	.991	.000
Task-switch × group	1	52	0.388	.536	.007
Time × group	3.60	187.10	0.775	.530	.015
Congruency × task-switch × group	1	52	0.263	.611	.005
Congruency × time × group	3.84	199.87	0.834	.501	.016
Task-switch × time × group	4.25	221.08	1.001	.411	.019
Congruency × task-switch × time × group	3.50	181.88	0.283	.866	.005
TGT task[a]	DF	DF_{error}	*F*	*p*	η_p^2
Group	1	58	0.003	.959	.000
Condition × group	1	58	0.468	.496	.008
Time × group	3.34	193.71	0.748	.538	.013
Condition × time × group	3.65	211.69	0.406	.787	.007

[a]Statistical results after removing variance predicted by age (WM, TSI, and TGT tasks).
[b]Statistical results after removing variance predicted by age and gender (SCAP task).
DF = degrees of freedom; WM = Working Memory; SCAP = Spatial Capacity; TSI = Task-Switch Inertia; TGT = Thought Generation Task; * = $p < .05$.

Table 5.15. 4-task fMRI-CPCA, sensorimotor network (component 3): Mixed model ANOVA results for effects/interactions involving group differences for each task after regressing out variance predicted by confounding variables. Significant results are presented in bold font.

Sensorimotor network (component 3)					
WM task[a]	DF	DF_{error}	*F*	*p*	η_p^2
Group	1	52	1.272	.265	.024
Load × group	1	52	0.028	.868	.001
Delay × group	1	52	0.035	.853	.001
Time × group	3.21	166.70	0.183	.918	.003
Load × delay × group	1	52	0.062	.804	.001
Load × time × group	4.98	259.10	1.818	.110	.034
Delay × time × group	4.15	215.78	0.979	.422	.018
Load × delay × time × group	5.60	291.45	0.351	.899	.007
SCAP task[b]	DF	DF_{error}	*F*	*p*	η_p^2
Group	1	86	0.736	.393	.008
Load × group	**2.51**	**215.64**	**3.018**	**.039***	**.034**
Delay × group	2	172	0.755	.471	.009
Time × group	2.71	233.16	0.453	.696	.005
Load × delay × group	6	516	1.931	.074	.022
Load × time × group	14.12	1,213.96	1.073	.378	.012
Delay × time × group	10.13	871.44	0.903	.531	.010
Load × delay × time × group	25.52	2,194.42	0.890	.623	.010
TSI task[a]	DF	DF_{error}	*F*	*p*	η_p^2
Group	1	52	0.816	.371	.015
Congruency × group	1	52	0.601	.442	.011
Task-switch × group	1	52	0.539	.466	.010
Time × group	4.36	226.73	1.247	.291	.023
Congruency × task-switch × group	1	52	0.802	.374	.015
Congruency × time × group	4.34	225.65	1.530	.190	.029
Task-switch × time × group	4.10	213.06	0.253	.911	.005
Congruency × task-switch × time × group	4.30	223.50	0.789	.541	.015
TGT task[a]	DF	DF_{error}	*F*	*p*	η_p^2
Group	1	58	0.972	.328	.016
Condition × group	1	58	0.238	.627	.004
Time × group	3.99	231.70	0.456	.768	.008
Condition × time × group	3.68	213.54	1.227	.301	.021

[a]Statistical results after removing variance predicted by age (WM, TSI, and TGT tasks).
[b]Statistical results after removing variance predicted by age and gender (SCAP task).
DF = degrees of freedom; WM = Working Memory; SCAP = Spatial Capacity; TSI = Task-Switch Inertia; TGT = Thought Generation Task; * = $p < .05$.

Table 5.16. 4-task fMRI-CPCA, motor response network (component 4): Mixed model ANOVA results for effects/interactions involving group differences for each task after regressing out variance predicted by confounding variables. Significant results are presented in bold font.

Motor network (component 4)					
WM task[a]	DF	DF_{error}	*F*	*p*	η_p^2
Group	1	52	0.417	.521	.008
Load × group	**1**	**52**	**5.919**	**.018***	**.102**
Delay × group	1	52	0.000	.984	.000
Time × group	2.43	126.20	2.433	.081	.045
Load × delay × group	1	52	2.435	.125	.045
Load × time × group	5.22	271.44	1.178	.320	.022
Delay × time × group	3.81	198.20	1.806	.132	.034
Load × delay × time × group	5.47	284.43	1.020	.409	.019
SCAP task[b]	DF	DF_{error}	*F*	*p*	η_p^2
Group	1	86	0.865	.355	.010
Load × group	2.67	229.60	0.473	.679	.005
Delay × group	**2**	**172**	**4.859**	**.009****	**.053**
Time × group	**2.99**	**257.41**	**2.651**	**.049***	**.030**
Load × delay × group	4.88	419.40	0.367	.867	.004
Load × time × group	15.68	1,348.36	0.793	.693	.009
Delay × time × group	10.83	931.28	1.360	.188	.016
Load × delay × time × group	24.69	2,122.91	0.877	.638	.010
TSI task[a]	DF	DF_{error}	*F*	*p*	η_p^2
Group	1	52	2.862	.097	.052
Congruency × group	1	52	0.055	.815	.001
Task-switch × group	1	52	1.230	.272	.023
Time × group	**4.23**	**219.89**	**3.203**	**.012***	**.058**
Congruency × task-switch × group	1	52	0.168	.683	.003
Congruency × time × group	5.70	296.41	0.723	.624	.014
Task-switch × time × group	4.57	237.47	0.471	.781	.009
Congruency × task-switch × time × group	5.14	267.14	0.792	.559	.015
TGT task[a]	DF	DF_{error}	*F*	*p*	η_p^2
Group	1	58	0.955	.333	.016
Condition × group	1	58	0.427	.516	.007
Time × group	3.33	192.87	0.596	.636	.010
Condition × time × group	3.62	210.22	1.520	.202	.026

[a]Statistical results after removing variance predicted by age (WM, TSI, and TGT tasks).
[b]Statistical results after removing variance predicted by age and gender (SCAP task).
DF = degrees of freedom; WM = Working Memory; SCAP = Spatial Capacity; TSI = Task-Switch Inertia; TGT = Thought Generation Task; * = $p < .05$; ** = $p < .01$.

Table 5.17. 4-task fMRI-CPCA, visual attention network (component 5): Mixed model ANOVA results for effects/interactions involving group differences for each task after regressing out variance predicted by confounding variables. Significant results are presented in bold font.

Visual attention network (component 5)					
WM task[a]	DF	DF_{error}	*F*	*p*	η_p^2
Group	1	52	0.107	.744	.002
Load × group	1	52	0.622	.434	.012
Delay × group	1	52	0.238	.628	.005
Time × group	2.49	129.59	0.893	.431	.017
Load × delay × group	1	52	0.850	.361	.016
Load × time × group	**4.79**	**249.08**	**2.656**	**.025***	**.049**
Delay × time × group	3.95	205.52	0.558	.692	.011
Load × delay × time × group	5.26	273.57	0.759	.587	.014
SCAP task[b]	DF	DF_{error}	*F*	*p*	η_p^2
Group	1	86	3.055	.084	.034
Load × group	2.60	223.55	0.106	.940	.001
Delay × group	2	172	2.242	.109	.025
Time × group	**2.97**	**255.12**	**4.246**	**.006****	**.047**
Load × delay × group	6	516	0.211	.973	.002
Load × time × group	**13.11**	**1,127.70**	**1.890**	**.027***	**.022**
Delay × time × group	8.55	734.89	0.851	.564	.010
Load × delay × time × group	21.60	1,857.23	1.349	.130	.015
TSI task[a]	DF	DF_{error}	*F*	*p*	η_p^2
Group	1	52	0.236	.629	.005
Congruency × group	1	52	0.072	.789	.001
Task-switch × group	1	52	0.612	.438	.012
Time × group	4.43	230.17	0.592	.686	.011
Congruency × task-switch × group	1	52	0.019	.891	.000
Congruency × time × group	4.56	237.08	0.391	.838	.007
Task-switch × time × group	5.16	268.08	0.574	.725	.011
Congruency × task-switch × time × group	3.84	199.69	0.825	.507	.016
TGT task[a]	DF	DF_{error}	*F*	*p*	η_p^2
Group	**1**	**58**	**4.362**	**.041***	**.070**
Condition × group	1	58	0.583	.448	.010
Time × group	**9**	**522**	**7.025**	**<.001*****	**.108**
Condition × time × group	3.49	202.36	1.017	.393	.017

[a]Statistical results after removing variance predicted by age (WM, TSI, and TGT tasks).
[b]Statistical results after removing variance predicted by age and gender (SCAP task).
DF = degrees of freedom; WM = Working Memory; SCAP = Spatial Capacity; TSI = Task-Switch Inertia; TGT = Thought Generation Task; * = $p < .05$; ** = $p < .01$; *** = $p < .001$.

Table 5.18. 4-task fMRI-CPCA, occipital network (component 7): Mixed model ANOVA results for effects/interactions involving group differences for each task after regressing out variance predicted by confounding variables. Significant results are presented in bold font.

Occipital network (component 7)					
WM task[a]	DF	DF_{error}	*F*	*p*	η_p^2
Group	1	52	0.235	.630	.004
Load × group	1	52	0.544	.464	.010
Delay × group	1	52	0.461	.500	.009
Time × group	2.83	147.00	0.753	.515	.014
Load × delay × group	1	52	1.623	.208	.030
Load × time × group	6.13	318.98	0.194	.980	.004
Delay × time × group	4.50	233.82	0.698	.610	.013
Load × delay × time × group	6.69	348.06	0.772	.606	.015
SCAP task[b]	DF	DF_{error}	*F*	*p*	η_p^2
Group	1	86	0.003	.958	.000
Load × group	2.65	227.90	1.470	.227	.017
Delay × group	2	172	0.620	.539	.007
Time × group	3.23	278.19	0.245	.878	.003
Load × delay × group	5.09	437.62	0.859	.510	.010
Load × time × group	15.69	1,349.10	1.163	.293	.013
Delay × time × group	11.72	1,007.67	0.900	.544	.010
Load × delay × time × group	26.50	2,278.65	1.254	.174	.014
TSI task[a]	DF	DF_{error}	*F*	*p*	η_p^2
Group	1	52	2.491	.121	.046
Congruency × group	1	52	0.140	.710	.003
Task-switch × group	1	52	0.844	.363	.016
Time × group	4.40	228.71	1.198	.312	.023
Congruency × task-switch × group	1	52	0.427	.517	.008
Congruency × time × group	5.57	289.56	0.613	.708	.012
Task-switch × time × group	5.35	278.34	0.577	.729	.011
Congruency × task-switch × time × group	5.86	304.70	0.531	.780	.010
TGT task[a]	DF	DF_{error}	*F*	*p*	η_p^2
Group	1	58	0.263	.610	.005
Condition × group	**1**	**58**	**9.122**	**.004****	**.136**
Time × group	**3.87**	**224.31**	**2.474**	**.047***	**.041**
Condition × time × group	3.40	197.08	0.862	.473	.015

[a]Statistical results after removing variance predicted by age (WM, TSI, and TGT tasks).
[b]Statistical results after removing variance predicted by age and gender (SCAP task).
DF = degrees of freedom; WM = Working Memory; SCAP = Spatial Capacity; TSI = Task-Switch Inertia; TGT = Thought Generation Task; * = $p < .05$; ** = $p < .01$.

5.14. Chapter 5 Figures

Figure 5.1. WM task performance: Percentage of correct responses for each load condition, averaged over delay to illustrate load × group interaction. Asterisk indicates significant interaction after removing variance predicted by age. * = $p < .05$.

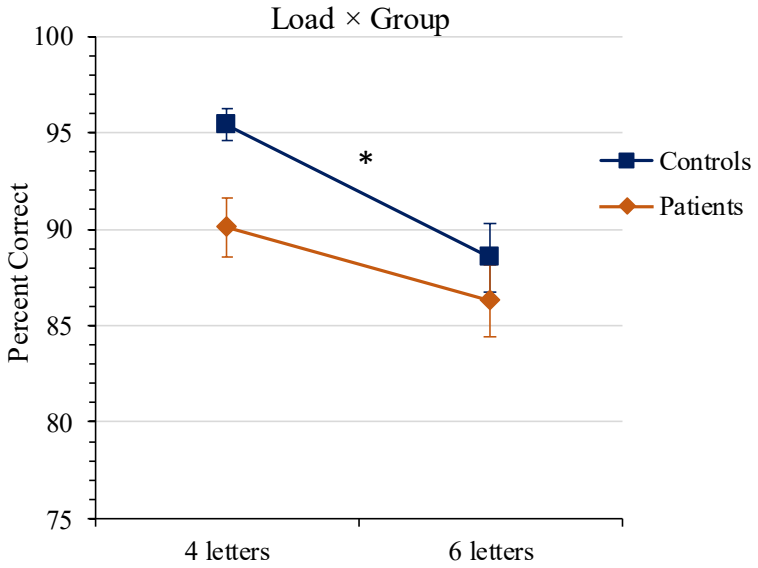

Figure 5.2. SCAP task performance: Percentage of correct responses for each load condition, averaged over delay to illustrate main effect of load. Asterisks indicate significant paired t-tests between adjacent load conditions. *** = $p < .001$.

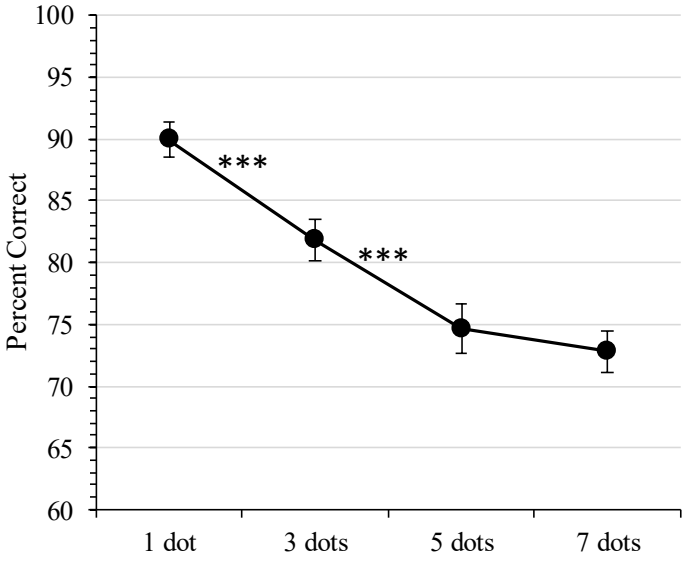

Figure 5.3. TSI task performance: Percentage of correct responses for each task condition, illustrating significant congruency × task-switch interaction. WN = neutral word-reading stimulus; WI = incongruent word-reading stimulus; cn = task-switch from neutral colour-naming block; ci = task-switch from incongruent colour-naming block; *** = $p < .001$.

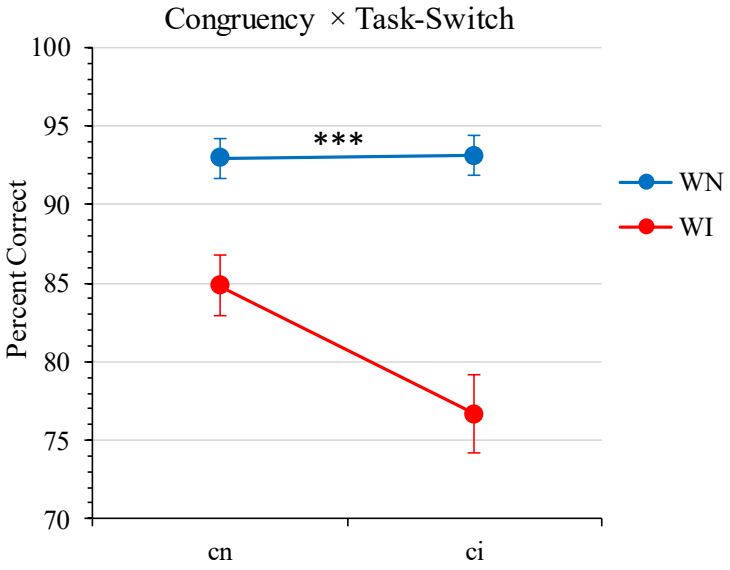

Figure 5.4. 4-task fMRI-CPCA: Summary of components 1-5 and 7. **A (top):** surface representations of top 10% loadings for each component. **B-E (bottom):** predictor weights plotted over post-stimulus time for each task and component (components 1 and 7 weights have been multiplied by -1 so that values below the X axis reflect deactivation and values above the X axis reflect activation for all components). DMN = default mode network; C = component.

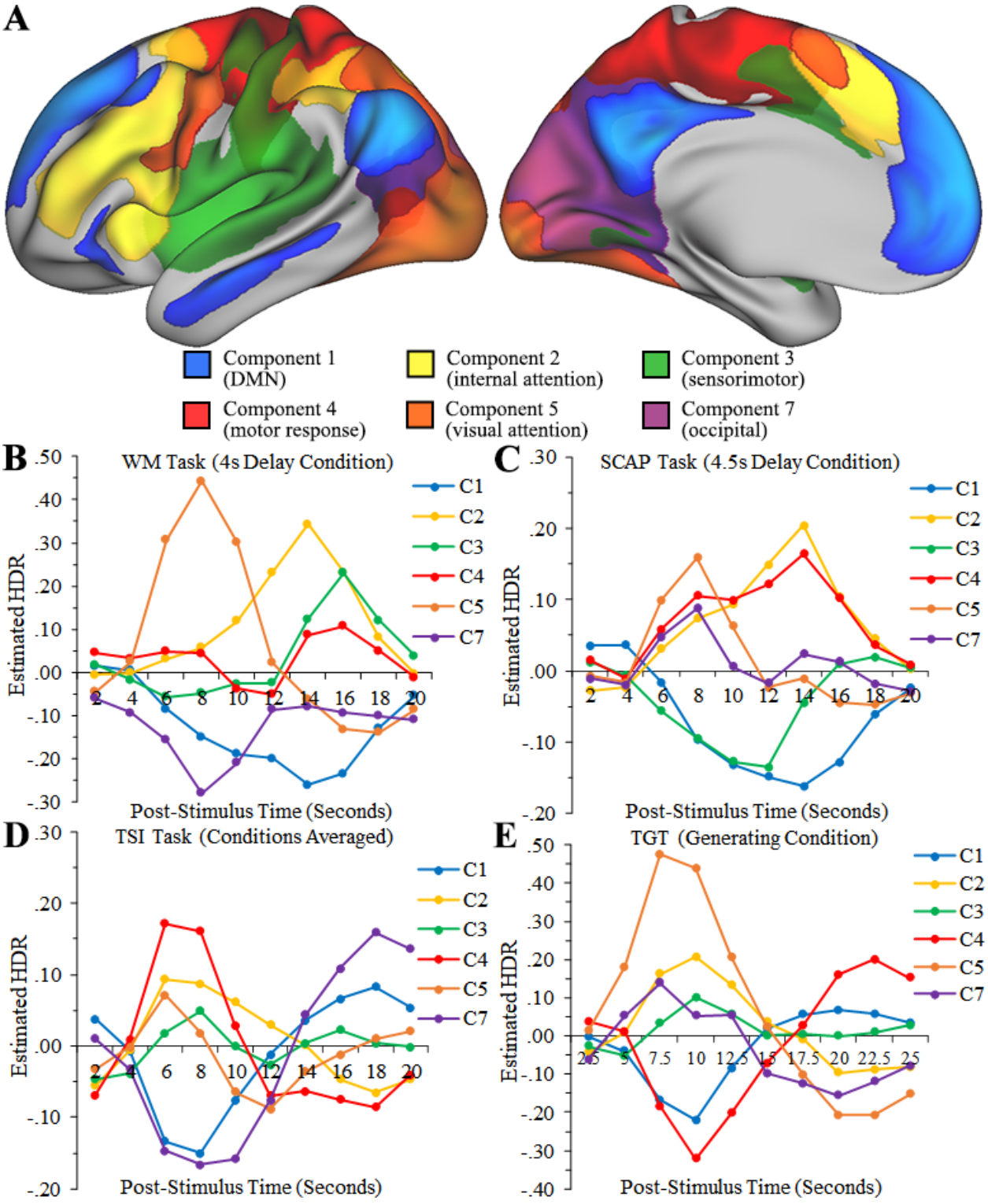

Figure 5.5. 4-task fMRI-CPCA, blood flow artifact (component 6): Anatomical and temporal characteristics. Many peak areas were outside of the brain, likely reflecting blood drainage after a neural response. **A (top)**: dominant 10% of loadings (red/yellow = positive loadings, min = 0.14, max = 0.28; no negative loadings above threshold). Images displayed in neurological orientation (left is left) with MNI coordinates. **B (bottom)**: HDR plots for each task. 4L = 4 letters; 6L = 6 letters; cn = task-switch from neutral colour-naming; ci = task-switch from incongruent colour-naming; WN = neutral word-reading stimulus; WI = incongruent word-reading stimulus.

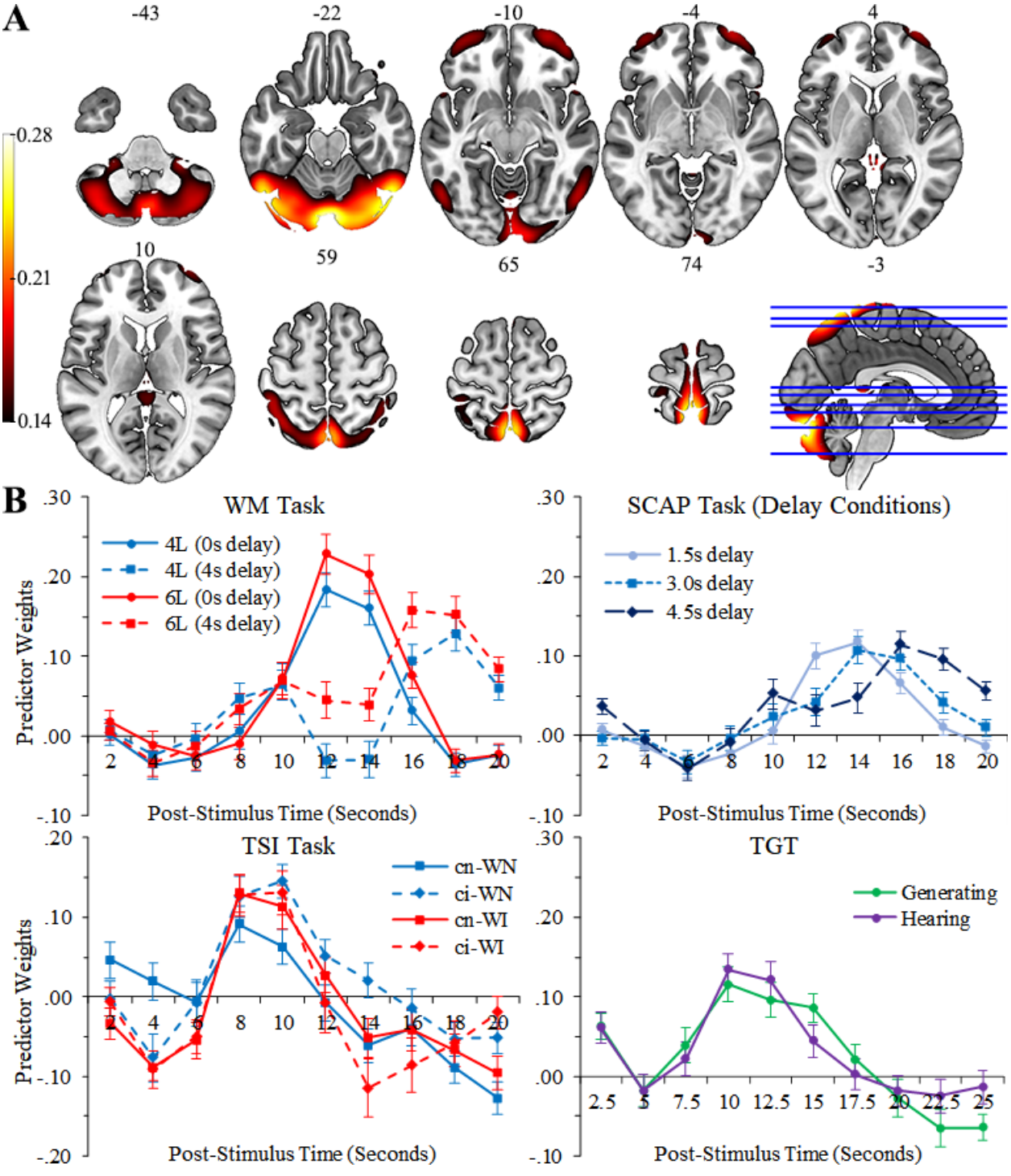

Figure 5.6. 4-task fMRI-CPCA, artifact (component 8): Anatomical and temporal characteristics. **A (top)**: dominant 10% of loadings (red/yellow = positive loadings, min = 0.12, max = 0.23; no negative loadings above threshold). Images are displayed in neurological orientation (left is left) with MNI coordinates. **B (bottom)**: HDR plots for each task. 4L = 4 letters; 6L = 6 letters; cn = task-switch from neutral colour-naming; ci = task-switch from incongruent colour-naming; WN = neutral word-reading stimulus; WI = incongruent word-reading stimulus.

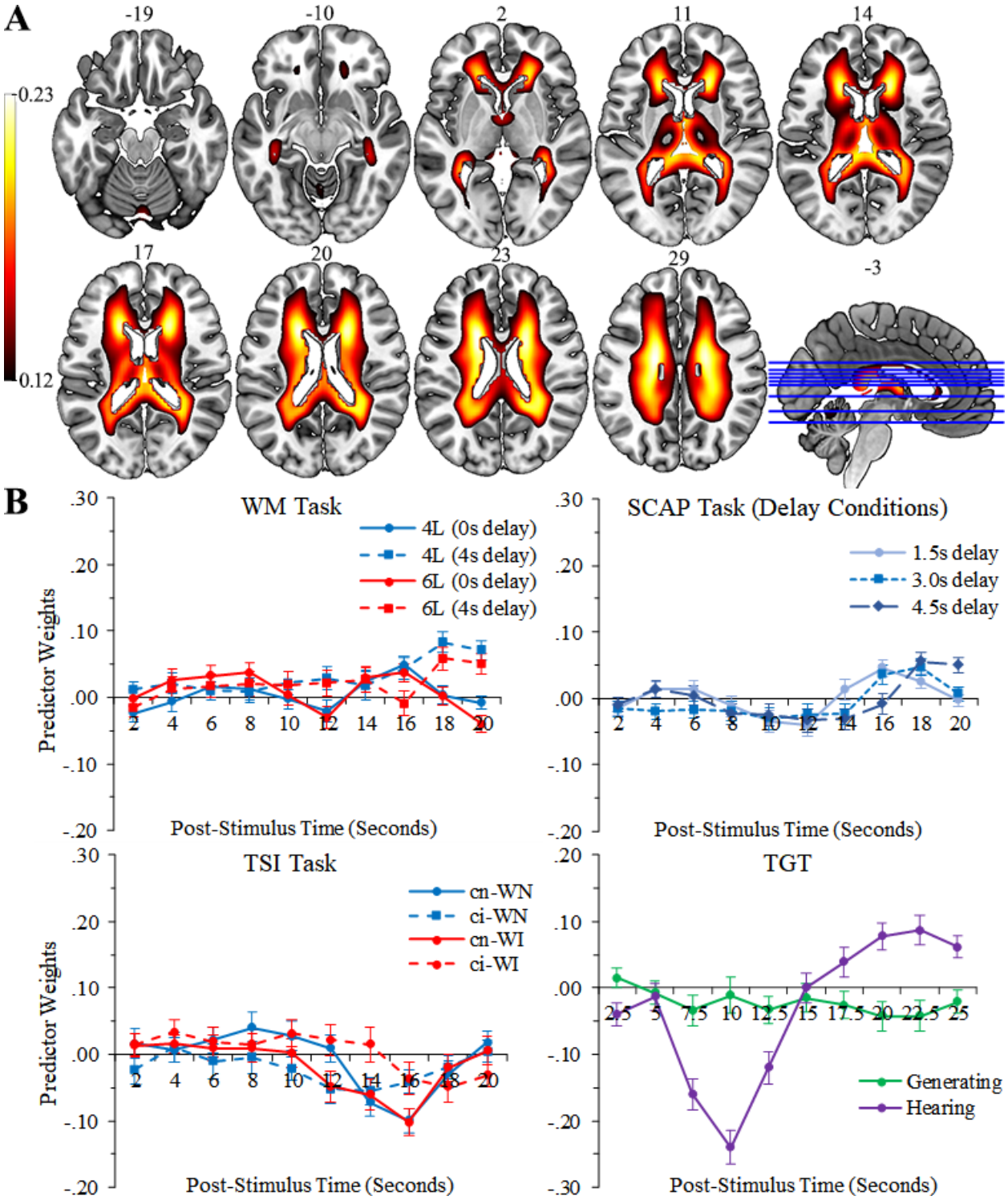

Figure 5.7. 4-task fMRI-CPCA, default mode network (DMN, component 1): Dominant 10% of component loadings (blue/green = negative loadings, min = -0.33, max = -0.18; no positive loadings above threshold). Images are displayed in neurological orientation (left is left) with MNI coordinates.

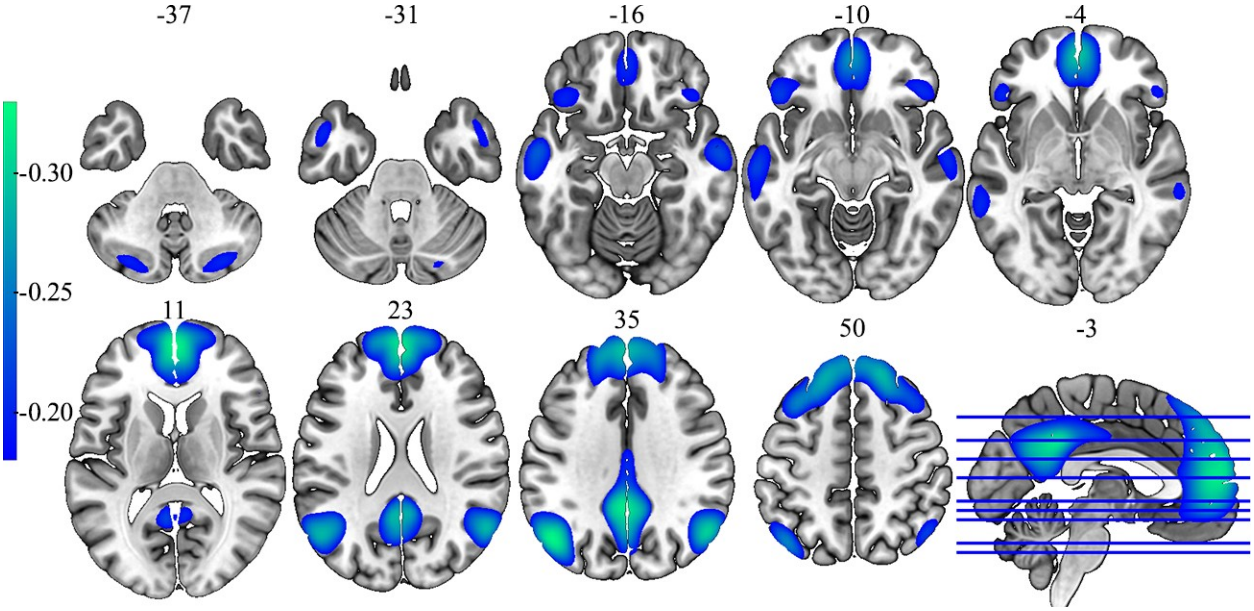

Figure 5.8. WM task from the 4-task fMRI-CPCA, DMN (component 1): Estimated HDR plots. Y axis is reversed (positive down, negative up) to facilitate interpretation (i.e., values below X axis reflect deactivation, and values above X axis reflect activation). 4L = 4-letter condition; 6L = 6-letter condition.

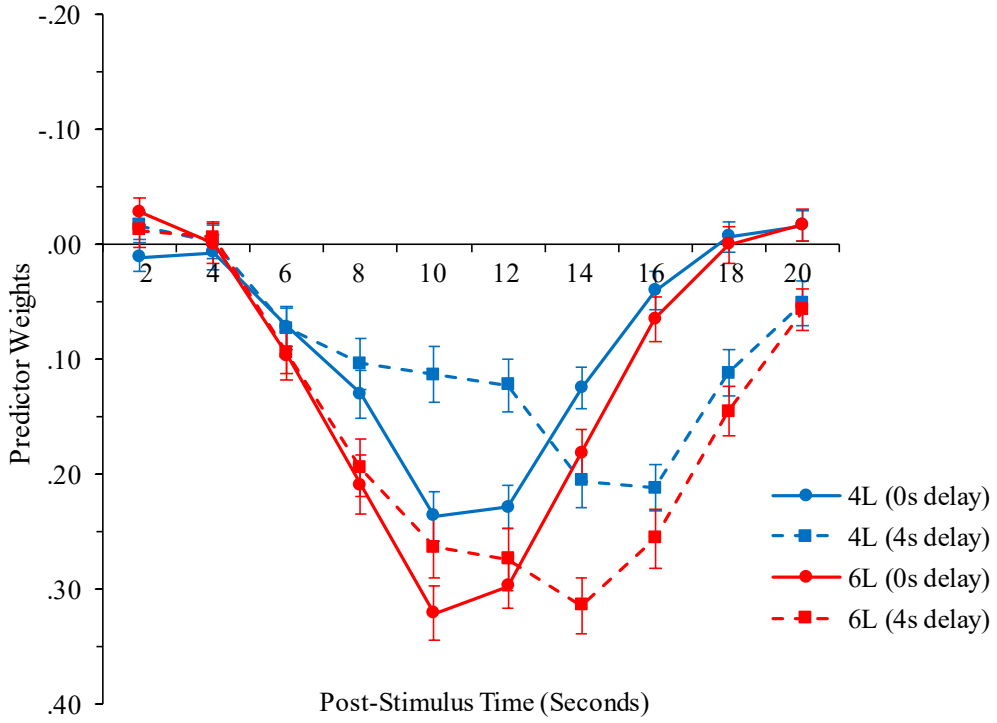

Figure 5.9. WM task from the 4-task fMRI-CPCA, DMN (component 1): Graphs illustrating effects of delay and load. Y axis orientation is reversed to facilitate interpretation (i.e., values below X axis reflect deactivation, and values above X axis reflect activation). **A (top)**: predictor weights plotted over post-stimulus time for each delay condition (asterisks indicate significant 0s vs. 4s delay × time contrasts between adjacent time bins). **B (bottom)**: mean predictor weights illustrating significant load × delay interaction. * = $p < .05$; *** = $p < .001$.

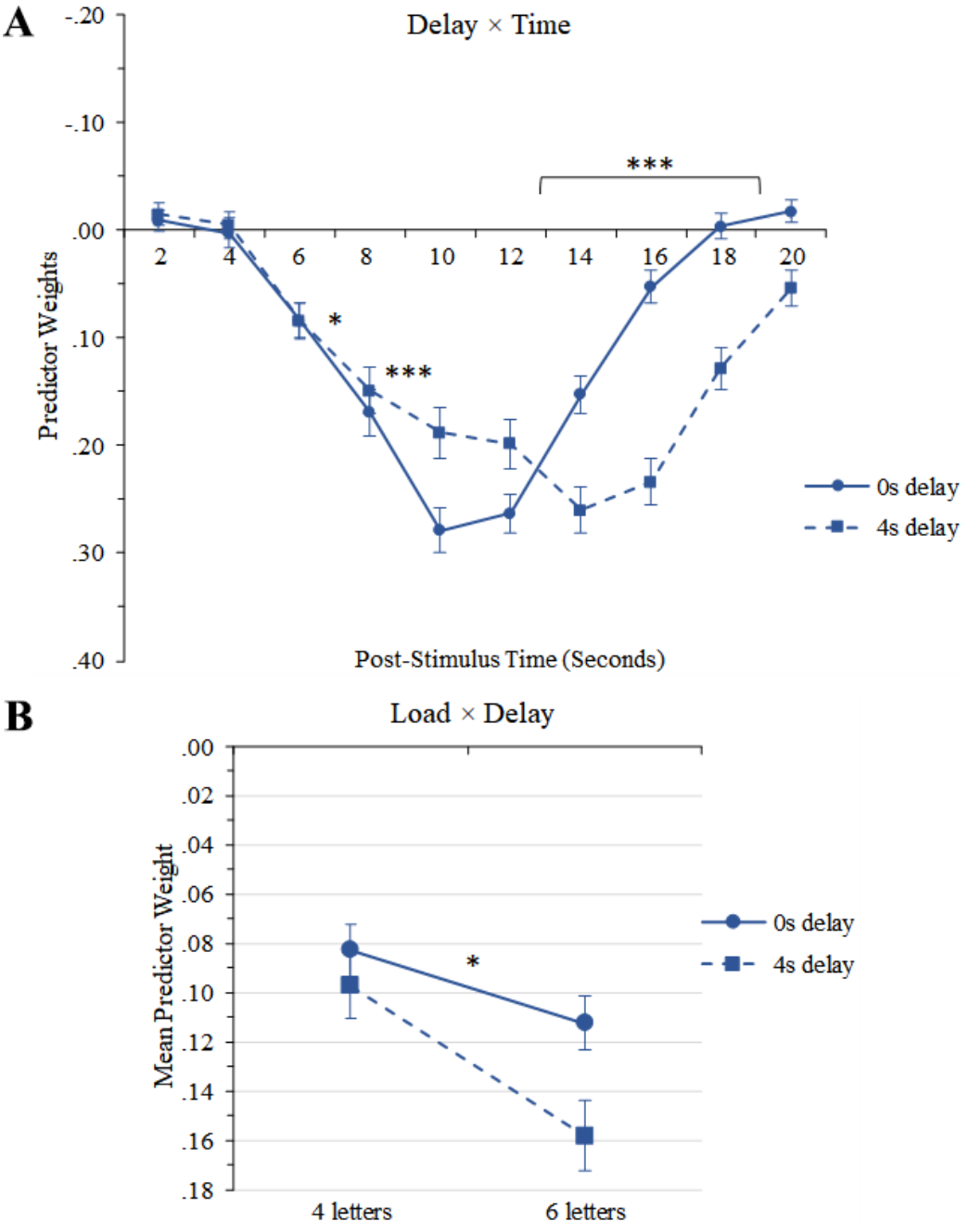

Figure 5.10. SCAP task from the 4-task fMRI-CPCA, DMN (component 1): Estimated HDR plots for all task conditions (each load level displayed on a separate graph). Y axis is reversed (positive down, negative up) to facilitate interpretation of HDR shapes (values below X axis reflect deactivation, and values above X axis reflect activation).

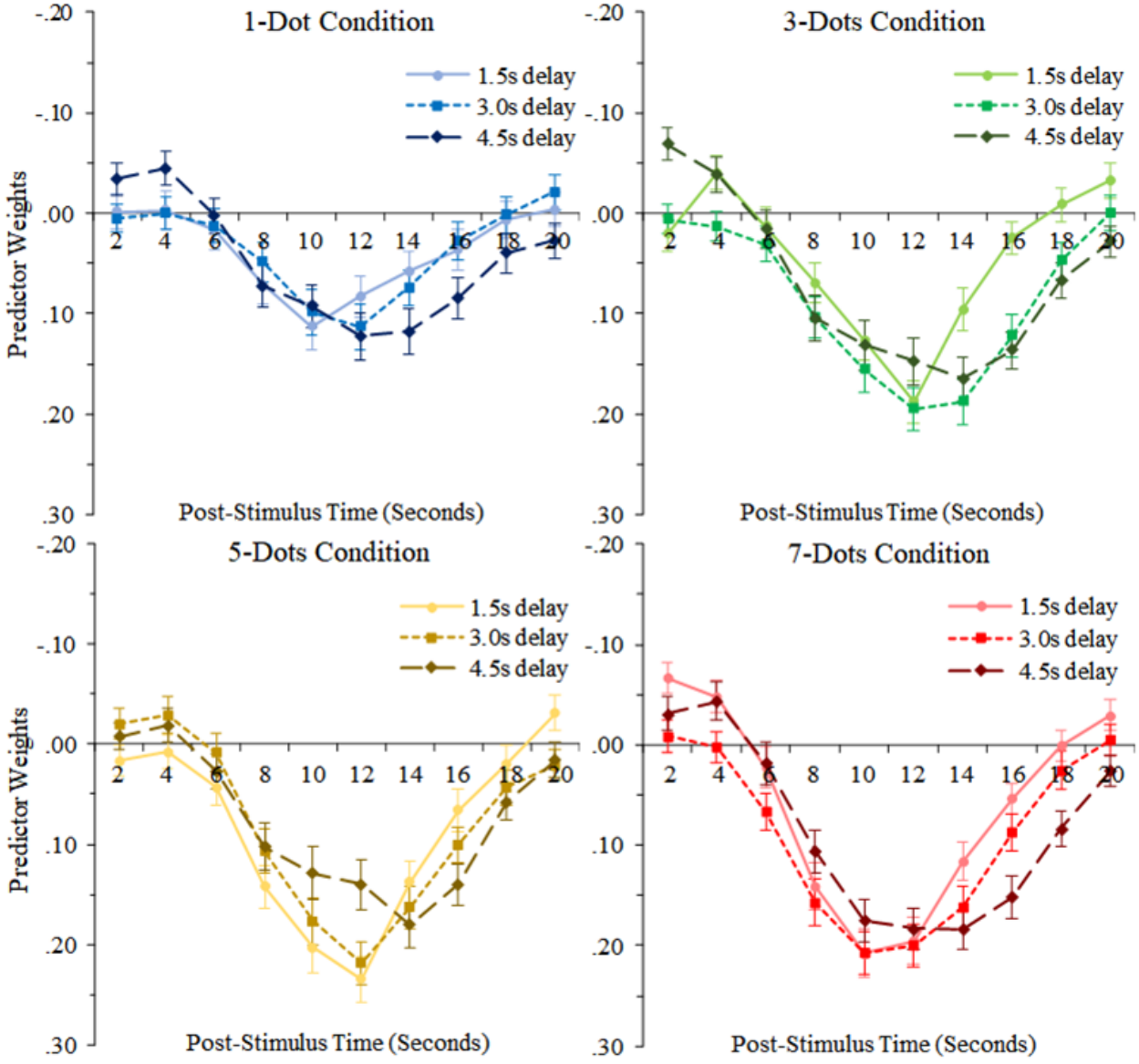

Figure 5.11. SCAP task from the 4-task fMRI-CPCA, DMN (component 1): Graphs illustrating effects of cognitive load and delay length. Y axes are reversed (negative up, positive down) to facilitate interpretation (i.e., values below X axis reflect deactivation and values above X axis reflect activation). **A (top left)**: mean predictor weights illustrating main effect of load (asterisks indicate significant paired t-tests between adjacent load conditions). **B (top right)**: mean predictor weights illustrating main effect of delay (asterisks indicate significant paired t-tests between adjacent delay conditions). **C (bottom)**: predictor weights averaged over load to illustrate delay × time interaction (asterisks indicate significant delay × time contrasts between adjacent time bins; contrast with the greatest effect size is flagged). a = linear effect of delay; b = quadratic effect of delay; * = $p < .05$; ** = $p < .01$; *** = $p < .001$.

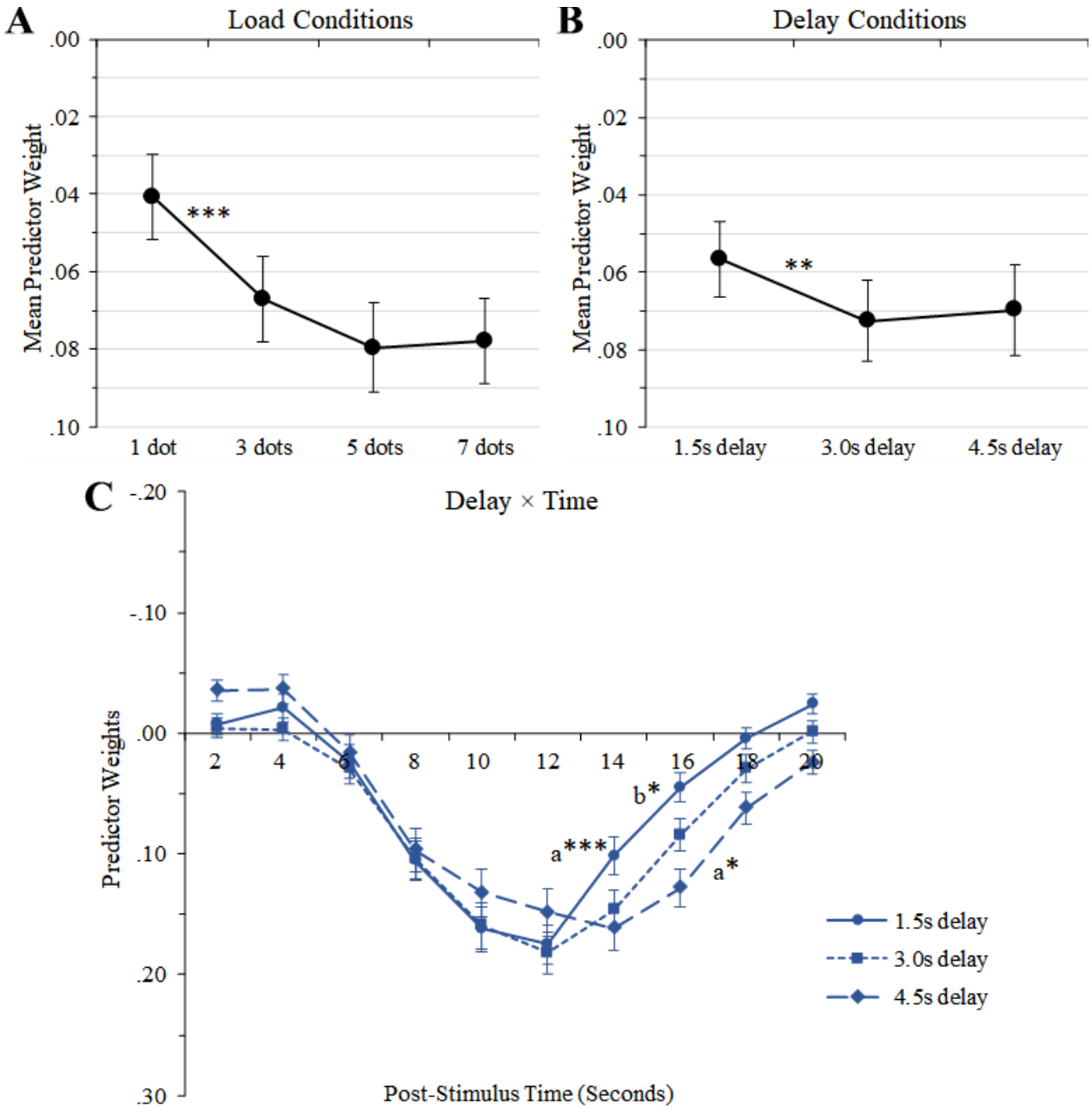

Figure 5.12. TSI task from the 4-task fMRI-CPCA, DMN (component 1): Estimated HDR plots for all word-reading conditions. Y axis is reversed to facilitate interpretation (values above X axis reflect activation, and values below X axis reflect deactivation). cn = task-switch from neutral colour-naming block; ci = task-switch from incongruent colour-naming block; WN = neutral word-reading stimulus; WI = incongruent word-reading stimulus.

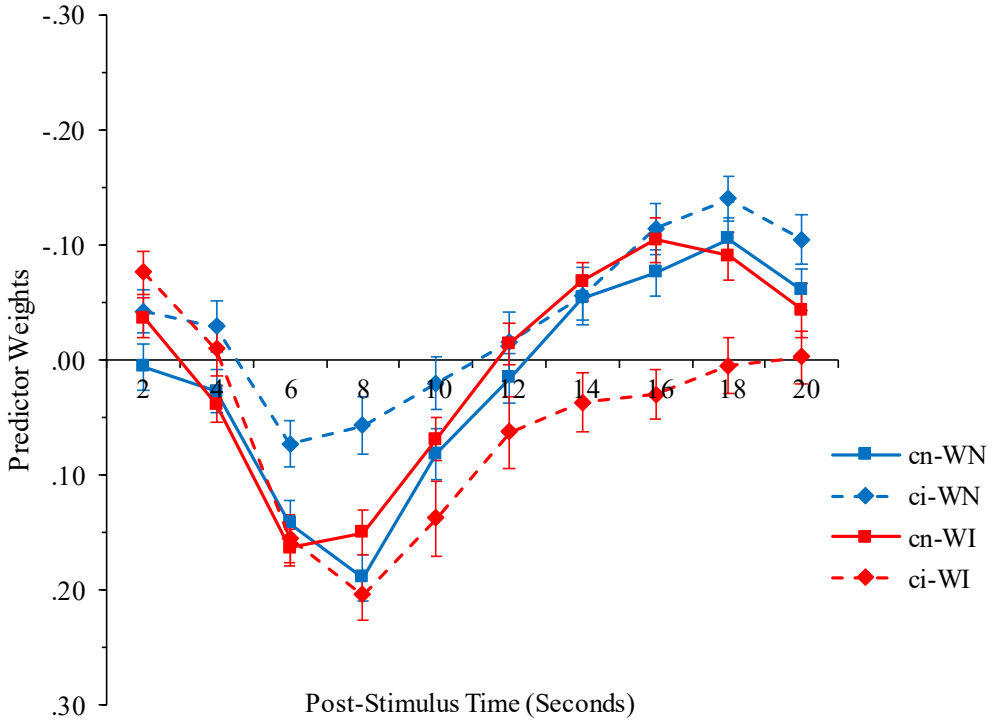

Figure 5.13. TSI task from the 4-task fMRI-CPCA, DMN (component 1): Graphs illustrating effects of stimulus congruency and task-switch condition. Y axis is reversed (negative up, positive down) to facilitate interpretation (values above X axis reflect activation, and values below X axis reflect deactivation). **A (top)**: predictor weights plotted over post-stimulus time, illustrating congruency × time interaction (asterisks indicate significant congruency × time contrasts between adjacent time bins). **B (bottom)**: mean predictor weights illustrating significant congruency × task-switch interaction. * = $p < .05$; *** = $p < .001$.

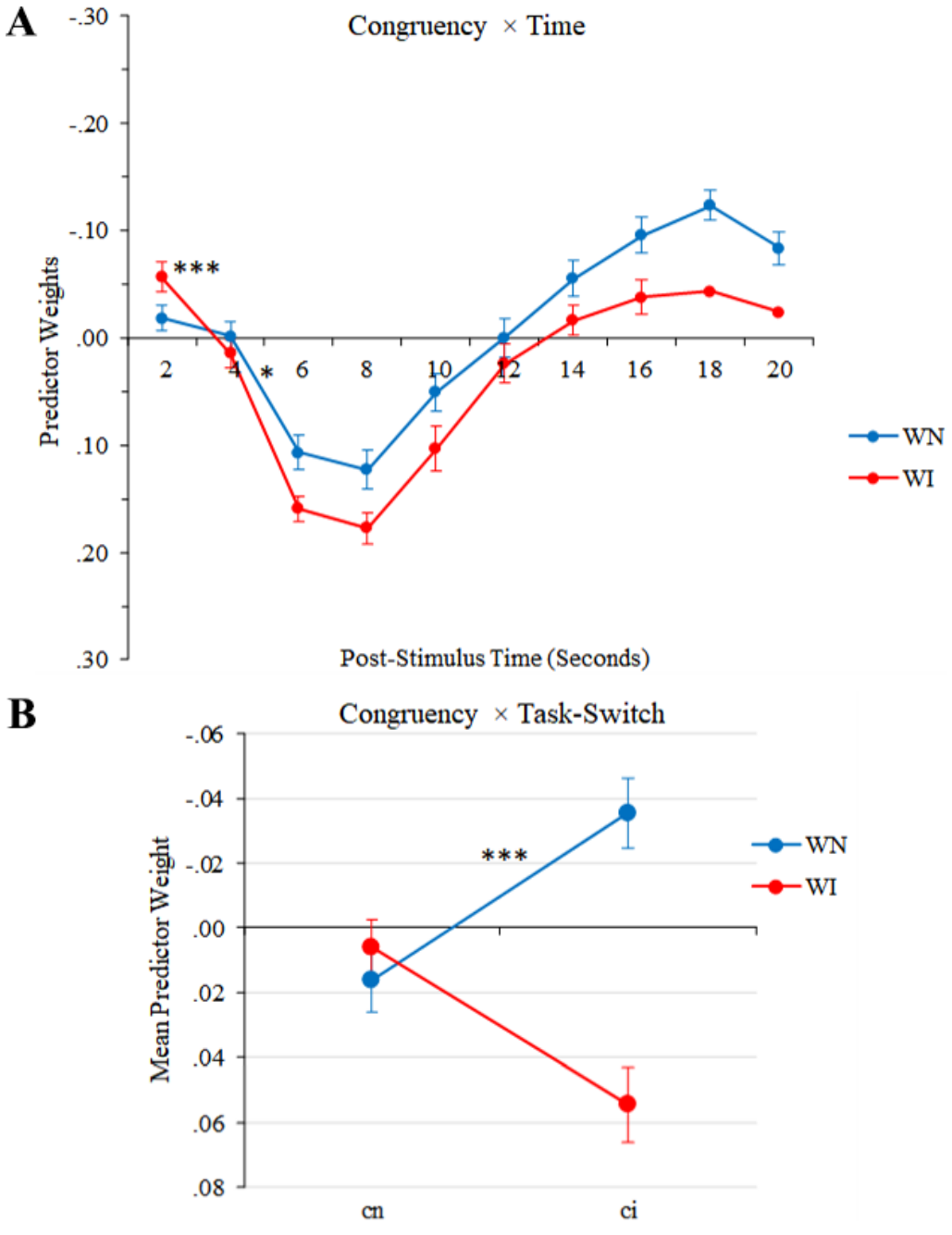

Figure 5.14. TGT task from the 4-task fMRI-CPCA, DMN (component 1): Estimated HDR plots for both task conditions. Y axis is reversed (negative up, positive down) to facilitate interpretation (values above X axis reflect activation and values below X axis reflect deactivation). Asterisks indicate significant condition × time contrasts between adjacent time bins. ** = $p < .01$; *** = $p < .001$.

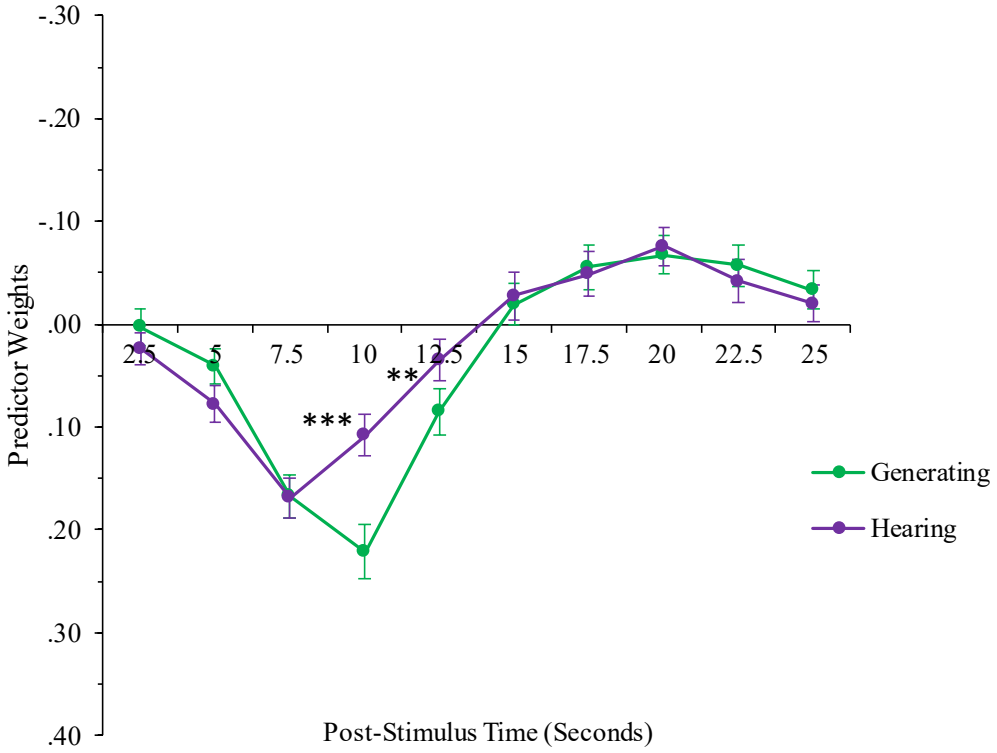

Figure 5.15. 4-task fMRI-CPCA, internal attention network (component 2): Dominant 10% of component loadings (red/yellow = positive loadings, min = 0.18, max = 0.36; no negative loadings above threshold). Images are displayed in neurological orientation (left is left) with MNI coordinates.

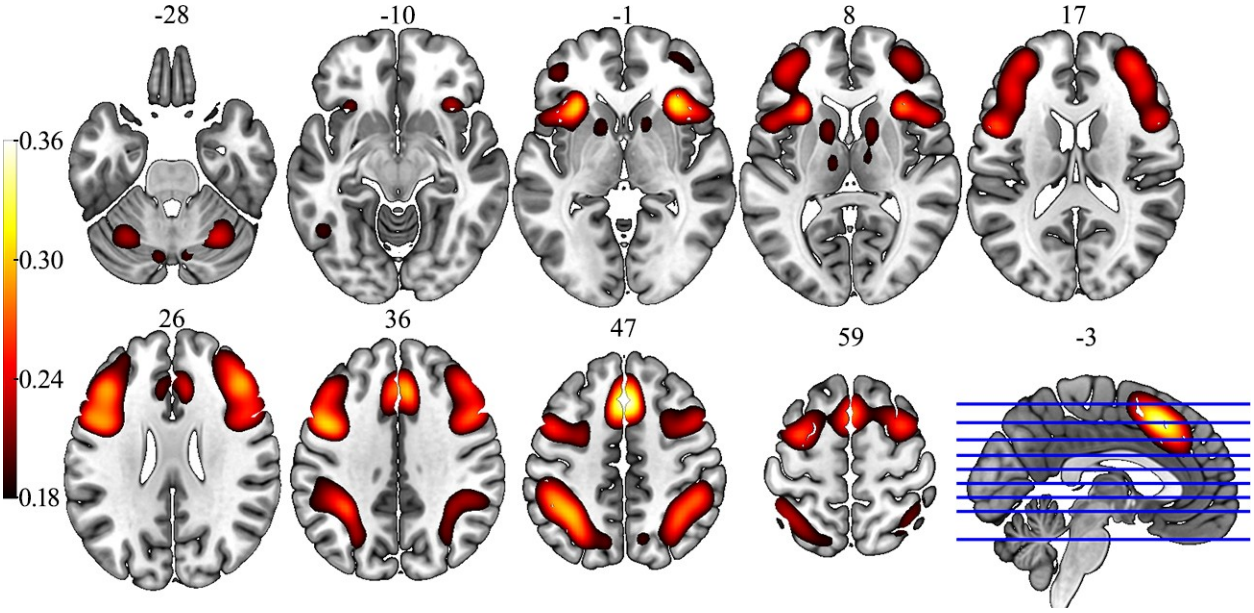

Figure 5.16. WM task from the 4-task fMRI-CPCA, internal attention network (component 2): Estimated HDR plots for all task conditions. 4L = 4 letters; 6L = 6 letters.

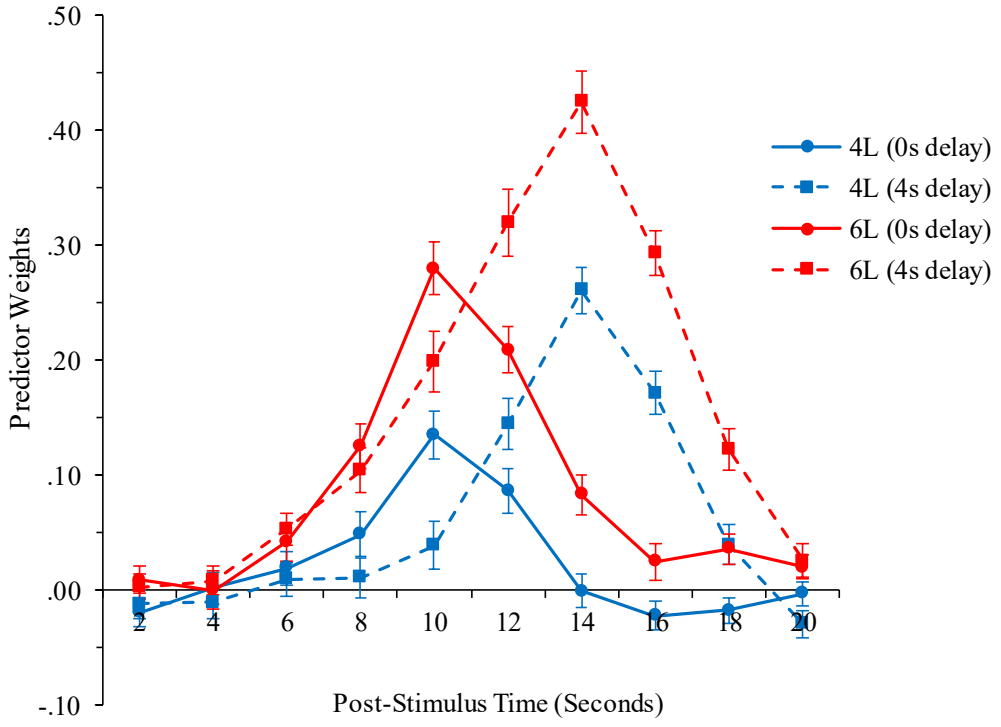

Figure 5.17. WM task from the 4-task fMRI-CPCA, internal attention network (component 2): Graphs illustrating effects of cognitive load and delay length. **A (top)**: predictor weights averaged over load to illustrate delay × time interaction (asterisks indicate significant delay × time contrasts between adjacent time bins). **B (bottom)**: mean predictor weights illustrating significant load × delay interaction. ** = $p < .01$; *** = $p < .001$.

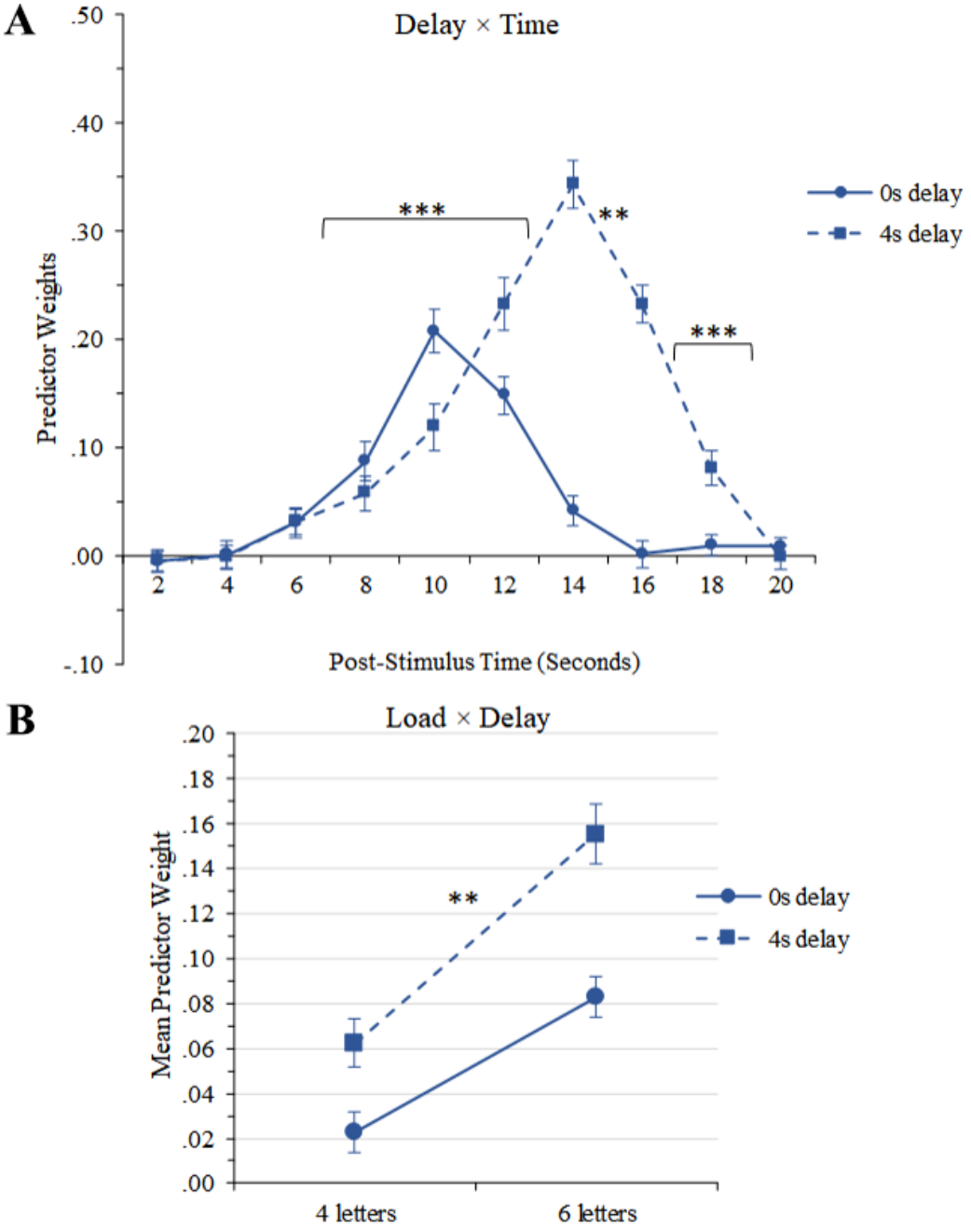

Figure 5.18. SCAP task from the 4-task fMRI-CPCA, internal attention network (component 2): Estimated HDR plots for all task conditions (each load level is presented on a separate graph).

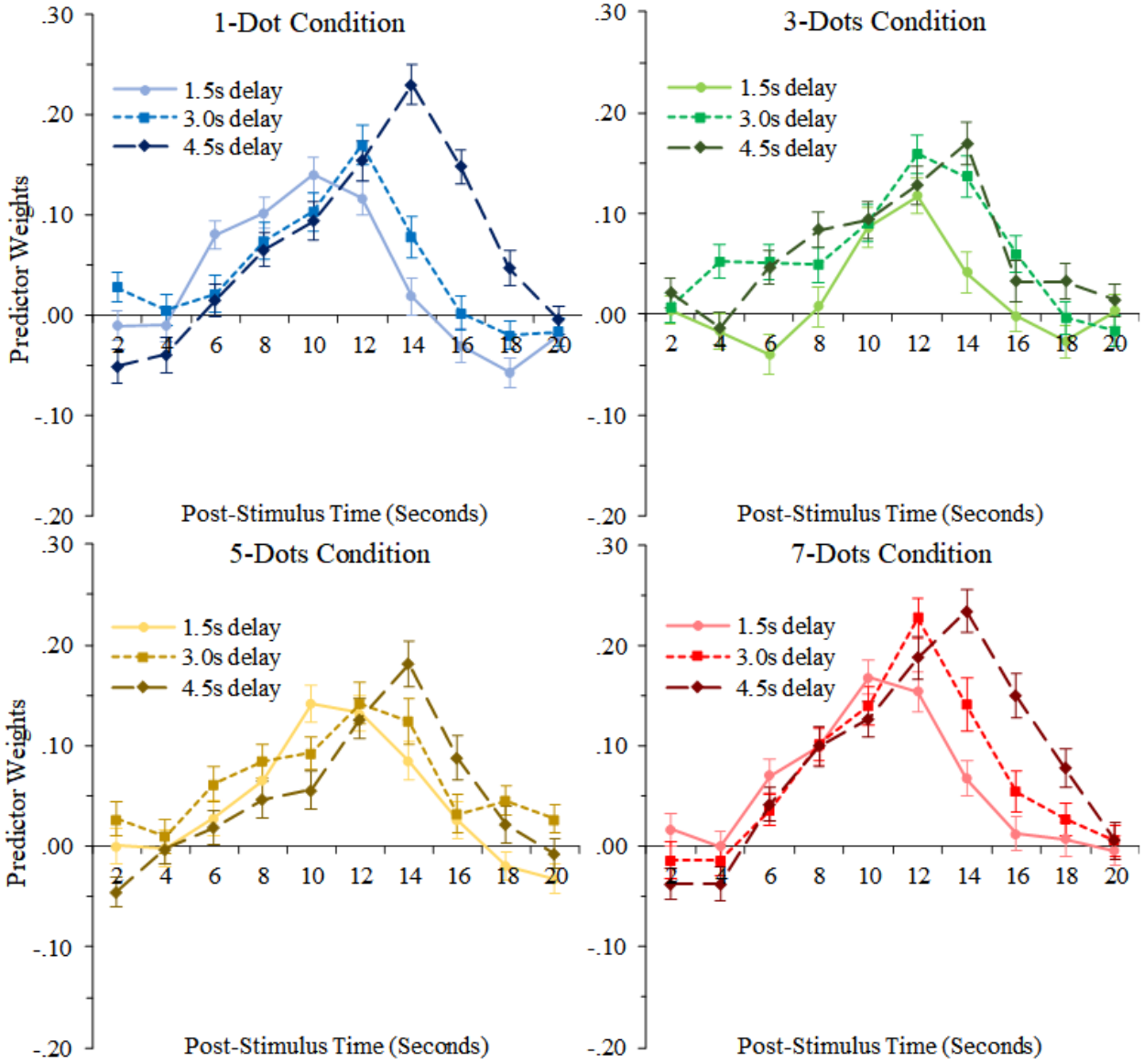

Figure 5.19. SCAP task from the 4-task fMRI-CPCA, internal attention network (component 2): Graphs illustrating effects of cognitive load and delay length. **A (top left)**: mean predictor weights illustrating main effect of load (asterisks indicate significant paired t-tests between adjacent load conditions). **B (top right)**: mean predictor weights illustrating main effect of delay (asterisks indicate significant paired t-tests between adjacent delay conditions). **C (bottom)**: predictor weights averaged over load to illustrate delay × time interaction (asterisks indicate significant delay × time contrasts between adjacent time bins; contrast with the greatest effect size is flagged). a = linear effect of delay; b = quadratic effect of delay; * = $p < .05$; ** = $p < .01$; *** = $p < .001$.

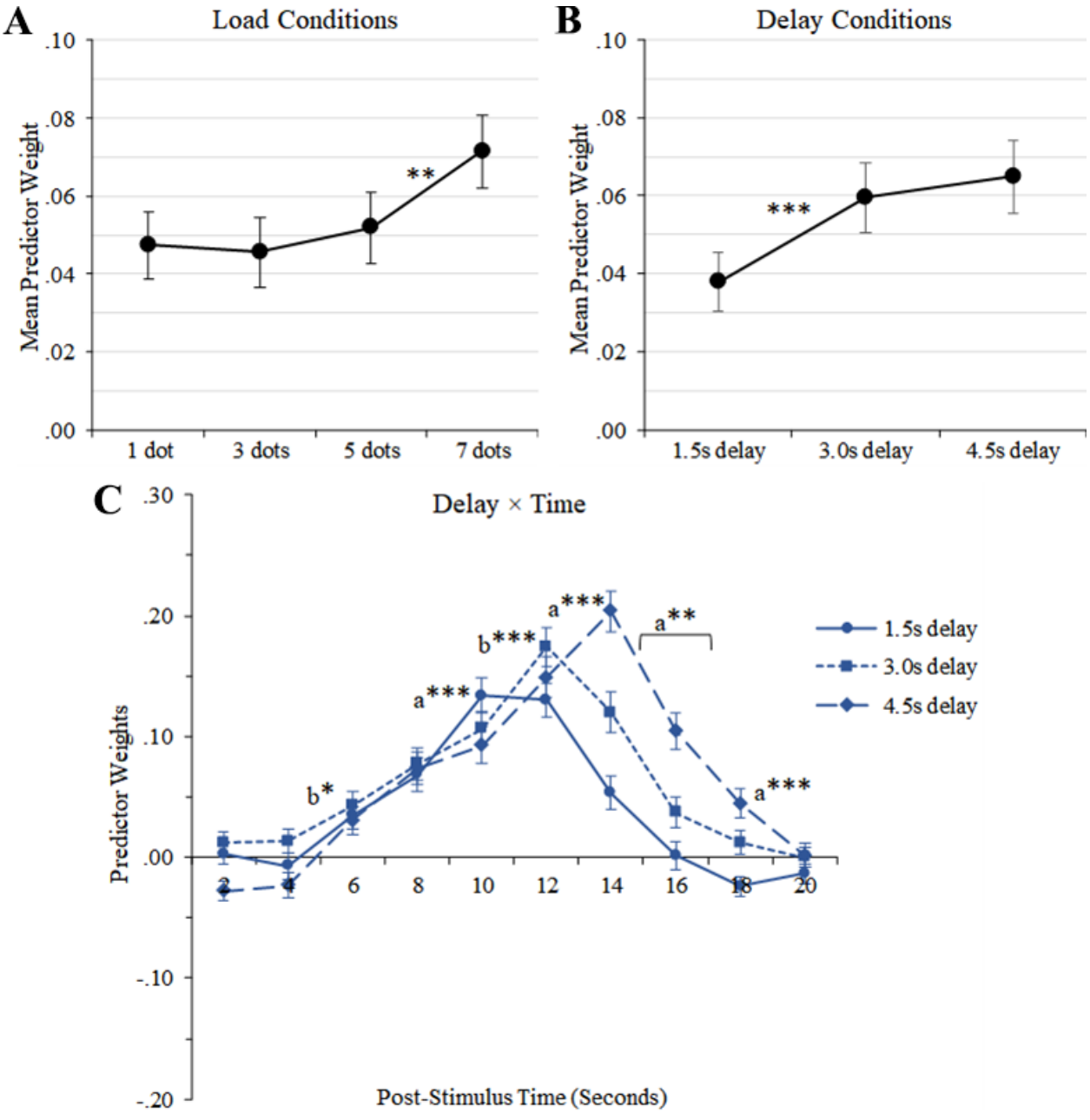

Figure 5.20. SCAP task from the 4-task fMRI-CPCA, internal attention network (component 2): Estimated HDRs illustrating group differences. **A (top)**: predictor weights averaged over all task conditions to illustrate group × time interaction (asterisks indicate significant group × time contrasts between adjacent time bins after removing variance predicted by age). **B (bottom)**: predictor weights averaged over load to illustrate delay × time × group interaction (asterisks indicate significant contrasts between adjacent time bins underlying the delay × time × group interaction after removing variance predicted by age, and therefore indicate where the delay × time interaction differed between groups). a = significant group difference in the linear effect of delay; b = significant group difference in the quadratic effect of delay; * = $p < .05$; ** = $p < .01$.

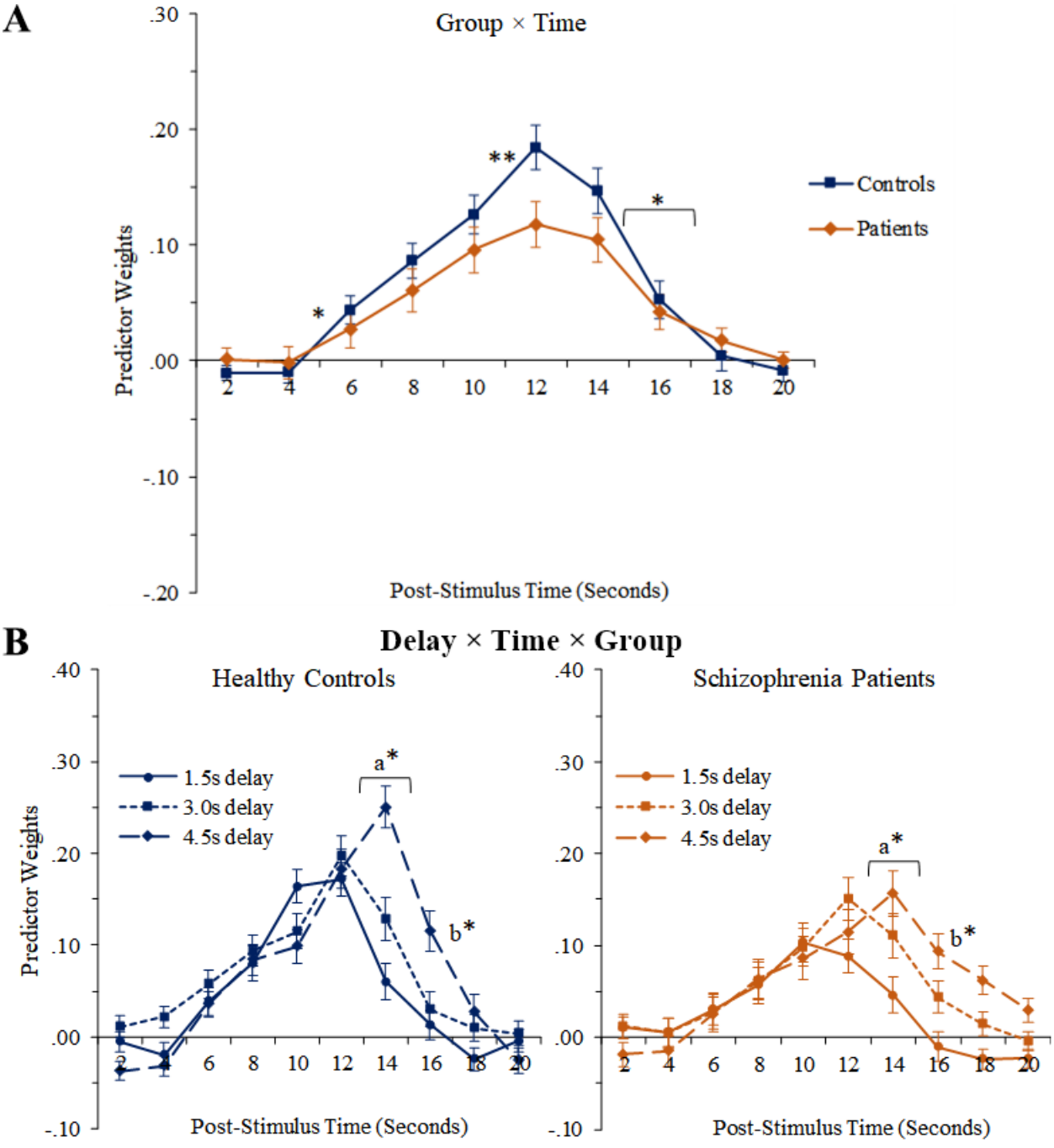

Figure 5.21. TSI task from the 4-task fMRI-CPCA, internal attention network (component 2): Estimated HDR plots for all word-reading conditions. cn = task-switch from neutral colour-naming block; ci = task-switch from incongruent colour-naming block; WN = neutral word-reading stimulus; WI = incongruent word-reading stimulus.

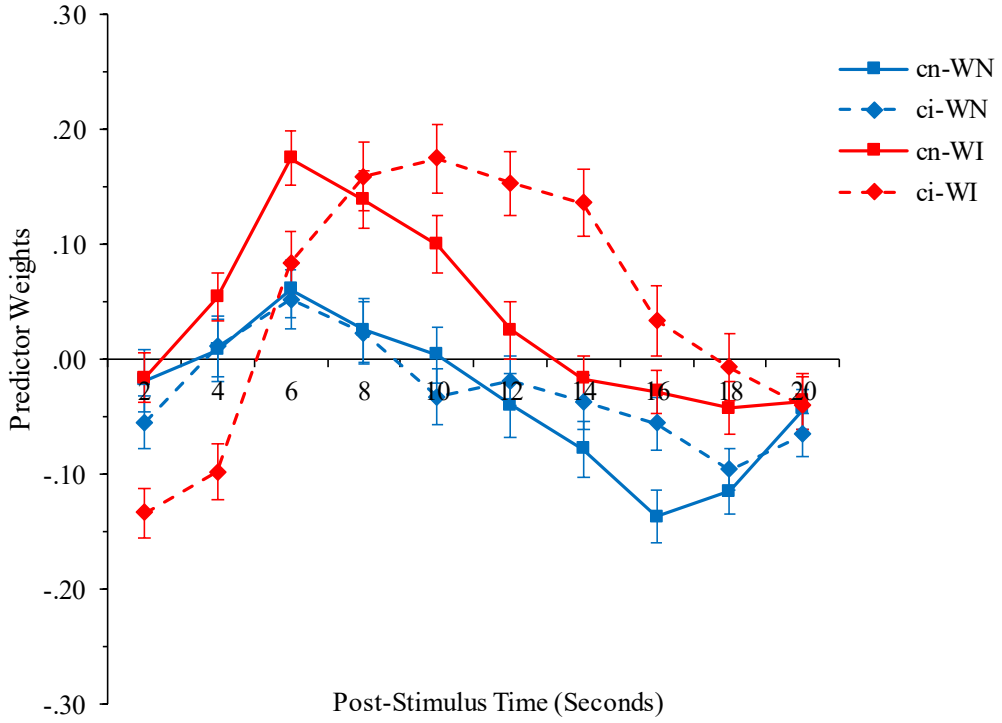

Figure 5.22. TSI task from 4-task fMRI-CPCA, internal attention network (component 2): Estimated HDRs illustrating stimulus congruency and task-switch effects. Asterisks indicate significant condition × time contrasts between adjacent time bins. **A (top)**: predictor weights averaged over task-switch to illustrate congruency × time interaction. **B (bottom)**: predictor weights averaged over congruency to illustrate task-switch × time interaction. WN = neutral word-reading stimulus; WI = incongruent word-reading stimulus; cn = task-switch from neutral colour-naming block; ci = task-switch from incongruent colour-naming block; ** = $p < .01$; *** = $p < .001$.

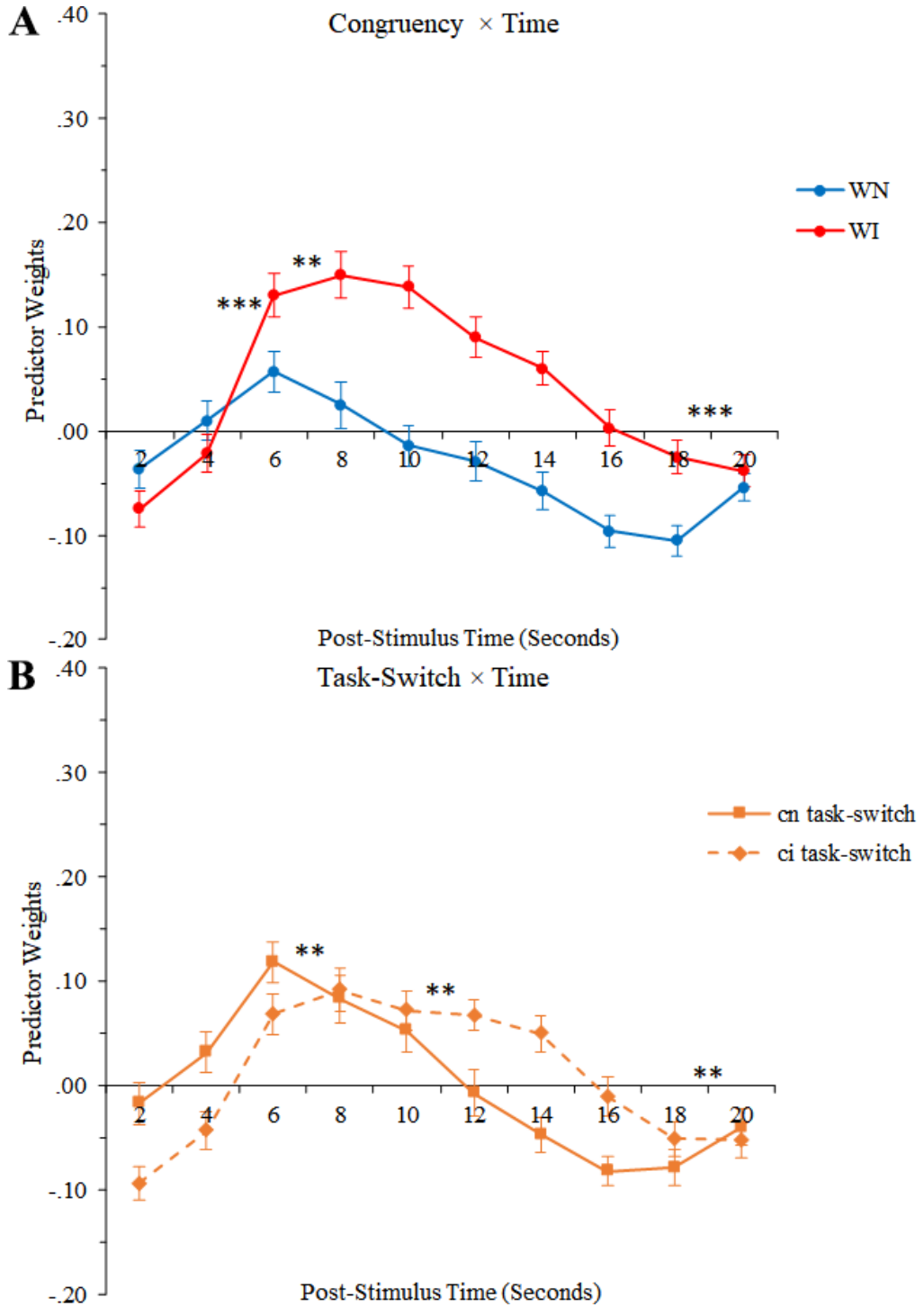

Figure 5.23. TGT task from the 4-task fMRI-CPCA, internal attention network (component 2): Estimated HDR plots for both task conditions. Asterisks indicate significant condition × time contrasts between adjacent time bins. ** = $p < .01$; *** = $p < .001$.

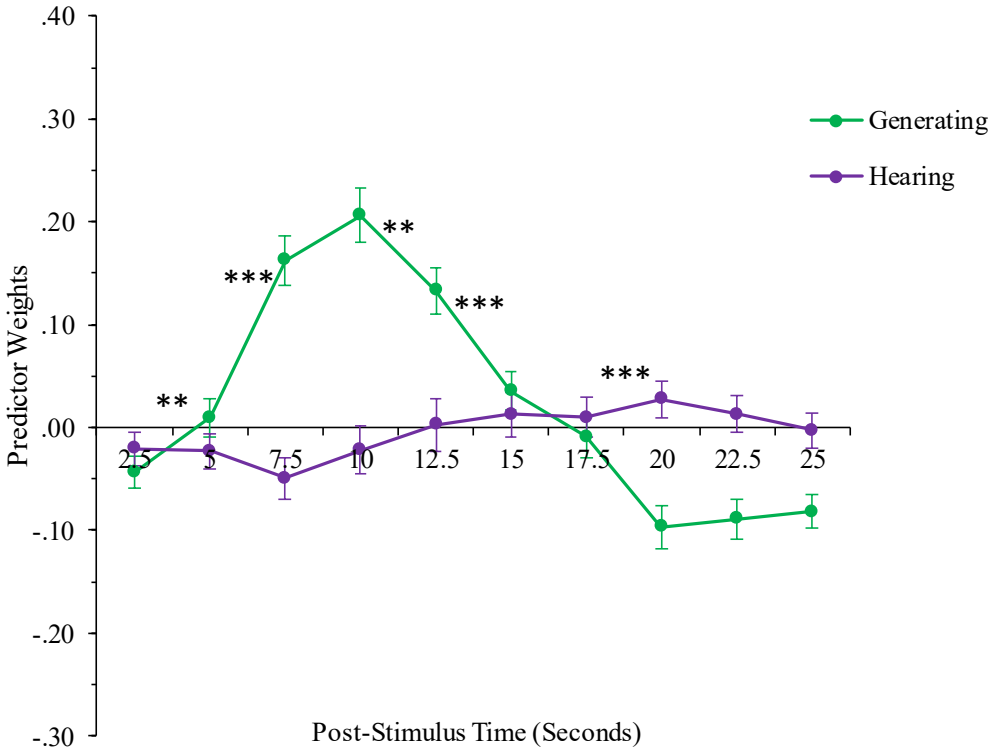

Figure 5.24. 4-task fMRI-CPCA, sensorimotor network (component 3): Dominant 10% of component loadings (red/yellow = positive loadings, min = 0.17, max = 0.33; no negative loadings above threshold). Images are displayed in neurological orientation (left is left) with MNI coordinates.

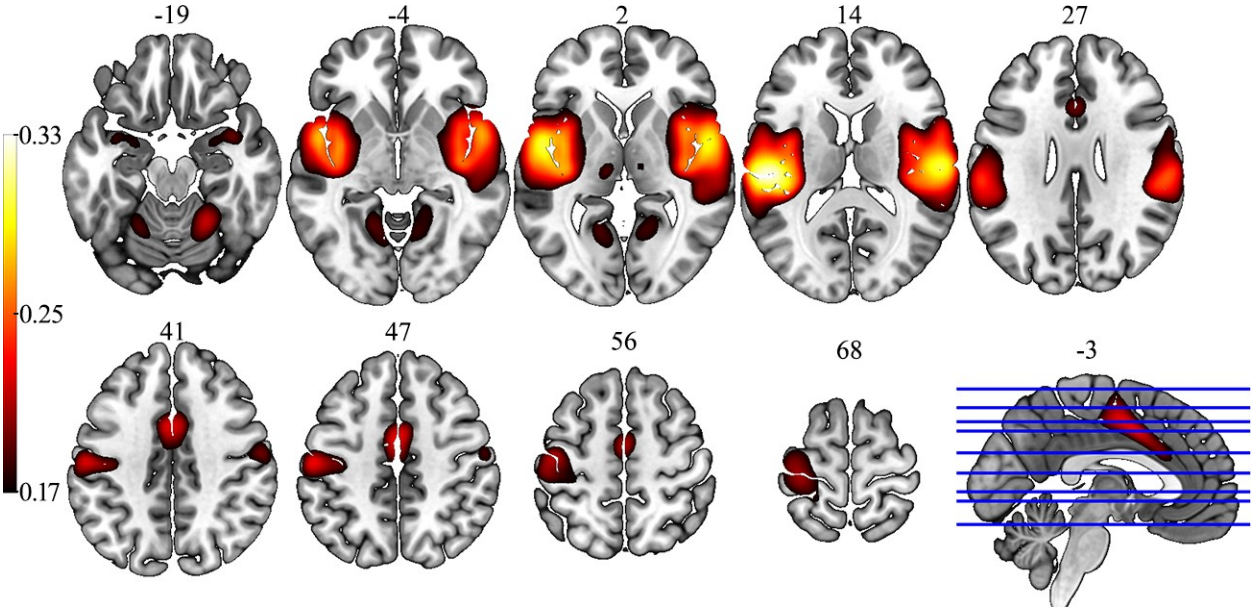

Figure 5.25. WM task from the 4-task fMRI-CPCA, sensorimotor network (component 3): Estimated HDR plots for all task conditions. 4L = 4 letters; 6L = 6 letters.

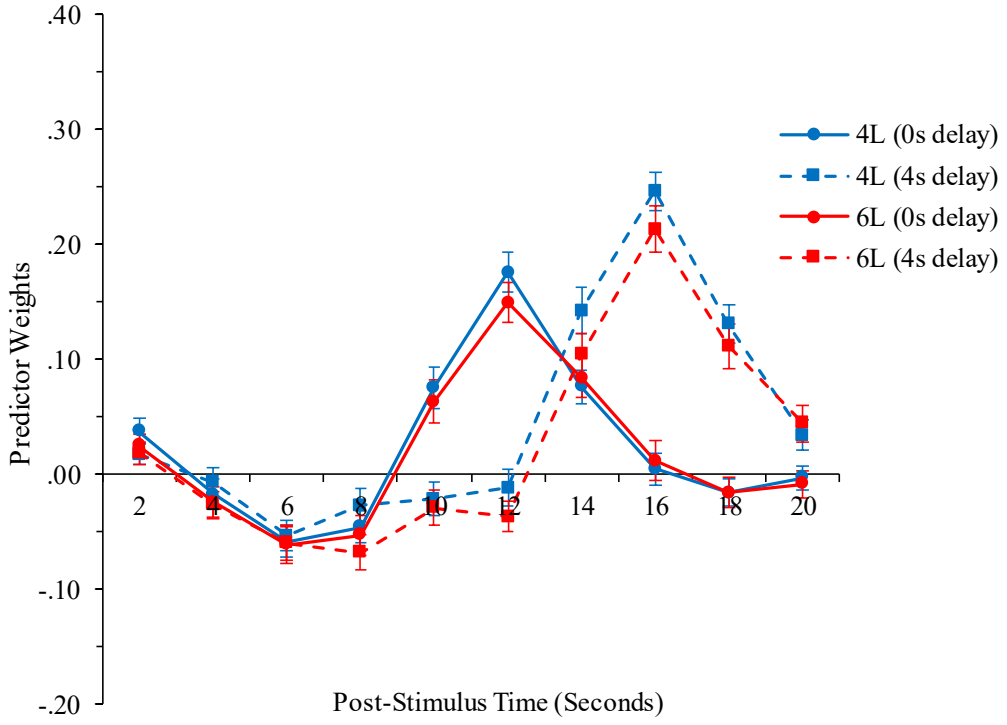

Figure 5.26. WM task from the 4-task fMRI-CPCA, sensorimotor network (component 3): Estimated HDRs illustrating delay × time interaction (asterisks indicate significant delay × time contrasts between adjacent time bins). *** = $p < .001$.

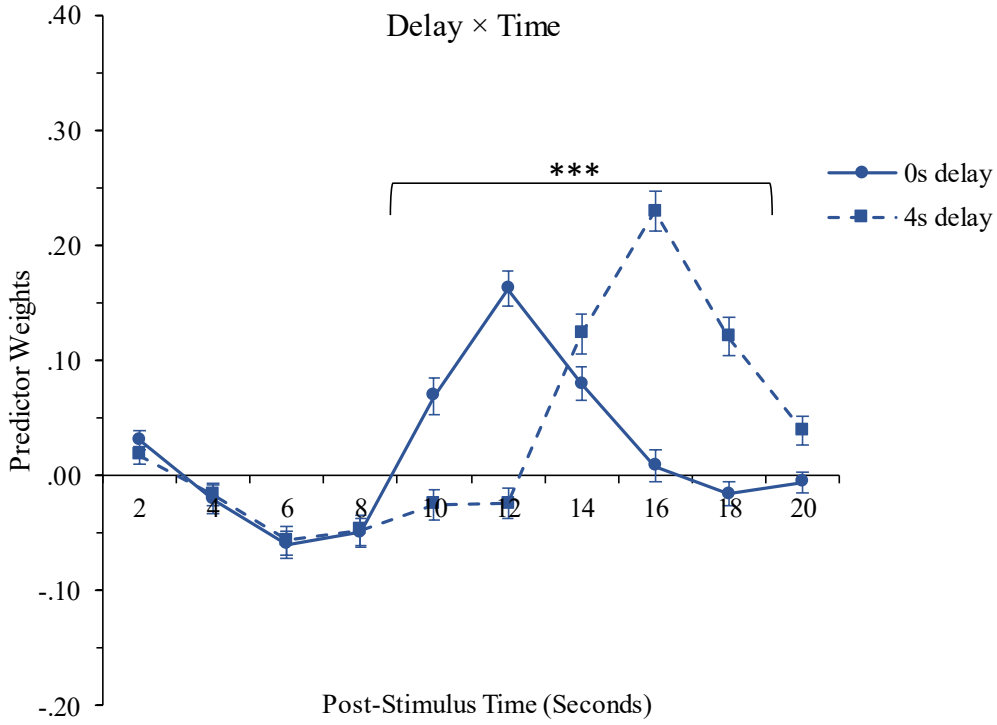

Figure 5.27. SCAP task from the 4-task fMRI-CPCA, sensorimotor network (component 3): Estimated HDR plots (each load level presented on a separate graph).

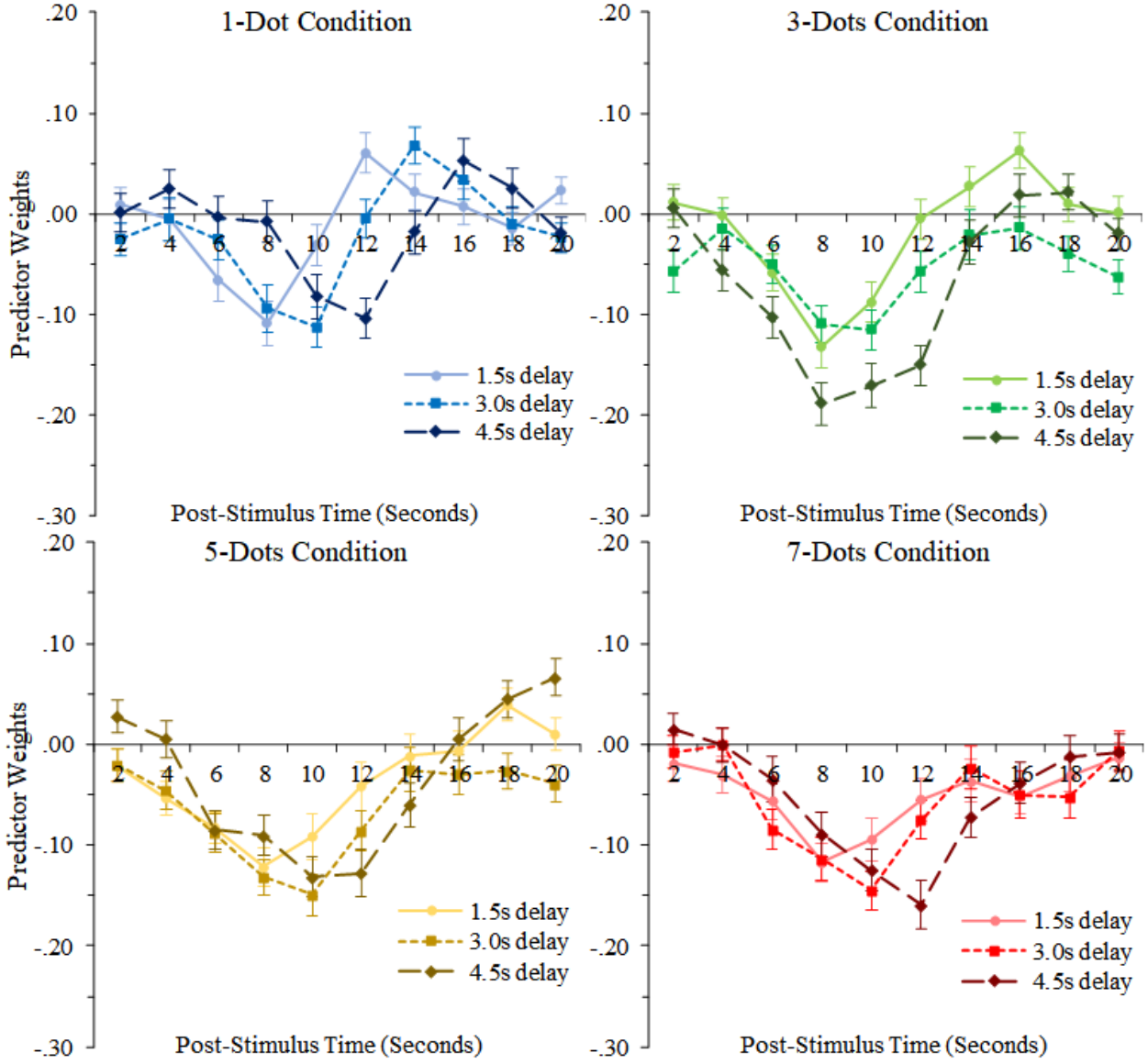

Figure 5.28. SCAP task from the 4-task fMRI-CPCA, sensorimotor network (component 3): Graphs illustrating effects of cognitive load and delay length. **A (top left):** mean predictor weights illustrating main effect of load (asterisks indicate significant paired t-tests between adjacent load conditions). **B (top right):** mean predictor weights illustrating main effect of delay (asterisks indicate significant paired t-tests between adjacent delay conditions). **C (bottom):** predictor weights averaged over load to illustrate delay × time interaction (asterisks indicate significant delay × time contrasts between adjacent time bins; contrast with the greatest effect size is flagged). a = linear effect of delay; b = quadratic effect of delay; * = $p < .05$; ** = $p < .01$; *** = $p < .001$.

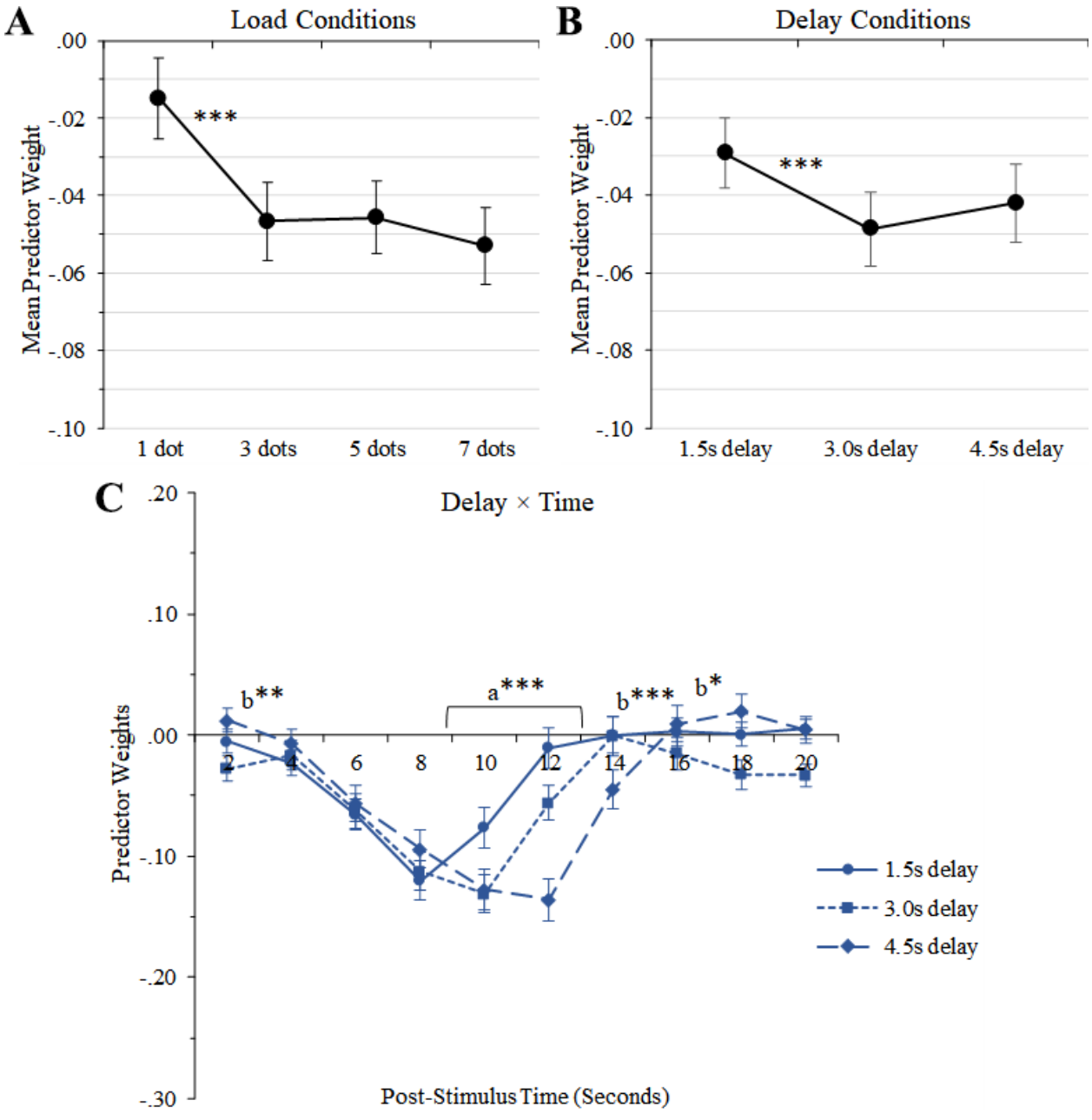

Figure 5.29. SCAP task from the 4-task fMRI-CPCA, sensorimotor network (component 3): Mean predictor weights illustrating load × group interaction, explained by significant difference in quadratic contrast.

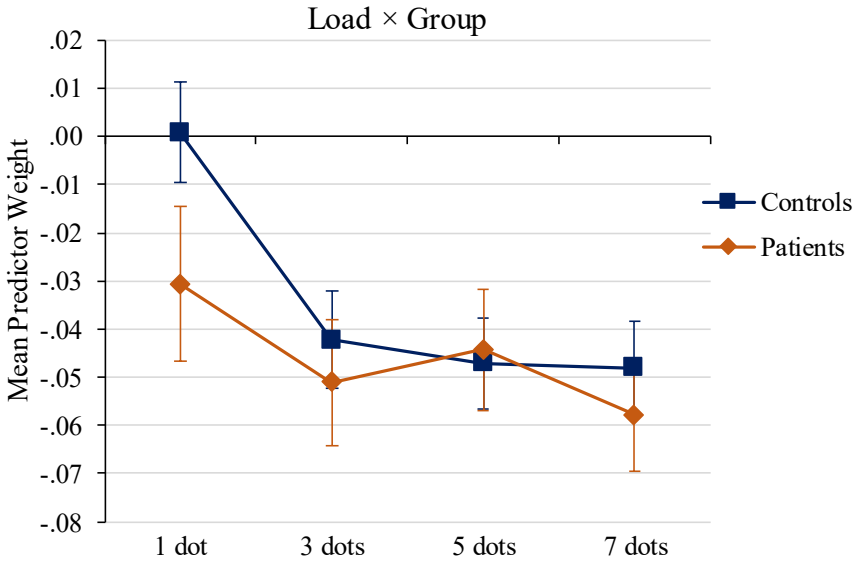

Figure 5.30. TSI task from the 4-task fMRI-CPCA, sensorimotor network (component 3): Estimated HDR plots for all word-reading conditions. cn = task-switch from neutral colour-naming block; ci = task-switch from incongruent colour-naming block; WN = neutral word-reading stimulus; WI = incongruent word-reading stimulus.

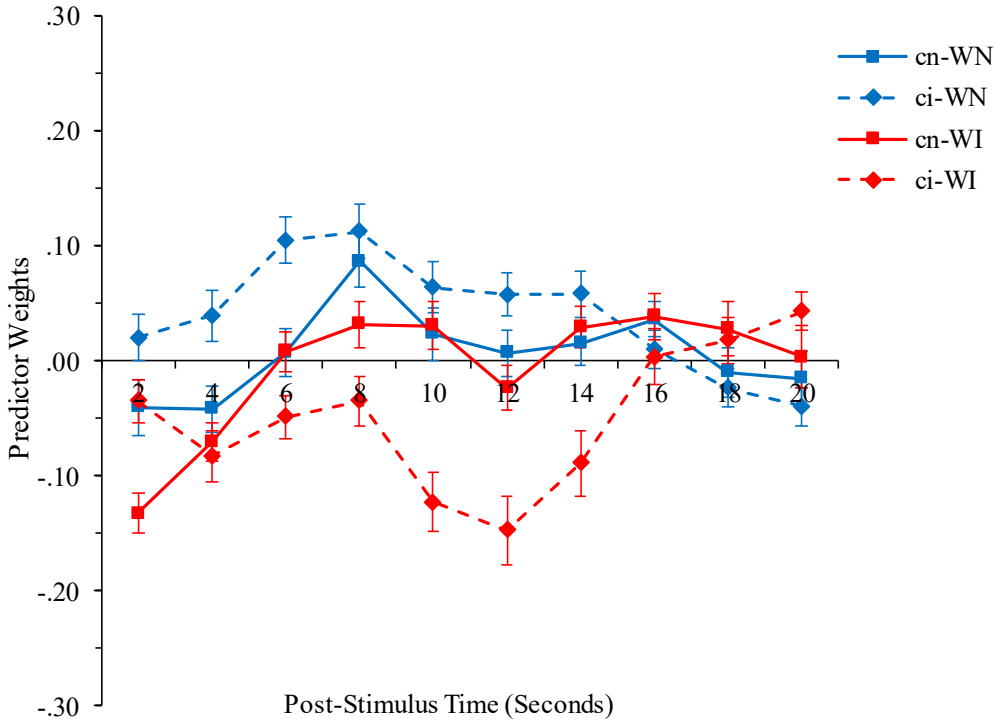

Figure 5.31. TSI task from the 4-task fMRI-CPCA, sensorimotor network (component 3): Estimated HDRs illustrating stimulus congruency and task-switch effects. **A (top)**: predictor weights averaged over task-switch to illustrate congruency × time interaction (asterisks indicate significant congruency × time contrasts between adjacent time bins). **B (bottom)**: mean predictor weights illustrating significant congruency × task-switch interaction. WN = neutral word-reading stimulus; WI = incongruent word-reading stimulus; cn = task-switch from neutral colour-naming block; ci = task-switch from incongruent colour-naming block. ** = $p < .01$; *** = $p < .001$.

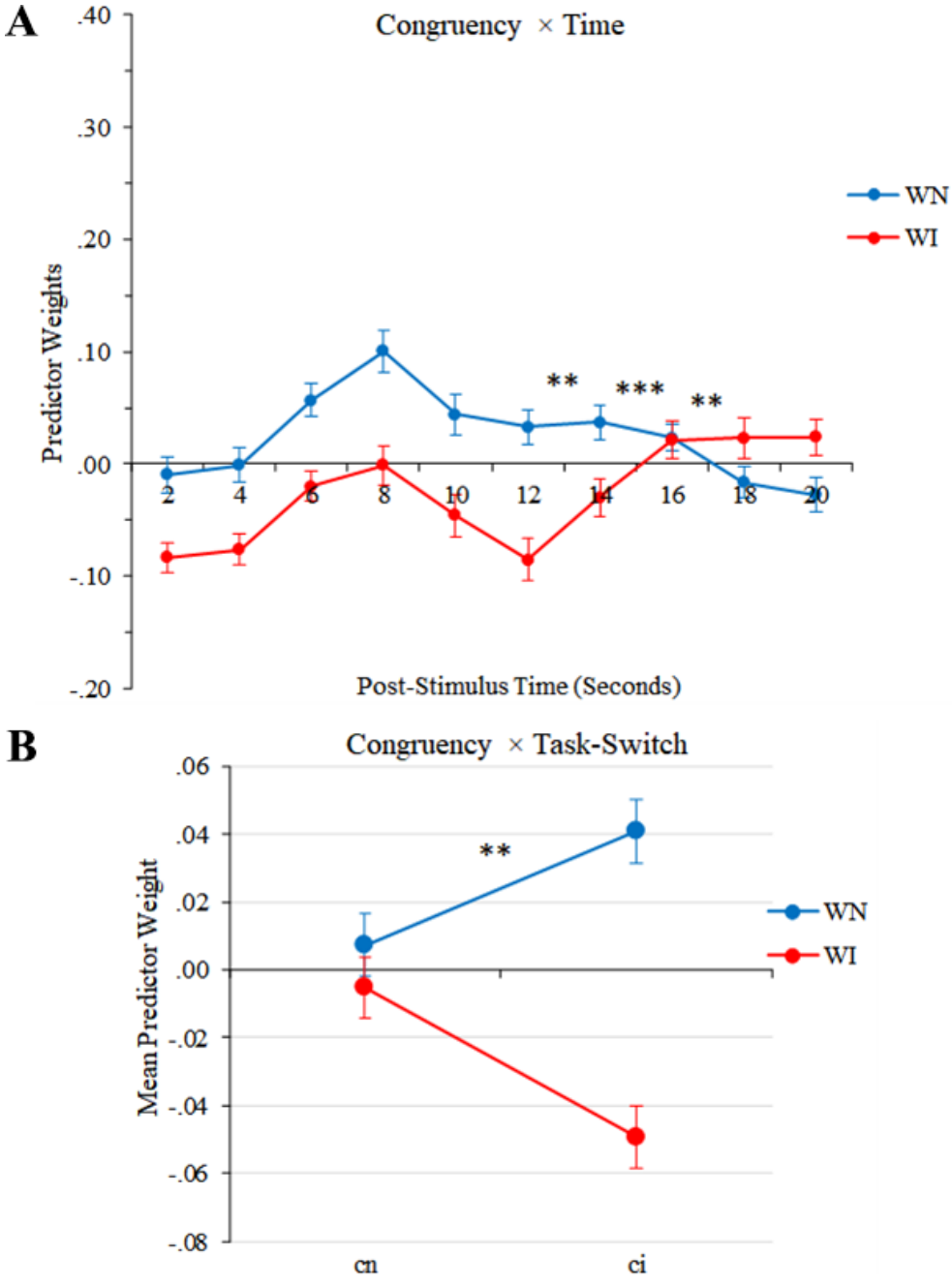

Figure 5.32. TGT task from the 4-task fMRI-CPCA, sensorimotor network (component 3): Estimated HDR plots for both task conditions. Asterisks indicate significant condition × time contrasts between adjacent time bins. * = $p < .05$; ** = $p < .01$; *** = $p < .001$.

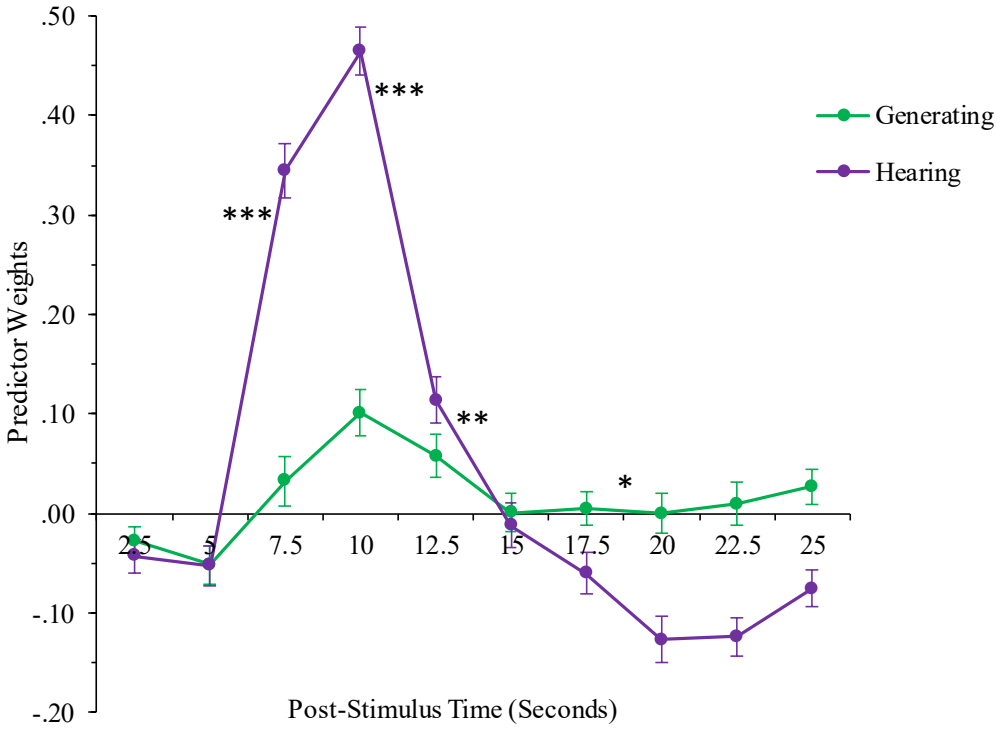

Figure 5.33. 4-task fMRI-CPCA, motor response network (component 4): Dominant 10% of component loadings (red/yellow = positive loadings, min = 0.17, max = 0.32; no negative loadings above threshold). Images are displayed in neurological orientation (left is left) with MNI coordinates.

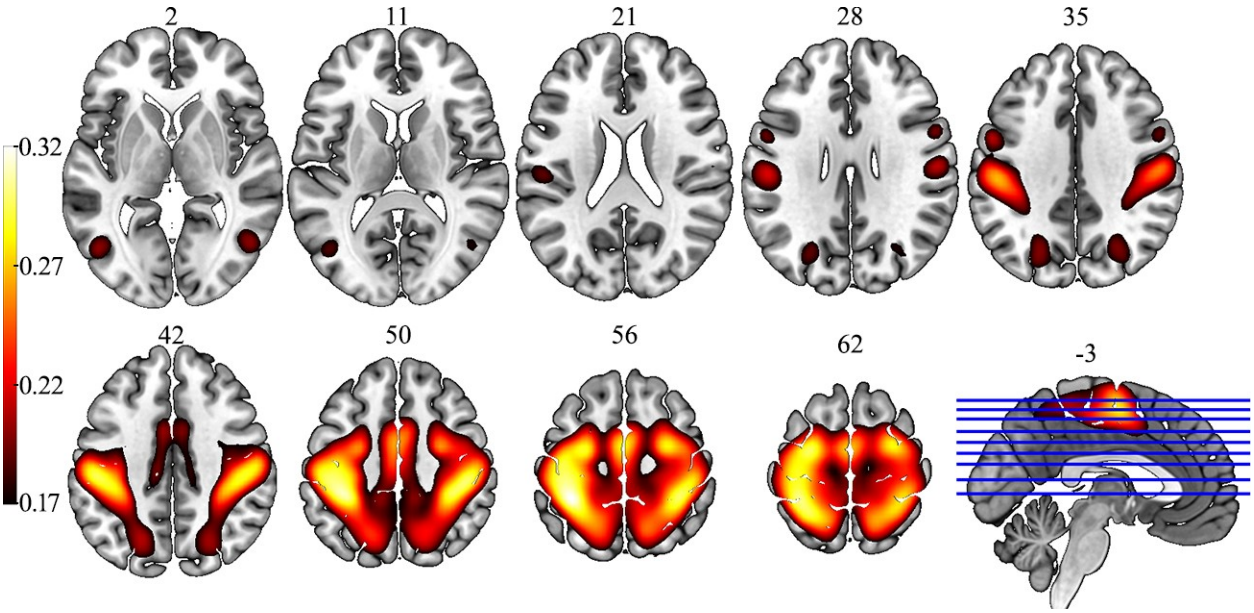

Figure 5.34. WM task from the 4-task fMRI-CPCA, motor response network (component 4): Estimated HDR plots for all task conditions. 4L = 4-letter load condition; 6L = 6-letter load condition.

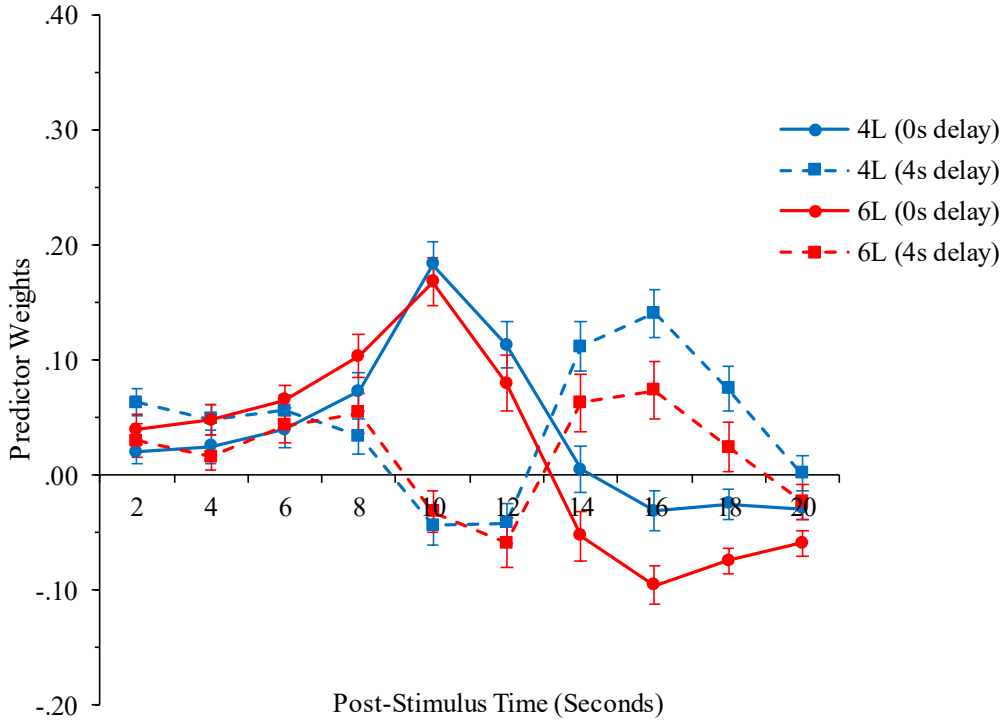

Figure 5.35. WM task from the 4-task fMRI-CPCA, motor response network (component 4): Estimated HDR plots illustrating delay × time interaction (asterisks indicate significant delay × time contrasts between adjacent time bins). ** = $p < .01$; *** = $p < .001$.

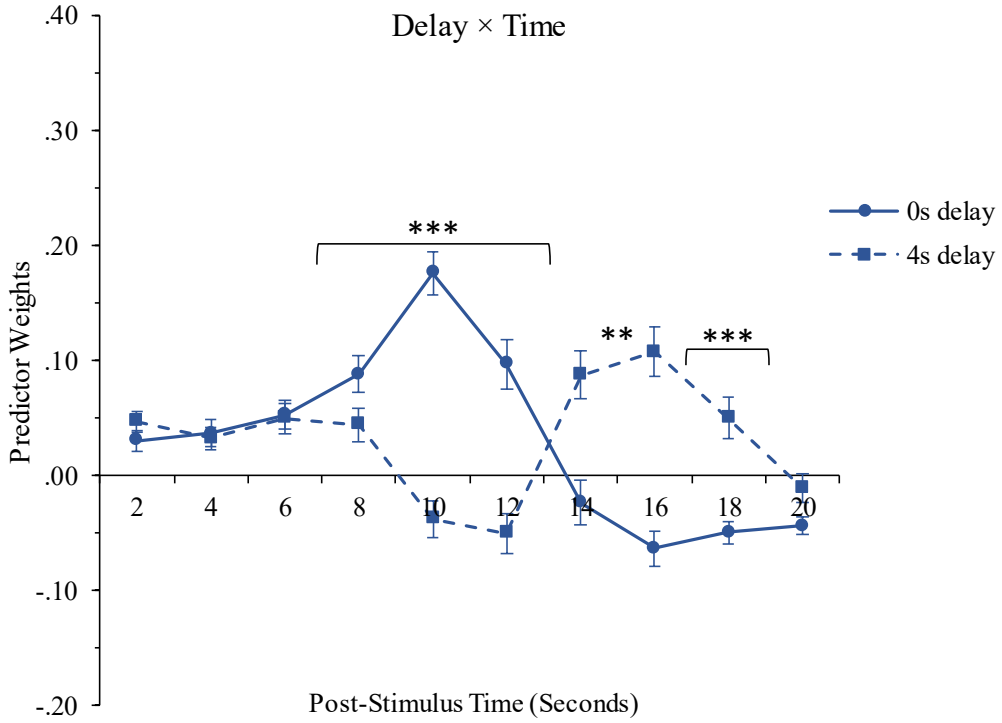

Figure 5.36. WM task from the 4-task fMRI-CPCA, motor response network (component 4): mean predictor weights illustrating load × group interaction. Asterisk indicates significant load × group interaction after removing variance predictable from age. * = $p < .05$.

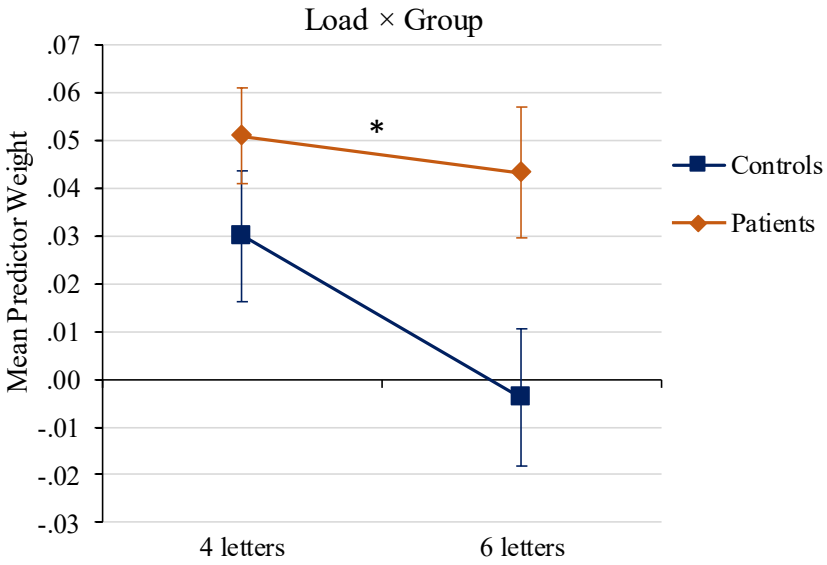

Figure 5.37. SCAP task from the 4-task fMRI-CPCA, motor response network (component 4): Estimated HDR plots for all task conditions (load levels displayed on separate graphs).

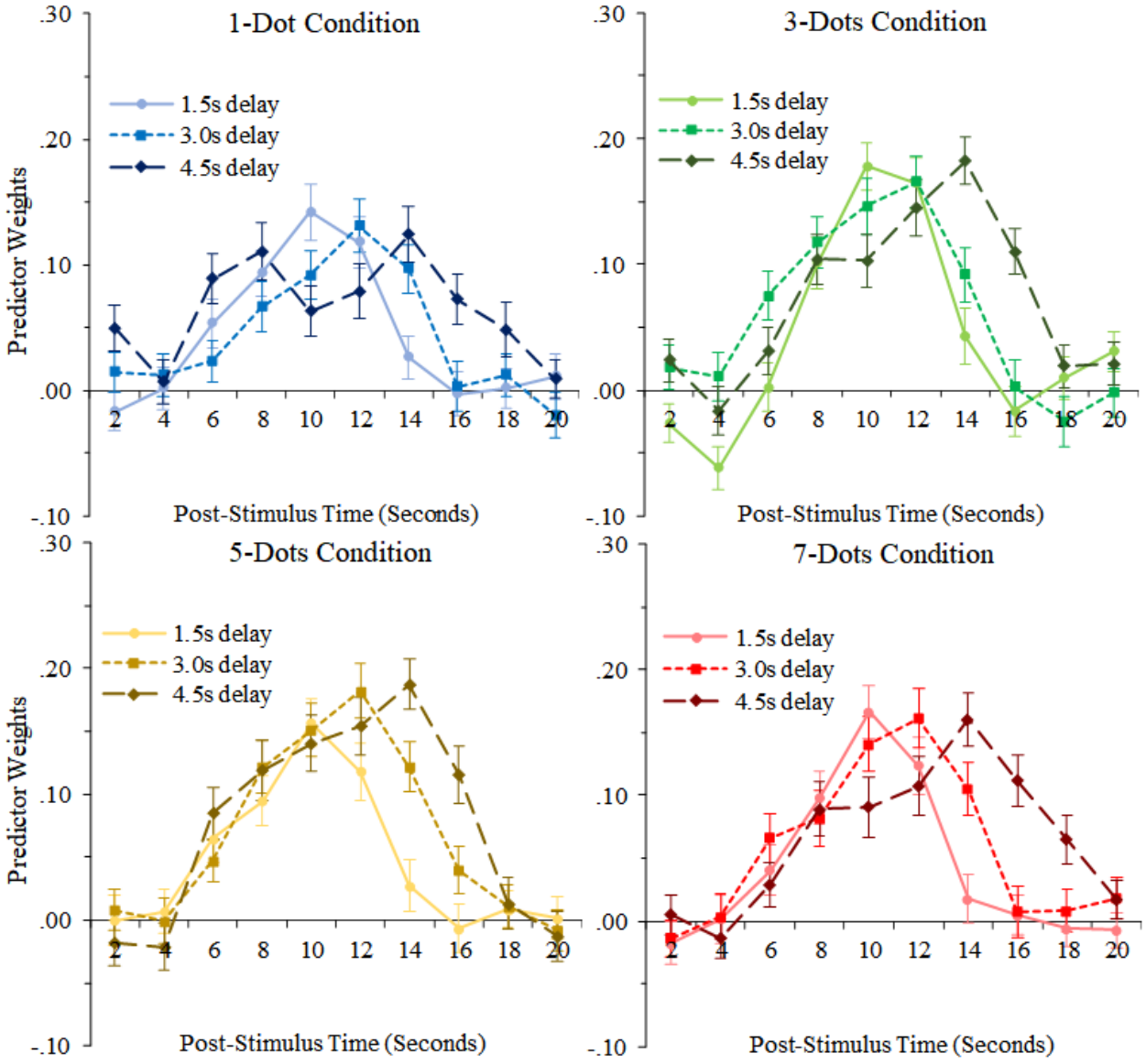

Figure 5.38. SCAP task from the 4-task fMRI-CPCA, motor response network (component 4): Graphs illustrating effects of delay length. **A (top)**: mean predictor weights illustrating main effect of delay (asterisks indicate significant paired t-tests between adjacent delay conditions). **B (bottom)**: predictor weights averaged over load to illustrate delay × time interaction (asterisks indicate significant delay × time contrasts between adjacent time bins; contrast with the greatest effect size is flagged). a = linear effect of delay; b = quadratic effect of delay; * = $p < .05$; ** = $p < .01$; *** = $p < .001$.

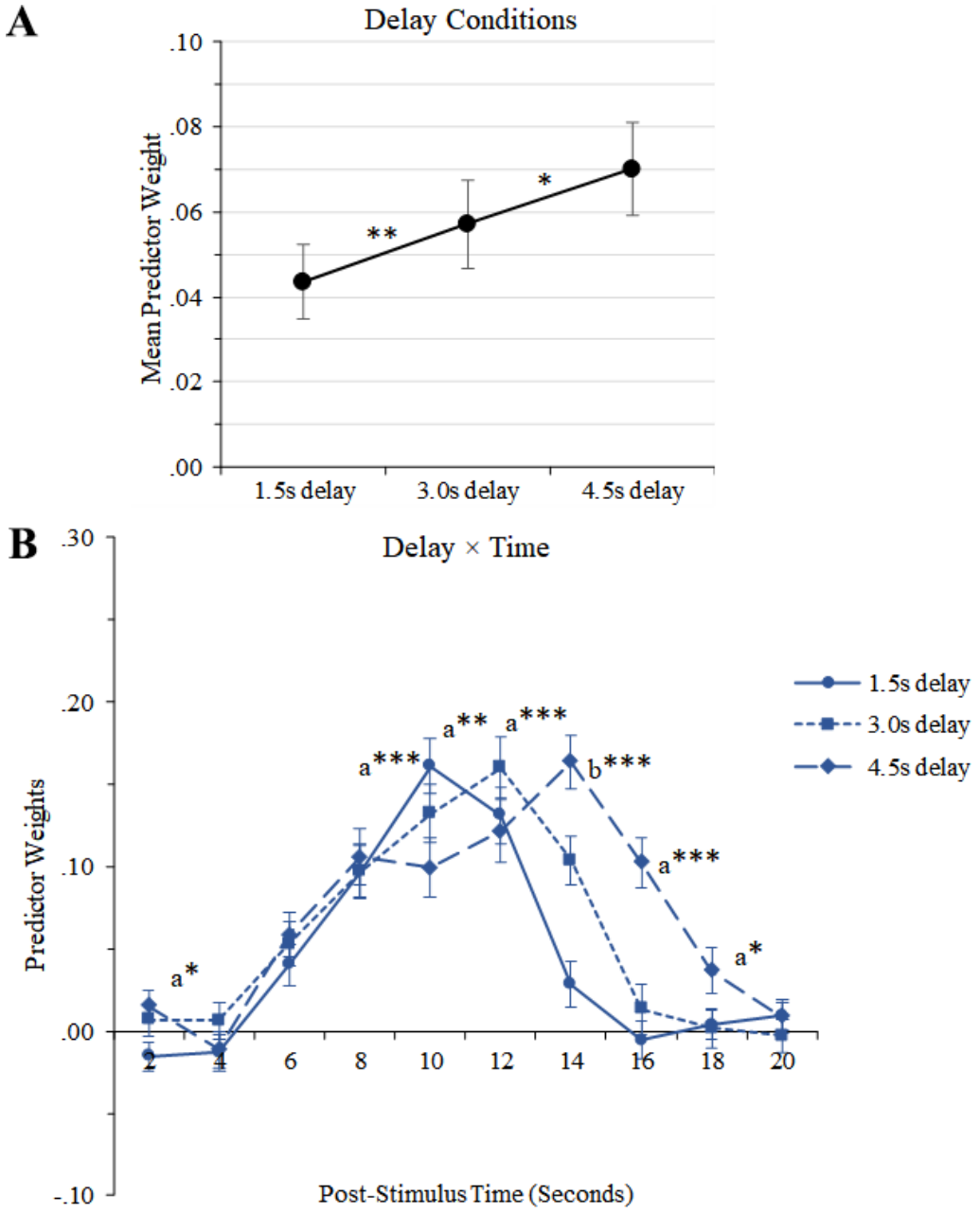

Figure 5.39. SCAP task from the 4-task fMRI-CPCA, motor response network (component 4): Graphs illustrating group differences. **A (top)**: mean predictor weights, averaged over load to illustrate delay × group interaction, explained by significant difference in quadratic contrast. **B (bottom)**: predictor weights averaged over all task conditions to illustrate group × time interaction (asterisk indicates significant group × time contrast between adjacent time bins after removing variance predicted by age). * = $p < .05$.

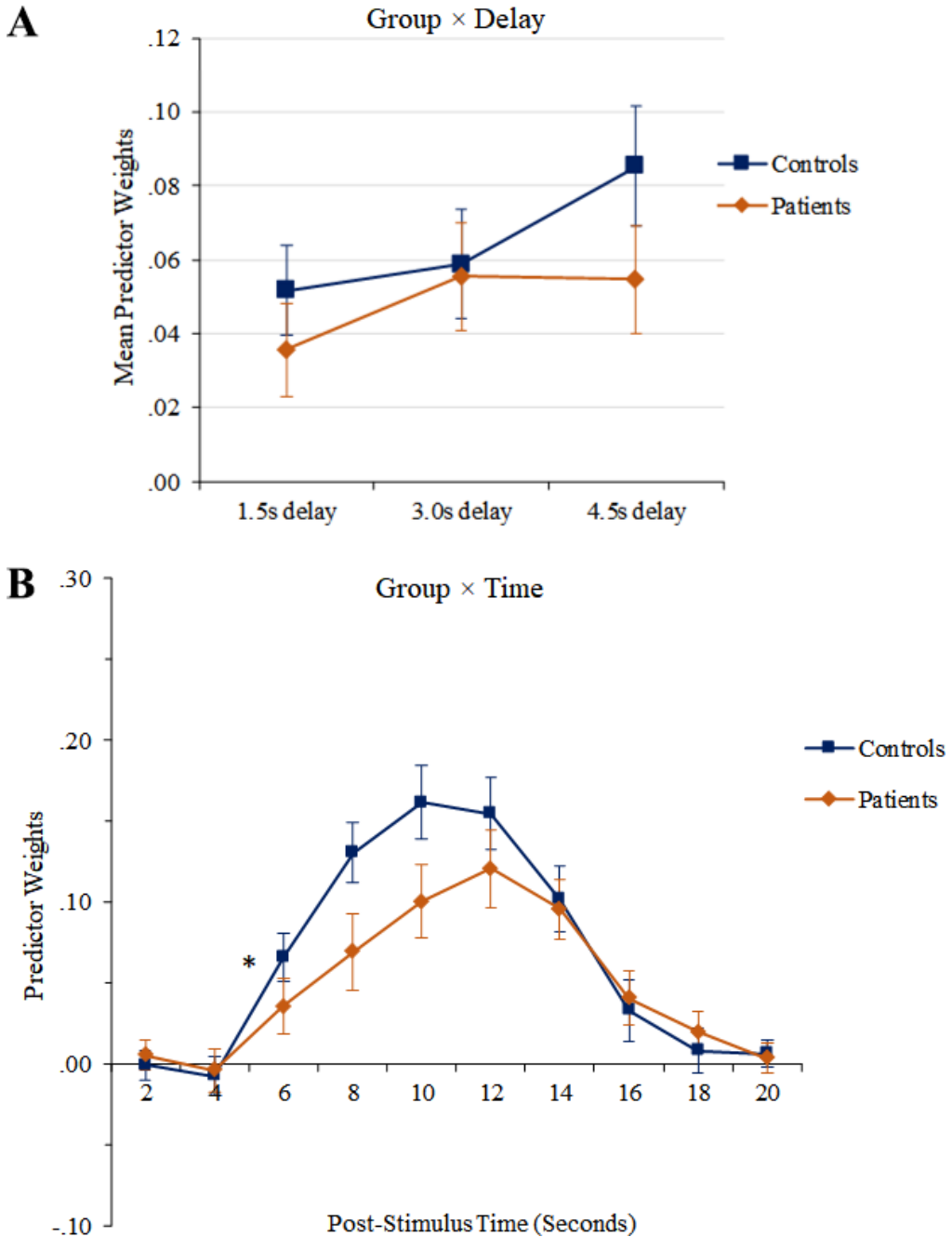

Figure 5.40. TSI task from the 4-task fMRI-CPCA, motor response network (component 4): Estimated HDR plots for all word-reading conditions. cn = task-switch from neutral colour-naming block; ci = task-switch from incongruent colour-naming block; WN = neutral word-reading stimulus; WI = incongruent word-reading stimulus.

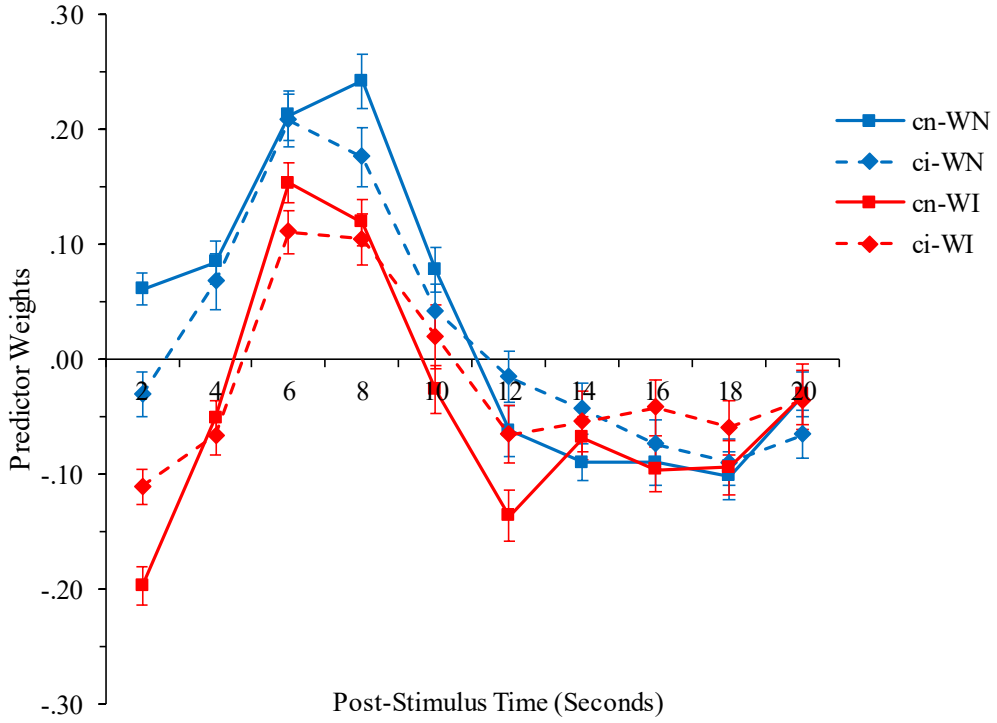

Figure 5.41. TSI task from the 4-task fMRI-CPCA, motor response network (component 4): Estimated HDR plots illustrating stimulus congruency and task-switch effects. **A (top)**: mean predicter weights illustrating congruency × time interaction. **B (bottom)**: mean predictor weights illustrating task-switch × time interaction. Asterisks indicate significant condition × time contrasts between adjacent time bins. WN = neutral word-reading stimulus; WI = incongruent word-reading stimulus; cn = task-switch from neutral colour-naming block; ci = task-switch from incongruent colour-naming block; * = $p < .05$; ** = $p < .01$; *** = $p < .001$.

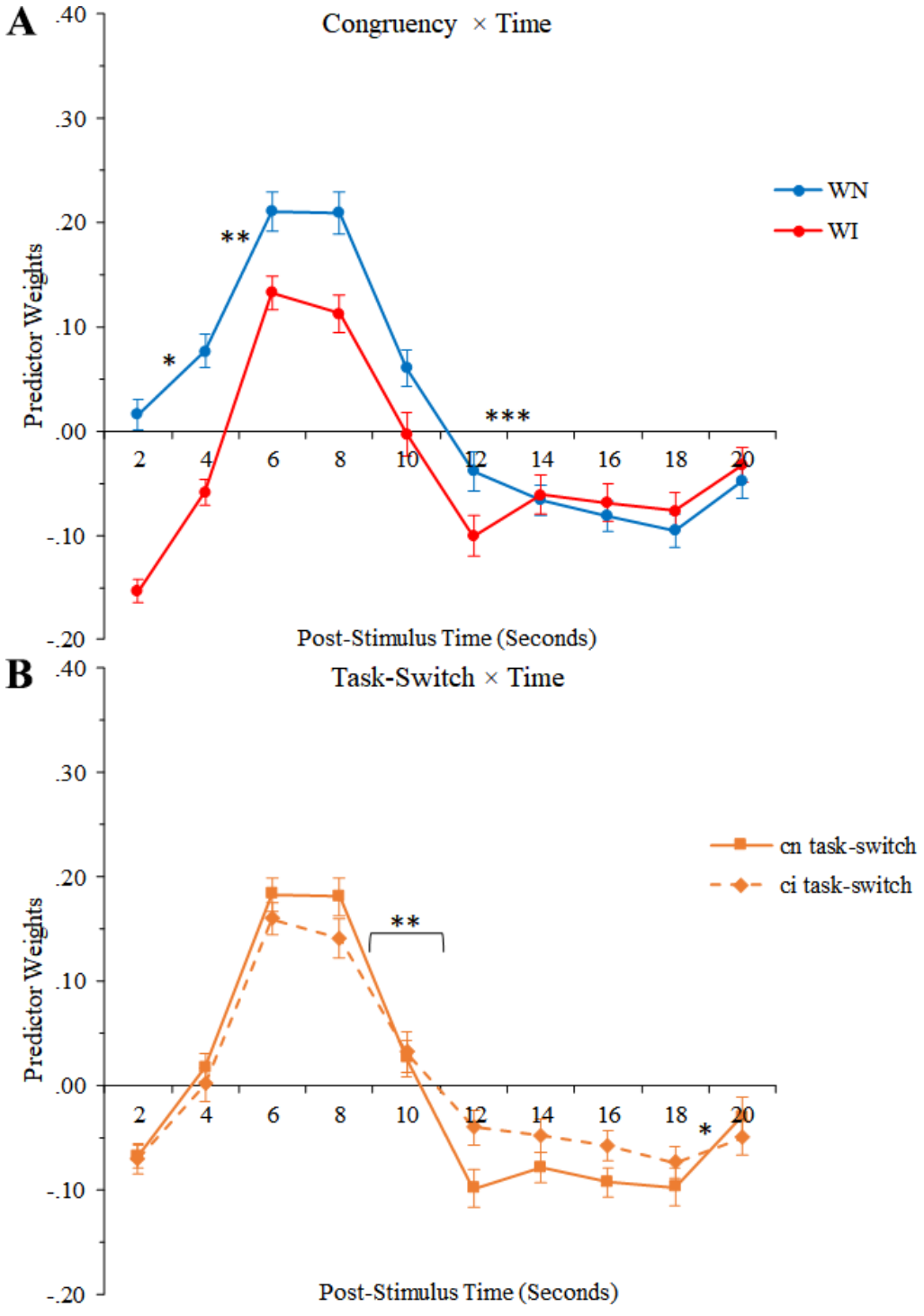

Figure 5.42. TSI task from the 4-task fMRI-CPCA, motor response network (component 4): Estimated HDRs illustrating group × time interaction. Asterisks indicate significant group × time contrast between adjacent time bins after removing variance predictable by age. ** = $p < .01$.

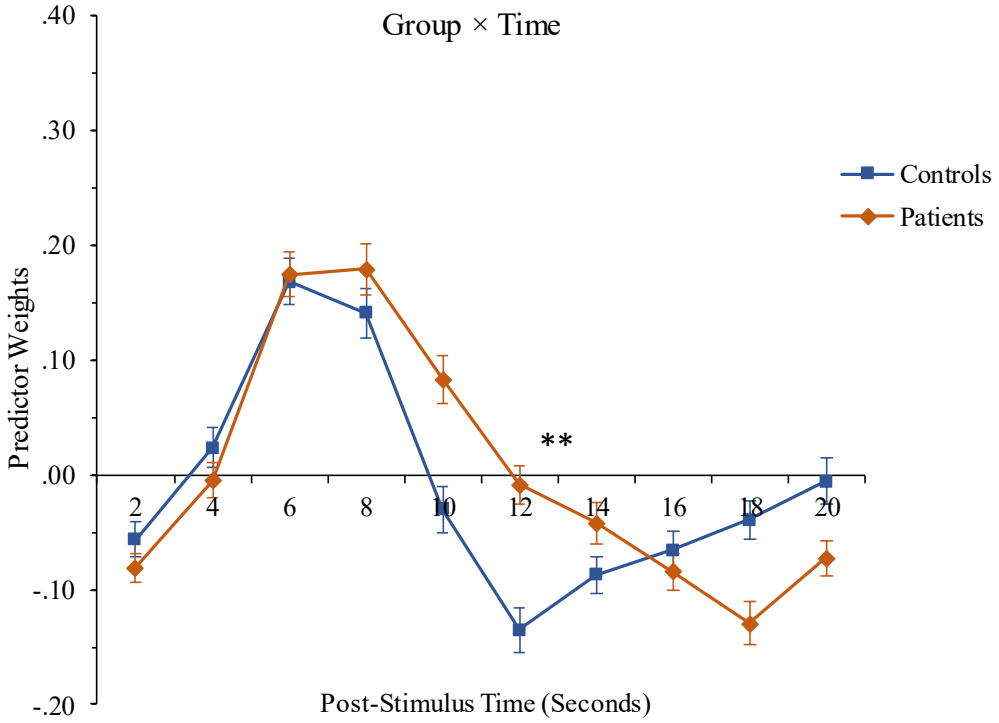

Figure 5.43. TGT task from the 4-task fMRI-CPCA, motor response network (component 4): Estimated HDR plots for both task conditions.

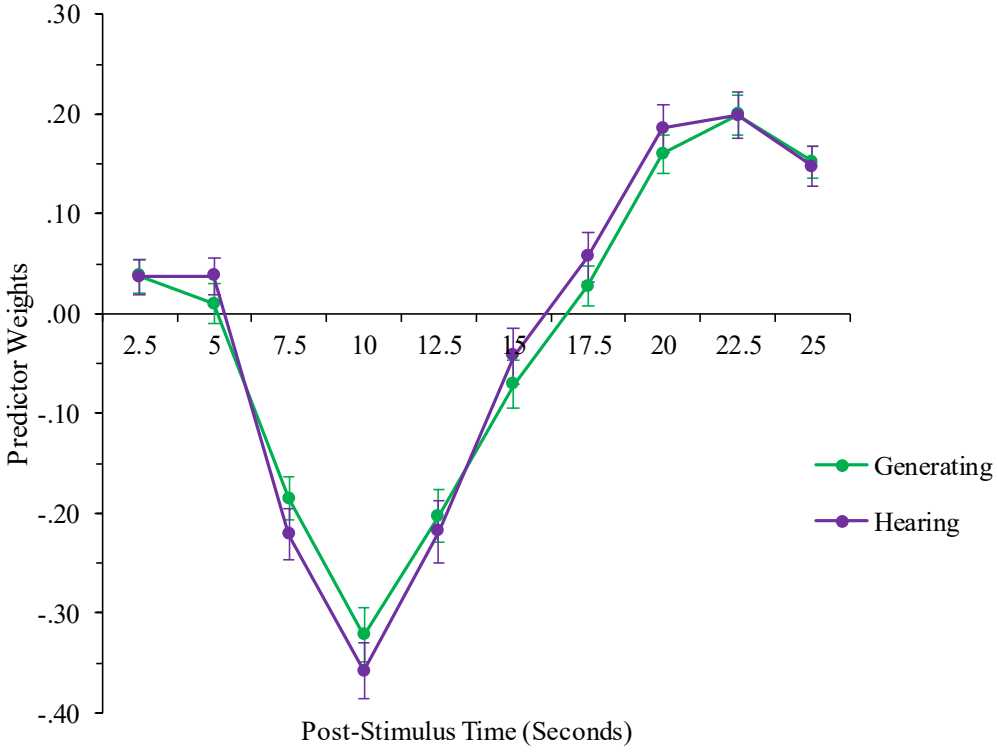

Figure 5.44. 4-task fMRI-CPCA, visual attention network (component 5): Dominant 10% of component loadings (red/yellow = positive loadings, min = 0.13, max = 0.47; no negative loadings above threshold). Images are displayed in neurological orientation (left is left) with MNI coordinates.

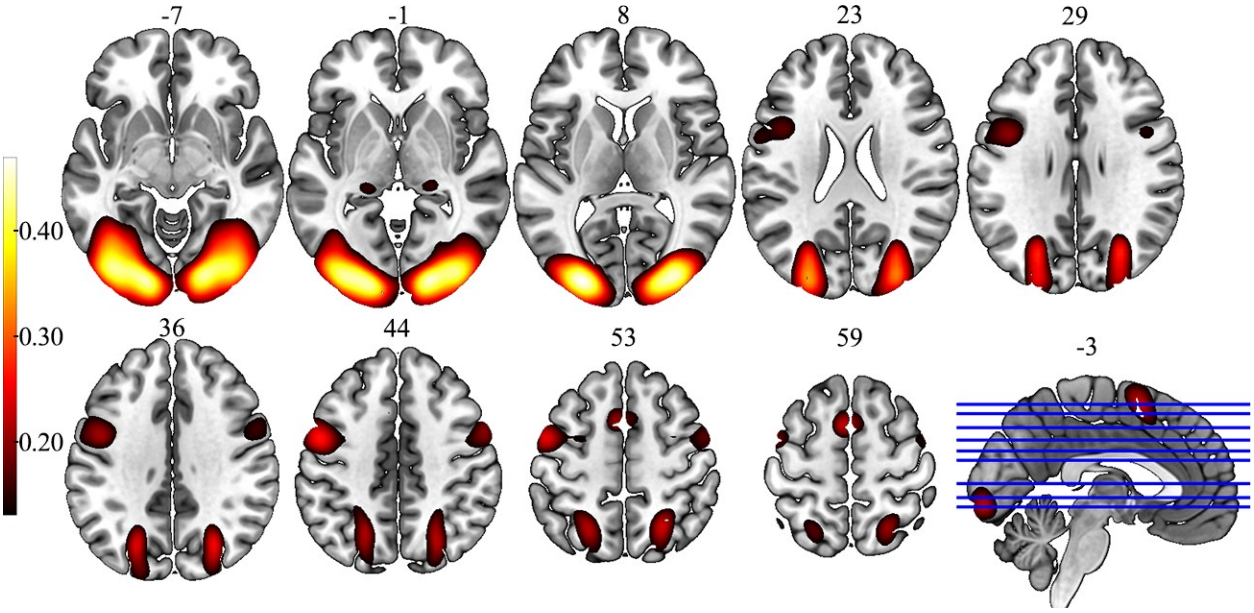

Figure 5.45. WM task from the 4-task fMRI-CPCA, visual attention network (component 5): Estimated HDR plots for all task conditions. 4L = 4 letters; 6L = 6 letters.

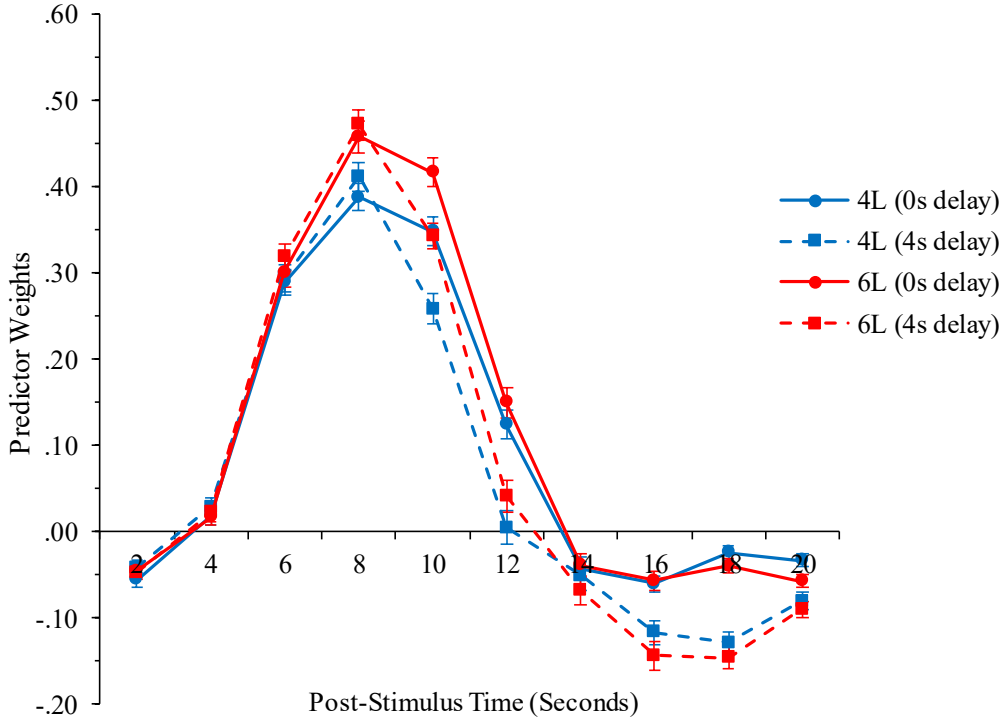

Figure 5.46. WM task from the 4-task fMRI-CPCA, visual attention network (component 5): Estimated HDRs illustrating delay × time interaction. Asterisks indicate significant delay × time contrasts between adjacent time bins. ** = $p < .01$; *** = $p < .001$.

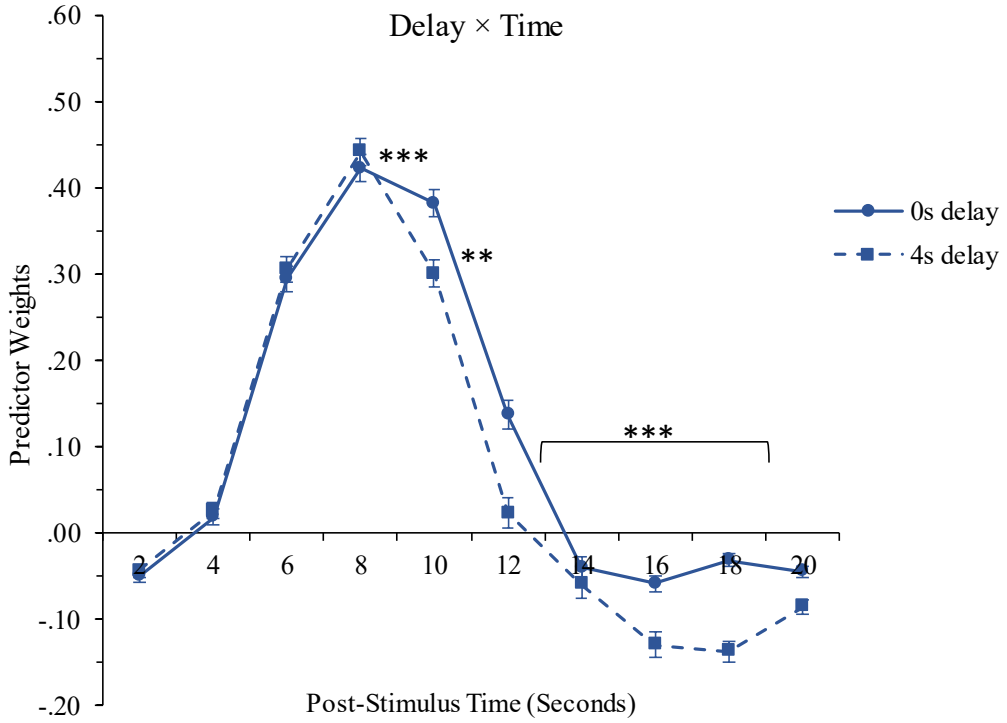

Figure 5.47. WM task from the 4-task fMRI-CPCA, visual attention network (component 5): Plots illustrating the load × time × group interaction. **A (top):** predictor weights plotted over post-stimulus time to illustrate load × time × group interaction; asterisk indicates significant load × time × group contrast between adjacent time bins after removing variance predictable from age. **B (bottom):** residuals obtained by regressing component 5 predictor weights onto age, plotted over post-stimulus time to illustrate load × time × group interaction (which was non-significant prior to removing variance predictable from age); asterisk indicates significant load × time × group contrast between adjacent time bins. * = $p < .05$.

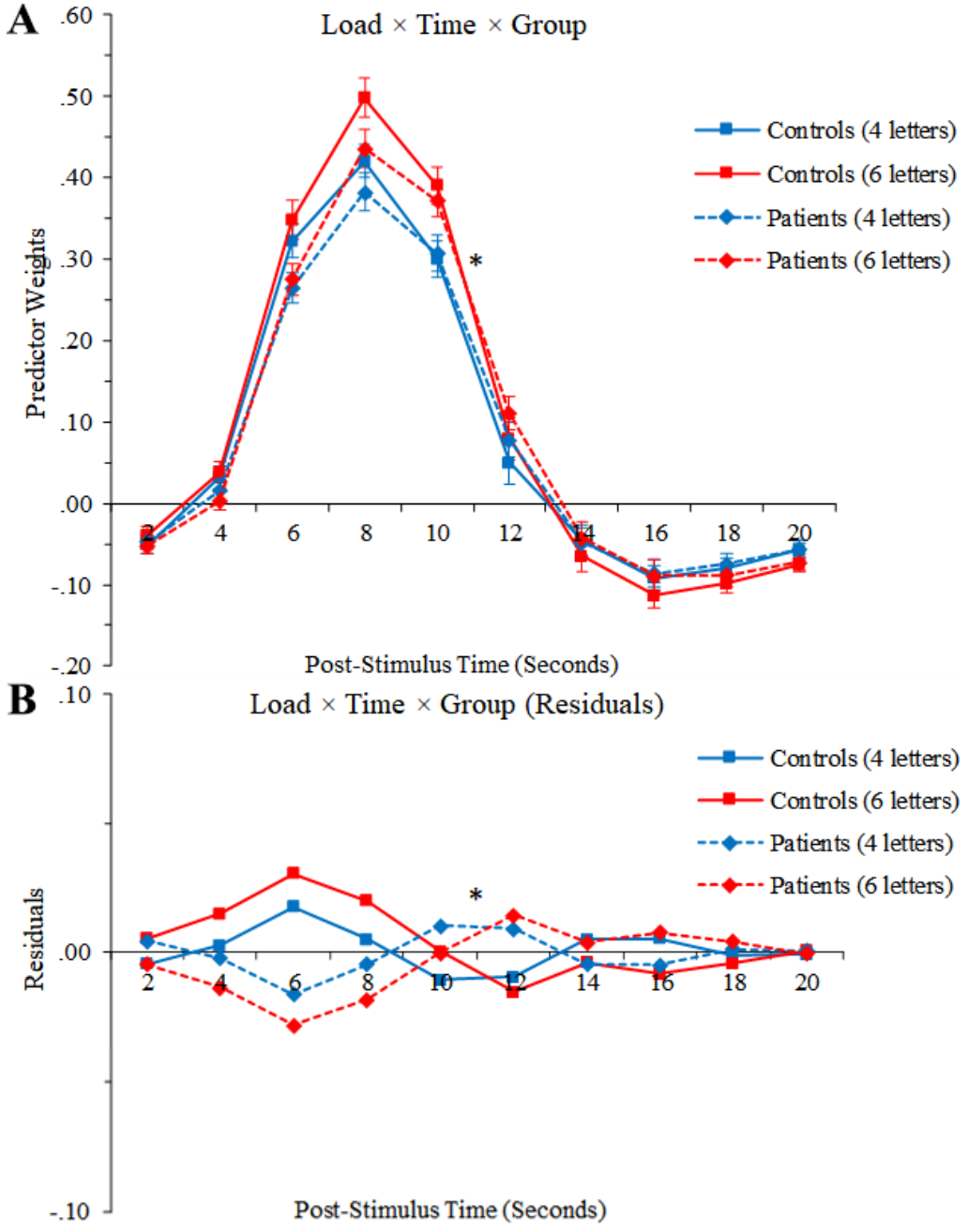

Figure 5.48. SCAP task from the 4-task fMRI-CPCA, visual attention network (component 5): Estimated HDR plots for all task conditions (each load level displayed on a separate graph).

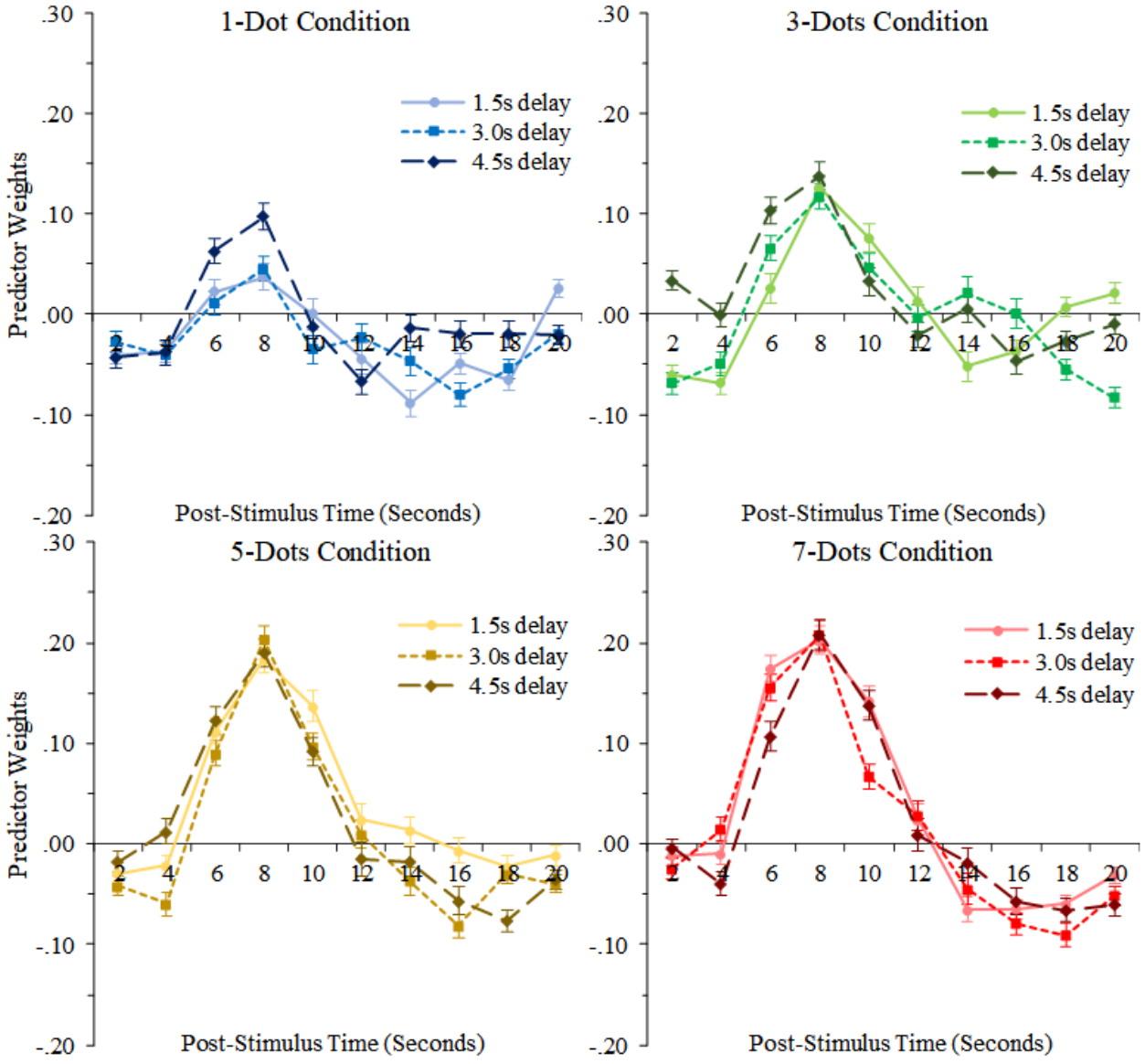

Figure 5.49. SCAP task from the 4-task fMRI-CPCA, visual attention network (component 5): Graphs illustrating effects of cognitive load and delay length. **A (top left):** mean predictor weights illustrating main effect of load (asterisks indicate significant paired t-tests between adjacent load conditions). **B (top right):** mean predictor weights illustrating main effect of delay (asterisks indicate significant paired t-tests between adjacent delay conditions). **C (bottom):** predictor weights averaged over load to illustrate delay × time interaction (asterisks indicate significant delay × time contrasts between adjacent time bins; contrast with the greatest effect size is flagged). a = linear effect of delay; b = quadratic effect of delay; ** = $p < .01$; *** = $p < .001$.

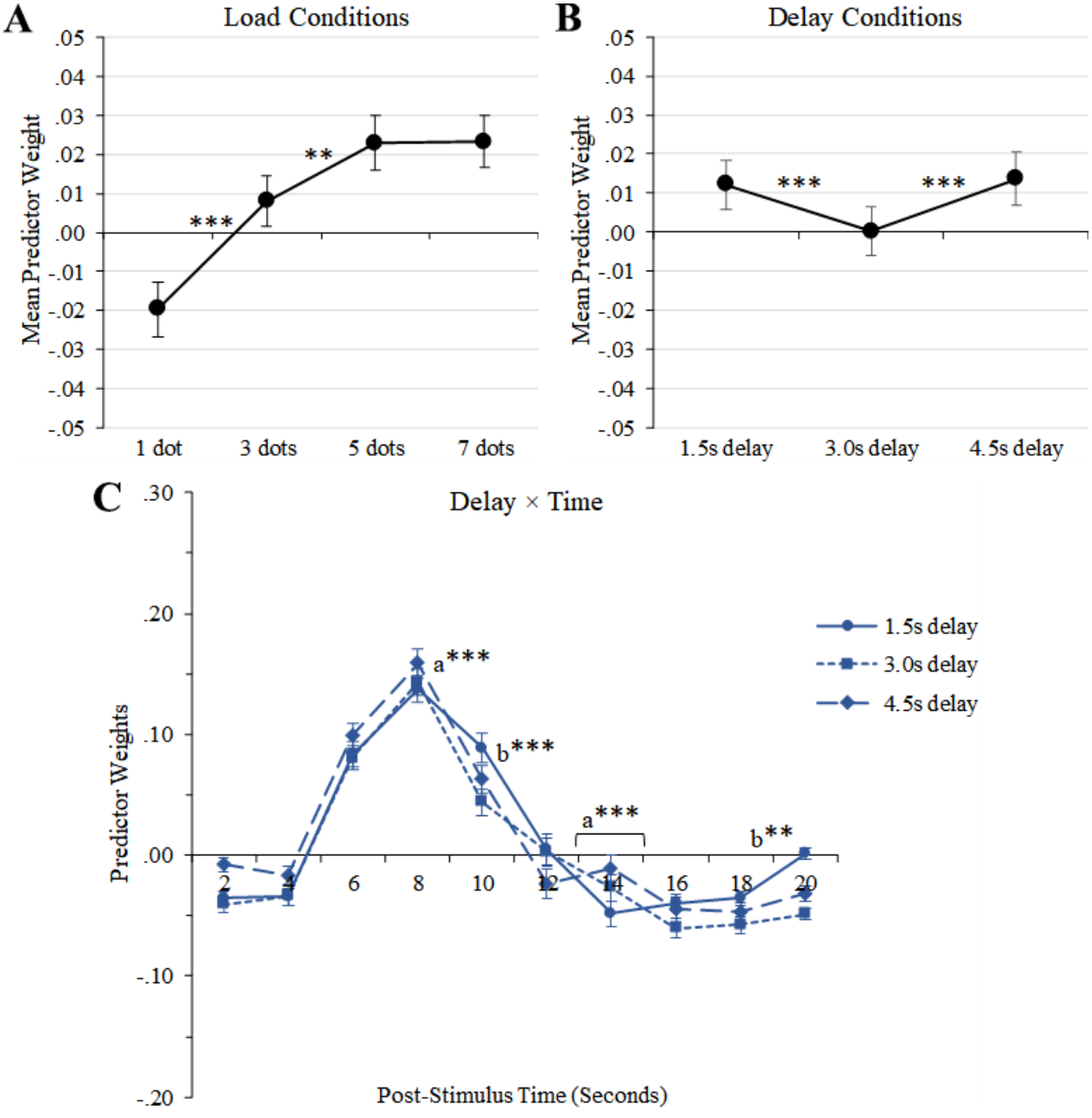

Figure 5.50. SCAP task from the 4-task fMRI-CPCA, visual attention network (component 5): Estimated HDRs illustrating group differences. **A (top):** predictor weights averaged over all task conditions to illustrate group × time interaction (asterisks indicate significant group × time contrasts between adjacent time bins after removing variance predictable from age and gender). **B (bottom):** predictor weights averaged over delay to illustrate load × time × group interaction (asterisks indicate significant contrasts between adjacent time bins underlying the load × time × group interaction after removing variance predicted by age and gender). a = significant group difference in the linear effect of load; b = significant group difference in the quadratic effect of load; c = significant group difference in the cubic effect of load; * = $p < .05$; ** = $p < .01$.

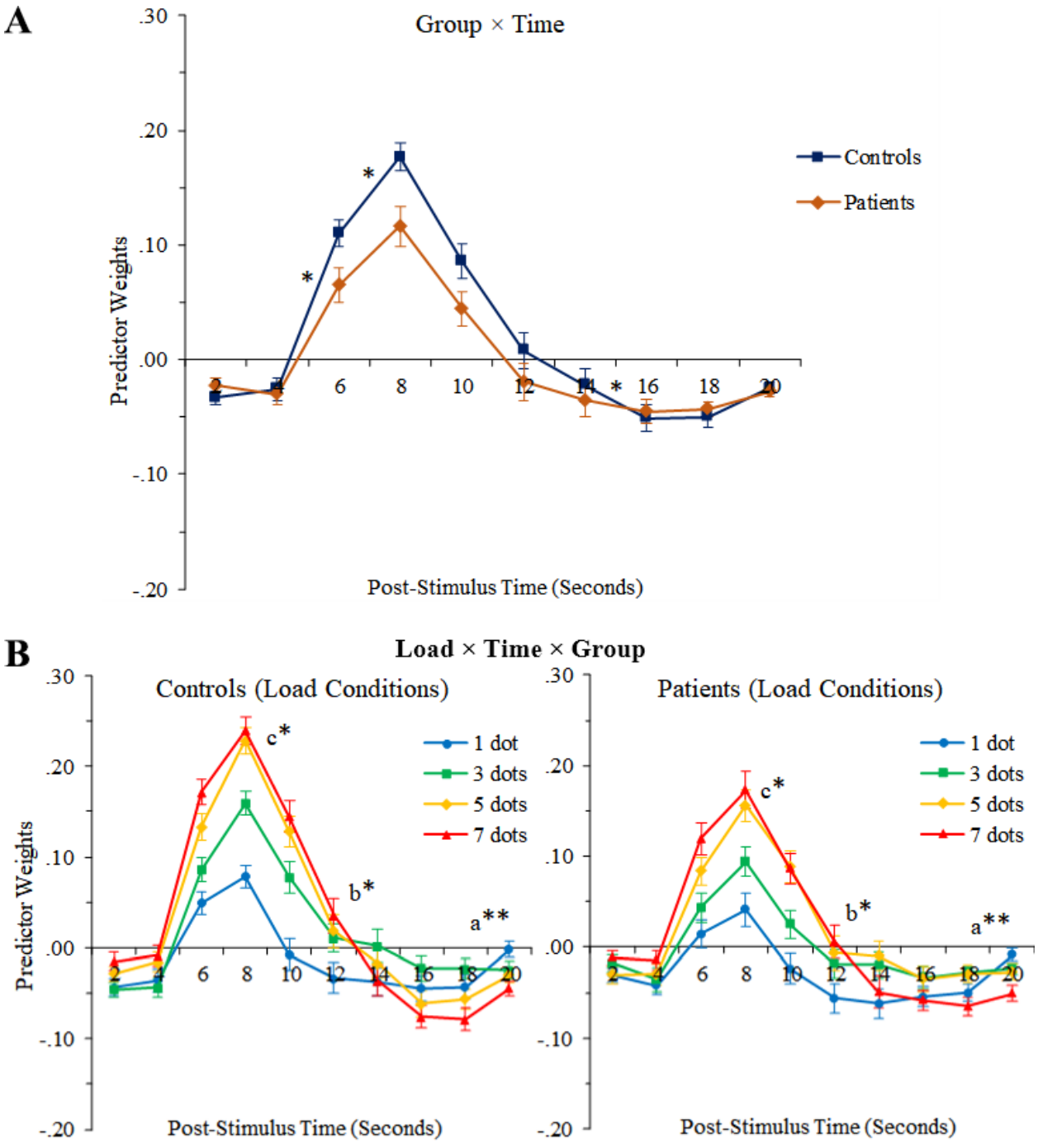

Figure 5.51. TSI task from the 4-task fMRI-CPCA, visual attention network (component 5): Estimated HDR plots for all word-reading conditions. cn = task-switch from neutral colour-naming block; ci = task-switch from incongruent colour-naming block; WN = neutral word-reading stimulus; WI = incongruent word-reading stimulus.

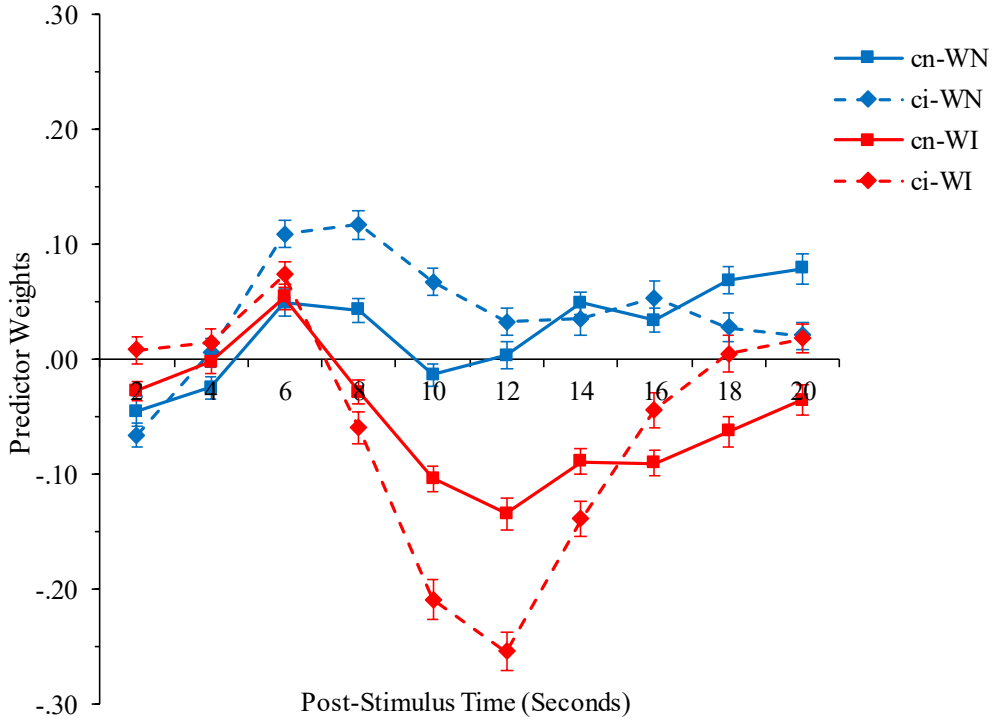

Figure 5.52. TSI task from the 4-task fMRI-CPCA, visual attention network (component 5): Estimated HDRs illustrating stimulus congruency and task-switch effects. **A (top)**: mean predictor weights illustrating congruency × time interaction. **B (bottom)**: mean predictor weights illustrating task-switch × time interaction. Asterisks indicate significant condition × time contrasts between adjacent time bins. WN = neutral word-reading stimulus; WI = incongruent word-reading stimulus; cn = task-switch from neutral colour-naming block; ci = task-switch from incongruent colour-naming block; * = $p \leq .05$; ** = $p < .01$; *** = $p < .001$.

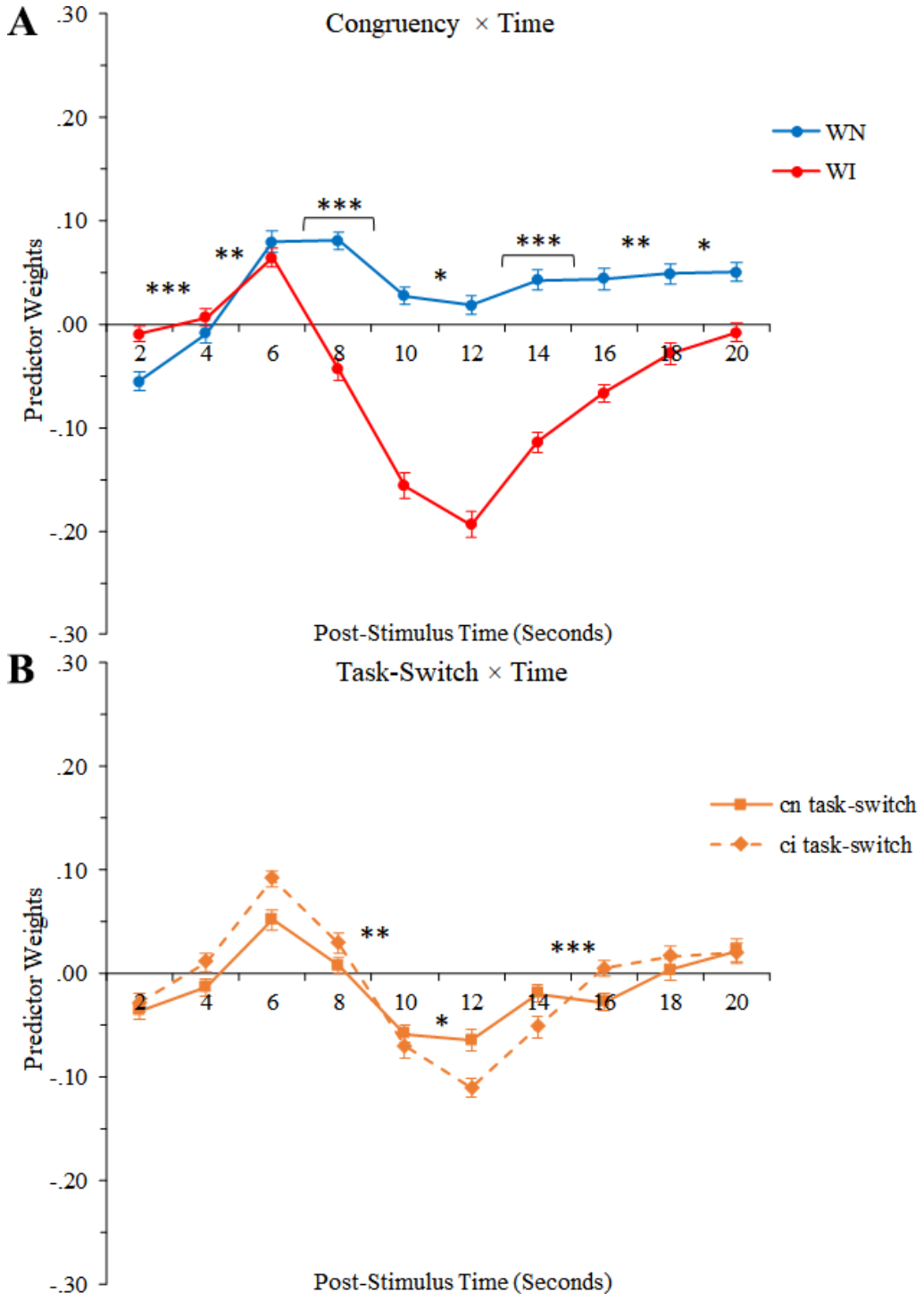

Figure 5.53. TGT task from the 4-task fMRI-CPCA, visual attention network (component 5): Estimated HDR plots for both task conditions. Asterisks indicate significant generating vs. hearing × time contrasts between adjacent time bins. ** = $p < .01$; *** = $p < .001$.

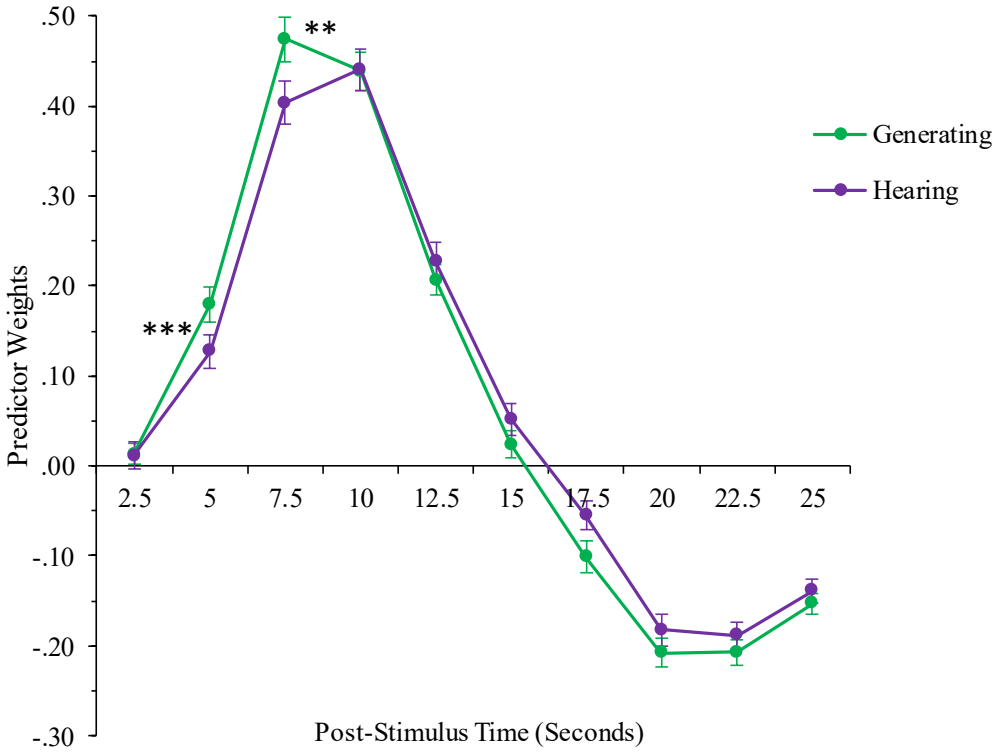

Figure 5.54. TGT task from the 4-task fMRI-CPCA, visual attention network (component 5): Estimated HDRs illustrating group × time interaction. Asterisks indicate significant group × time contrasts between adjacent time bins after removing variance predictable from age. * = $p < .05$; ** = $p < .01$.

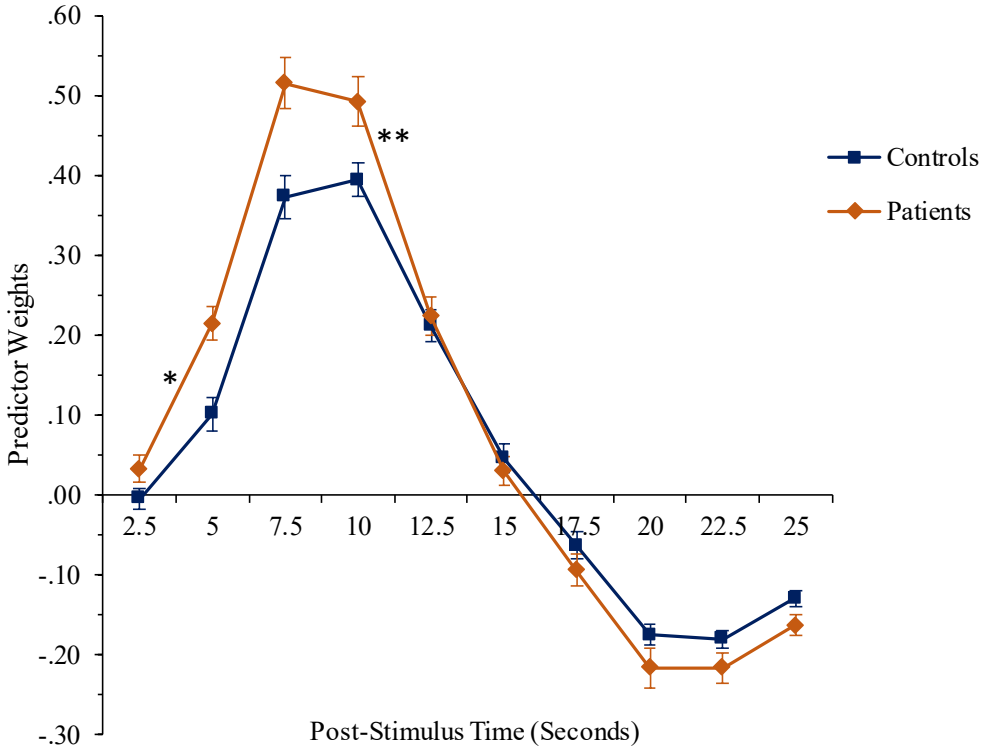

Figure 5.55. 4-task fMRI-CPCA, occipital network (component 7): Dominant 10% of component loadings (blue/green = negative loadings, min = -0.31, max = -0.12; no positive loadings above threshold). Images are displayed in neurological orientation (left is left) with MNI coordinates.

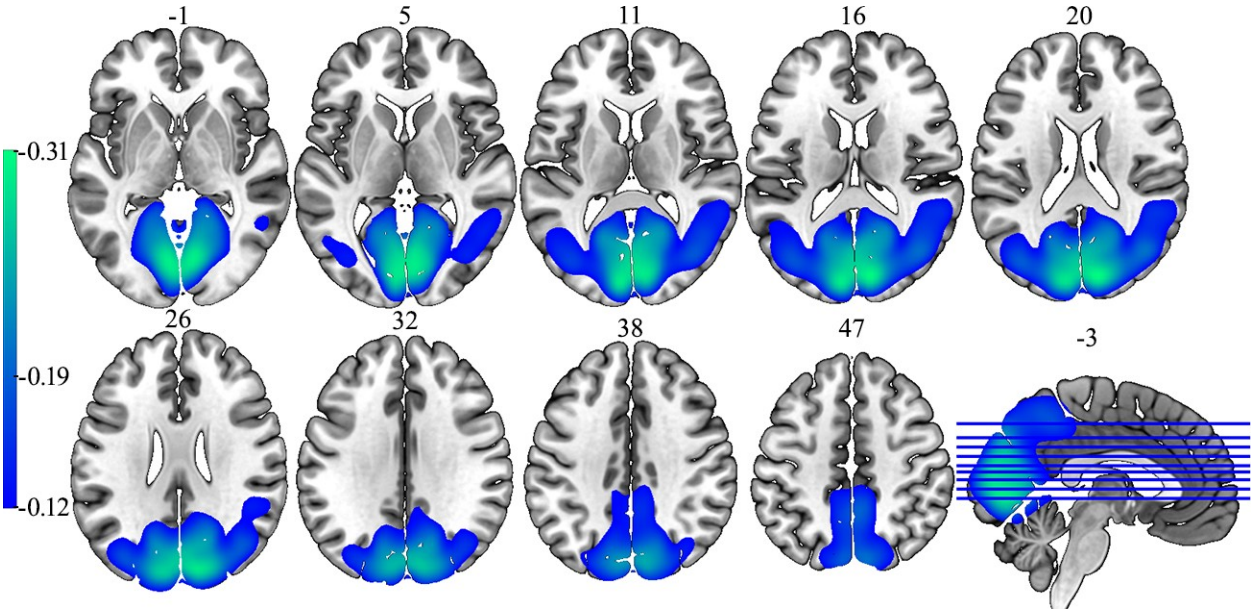

Figure 5.56. WM task from the 4-task fMRI-CPCA, occipital network (component 7): Estimated HDR plots for all task conditions. Y axis is reversed (negative up, positive down) to facilitate interpretation (i.e., values above X axis reflect activation, and values below X axis reflect deactivation). 4L = 4 letters; 6L = 6 letters.

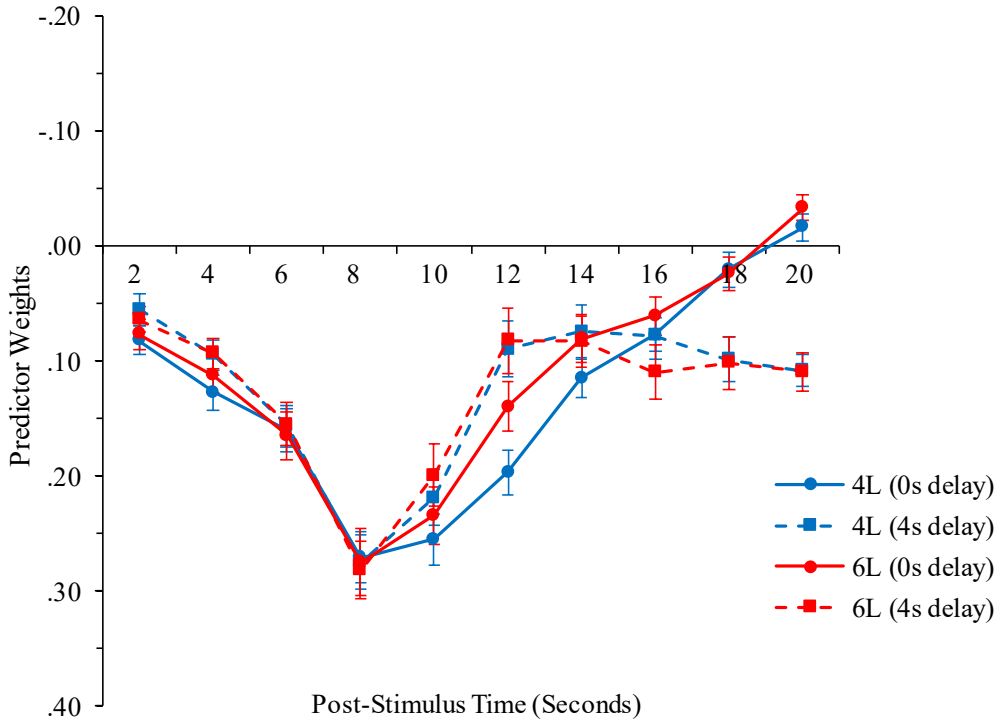

Figure 5.57. WM task from the 4-task fMRI-CPCA, occipital network (component 7): Estimated HDRs illustrating delay × time interaction (asterisks indicate significant delay × time contrasts between adjacent time bins). Y axis is reversed to facilitate interpretation (i.e., values above X axis reflect activation, and values below X axis reflect deactivation). * = $p < .05$; ** = $p < .01$.

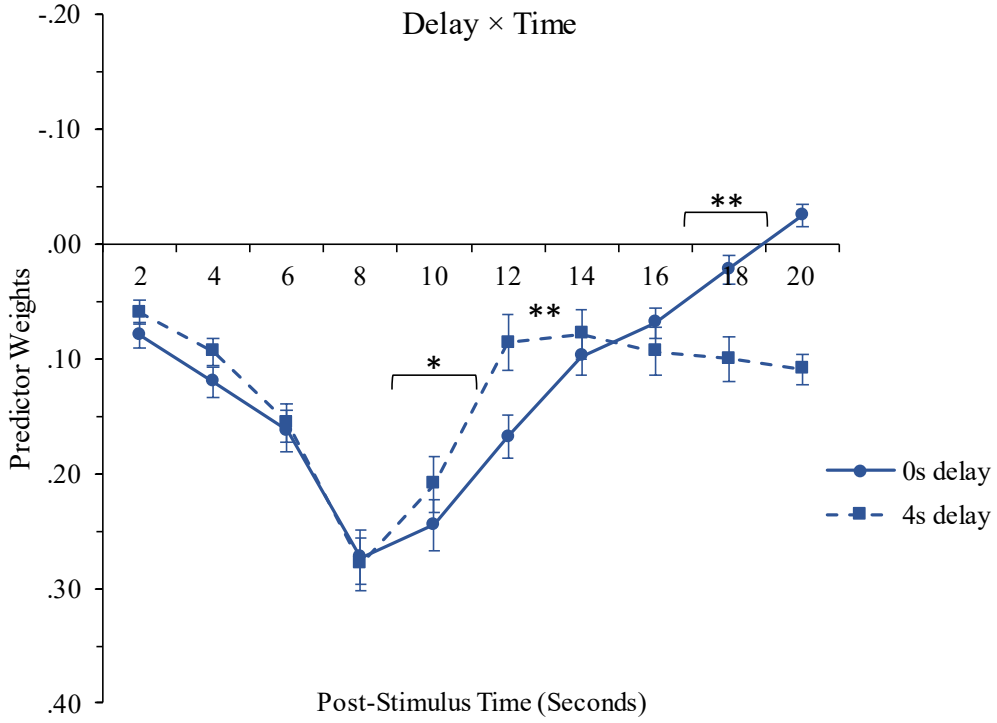

Figure 5.58. SCAP task from the 4-task fMRI-CPCA, occipital network (component 7): Estimated HDR plots for all task conditions (load levels displayed on separate graphs). Y axis is reversed (negative up, positive down) to facilitate interpretation (values above X axis reflect activation, and values below X axis reflect deactivation).

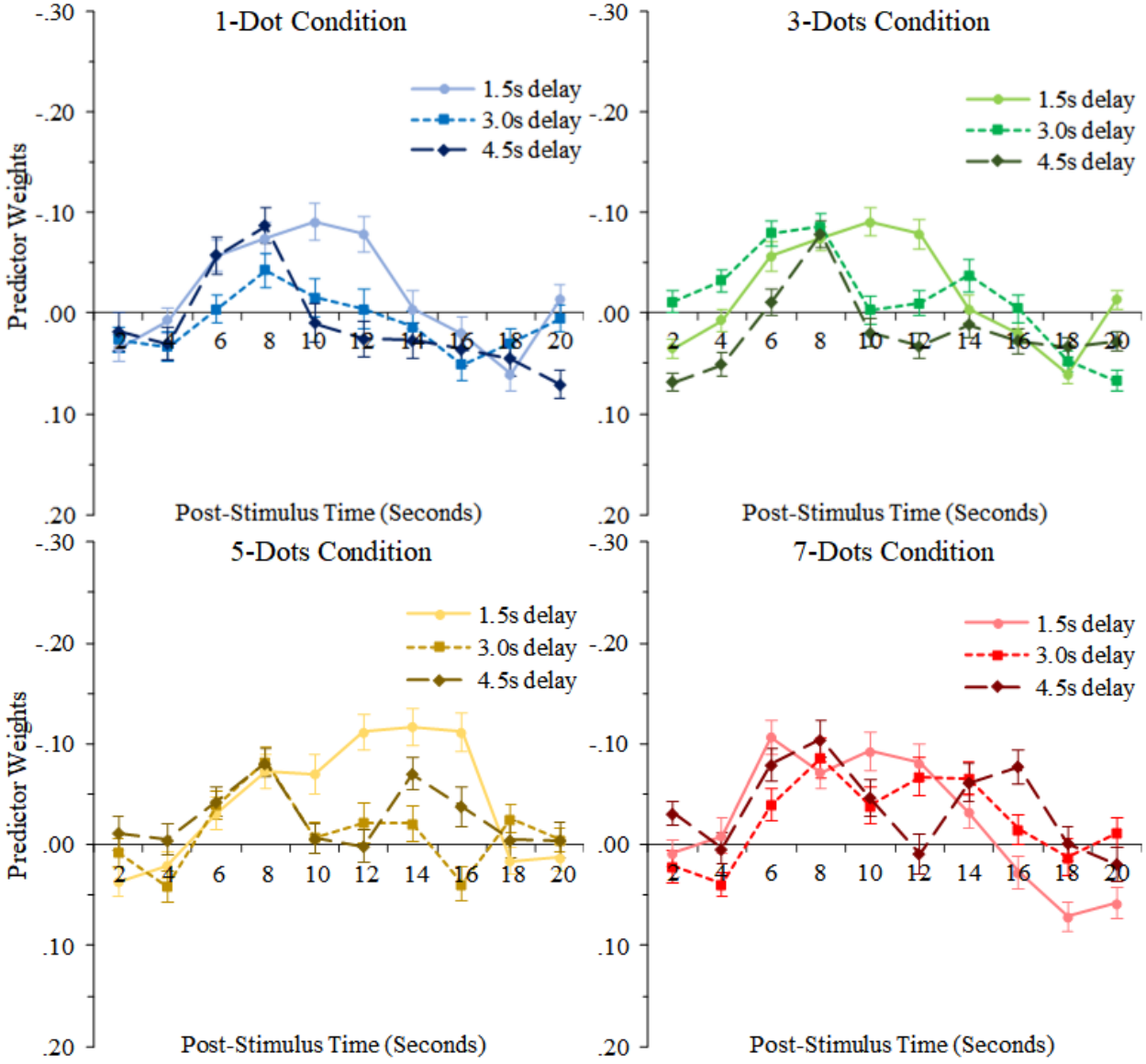

Figure 5.59. SCAP task from the 4-task fMRI-CPCA, occipital network (component 7): Graphs illustrating effects of cognitive load and delay length. Y axes are reversed (negative up, positive down) to facilitate interpretation (i.e., values below X axis reflect deactivation and values above X axis reflect activation). **A (top left)**: mean predictor weights illustrating main effect of load (asterisks indicate significant paired t-tests between adjacent load conditions). **B (top right)**: mean predictor weights illustrating main effect of delay (asterisks indicate significant paired t-tests between adjacent delay conditions). **C (bottom)**: predictor weights averaged over load to illustrate delay × time interaction (asterisks indicate significant delay × time contrasts between adjacent time bins; contrast with the greatest effect size is flagged). a = linear effect of delay; b = quadratic effect of delay; * = $p < .05$; ** = $p < .01$; *** = $p < .001$.

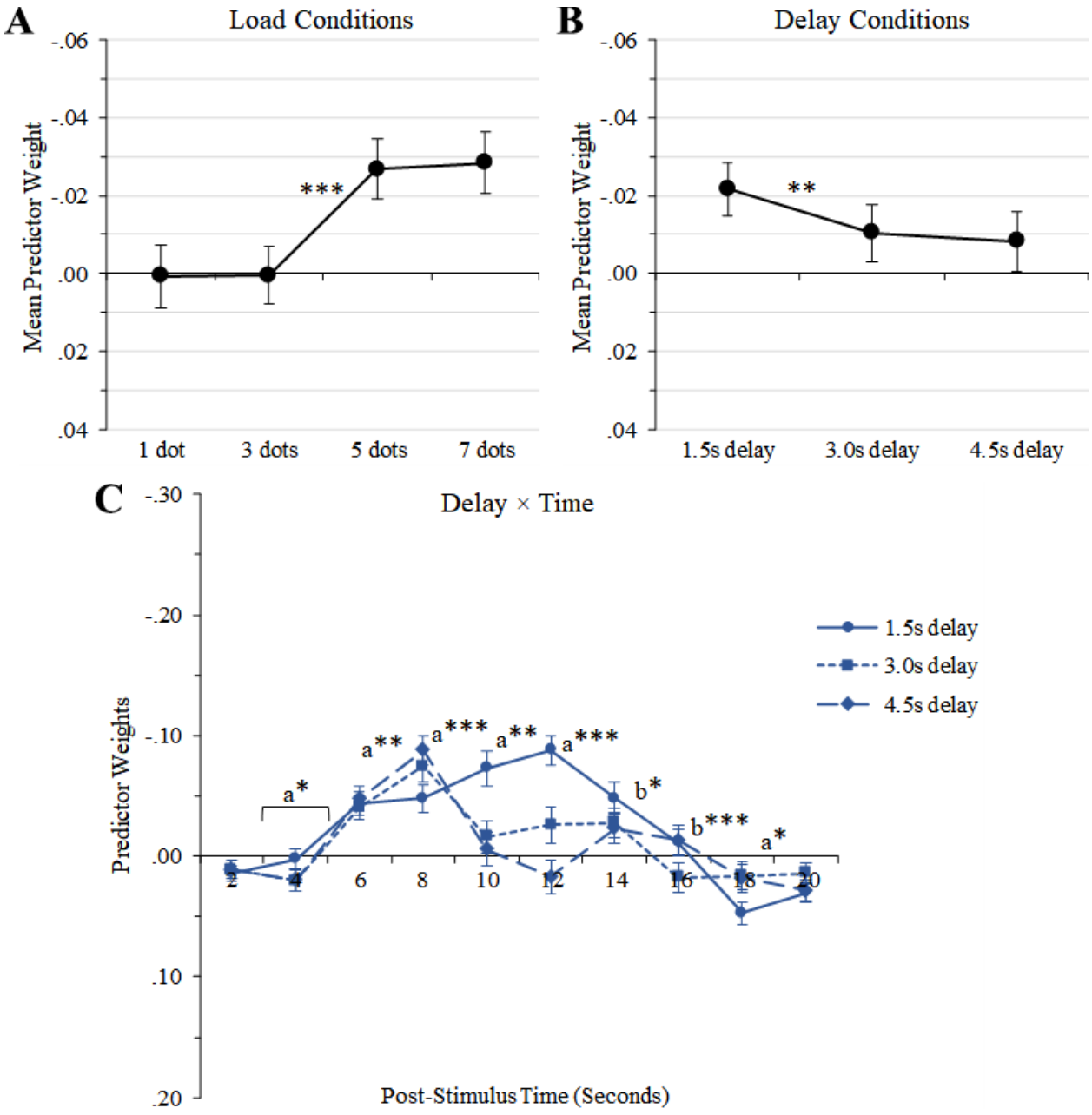

Figure 5.60. TSI task from the 4-task fMRI-CPCA, occipital network (component 7): Estimated HDRs for all word-reading conditions. Y axis is reversed (negative up, positive down) to facilitate interpretation (values above X axis reflect activation, and values below X axis reflect deactivation). cn = task-switch from neutral colour-naming block; ci = task-switch from incongruent colour-naming block; WN = neutral word-reading stimulus; WI = incongruent word-reading stimulus.

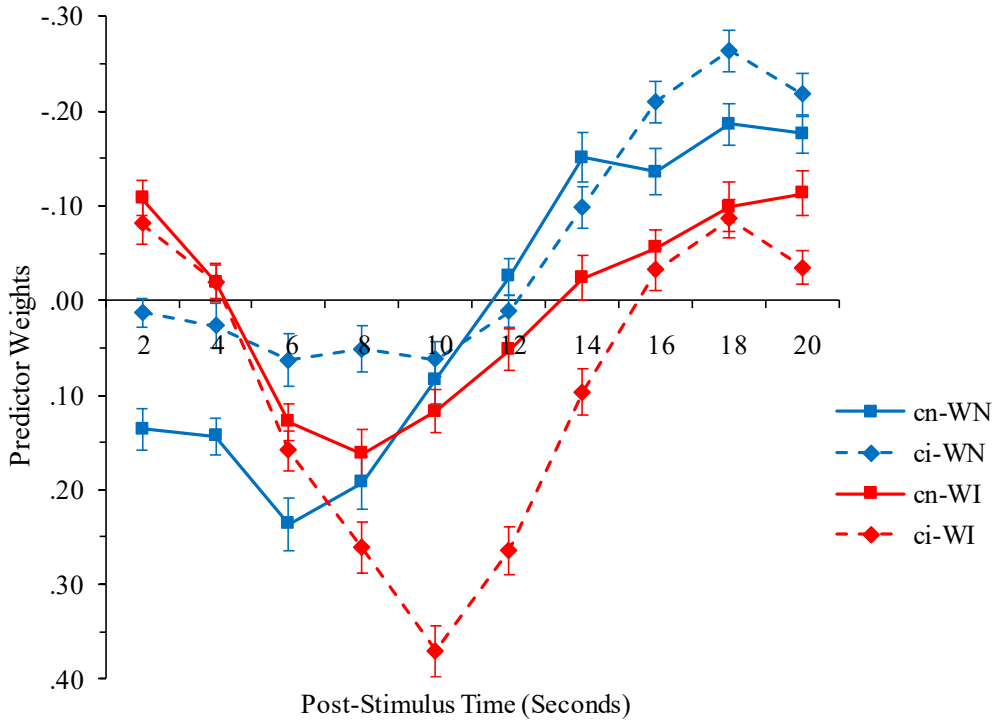

Figure 5.61. TSI task from the 4-task fMRI-CPCA, occipital network (component 7): Estimated HDRs illustrating effects of stimulus congruency and task-switch condition. Y axes are reversed (negative up, positive down) to facilitate interpretation (i.e., values above X axis reflect activation, and values below X axis reflect deactivation). **A (top left):** predictor weights averaged over task-switch to illustrate congruency × time interaction (asterisks indicate significant congruency × time contrasts between adjacent time bins). **B (top right):** predictor weights averaged over congruency to illustrate task-switch × time interaction (asterisks indicate significant task-switch × time contrasts between adjacent time bins). **C (bottom):** mean predictor weights illustrating significant congruency × task-switch interaction. WN = neutral word-reading stimulus; WI = incongruent word-reading stimulus; cn = task-switch from neutral colour-naming block; ci = task-switch from incongruent colour-naming block; * = $p < .05$; ** = $p < .01$; *** = $p < .001$.

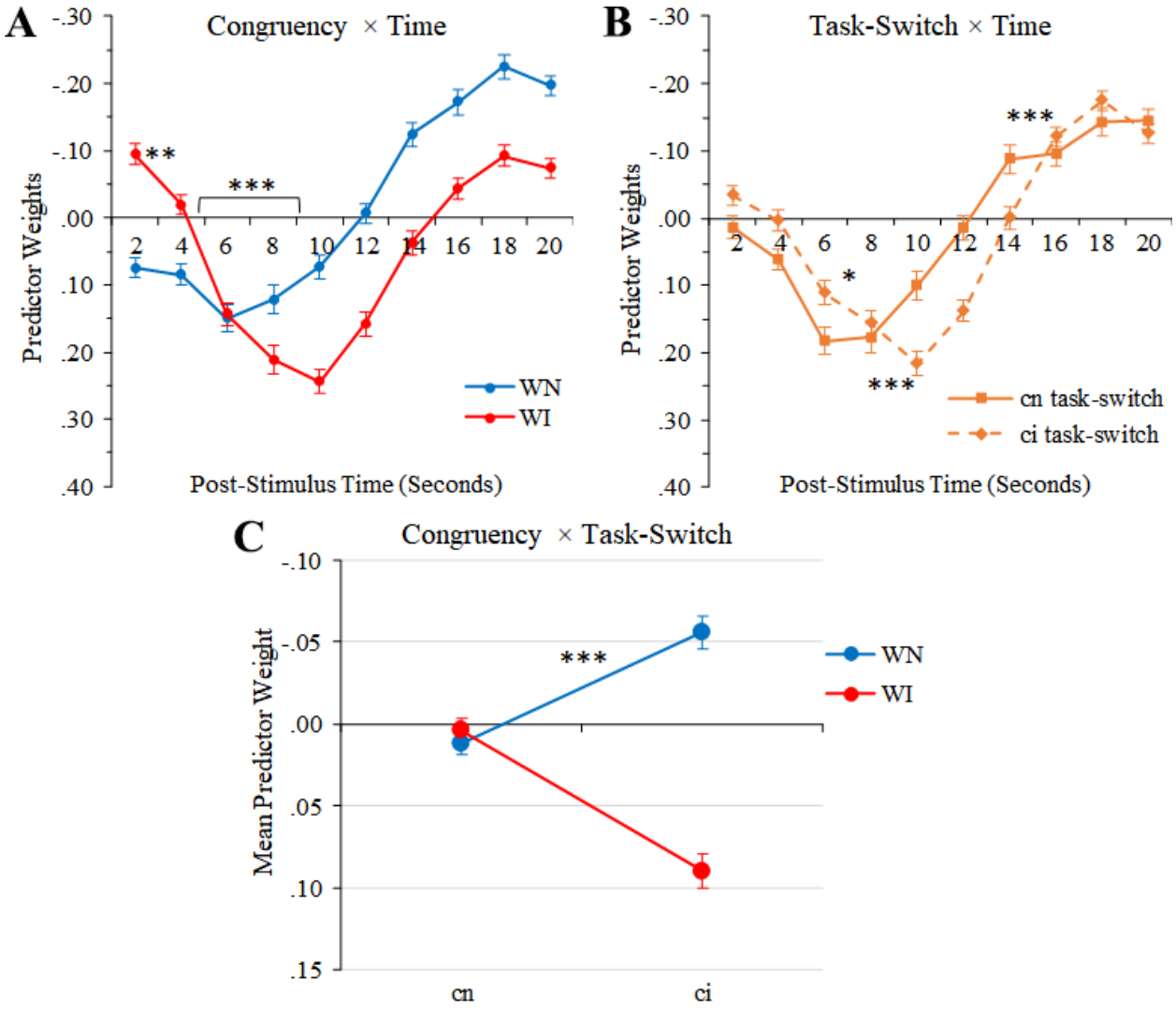

Figure 5.62. TGT task from the 4-task fMRI-CPCA, occipital network (component 7): Estimated HDR plots for both task conditions.

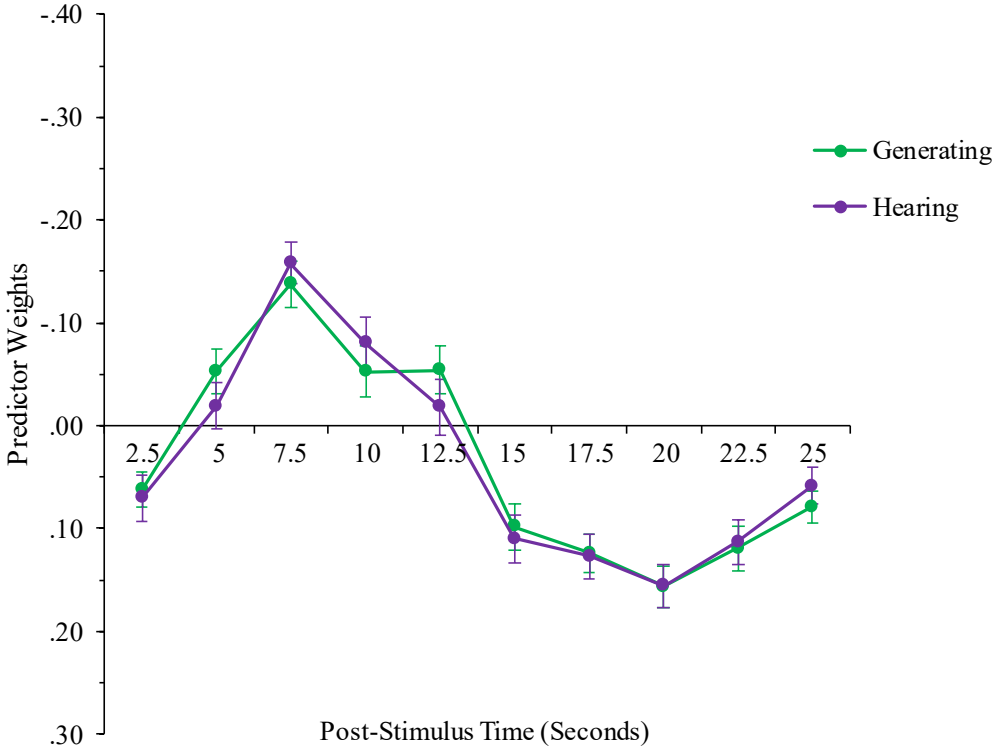

Figure 5.63. TGT task from the 4-task fMRI-CPCA, occipital network (component 7): Graphs illustrating group differences. **A (top)**: mean predictor weights for each condition, illustrating significant condition × group interaction. **B (bottom)**: predictor weights averaged over task condition to illustrate group × time interaction (asterisks indicate significant group × time contrasts between adjacent time bins after removing variance predicted by age). * = $p < .05$; ** = $p < .01$.

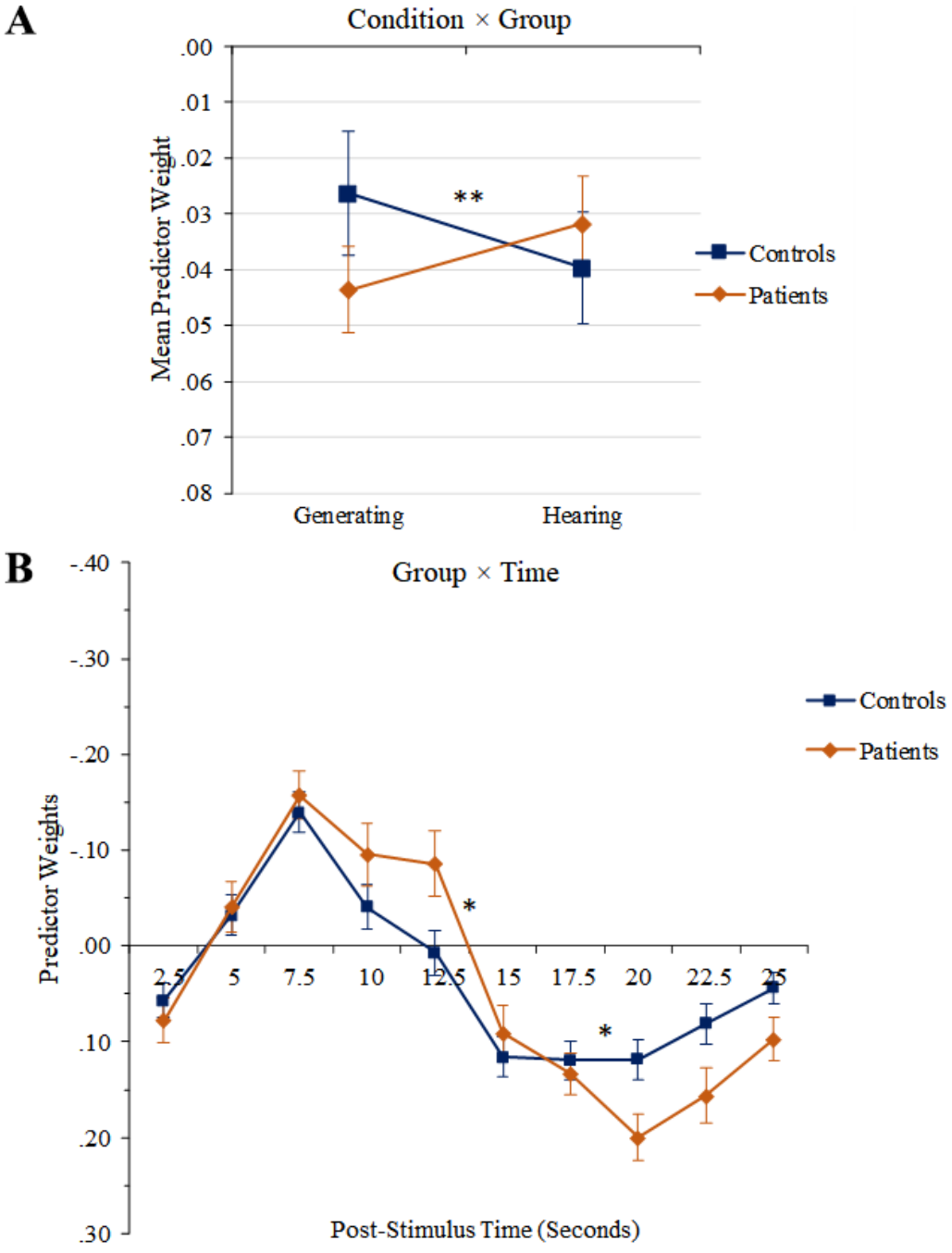

Chapter 6: Conclusion

6.1. Summary

Neurocognitive impairment is a core aspect of schizophrenia which has a substantial impact on functional outcome (Lepage et al., 2014). It has been widely thought that dysfunction in the DLPFC is a fundamental basis of WM deficits; however, with the expansion of functional connectivity research, it has become apparent that WM deficits likely arise from dysconnectivity in more distributed networks of brain regions. Moreover, dysfunction in schizophrenia is not exclusive to networks comprising the DLPFC. This is consistent with the notion of schizophrenia being a disorder of brain connectivity.

In task-state fMRI research, the evaluation of network-specific HDR shapes over the course of a task trial aids with interpreting the task-related function of each network. However, the coarse temporal resolution of the BOLD signal presents significant challenges in delineating task-related networks and their evoked HDRs, such that a given network may actually reflect a composite of temporally correlated cognitive processes. In the present work, a multi-experiment approach was used which helped address this problem in the context of delineating networks underlying WM. In addition to finer separation of task-related networks, the multi-experiment results extended previous analyses of brain networks involved in WM by allowing the examination of the dynamics of these networks across different types of task demands. This allowed for a more refined evaluation of the WM-related networks altered in schizophrenia.

The predictions for the role of the DLPFC in WM deficits were partially confirmed; that is, there was evidence of hypoactivity in schizophrenia patients in a network comprising DLPFC, paracingulate/superior frontal gyrus, posterior parietal, and anterior insula regions (i.e., the internal attention network) during the SCAP task. However, this network was not directly correlated

with task performance or WM capacity. Rather, a network that seemingly subserved the encoding phase of the WM tasks, comprising mainly visual cortex activation, precentral gyrus, SMA/superior frontal gyrus, and thalamus (i.e., the visual attention network), was the most predictive of task performance and WM capacity (measured outside the scanner) in both the verbal and the visuospatial WM tasks. This network also exhibited attenuation in schizophrenia patients, but did not comprise the DLPFC region that has typically been associated with WM.

6.2. Comparison of Findings Across Chapters

6.2.1. Two- versus four-task CPCA results

The multi-experiment analyses demonstrated that a more refined characterization of networks can occur with tasks comprising a mix of overlapping and non-overlapping cognitive demands. This is evident even from the 2-task WM-TGT analysis reported in Chapter 3, which produced networks seeming to reflect motor response processes, visual attention, internal attention, DMN deactivation, an occipital network, and an auditory network. While similar networks emerged when four tasks were analyzed in Chapter 5, further delineation of processes coinciding with the motor response was observed as well, and the greater variety of cognitive domains that were incorporated allowed for a better understanding of the functions served by the networks that emerged.

The most consistent networks across the multi-experiment analyses were the visual attention network, internal attention network, and DMN. Notably, the role of the internal attention network became more apparent with the additions of the SCAP and TSI tasks. Its engagement in the SCAP task – exhibiting the same dynamics and relation to task conditions as observed in the verbal WM task – confirmed that it does not specifically underlie inner speech, and may support maintenance of either verbal or visuospatial stimuli. The sustained HDR of the internal attention

network in the TSI task provided further support for the suggestion that this network underlies internally-oriented attention (likely in the form of error monitoring or reflecting on the task rules), as it extended beyond the motor response HDR (Figure 5.4D).

The response network from the WM-TGT analysis (Figure 3.8) appeared to further separate into a bilateral motor response network (component 4, Figure 5.33) and a sensorimotor network (component 3, Figure 5.24) that included the SMA, dorsal anterior cingulate, left-lateralized pre/post-central gyri, and posterior insula aspects of the WM-TGT response network. However, this sensorimotor network also included primary auditory cortex and surrounding regions that had previously only exhibited activation in the TGT task (specifically the hearing condition).

6.2.2. Single- versus four-task CPCA results

The samples included in the single-task analyses did not consist of entirely the same participants as those who were included in the 4-task analysis, as only healthy control data were included in the individual single-task analyses (and in some cases only a subset of these healthy controls were subsequently included in the 4-task analysis). Nevertheless, some observations may be made with respect to key findings across the different analyses.

6.2.2.1. WM task

As previously discussed in detail, the most striking difference between the WM task network compositions before versus after merging with another task was the apparent decomposition of the response-related network, which allowed for the internal attention network to emerge independently. This was observed with the addition of the TGT task only, and then even further with the 4-task fMRI-CPCA as described in the previous section, although the internal attention network remained anatomically and temporally consistent between the 2-task results (Figure

3.12) and 4-task results (Figures 5.15 and 5.16 for anatomical and temporal characteristics, respectively). Interestingly, the visual attention network remained quite stable; regardless of whether the WM task was analyzed in isolation (Figure 4.3), with just the TGT task (Figure 3.10), or with the SCAP and TSI tasks as well (Figures 5.44 and 5.45 for anatomical and temporal characteristics, respectively), this network exhibited virtually identical anatomical and temporal characteristics in the WM task. This is especially noteworthy given that the visual attention network did not emerge in other tasks when analyzed individually; however, there are some notable similarities with the language network that emerged in the TGT single-task analysis (Figure 4.18), as discussed later (Section 6.2.2.4).

6.2.2.2. SCAP task

Only two components emerged when the SCAP task was analyzed alone, one of which reflected a typical pattern of sustained DMN deactivation (component 2, Figure 4.10). The SCAP task external attention network (component 1; Figure 4.8) may have reflected a similar composite of response and cognitive processes as is thought to have occurred in the verbal WM task on its own. Anatomically, this network appeared to comprise aspects of task-positive networks that emerged in the 4-task analysis; for example, the superior lateral peaks in the parietal cortex and the middle/superior frontal cortex overlap with similar clusters in the internal attention network (Figure 5.15), while the dorsomedial prefrontal cortex and lateral occipital cortex peaks overlap with those aspects of the visual attention network (Figure 5.44). Although this is speculative, the notion of this network reflecting a composite of temporally correlated processes that subsequently separated in the multi-experiment analysis is consistent with what was more clearly observed in the verbal WM task, and would help to explain why this network as a whole did not emerge in the 4-task analysis. The finding that best highlights an advantage of the multi-experiment ap-

proach was the ensuing engagement of the visual attention network in the SCAP task; namely, this network turned out to be the most predictive of task performance and WM capacity in both the verbal WM and the SCAP datasets, and yet it did not separate onto its own component when the SCAP task was analyzed in isolation.

6.2.2.3. TSI task

Although not identical between analyses, the two task-positive networks that emerged in the TSI single-task analysis (response network and evaluation network; Figures 4.14 and 4.16, respectively) exhibit a relatively clear resemblance to networks extracted from the 4-task analysis. Namely, the TSI task response network (component 2; Figure 4.14A and B for anatomical and HDR characterizations, respectively), which was theorized to underlie bilateral motor responses, is most similar to the motor response network that emerged in the 4-task analysis (Figures 5.33 and 5.40 for anatomical and HDR characterizations, respectively). Both of these response networks exhibited peaks at 6-8 seconds, and were more engaged in the neutral stimulus conditions than in the incongruent stimulus conditions. The TSI task evaluation network (component 3; Figure 4.16A and B for anatomical and HDR characterizations, respectively) most closely resembles the internal attention network from the 4-task analysis (Figures 5.15 and 5.21 for anatomical and HDR characterizations, respectively), with sustained HDRs that extended beyond those of the response network in both analyses, but with slightly earlier peaks in the 4-task internal attention network. In both analyses, there was a substantial effect of stimulus congruency whereby this network was more engaged on incongruent stimulus trials than on neutral stimulus trials (Figures 4.17 and 5.22A for single- and 4-task results, respectively). However, only the 4-task CPCA internal attention network exhibited a statistically significant effect of task-switch condition (i.e., a more sustained response on trials following an incongruent colour-naming

block; Figure 5.22B). The TSI task DMN/occipital network (component 1; Figure 4.12), while appearing in part to reflect DMN deactivation, also comprised widespread medial occipital deactivation which closely resembles the occipital network that emerged in the 4-task analysis (Figures 5.55 and 5.60 for anatomical and HDR characterizations, respectively). Therefore, it is likely that the TSI task DMN/occipital network reflects a combination of the DMN and occipital network deactivations that were separated onto different networks in the 4-task analysis. This occipital deactivation is speculated to reflect suppression of visual scanning/focusing on basic visual features (which may be important for focusing instead on the semantic meaning of a word rather than the font colour in which it is printed).

6.2.2.4. TGT task

As noted in Chapter 4, the TGT results were perhaps the most distinctive, especially with respect to the task-negative networks that emerged (comprising sub-components of the DMN along with additional clusters; Figures 4.19 and 4.20). Therefore, it is notable that the 4-task networks – including the DMN – were largely engaged in the TGT task despite there being little overlap with networks observed in the single-task TGT analysis. While it could be perceived as a drawback of the multi-experiment approach that some task-specific networks such as the DMN sub-components are "lost", it is valuable for distinguishing networks that are reproducible across tasks. An alternative combination of language-related tasks may be more appropriate for research questions centered around semantic processing or a similar domain rather than WM. Nevertheless, the language network from the TGT single-task analysis (component 1; Figure 4.18) may reflect meaningful overlap with the visual attention network that emerged in the multi-experiment analyses (Figures 5.44 and 5.53 for anatomical and temporal characteristics, respectively). The TGT language network (Figure 4.18) included the same superior dorsomedial pre-

frontal cluster (i.e., SMA/superior frontal gyrus) and the same widespread activity in lateral visual cortex that emerged in the 4-task visual attention network (Figure 5.44). Regions that did *not* overlap with the visual attention network included known language regions (Broca's area in left inferior frontal gyrus and Wernicke's area in superior temporal gyri); further, the superior lateral occipital cortex and the thalamus were left-lateralized rather than bilateral. The SMA/superior frontal gyrus region could be a domain-general anchor around which more domain-specific regions connect depending on the task; this could explain why the visual attention network exhibited substantial engagement in the TGT task but with a less sizeable difference between task conditions (as compared to the effect of condition in the language network when the TGT data were analyzed alone; compare Figures 4.18 and 5.53). Based on comprehensive evaluations of frontal lobe lesion studies, Stuss (2011) proposed that dorsomedial prefrontal cortex subserves energization of the required response set in a task; such a characterization may be consistent with the pattern of results observed in the visual attention network, the basis of which could lie in the SMA/superior frontal gyrus cluster.

6.3. Implications

WM impairment is a core feature of schizophrenia, and the current gold standard of treatment for WM and other cognitive deficits is cognitive remediation therapy (CRT). CRT is effective for a variety of cognitive abilities in schizophrenia, with verbal WM and verbal learning/memory comprising some of the most reliable effects (McGurk, Twamley, Sitzer, McHugo, & Mueser, 2007; Wykes, Huddy, Cellard, McGurk, & Czobor, 2011). However, CRT requires considerable motivation from the patient, is less effective in severely affected individuals (particularly as it can be discouraging for individuals who struggle with the training), and at best shows only moderate effects (McGurk et al., 2007; Wykes et al., 2011). There is growing interest

in the development of transcranial electrical neuromodulation as a potential treatment for individuals with neuropsychiatric disorders who do not respond to more conventional treatment approaches (Bikson et al., 2018). With recent advances in high-density (e.g., 256 channels) electrode montages, neuromodulation may eventually be able to target brain networks rather than individual regions. Another advance in neuromodulation uses real-time fMRI neurofeedback to train individuals to control their brain activity in specific regions (Rance et al., 2018). The present findings reflect an important step in identifying potential targets of such treatments; for example, the visual attention network may be an appropriate target for treatment aiming to enhance encoding of memory sets.

The present findings suggest that disruption in encoding may underlie WM deficits in schizophrenia. However, it is possible that a disruption in early cognitive energization is not limited to WM function, but may be a domain-general deficit that depends on early activation in the visual attention network. Group differences also emerged in the TGT task, though in the opposite direction (i.e., patients exhibited greater engagement of the visual attention network than did controls). Nevertheless, the commonality of group differences in this network may be meaningful, and whether dysfunction manifests as greater or lesser activation may depend on the task. As discussed above (Section 6.2.2.4), the visual attention network may be closely related to the language network that emerged in the TGT task alone, with shared nodes in the SMA/superior frontal gyrus and in visual cortex. A domain-general deficit that is potentially anchored in a specific region would have practical clinical implications, as neurocognitive impairment in schizophrenia is not limited to WM.

The present findings also have theoretical implications for cognitive neuroscience research aiming to describe the role of frontopartietal connectivity in WM tasks. Four of the net-

works that emerged in the 4-task analysis exhibited varying configurations of connectivity with activation in dorsomedial prefrontal cortex, and each network exhibited some degree of domain-generality (at least with respect to the cognitive domains examined). However, a comparison between network HDRs clearly demonstrates a degree of functional specificity for each, proposed to reflect visual attention, internal attention, response, and sensorimotor processes. While resting-state and other component-based task-state studies have also demonstrated a differentiation of prefrontal cortex-related networks, fMRI-CPCA adds richness and precision by computing the estimated time courses of each network as a means of illustrating the functional delineation of the networks that emerge.

The use of multi-experiment analyses has been identified as an important direction in the aim of structure-function mapping in fMRI research (Poldrack & Yarkoni, 2016). Therefore, methodology that allows merging of data from different tasks, different samples, and even different scanners is highly desirable for the advancement of cognitive neuroscience, especially given the growth of publicly available fMRI data on a wide range of tasks (e.g., the UCLA Consortium for Neuropsychiatric Phenomics study from which the SCAP data were obtained, http://www.phenomics.ucla.edu/index.asp; the Functional Biomedical Informatics Research Network, https://www.nitrc.org/projects/fbirn/; and many other sources). As it is important for fMRI sessions to be concise and tolerable for participants – especially in certain clinical populations and children – the application of multi-experiment fMRI-CPCA to existing datasets provides a practical and cost-effective alternative to running studies that utilize complex tasks with numerous experimental manipulations.

6.4. Limitations

The multi-experiment analyses combined primarily separate groups of participants originating from different fMRI studies. Although many of these studies were carried out in the same research group with the same MRI scanning facilities, comparisons between tasks were still limited to between-groups analyses (except for participants who completed the verbal WM and TSI tasks). However, given that the multi-experiment component solutions were derived from all datasets simultaneously, the present methodology is a significant improvement over side-by-side comparisons of studies because the replication of each network across experiments could be directly evaluated.

Although the analyses in the present research were based primarily on the temporal rather than spatial characteristics of the networks observed, a limitation regarding the boundaries of networks obtained from PCA should be noted. As the maps produced from PCA are comprised of component loadings which have been thresholded at an experimenter-defined value (the highest 10% absolute values in the present work), the visualized boundaries of these networks may not precisely line up with known anatomical boundaries. A more precise visualization could be obtained by supplementing this work with a more anatomically-focused analysis such as computing local gradients (Schaefer et al., 2018). In any case, the anatomical distinctions between networks should be discussed in terms of where the *peak* regions of activity/deactivity are located, as boundaries may not be as well defined and a given brain region could be involved in multiple task-related functions.

Although meaningful relationships were found between digit span, fMRI task performance, and brain activity in Chapter 5 (most notably in the visual attention network), correlations between activity increases/decreases and behavioural measures such as task accuracy do

not necessarily indicate that the network in question *underlies* that particular cognitive construct. Although comprehensive evaluations of network dynamics were carried out to consider where in the post-stimulus time series an effect emerged, the direction of causality was not always clear; for example, the response network exhibited a significant negative correlation between degree of sustained activation in the return-to-baseline phase of the HDR and response accuracy, which could indicate that rapid deactivation of this network is important for accuracy on the subsequent trial (e.g., reflecting a "reset" of motor response inhibition) or that this network deactivates quicker following a correct response, or some combination of both. With respect to the visual attention network, however, the relationship is somewhat clearer because the HDR initiated and peaked early enough in the post-stimulus time series to preclude the possibility of correct responses *producing* greater activity.

The schizophrenia patients who participated in this research were stabilized outpatients, with the majority taking antipsychotic medication; this raises the question as to how well these samples represent the wider population of individuals with a diagnosis of schizophrenia. However, WM impairment in schizophrenia is known to be present prior to the first episode of psychosis (Carrión et al., 2018) and in drug-naïve schizophrenia patients (Fatouros-Bergman et al., 2014), and it is nevertheless of clinical and scientific value to investigate dysfunction that may persist in stabilized patients. A more serious issue is the possibility that neurological findings may reflect changes due to effects of medications rather than being intrinsic to schizophrenia. This is a prevailing confound in schizophrenia research, as it is rarely feasible to study large samples of schizophrenia patients who are medication-free, and it is difficult to separate the effects of medication dosage from illness severity. While there is some evidence to suggest that antipsychotics may contribute to cortical thinning (Emsley et al., 2017), modulatory effects of

antipsychotics and other medications on functional connectivity are as yet undetermined, and the present findings should be interpreted with this limitation in mind.

6.5. Future Directions

The present work provides a basis for future research combining a variety of other cognitive constructs that were not investigated here, but are also affected in schizophrenia (e.g., verbal memory and processing speed). In addition, analyses of symptom state-related domains could be carried out to investigate differences between acutely psychotic patients and remitted schizophrenia patients. Longitudinal studies would be especially valuable for distinguishing signatures of dysconnectivity that remain stable as psychotic symptoms fluctuate versus connectivity that is dependent on the severity of specific symptoms. Such an analysis has not been carried out in a multi-experiment framework. Combining a mix of constructs that are thought to persist independent of psychotic state (e.g., WM and other neurocognitive domains) and constructs that are thought to be state-related (e.g., cognitive biases related to delusions) would be especially informative.

fMRI-CPCA reveals multiple networks simultaneously engaged in a task and does not rely on ROIs or HRFs. Although this is important for research questions requiring a data-driven approach, a drawback is the inability to characterize topological relationships between distant clusters of activity within each network, such as the modulation of one region over another (i.e., effective connectivity). Questions related to effective connectivity and efficiency of network connections require a more targeted investigation such as dynamic causal modelling (Friston, Harrison, & Penny, 2003) or graph theory (Bullmore & Sporns, 2009). Using the cluster peaks of the networks obtained with fMRI-CPCA to select ROIs, an analysis of effective connectivity – performed on the task-related variance in BOLD signal – could be employed to determine the

directions of information flow from one brain region to another, and whether information transfer is disrupted in schizophrenia. Alternatively, a graph theory-based analysis could be performed using the clusters extracted from fMRI-CPCA to define nodes of a given network of interest (e.g., visual attention), and constructing the connections from the task-related variance in BOLD signal. Graphs could then be compared between patient and control groups to evaluate whether observed hypoactivity in a given network is due to inefficient organization of connections in schizophrenia, or whether networks are topologically identical but exhibit differing degrees of activity for other reasons. Such approaches will be important avenues of research to confirm the underlying bases of network alterations observed in the present findings.

6.6. Conclusions

This research presents a novel approach to functional brain mapping of WM engagement in schizophrenia. The multi-experiment approach illustrates important advantages over conventional analyses; not only does it allow a greater number of finer-grained networks to be extracted, but also the interpretations of individual networks are greatly facilitated. For example, distinct cognitive/behavioral processes that load onto a single network due to being temporally correlated may separate onto different networks when data are analyzed with a task involving different types of cognitive demands. In addition, interpretation can be greatly enhanced with direct comparisons of the role of a particular network across several different forms of cognitive demand.

As detected with task-state fMRI, several frontoparietal networks may subserve WM and cognitive sub-processes which overlap with other domains. These include but may not necessarily be limited to visual attention, internal attention, and response processes. The visual attention network, comprised of superior dorsomedial prefrontal cortex (SMA/superior frontal gyrus), precentral gyrus, lateral visual cortex, and thalamus, may drive encoding during WM tasks, and dis-

ruption in this network may lead to deficits in WM capacity. Similar configurations of this network, anchored in the SMA/superior frontal gyrus, may drive energization of the required response set in other tasks (e.g., engagement of required language domains in a semantic processing task). The internal attention network, comprised of more anterior prefrontal regions – including DLPFC – as well as anterior insula and intraparietal sulcus, may support maintenance of the memory set during a WM task, but also a variety of other internally-oriented processes in other tasks such as monitoring errors and/or task instructions, or volitional thought generation. Maintenance of information to hold in memory is neurologically separable from initial attention to encoded stimuli and from response processes, but observing this separation may require innovative approaches when the temporal resolution of the neuroimaging modality is limited (as it is with fMRI).

Dysfunction of WM task-related networks in schizophrenia may not be limited to networks comprising DLPFC. Moreover, observed dysfunction/attenuation of a particular network may not necessarily indicate that that network directly underlies impairment as measured by the cognitive construct per se. Deficits in WM capacity may arise from problems during the encoding phase in particular, and less so during maintenance of the memory set or during recall/recognition. Therefore, future treatments that aim to directly modulate brain networks may benefit from a focus on the visual attention network observed here, and with the specific aim of improving engagement of this network at the onset of a WM task. Further study using creative methods to isolate cognitive sub-processes would be a constructive avenue of research in WM and other domains affected in schizophrenia.

Bibliography

Aguirre, G. K., Zarahn, E., & D'Esposito, M. (1998). The variability of human, BOLD hemodynamic responses. *NeuroImage, 8*, 360-369. doi:10.1006/nimg.1998.0369

American Psychiatric Association. (2013). *Diagnostic and Statistical Manual of Mental Disorders* (5 ed.). Washington, DC: Author.

Andreasen, N. C. (1984a). *Scale for the Assessment of Negative Symptoms (SANS)*. Iowa City, IA: University of Iowa.

Andreasen, N. C. (1984b). *Scale for the Assessment of Positive Symptoms (SAPS)*. Iowa City, IA: University of Iowa.

Annett, M. A. (1970). A classification of hand preference by association analysis. *British Journal of Psychiatry, 61*, 303-321. doi:10.1111/j.2044-8295.1970.tb01248.x

Arnsten, A. F. T., Girgis, R. R., Gray, D. L., & Mailman, R. B. (2017). Novel dopamine therapeutics for cognitive deficits in schizophrenia. *Biological Psychiatry, 81*, 67-77. doi:10.1016/j.biopsych.2015.12.028

Baddeley, A. (2012). Working memory: Theories, models, and controversies. *Annual Review of Psychology, 63*, 1-29.

Baddeley, A., & Hitch, G. J. (1974). Working memory. In G. Bower (Ed.), *Recent Advances in Learning and Motivation*. New York: Academic Press.

Barch, D. M., & Ceaser, A. (2012). Cognition in schizophrenia: Core psychological and neural mechanisms. *Trends in Cognitive Sciences, 16*, 27-34. doi:10.1016/j.tics.2011.11.015

Bastin, J., Deman, P., David, O., Gueguen, M., Benis, D., Minotti, L., . . . Jerbi, K. (2016). Direct Recordings from Human Anterior Insula Reveal its Leading Role within the Error-Monitoring Network. *Cerebral Cortex, 27*, 1545-1557. doi:10.1093/cercor/bhv352

Bikson, M., Brunoni, A. R., Charvet, L. E., Clark, V. P., Cohen, L. G., Deng, Z.-D., . . . Lisanby, S. H. (2018). Rigor and reproducibility in research with transcranial electrical stimulation: An NIMH-sponsored workshop. *Brain Stimulation, 11*, 465-480. doi:10.1016/j.brs.2017.12.008

Bodnar, M., Malla, A., Joober, R., & Lepage, M. (2008). Cognitive markers of short-term clinical outcome in first-episode psychosis. *British Journal of Psychiatry, 193*, 297-304. doi:10.1192/bjp.bp.107.040410

Bowie, C. R., Leung, W. W., Reichenberg, A., McClure, M. M., Patterson, T. L., Heaton, R. K., & Harvey, P. D. (2008). Predicting schizophrenia patients' real-world behavior with specific neuropsychological and functional capacity measures. *Biological Psychiatry, 63*, 505-511. doi:10.1016/j.biopsych.2007.05.022

Braunlich, K., Gomez-Lavin, J., & Seger, C. A. (2015). Frontoparietal networks involved in categorization and item working memory. *NeuroImage, 107*, 146-162. doi:10.1016/j.neuroimage.2014.11.051

Buckner, R. L., Andrews-Hanna, J. R., & Schacter, D. L. (2008). The brain's default network: anatomy, function, and relevance to disease. *Ann N Y Acad Sci, 1124*, 1-38. doi:10.1196/annals.1440.011

Buckner, R. L., Krienen, F. M., Castellanos, A., Diaz, J. C., & Yeo, B. T. (2011). The organization of the human cerebellum estimated by intrinsic functional connectivity. *Journal of Neurophysiology, 106*, 2322-2345. doi:10.1152/jn.00339.2011

Bullmore, E., & Sporns, O. (2009). Complex brain networks: Graph theoretical analysis of structural and functional systems. *Nature Reviews Neuroscience, 10*, 186-198. doi:10.1038/nrn2575

Burock, M. A., Buckner, R. L., Woldorff, M. G., Rosen, B. R., & Dale, A. M. (1998). Randomized event-related experimental designs allow for extremely rapid presentation rates using functional MRI. *NeuroReport, 9*, 3735-3739. doi:10.1097/00001756-199811160-00030

Calhoun, V. D., Adali, T., Kiehl, K. A., Astur, R., Pekar, J. J., & Pearlson, G. D. (2006). A method for multitask fMRI data fusion applied to schizophrenia. *Human Brain Mapping, 27*, 598-610. doi:10.1002/hbm.20204

Callicott, J. H., Mattay, V. S., Verchinski, B. A., Marenco, S., Egan, M. F., & Weinberger, D. R. (2003). Complexity of prefrontal cortical dysfunction in schizophrenia: More than up or down. *American Journal of Psychiatry, 160*, 2209-2215. doi:10.1176/appi.ajp.160.12.2209

Canuet, L., Aoki, Y., Ishii, R., & Maestú, F. (2016). The role of functional networks in neuropsychiatric disorders. In S. Palva (Ed.), *Multimodal Oscillation-based Connectivity Theory* (pp. 123-147). Cham: Springer International Publishing.

Carp, J. (2012). On the plurality of (methodological) worlds: Estimating the analytic flexibility of fMRI experiments. *Frontiers in Neuroscience, 6*, 149. doi:10.3389/fnins.2012.00149

Carrión, R. E., Walder, D. J., Auther, A. M., McLaughlin, D., Zyla, H. O., Adelsheim, S., . . . Cornblatt, B. A. (2018). From the psychosis prodrome to the first-episode of psychosis: No evidence of a cognitive decline. *Journal of Psychiatric Research, 96*, 231-238. doi:10.1016/j.jpsychires.2017.10.014

Carter, C. S., Barch, D. M., Buchanan, R. W., Bullmore, E., Krystal, J. H., Cohen, J., . . . Heinssen, R. (2008). Identifying cognitive mechanisms targeted for treatment development in schizophrenia: An overview of the first meeting of the cognitive neuroscience treatment research to improve cognition in schizophrenia initiative. *Biological Psychiatry, 64*, 4-10. doi:10.1016/j.biopsych.2008.03.020

Cattell, R. B. (1966). The scree test for the number of factors. *Multivariate Behavioral Research, 1*, 245-276. doi:10.1207/s15327906mbr0102_10

Cattell, R. B., & Vogelmann, S. (1977). A comprehensive trial of the scree and kg criteria for determining the number of factors. *Multivariate Behavioral Research, 12*, 289-325. doi:10.1207/s15327906mbr1203_2

Cauda, F., D'Agata, F., Sacco, K., Duca, S., Geminiani, G., & Vercelli, A. (2011). Functional connectivity of the insula in the resting brain. *NeuroImage, 55*, 8-23. doi:10.1016/j.neuroimage.2010.11.049

Choi, E. Y., Yeo, B. T., & Buckner, R. L. (2012). The organization of the human striatum estimated by intrinsic functional connectivity. *Journal of Neurophysiology, 108*, 2242-2263. doi:10.1152/jn.00270.2012

Cohen, J. R., & D'Esposito, M. (2016). The segregation and integration of distinct brain networks and their relationship to cognition. *The Journal of Neuroscience, 36*, 12083-12094. doi:10.1523/JNEUROSCI.2965-15.2016

Cohen, J. R., Sreenivasan, K. K., & D'Esposito, M. (2014). Correspondence between stimulus encoding- and maintenance-related neural processes underlies successful working memory. *Cerebral Cortex, 24*, 593–599. doi:10.1093/cercor/bhs339

Coltheart, M. (1981). The MRC Psycholinguistic Database. *The Quarterly Journal of Experimental Psychology Section A, 33*, 497-505. doi:10.1080/14640748108400805

D'Esposito, M., & Postle, B. R. (2015). The cognitive neuroscience of working memory. *Annual Review of Psychology, 66*, 115-142. doi:10.1146/annurev-psych-010814-015031

Dale, A. M. (1999). Optimal experimental design for event-related fMRI. *Human Brain Mapping, 8*, 109-114. doi:10.1002/(SICI)1097-0193(1999)8:2/3<109::AID-HBM7>3.0.CO;2-W

Duncan, J. (2010). The multiple-demand (MD) system of the primate brain: Mental programs for intelligent behaviour. *Trends in Cognitive Sciences, 14*, 172-179. doi:10.1016/j.tics.2010.01.004

Duncan, J., & Owen, A. M. (2000). Common regions of the human frontal lobe recruited by diverse cognitive demands. *Trends in Neurosciences, 23*, 475-483. doi:10.1016/S0166-2236(00)01633-7

Edwards, B. G., Calhoun, V. D., & Kiehl, K. A. (2012). Joint ICA of ERP and fMRI during error-monitoring. *NeuroImage, 59*, 1896-1903. doi:10.1016/j.neuroimage.2011.08.088

Emch, M., von Bastian, C. C., & Koch, K. (2019). Neural correlates of verbal working memory: An fMRI meta-analysis. *Frontiers in Human Neuroscience, 13*, 180. doi:10.3389/fnhum.2019.00180

Emsley, R., Asmal, L., du Plessis, S., Chiliza, B., Phahladira, L., & Kilian, S. (2017). Brain volume changes over the first year of treatment in schizophrenia: Relationships to antipsychotic treatment. *Psychological Medicine, 47*, 2187-2196. doi:10.1017/S0033291717000642

Fatouros-Bergman, H., Cervenka, S., Flyckt, L., Edman, G., & Farde, L. (2014). Meta-analysis of cognitive performance in drug-naïve patients with schizophrenia. *Schizophrenia Research, 158*, 156-162. doi:10.1016/j.schres.2014.06.034

Fedorenko, E., Duncan, J., & Kanwisher, N. (2013). Broad domain generality in focal regions of frontal and parietal cortex. *Proceedings of the National Academy of Sciences of the United States of America, 110*, 16616-16621. doi:10.1073/pnas.1315235110

First, M. B., Spitzer, R. L., Gibbon, M., & Williams, J. B. W. (2002). *Structured Clinical Interview for DSM-IV-TR Axis I Disorders, Research Version, Patient Edition.*

Flinker, A., Korzeniewska, A., Shestyuk, A. Y., Franaszczuk, P. J., Dronkers, N. F., Knight, R. T., & Crone, N. E. (2015). Redefining the role of Broca's area in speech. *Proceedings of the National Academy of Sciences, 112*, 2871-2875. doi:10.1073/pnas.1414491112

Friston, K. J. (1999). Schizophrenia and the disconnection hypothesis. *Acta Psychiatrica Scandinavica, 99*, 68-79. doi:10.1111/j.1600-0447.1999.tb05985.x

Friston, K. J., Harrison, L., & Penny, W. (2003). Dynamic causal modelling. *NeuroImage, 19*, 1273-1302. doi:10.1016/S1053-8119(03)00202-7

Fuster, J. n. M. (2004). Upper processing stages of the perception–action cycle. *Trends in Cognitive Sciences, 8*, 143-145. doi:10.1016/j.tics.2004.02.004

Gazzaley, A., Rissman, J., & D'Esposito, M. (2004). Functional connectivity during working memory maintenance. *Cognitive, Affective, & Behavioral Neuroscience, 4*, 580-599. doi:10.3758/CABN.4.4.580

Glausier, J. R., & Lewis, D. A. (2018). Mapping pathologic circuitry in schizophrenia. In I. Huitinga & M. J. Webster (Eds.), *Handbook of Clinical Neurology* (Vol. 150, pp. 389-417): Elsevier.

Grady, C. L., Springer, M. V., Hongwanishkul, D., McIntosh, A. R., & Gordon Winocur, G. (2006). Age-related changes in brain activity across the adult lifespan. *Journal of Cognitive Neuroscience, 18*, 227-241. doi:10.1162/089892906775783705

Green, M. F., Nuechterlein, K. H., Gold, J. M., Barch, D. M., Cohen, J., Essock, S., . . . Marder, S. R. (2004). Approaching a consensus cognitive battery for clinical trials in schizophrenia: The NIMH-MATRICS conference to select cognitive domains and test criteria. *Biological Psychiatry, 56*, 301-307. doi:10.1016/j.biopsych.2004.06.023

Hoffmann, S., Labrenz, F., Themann, M., Wascher, E., & Beste, C. (2014). Crosslinking EEG time–frequency decomposition and fMRI in error monitoring. *Brain Structure and Function, 219*, 595-605. doi:10.1007/s00429-013-0521-y

Hu, M.-L., Zong, X.-F., Mann, J. J., Zheng, J.-J., Liao, Y.-H., Li, Z.-C., . . . Tang, J.-S. (2017). A Review of the Functional and Anatomical Default Mode Network in Schizophrenia. *Neuroscience Bulletin, 33*, 73-84. doi:10.1007/s12264-016-0090-1

Hunter, M. A., & Takane, Y. (2002). Constrained principal component analysis: Various applications. *Journal of Educational and Behavioral Statistics, 27*, 105-145. doi:10.3102/10769986027002105

Iannaccone, R., Hauser, T. U., Staempfli, P., Walitza, S., Brandeis, D., & Brem, S. (2015). Conflict monitoring and error processing: New insights from simultaneous EEG–fMRI. *NeuroImage, 105*, 395-407. doi:10.1016/j.neuroimage.2014.10.028

Kaiser, H. F. (1958). The varimax criterion for analytic rotation in factor analysis. *Psychometrika, 23*, 187-200. doi:10.1007/BF02289233

Karlsgodt, K. H., Glahn, D. C., van Erp, T. G., Therman, S., Huttunen, M., Manninen, M., . . . Cannon, T. D. (2007). The relationship between performance and fMRI signal during working memory in patients with schizophrenia, unaffected co-twins, and control subjects. *Schizophrenia Research, 89*, 191-197. doi:10.1016/j.schres.2006.08.016

Karlsgodt, K. H., Sanz, J., van Erp, T. G. M., Bearden, C. E., Nuechterlein, K. H., & Cannon, T. D. (2009). Re-evaluating dorsolateral prefrontal cortex activation during working memory in schizophrenia. *Schizophrenia Research, 108*, 143-150. doi:10.1016/j.schres.2008.12.025

Karlsgodt, K. H., Sun, D., Jimenez, A. M., Lutkenhoff, E. S., Willhite, R., van Erp, T. G. M., & Cannon, T. D. (2008). Developmental disruptions in neural connectivity in the pathophysiology of schizophrenia. *Development and Psychopathology, 20*, 1297-1327. doi:10.1017/S095457940800062X

Keefe, R. S. E., Bilder, R. M., Harvey, P. D., Davis, S. M., Palmer, B. W., Gold, J. M., . . . Lieberman, J. A. (2006). Baseline neurocognitive deficits in the CATIE schizophrenia trial. *Neuropsychopharmacology, 31*, 2033-2046. doi:10.1038/sj.npp.1301072

Kim, D. I., Manoach, D. S., Mathalon, D. H., Turner, J. A., Mannell, M., Brown, G. G., . . . Calhoun, V. D. (2009). Dysregulation of working memory and default-mode networks in schizophrenia using independent component analysis, an fBIRN and MCIC study. *Human Brain Mapping, 30*, 3795-3811. doi:10.1002/hbm.20807

Kim, M. A., Tura, E., Potkin, S. G., Fallon, J. H., Manoach, D. S., Calhoun, V. D., & Turner, J. A. (2010). Working memory circuitry in schizophrenia shows widespread cortical inefficiency and compensation. *Schizophrenia Research, 117*, 42-51. doi:10.1016/j.schres.2009.12.014

Lavigne, K. M., Menon, M., & Woodward, T. S. (2016). Impairment in subcortical suppression in schizophrenia: Evidence from the fBIRN Oddball Task. *Human Brain Mapping, 37*, 4640-4653. doi:10.1002/hbm.23334

Lavigne, K. M., Metzak, P. D., & Woodward, T. S. (2015). Functional brain networks underlying detection and integration of disconfirmatory evidence. *NeuroImage, 112*, 138-151. doi:10.1016/j.neuroimage.2015.02.043

Lavigne, K. M., Rapin, L. A., Metzak, P. M., Whitman, J. C., Jung, K., Dohen, M., . . . Woodward, T. S. (2015). Left-dominant temporal-frontal hypercoupling in schizophrenia patients with hallucinations during speech perception. *Schizophrenia bulletin, 41*, 259-267. doi:10.1093/schbul/sbu004

Lavigne, K. M., & Woodward, T. S. (2018). Hallucination- and speech-specific hypercoupling in frontotemporal auditory and language networks in schizophrenia using combined task-based fMRI data: An fBIRN study. *Human Brain Mapping, 39*, 1582-1595. doi:10.1002/hbm.23934

Lepage, M., Bodnar, M., & Bowie, C. R. (2014). Neurocognition: Clinical and functional outcomes in schizophrenia. *The Canadian Journal of Psychiatry, 59*, 5-12. doi:10.1177/070674371405900103

Li, X., Xiao, Y.-h., Zhao, Q., Leung, A. W. W., Cheung, E. F. C., & Chan, R. C. K. (2015). The neuroplastic effect of working memory training in healthy volunteers and patients with schizophrenia: Implications for cognitive rehabilitation. *Neuropsychologia, 75*, 149-162. doi:10.1016/j.neuropsychologia.2015.05.029

Liddle, E. B., Bates, A. T., Das, D., White, T. P., Groom, M. J., Jansen, M., . . . Liddle, P. F. (2013). Inefficient cerebral recruitment as a vulnerability marker for schizophrenia. *Psychological Medicine, 43*, 169-182. doi:10.1017/S0033291712000992

Liddle, P. F., Ngan, E. T. C., Duffield, G., & Warren, A. J. (2002). Signs and Symptoms of Psychotic Illness (SSPI): A rating scale. *The British Journal of Psychiatry, 180*, 45-50. doi:10.1192/bjp.180.1.45

Logothetis, N. K., & Wandell, B. A. (2004). Interpreting the BOLD signal. *Annual Review of Physiology, 66*, 735-769.

Lutgens, D., Lepage, M., Iyer, S., & Malla, A. (2014). Predictors of cognition in first episode psychosis. *Schizophrenia Research, 152*, 164-169. doi:10.1016/j.schres.2013.10.044

Mahmoudi, A., Takerkart, S., Regragui, F., Boussaoud, D., & Brovelli, A. (2012). Multivoxel pattern analysis for fMRI data: A review. *Computational and Mathematical Methods in Medicine, 2012*, 961257-961257. doi:10.1155/2012/961257

Manoach, D. S. (2003). Prefrontal cortex dysfunction during working memory performance in schizophrenia: Reconciling discrepant findings. *Schizophrenia Research, 60*, 285-298. doi:10.1016/S0920-9964(02)00294-3

McGurk, S. R., Mueser, K. T., Harvey, P. D., LaPuglia, R., & Marder, J. (2003). Cognitive and symptom predictors of work outcomes for clients with schizophrenia in supported employment. *Psychiatric Services, 54*, 1129-1135. doi:10.1176/appi.ps.54.8.1129

McGurk, S. R., Twamley, E. W., Sitzer, D. I., McHugo, G. J., & Mueser, K. T. (2007). A meta-analysis of cognitive remediation in schizophrenia. *American Journal of Psychiatry, 164*, 1791-1802. doi:10.1176/appi.ajp.2007.07060906

McIntosh, A. R., & Lobaugh, N. J. (2004). Partial least squares analysis of neuroimaging data: Applications and advances. *NeuroImage, 23*, S250-S263. doi:10.1016/j.neuroimage.2004.07.020

Meda, S. A., Stevens, M. C., Folley, B. S., Calhoun, V. D., & Pearlson, G. D. (2009). Evidence for anomalous network connectivity during working memory encoding in schizophrenia: An ICA based analysis. *PLoS ONE, 4*, e7911. doi:10.1371/journal.pone.0007911

Metzak, P. D., Feredoes, E., Takane, Y., Wang, L., Weinstein, S., Cairo, T., . . . Woodward, T. S. (2011). Constrained principal component analysis reveals functionally connected load-dependent networks involved in multiple stages of working memory. *Human Brain Mapping, 32*, 856-871. doi:10.1002/hbm.21072

Metzak, P. D., Riley, J. D., Wang, L., Whitman, J. C., Ngan, E. T., & Woodward, T. S. (2012). Decreased efficiency of task-positive and task-negative networks during working memory in schizophrenia. *Schizophrenia bulletin, 38*, 803-813. doi:10.1093/schbul/sbq154; 10.1093/schbul/sbq154

Mortimer, A. M., & Bowen, K. (1999). Measuring IQ in schizophrenia research: an update of the Quick Test in estimating IQ decline. *Cognitive Neuropsychiatry, 4*, 81-88. doi:10.1080/135468099395972

O'Tuathaigh, C. M. P., Moran, P. M., Zhen, X. C., & Waddington, J. L. (2017). Translating advances in the molecular basis of schizophrenia into novel cognitive treatment strategies. *British Journal of Pharmacology, 174*, 3173-3190. doi:10.1111/bph.13938

Oldfield, R. C. (1971). The assessment and analysis of handedness: The Edinburgh inventory. *Neuropsychologia, 9*, 97-113. doi:10.1016/0028-3932(71)90067-4

Pencer, A., & Addington, J. (2003). Substance use and cognition in early psychosis. *Journal of Psychiatry and Neuroscience, 28*, 48-54.

Poldrack, R. A. (2010). Mapping mental function to brain structure: How can cognitive neuroimaging succeed? *Perspectives on Psychological Science, 5*, 753-761. doi:10.1177/1745691610388777

Poldrack, R. A., Congdon, E., Triplett, W., Gorgolewski, K. J., Karlsgodt, K. H., Mumford, J. A., . . . Bilder, R. M. (2016). A phenome-wide examination of neural and cognitive function. *Scientific Data, 3*, 160110. doi:10.1038/sdata.2016.110

Poldrack, R. A., & Yarkoni, T. (2016). From brain maps to cognitive ontologies: Informatics and the search for mental structure. *Annual Review of Psychology, 67*, 587-612. doi:10.1146/annurev-psych-122414-033729

Potkin, S. G., Turner, J. A., Brown, G. G., McCarthy, G., Greve, D. N., Glover, G. H., . . . Lim, K. O. (2009). Working memory and DLPFC inefficiency in schizophrenia: The FBIRN study. *Schizophrenia bulletin, 35*, 19-31. doi:10.1093/schbul/sbn162

Procyshyn, R. M., Bezchlibnyk-Butler, K. Z., & Jeffries, J. J. (2017). *Clinical Handbook of Psychotropic Drugs* (22 ed.): Hogrefe.

Raichle, M. E. (2015). The brain's default mode network. *Annual Review of Neuroscience, 38*, 433-447. doi:10.1146/annurev-neuro-071013-014030

Rajkowska, G., & Goldman-Rakic, P. S. (1995). Cytoarchitectonic definition of prefrontal areas in the normal human cortex: I. Remapping of areas 9 and 46 using quantitative criteria. *Cerebral Cortex, 5*, 307-322. doi:10.1093/cercor/5.4.307

Ramezani, M., Marble, K., Trang, H., Johnsrude, I. S., & Abolmaesumi, P. (2015). Joint sparse representation of brain activity patterns in multi-task fMRI data. *IEEE Transactions on Medical Imaging, 34*, 2-12. doi:10.1109/TMI.2014.2340816

Rance, M., Walsh, C., Sukhodolsky, D. G., Pittman, B., Qiu, M., Kichuk, S. A., . . . Hampson, M. (2018). Time course of clinical change following neurofeedback. *NeuroImage, 181*, 807-813. doi:10.1016/j.neuroimage.2018.05.001

Rapin, L., Loevenbruck, H., Dohen, M., Metzak, P. D., Whitman, J. C., & Woodward, T. S. (2012). Hyperintensity of functional networks involving voice-selective cortical regions during silent thought in schizophrenia. *Psychiatry Research: Neuroimaging, 202*, 110-117. doi:10.1016/j.pscychresns.2011.12.014

Ribary, U., Mackay, A. L., Rauscher, A., Tipper, C. M., Giaschi, D., Woodward, T. S., . . . Moiseev, A. (2017). Emerging neuroimaging technologies: Towards future personalized diagnostics, prognosis, targeted intervention and ethical challenges. In J. Illes (Ed.), *Neuroethics: Anticipating the Future*. New York, NY: Oxford University Press.

Rissman, J., Gazzaley, A., & D'Esposito, M. (2004). Measuring functional connectivity during distinct stages of a cognitive task. *NeuroImage, 23*, 752-763. doi:10.1016/j.neuroimage.2004.06.035

Rogers, R. D., & Monsell, S. (1995). Costs of a predictible switch between simple cognitive tasks. *Journal of Experimental Psychology: General, 124*, 207-231. doi:10.1037/0096-3445.124.2.207

Rottschy, C., Langner, R., Dogan, I., Laird, A. R., Schulz, J. B., Fox, P. T., & Eickhoff, S. B. (2012). Modelling neural correlates of working memory: A coordinate-based meta-analysis. *NeuroImage, 60*, 830-846. doi:10.1016/j.neuroimage.2011.11.050

Rubinov, M., & Sporns, O. (2010). Complex network measures of brain connectivity: Uses and interpretations. *NeuroImage, 52*, 1059-1069. doi:10.1016/j.neuroimage.2009.10.003

Santangelo, V., & Bordier, C. (2019). Large-scale brain networks underlying successful and unsuccessful encoding, maintenance, and retrieval of everyday scenes in visuospatial working memory. *Frontiers in Psychology, 10*, 233. doi:10.3389/fpsyg.2019.00233

Schaefer, A., Kong, R., Gordon, E. M., Laumann, T. O., Zuo, X. N., Holmes, A. J., . . . Yeo, B. T. T. (2018). Local-global parcellation of the human cerebral cortex from intrinsic functional connectivity MRI. *Cerebral Cortex, 28*, 3095-3114. doi:10.1093/cercor/bhx179

Seghier, M., & Price, C. (2012). Functional heterogeneity within the default network during semantic processing and speech production. *Frontiers in Psychology, 3*, 281. doi:10.3389/fpsyg.2012.00281

Seghier, M. L., Fagan, E., & Price, C. J. (2010). Functional subdivisions in the left angular gyrus where the semantic system meets and diverges from the default network. *The Journal of Neuroscience, 30*, 16809-16817. doi:10.1523/JNEUROSCI.3377-10.2010

Serences, J. T. (2004). A comparison of methods for characterizing the event-related BOLD timeseries in rapid fMRI. *NeuroImage, 21*, 1690-1700. doi:10.1016/j.neuroimage.2003.12.021

Sheehan, D. V., Lecrubier, Y., Sheehan, K. H., Amorim, P., Janavs, J., Weiller, E., . . . Dunbar, G. C. (1998). The Mini-International Neuropsychiatric Interview (MINI): The development and validation of a structured diagnostic psychiatric interview for DSM-IV and ICD-10. *The Journal of Clinical Psychiatry, 59*, 22-33.

Slifstein, M., van de Giessen, E., Van Snellenberg, J., Thompson, J. L., Narendran, R., Gil, R., . . . Abi-Dargham, A. (2015). Deficits in prefrontal cortical and extrastriatal dopamine release in schizophrenia: A positron emission tomographic functional magnetic resonance imaging study. *JAMA Psychiatry, 72*, 316-324. doi:10.1001/jamapsychiatry.2014.2414

Steffener, J., Habeck, C. G., & Stern, Y. (2012). Age-related changes in task related functional network connectivity. *PLoS ONE, 7*, e44421. doi:10.1371/journal.pone.0044421

Sternberg, S. (1966). High-speed scanning in human memory. *Science, 153*, 652-654. doi:10.1126/science.153.3736.652

Stone, J. V. (2004). *Independent component analysis: A tutorial introduction*. Cambridge, Mass: MIT Press.

Stuss, D. T. (2006). Frontal lobes and attention: Processes and networks, fractionation and integration. *Journal of the International Neuropsychological Society, 12*, 261-271. doi:10.1017/S1355617706060358

Stuss, D. T. (2011). Functions of the frontal lobes: Relation to executive functions. *Journal of the International Neuropsychological Society, 17*, 759-765. doi:10.1017/S1355617711000695

Sui, J., Adali, T., Pearlson, G., Yang, H., Sponheim, S. R., White, T., & Calhoun, V. D. (2010). A CCA + ICA based model for multi-task brain imaging data fusion and its application to schizophrenia. *NeuroImage, 51*, 123-134. doi:10.1016/j.neuroimage.2010.01.069

Takane, Y., & Hunter, M. A. (2001). Constrained principal component analysis: A comprehensive theory. *Applicable Algebra in Engineering, Communication and Computing, 12*, 391-419. doi:10.1007/s002000100081

Turkeltaub, P. E., Eden, G. F., Jones, K. M., & Zeffiro, T. A. (2002). Meta-analysis of the functional neuroanatomy of single-word reading: Method and validation. *NeuroImage, 16*, 765-780. doi:10.1006/nimg.2002.1131

Van Snellenberg, J. X., Girgis, R. R., Horga, G., van de Giessen, E., Slifstein, M., Ojeil, N., . . . Abi-Dargham, A. (2016). Mechanisms of working memory impairment in schizophrenia. *Biological Psychiatry, 80*, 617-626. doi:10.1016/j.biopsych.2016.02.017

Vasic, N., Walter, H., Sambataro, F., & Wolf, R. C. (2009). Aberrant functional connectivity of dorsolateral prefrontal and cingulate networks in patients with major depression during working memory processing. *Psychological Medicine, 39*, 977-987. doi:10.1017/S0033291708004443

Vatansever, D., Menon, D. K., Manktelow, A. E., Sahakian, B. J., & Stamatakis, E. A. (2015). Default mode dynamics for global functional integration. *The Journal of Neuroscience, 35*, 15254-15262. doi:10.1523/JNEUROSCI.2135-15.2015

Wechsler, D. (2008). *Wechsler Adult Intelligence Scale* (4th ed.). San Antonio, TX: Pearson.

Wechsler, D. (2009). *WMS-IV: Wechsler Memory Scale-Fourth Edition*. San Antonio, TX: Pearson.

Wobrock, T., Falkai, P., Schneider-Axmann, T., Hasan, A., Galderisi, S., Davidson, M., . . . Fleischhacker, W. W. (2013). Comorbid substance abuse in first-episode schizophrenia: Effects on cognition and psychopathology in the EUFEST study. *Schizophrenia Research, 147*, 132-139. doi:10.1016/j.schres.2013.03.001

Wolf, R. C., Sambataro, F., Vasic, N., Schönfeldt-Lecuona, C., Ecker, D., & Landwehrmeyer, B. (2008). Aberrant connectivity of lateral prefrontal networks in presymptomatic Huntington's disease. *Experimental Neurology, 213*, 137-144. doi:10.1016/j.expneurol.2008.05.017

Wong, C. G., & Stevens, M. C. (2012). The effects of stimulant medication on working memory functional connectivity in attention-deficit/hyperactivity disorder. *Biological Psychiatry, 71*, 458-466. doi:10.1016/j.biopsych.2011.11.011

Woodward, T. S., Cairo, T. A., Ruff, C. C., Takane, Y., Hunter, M. A., & Ngan, E. T. (2006). Functional connectivity reveals load dependent neural systems underlying encoding and maintenance in verbal working memory. *Neuroscience, 139*, 317-325. doi:10.1016/j.neuroscience.2005.05.043

Woodward, T. S., Feredoes, E., Metzak, P. D., Takane, Y., & Manoach, D. S. (2013). Epoch-specific functional networks involved in working memory. *NeuroImage, 65*, 529-539. doi:10.1016/j.neuroimage.2012.09.070

Woodward, T. S., Leong, K., Sanford, N., Tipper, C. M., & Lavigne, K. M. (2016). Altered balance of functional brain networks in schizophrenia. *Psychiatry Research: Neuroimaging, 248*, 94-104. doi:10.1016/j.pscychresns.2016.01.003

Wykes, T., Huddy, V., Cellard, C., McGurk, S. R., & Czobor, P. (2011). A meta-analysis of cognitive remediation for schizophrenia: Methodology and effect sizes. *American Journal of Psychiatry, 168*, 472-485. doi:10.1176/appi.ajp.2010.10060855

Yeo, B. T., Krienen, F. M., Sepulcre, J., Sabuncu, M. R., Lashkari, D., Hollinshead, M., . . . Buckner, R. L. (2011). The organization of the human cerebral cortex estimated by intrinsic functional connectivity. *Journal of Neurophysiology, 106*, 1125-1165. doi:10.1152/jn.00338.2011

Yuan, P., & Raz, N. (2014). Prefrontal cortex and executive functions in healthy adults: A meta-analysis of structural neuroimaging studies. *Neuroscience & Biobehavioral Reviews, 42*, 180-192. doi:10.1016/j.neubiorev.2014.02.005